Effects of Polar Compounds on the Dynamics and Dielectric Properties of Room-Temperature Ionic Liquids

Dissertation
zur Erlangung des
Doktorgrades der Naturwissenschaften
(Dr. rer. nat.)
der Naturwissenschaftlichen Fakultät IV
Chemie und Pharmazie
der Universität Regensburg

vorgelegt von
Johannes Hunger
aus Kothmaißling

Regensburg 2009

Promotionsgesuch eingereicht am:	21.12.2009
Tag des Kolloquiums:	29.01.2010
Die Arbeit wurde angeleitet von:	Apl. Prof. Dr. R. Buchner
Prüfungsausschuss:	Apl. Prof. Dr. R. Buchner Prof. Dr. W. Kunz Prof. Dr. O. S. Wolfbeis Prof. em. Dr. Dr. h.c. J. Barthel (Vorsitzender)

meinen Eltern
und
Conny

Ein Problem zeigt sich des Angriffs wert,
wenn es sich dagegen wehrt.

Piet Hein

Contents

Vorwort

Diese Doktorarbeit entstand in der Zeit von September 2006 bis Dezember 2009 am Institut für Physikalische und Theoretische Chemie der naturwissenschaftlichen Fakultät IV – Chemie und Pharmazie – der Universität Regensburg.

An erster Stelle möchte ich mich bei Herrn Apl. Prof. Dr. Richard Buchner für die Erteilung des Themas und sein Interesse am Fortschreiten der Arbeit bedanken. Die großzügige Gewährung von akademischen Freiräumen und gleichzeitige Unterstützung und stete Bereitschaft zur Diskussion haben wesentlich zum Gelingen dieser Arbeit beigetragen.

Weiterhin gilt mein Dank dem Leiter des Lehrstuhls, Herrn Prof. Dr. Werner Kunz für die großzügige Unterstützung.

Ferner möchte ich mich bei den zahlreichen internationalen und nationale Kooperationspartnern bedanken, ohne deren Hilfe und Zuwendungen große Teile dieser Arbeit nicht möglich gewesen wären:

- Herrn Prof. Dr. Glenn Hefter, Murdoch University, Western Australia, sowie der ganzen Hefter Family, dafür dass sie mir zwei Forschungsaufenthalte in Perth, Australien ermöglicht haben. Die dort gesammelten Erfahrungen sind für mich von von unschätzbarem Wert.

- Herrn Dr. M. Walther, Freiburger Materialforschungszentrum (FMF), Institut für molekulare und optische Physik, Freiburg, sowie Herrn Dipl. Phys. A. Thoman für die Zusammenarbeit auf dem Gebiet der THz-Spektroskopie von Flüssigkeiten.

- Herrn Prof. Dr. Klaas Wynne und Herrn Dr. David Turton, Department of Physics, University of Strathclyde, für die fruchtbare Zusammenarbeit auf dem Gebiet der Ferninfrarot und Optischen-Kerr-Effekt-Spektroskopie.

- Herrn Prof. Dr. K. Marsh, Department of Chemical and Process Engineering, University of Canterbury und Prof. Dr. E. May, School of Mechanical Engineering, The University of Western Australia (UWA) sowie Herrn Dr. M. Kandil für die freundliche Aufnahme an der UWA und für die einzigartige Gelegenheit Studien an reinen Lösungsmitteln durchzuführen.

- Herrn Prof. Dr. O. Steinhauser, Department of Computational Biological Chemistry, University of Vienna, Austria sowie Herrn Dr. C. Schröder für Zusammenarbeit und das Bereitstellen Ihrer Molekulardynamik Ergebnisse.

- Frau Prof. Dr. M. Bešter-Rogač, Faculty of Chemistry and Chemical Technology, University of Ljubljana, Slovenia, für die Kooperation auf dem Gebiet Leitfähigkeitsmessungen.

Allen Mitarbeitern und Kollegen des Lehrstuhls danke ich für die freundschaftliche Atmosphäre, stete Hilfsbereitschaft, und auch für die außer-universitären Aktivitäten. Im Besonderen möchte ich die aktuellen, sowie ehemaligen Kollegen des AK Buchner, Herrn M. Phil. Hafiz Rahman, Herrn Dr. Simon, Schrödle, Frau M. Phil. Saadia Shaukat, Herrn Dipl. Chem. Alexander Stoppa und Herr Dr. Wolfgang Wachter hervorheben. Ohne deren Unterstützung hätten sich die letzten Jahre bei Weitem nicht so angenehm gestaltet. Ferner möchte ich allen Mitgliedern der mittäglichen Kaffeerunde besonders für die nicht-akademischen Diskussionen danken.

Der deutschen Forschungsgemeinschaft (DFG) sei für die Finanzierung sowie der Bereitstellung der Mittel zur Durchführung des Projektes im Rahmen des Schwerpunktprogramms 1191 gedankt.

Nicht zuletzt möchte ich allen Mitarbeitern der Werkstätten für die schnelle und gewissenhafte Erledigung der Aufträge meinen Dank aussprechen und meine besondere Hochachtung zum Ausdruck bringen.

Constants and symbols

Constants

Elementary charge	e_o	$= 1.60217739 \cdot 10^{-19}\,\mathrm{C}$
Electric field constant	ε_o	$= 8.854187816 \cdot 10^{-12}\,\mathrm{C^2(Jm)^{-1}}$
Avogadro's constant	N_A	$= 6.0221367 \cdot 10^{23}\,\mathrm{mol^{-1}}$
Speed of light	c	$= 2.99792458 \cdot 10^{8}\,\mathrm{m\,s^{-1}}$
Boltzmann's constant	k_B	$= 1.380658 \cdot 10^{-23}\,\mathrm{J\,K^{-1}}$
Permittivity of vacuum	μ_0	$= 4\pi \cdot 10^{-7}\,\mathrm{(Js)^2(C^2m)^{-1}}$
Planck's constant	h	$= 6.6260755 \cdot 10^{-34}\,\mathrm{Js}$

Symbols

$\vec{B}$	magnetic induction ($\mathrm{Vs\,m^{-2}}$)	$\vec{D}$	electric induction ($\mathrm{C\,m^{-2}}$)
ω	angular frequency ($\mathrm{s^{-1}}$)	$\vec{j}$	current density ($\mathrm{A\,m^{-2}}$)
$\vec{E}$	electric field strength ($\mathrm{V\,m^{-1}}$)	$\hat{\varepsilon}$	complex dielectric permittivity
$\vec{H}$	magnetic field strength ($\mathrm{A\,m^{-1}}$)	ε'	real part of $\hat{\varepsilon}$
$\vec{P}$	polarization ($\mathrm{C\,m^{-2}}$)	ε''	imaginary part of $\hat{\varepsilon}$
τ	relaxation time (s)	ε_∞	$\lim_{\nu\to\infty}(\varepsilon')$
η	viscosity (Pa s)	ε_s	$\lim_{\nu\to 0}(\varepsilon')$
T	temperature (K)	μ	dipole moment (C m)
t	time (s)	ν	frequency (Hz)
c	molarity ($\mathrm{mol\ dm^{-3}}$)	m	molality ($\mathrm{mol\ kg^{-1}}$)
κ	conductivity ($\mathrm{S\ m^{-1}}$)	ρ	density ($\mathrm{kg\,m^{-3}}$)

Acronyms

AN	acetonitrile	BI	N-butylimidazole
BN	benzonitrile	CC	Cole-Cole
CD	Cole-Davidson	CIP	contact ion-pair
D	Debye	DCA	dicyanamide
DCM	dichloromethane	DHO	damped harmonic oscillator
DMA	N,N-dimethylacetamide	DMF	N,N-dimethylformamide
DMSO	dimethylsulfoxide	DR(S)	dielectric relaxation (spectroscopy)
FIR	far-infrared	HN	Havriliak-Negami
IFM	interferometer	IL	ionic liquid
IR	infrared	KWW	Kohlrausch-Williams-Watt
MD	molecular dynamics	MeOH	methanol
MI	N-methylimidazole	NMR	nuclear magnetic resonance
NTf_2	bis(trifluoromethylsulfonyl)-imide	OKE	optical Kerr effect
PC	propylene carbonate	PRT	platinum resistance thermometer
PTFE	polytetrafluoroethylene	QM	quantum mechanics
RTIL	room temperature ionic liquid	SED	Stokes-Einstein-Debye
SIP	solvent separated ion-pair	SSIP	double solvent separated ion-pair
TDR	time-domain reflectometry	THz-TDS	terahertz time-domain spectroscopy
TI	triple ion-pair	vdW	van der Waals
VFT	Vogel-Fulcher-Tammann	VNA	vector network analyzer

Introduction

Ionic liquids

Ionic liquids (ILs) are defined as salts having a melting point below 100 °C. Especially room temperature ionic liquids (RTILs) have attracted particular interest over the last two decades.

The first RTIL consisting of solely ionic species was ethylammonium nitrate, discovered by Walden in 1914,[1] but it did not draw any significant attention at that time. The interest in room temperature molten salts emerged as late as 1992, when Wilkes *et al*[2] reported an air and water stable imidazolium salt. In particular, after a paper entitled "Designer solvents – ionic liquids may boost clean technology development" was published by Freemantle[3] about 10 years ago and highlighted the outstanding properties of ionic liquids, the interest of research groups all over the world became extraordinarily high. Nowadays about 1400 publications dealing with ionic liquids appear On RTILs in one year and a review is published every couple of days.[4]

Since the first studies, focusing on ionic liquids appeared, they were often considered as "designer solvents" or "green solvents" for various applications due their unique physicochemical properties, such as their wide liquidus temperature range,[5] low vapor pressure,[6] high thermal stability,[7] and large electrochemical window.[8] However, following increased attention over the last decade, it has been shown that ILs do not have zero vapor pressure,[6] that some analytical data on thermal stability might be misleading,[9] and that their toxicity is frequently underestimated.[10] Also the initially stated stability with respect to water has to be revised for some compounds.[11]

Nevertheless, there are about 10^6 possible combinations of different anions and cations expected to yield ionic liquids, in contrast to approximately 600 conventional molecular solvents currently used in industry.[12] Consequently, there are 10^{12} binary and 10^{18} ternary possible combinations. Therefore, it is indeed justified to consider ILs as "designer-solvents", since a compound can be optimized for any particular application by judicious combination of anion and cation. Hence, ILs are often considered as future solvents for catalysis,[13,14] chemical reactions,[15,16] extraction processes[17] or electrochemical applications.[18–20]

In 2006, at the beginning of this thesis work, the dielectric properties of RTILs were almost unexplored. The dielectric constants, ε, ranks among the most important dielectric properties and is a characteristic solvent property relevant amongst others for its solvation abilities. In the early days of IL research, the "polarity" was mainly deduced from empirical correlations using solvochromatic measurements,[21] which require a probe molecule

dissolved in the RTIL (dyes). Consequently, these measurements can not access a real bulk property, but can only provide information about their local environment. The lack of dielectric constants, being a bulk property related to the polarity, stems from the electrical conductance of the samples making traditional capacitance measurements not applicable.[22] Thus, the dielectric constant has to be obtained by determining the dielectric spectra and extrapolating to zero frequency. However, this method, dielectric relaxation spectroscopy (DRS), is experimentally more elaborate but besides the extraction of the dielectric constant, additional valuable information about the dynamics of these systems can be gained.[23,24]

Except for two early studies on the dielectric spectrum of ethylammonium nitrate at gigahertz frequencies in 2001[25] and terahertz spectra of 1-ethyl-3-methylimidazolium triflate mixed with acetonitrile in 2002[26] the interest in the dielectric properties of ILs emerged only in 2006. At the beginning of this thesis work very few publications about the dielectric properties of ILs had appeared. These reports focused either only on the estimation of the dielectric constant[27,28] or were limited with respect to the frequency range and the variety of investigated RTILs.[29,30] Also for mixtures of ILs with traditional molecular solvents, apart from two studies being limited to THz frequencies[26] or to very few compositions,[29] not much was known. As a natural consequence, most of these studies did not allow any detailed conclusions to be made about dynamics, and quantitative analysis was generally not attempted. Thus, the obtainable information, that can be deduced from the frequency dependent dielectric properties was not fully utilized.

Moreover, a wide spread range of dielectric constants could be found in literature (see e.g. Ref. 11 for an overview). Beside some studies applying inappropriate techniques to determine ε , also the model for the extrapolation from the dielectric spectra used at that time was problematic and consequently the uncertainty in the static permittivities in the early papers might have been underestimated, as will become apparent in this thesis.

Aims of this study

The general aim of this study is the application of dielectric spectroscopy at frequencies ranging from megahertz to terahertz to this new class of liquids. The present work can be subdivided into two parts:

First a detailed study of the dielectric spectra of a number of neat ILs is described. Additional insight into the dynamical mechanisms will be gained by measuring the dielectric spectra over a wide range of temperatures. The activation parameters so obtained yield more information on dynamical properties and permit a critical evaluation of the models used to describe the spectra. Simultaneously, the investigated frequency range will be enlarged to 89 GHz, compared to previous studies that were limited to $\nu \leq 20$ GHz, using the present equipment available in Regensburg. For selected ILs the spectral range will be enhanced to terahertz and far-infrared frequencies to fully characterize all relevant inter- and intramolecular modes in these substances. A special focus of these studies will be to elucidate the dynamics, by comparing the broad-band measurements to molecular dynamic simulations and to other experiments aiming at the dynamics because such comparisons did not give a coherent picture prior to the commencement of this work.

The second focus lies on the investigation of mixtures of ILs with polar solvents. Especially, the crossover from ionic-liquid-like dynamics to classical electrolyte-like behavior is of particular interest for many applications of ILs as solvents. At the beginning of this work there was only one dielectric study of binary mixtures of an IL with dichloromethane, indicating the formation of stable ion-pairs at low concentrations, which is rather common feature of traditional electrolyte solutions.[29] However, due to the limited number of compositions studied, the potential power of DRS was not fully exploited. Studies of binary mixtures in this work will focus on a detailed analysis of the dynamics and interactions within the mixtures as well as on the quantification of these ion-pairs. Hence, the transition from electrolyte solution to IL can be specified and also the influence of the solvent polarity on this transition will be addressed.

To address all matters mentioned above, high precision dielectric data over a broad range of frequencies are essential. Thus, this study will additionally focus on the development and evaluation of suitable experimental methods. Especially for the incorporation of far-infrared data, mathematical methods will be developed to obtain the dielectric spectra at these frequencies. Also at microwave frequencies, the experimental equipment based on a vector network analyzer (VNA) will be improved, evaluated, and new mathematical methods for data processing will be presented.

Of the vast range of RTILs currently available, those containing substituted imidazolium cations have been the most intensively studied.[31] This study will focus on these model ILs, because they are well characterized with respect to their physicochemical properties and they can be readily prepared in high purity and their stability has been studied extensively.

Chapter 1

Theoretical background

1.1 Basics of electrodynamics

1.1.1 Maxwell and constitutive equations

Interaction of electromagnetic fields with matter is based on the four Maxwell equations.[32,33] These four equations

$$\vec{\mathrm{rot}}\,\vec{H} = \vec{j} + \frac{\partial}{\partial t}\vec{D} \tag{1.1}$$

$$\vec{\mathrm{rot}}\,\vec{E} = -\frac{\partial}{\partial t}\vec{B} \tag{1.2}$$

$$\mathrm{div}\,\vec{D} = \rho_{\mathrm{el}} \tag{1.3}$$

$$\mathrm{div}\,\vec{B} = 0 \tag{1.4}$$

express the generation of electric fields (electric field strength, $\vec{E}$; Gauss's law, eq. 1.3) due to electric charges (electric charge density, ρ_{el}), the absence of magnetic monopoles (eq. 1.4), the generation of magnetic fields, $\vec{H}$ (magnetic field strength), by electrical currents (extended Ampère's law, eq. 1.1), and the induction of electric fields by time-dependent magnetic fields (Faraday's law of induction, eq. 1.2). $\vec{B}$ and $\vec{D}$ account for the magnetic and electric induction (magnetic flux density or electric displacement field), respectively.
Together with the Newton equation

$$m\frac{\partial^2}{\partial t^2}\vec{r} = q(\vec{E} + \vec{v} \times \vec{B}) \tag{1.5}$$

where q denotes a moving charge and $\vec{v}$ its velocity, eqs. 1.1 - 1.4 form a complete set of linear partial differential equations which theoretically allows the calculation of all kinds of electromagnetic phenomena.

For homogeneous, non-dispersive, isotropic materials, this set of equations is supplemented by the three constitutive equations,

$$\vec{D} = \varepsilon\varepsilon_0\vec{E} \tag{1.6}$$

$$\vec{j} = \kappa\vec{E} \tag{1.7}$$

$$\vec{B} = \mu\mu_0\vec{H} \tag{1.8}$$

where the $\vec{D}$ and $\vec{H}$ are related to $\vec{E}$ and $\vec{B}$ by time- and field strength-independent scalars (material properties): the relative electrical permittivity, ε, specific conductivity, κ, and relative magnetic permeability, μ. The quantities ε_0 and μ_0 are the absolute permittivity and permeability of free space, respectively.
eqs. 1.6 - 1.8 are valid only for the special case of a time-independent field response.

1.1.2 The electric displacement field

Considering the dynamic case, i.e. an harmonically oscillating electric field $\vec{E}$ of amplitude $\vec{E}_0$ and angular frequency $\omega = 2\pi\nu$,

$$\vec{E}(t) = \vec{E}_0\cos(\omega t) \tag{1.9}$$

condensed matter shows above a certain frequency, typically in the region of 1 MHz to 1 GHz, a significant phase delay, $\delta(\omega)$, between the electric field and the electric displacement field due to interaction or inertia within the system:

$$\vec{D}(t) = \vec{D}_0\cos(\omega t - \delta(\omega)) \tag{1.10}$$

Splitting eq. 1.10

$$\vec{D}(t) = \vec{D}_0\cos(\delta(\omega))\cos(\omega t) + \vec{D}_0\sin(\delta(\omega))\sin(\omega t) \tag{1.11}$$

and introducing

$$\vec{D}_0\cos(\delta(\omega)) = \varepsilon'(\omega)\varepsilon_0\vec{E}_0 \tag{1.12}$$

$$\vec{D}_0\sin(\delta(\omega)) = \varepsilon''(\omega)\varepsilon_0\vec{E}_0 \tag{1.13}$$

the electric displacement field can be expressed as follows

$$\vec{D}(t) = \varepsilon'(\omega)\varepsilon_0\vec{E}_0\cos(\omega t) + \varepsilon''(\omega)\varepsilon_0\vec{E}_0\sin(\omega t) \tag{1.14}$$

Accordingly, the relation between $\vec{D}(t)$ and $\vec{E}(t)$ is not longer characterized by an amplitude $\vec{D}_0$ and a phase shift $\delta(\omega)$, but by the real (in-phase response, dispersive part)

and an imaginary part (out-of-phase response, dissipative part) of the complex (relative) permittivity,

$$\hat{\varepsilon}(\omega) = \varepsilon'(\omega) - \mathrm{i}\varepsilon''(\omega) \tag{1.15}$$

To simplify the mathematical treatment, complex field vectors $\hat{\vec{E}}(t)$ and $\hat{\vec{D}}(t)$ are introduced:

$$\hat{\vec{E}}(t) = \vec{E}_0 \cos(\omega t) + \mathrm{i}\vec{E}_0 \sin(\omega t) = \vec{E}_0 \exp(\mathrm{i}\omega t) \tag{1.16}$$

$$\hat{\vec{D}}(t) = \vec{D}_0 \cos(\omega t - \delta) + \mathrm{i}\vec{D}_0 \sin(\omega t - \delta) = \vec{D}_0 \exp[\mathrm{i}(\omega t - \delta)] \tag{1.17}$$

Consequently, for the non-static case, the constitutive equations (eqs. 1.6 - 1.8) have to be rewritten as[34]

$$\hat{\vec{D}}(t) = \hat{\varepsilon}(\omega)\varepsilon_0 \hat{\vec{E}}(t) \tag{1.18}$$

$$\hat{\vec{j}}(t) = \hat{\kappa}(\omega)\hat{\vec{E}}(t) \tag{1.19}$$

$$\hat{\vec{B}}(t) = \hat{\mu}(\omega)\mu_0 \hat{\vec{H}}(t) \tag{1.20}$$

with the complex conductivity $\hat{\kappa}(\omega)$, and the complex relative magnetic permeability, $\hat{\mu}$. Thus, eqs. 1.18 - 1.20 in their complex representation extend the description to the frequency-dependent linear dielectric response of a dissipative system to alternating electromagnetic fields.

1.1.3 Wave equations

For harmonically oscillating electromagnetic fields,

$$\hat{\vec{E}}(t) = \vec{E}_0 \cos(\mathrm{i}\omega t) \tag{1.21}$$

$$\hat{\vec{H}}(t) = \vec{H}_0 \cos(\mathrm{i}\omega t) \tag{1.22}$$

the Maxwell equation (eq. 1.1) can be expressed as

$$\vec{\mathrm{rot}}\, \vec{H}_0 = (\hat{\kappa}(\omega) + \mathrm{i}\omega\hat{\varepsilon}(\omega)\varepsilon_0)\vec{E}_0 \tag{1.23}$$

including the complex constitutive equations (eqs. 1.18 - 1.20). Accordingly, eq. 1.2 can be transformed, yielding:

$$\vec{\mathrm{rot}}\, \vec{E}_0 = -\mathrm{i}\omega\hat{\mu}(\omega)\mu_0 \vec{H}_0 \tag{1.24}$$

Application of the rotation operator to eq. 1.23 in combination with eq. 1.24 and the Legendre vectorial identity,

$$\vec{\mathrm{rot}}\, \vec{\mathrm{rot}}\, \vec{H}_0 = \vec{\mathrm{grad}}\, \mathrm{div}\, \vec{H}_0 - \Delta\vec{H}_0 = \vec{\mathrm{grad}}\, (0) - \Delta\vec{H}_0 = -\Delta\vec{H}_0 \tag{1.25}$$

the reduced wave equation of the magnetic field is obtained:

$$\Delta\vec{H}_0 + \hat{k}^2\vec{H}_0 = 0 \tag{1.26}$$

The propagation constant, $\hat{k}$, in eq. 1.26 is given by

$$\hat{k}^2 = k_0^2\left(\hat{\mu}(\omega)\hat{\varepsilon}(\omega) + \frac{\hat{\mu}(\omega)\hat{\kappa}(\omega)}{\mathrm{i}\omega\varepsilon_0}\right) \tag{1.27}$$

where k_0 is the propagation constant of free space, $k_0 = \omega\sqrt{\varepsilon_0\mu_0} = 2\pi/\lambda_0$ with the wavelength of a monochromatic wave in vacuum, λ_0. In the case of a solenoidal medium ($\mathrm{div}\,\vec{E} = 0$) a reduced wave equation for $\vec{E}$ can be obtained:

$$\Delta\hat{\vec{E}}_0 + \hat{k}^2\hat{\vec{E}}_0 = 0 \tag{1.28}$$

In the case of non-magnetizable systems ($\hat{\mu} = 1$), the complex propagation constant, eq. 1.27, reduces to

$$\hat{k}^2 = k_0^2\left(\hat{\varepsilon}(\omega) + \frac{\hat{\kappa}(\omega)}{\mathrm{i}\omega\varepsilon_0}\right) \equiv k_0^2\hat{\eta}(\omega) \tag{1.29}$$

where $\hat{\eta}$ is the generalized complex permittivity, $\hat{\eta} = \eta' - \mathrm{i}\eta''$ with its real part, $\eta'(\omega) = \varepsilon'(\omega) - \frac{\kappa''(\omega)}{\omega\varepsilon_0}$ and the imaginary part, $\eta''(\omega) = \varepsilon''(\omega) + \frac{\kappa'(\omega)}{\omega\varepsilon_0}$.
The previous definitions show that the dielectric properties and the conductivity of the system cannot be measured independently. In order to split the two contributions, the dc conductivity $\hat{\kappa}(0) = \kappa'(0)$ is used to calculate the complex dielectric permittivity, $\hat{\varepsilon}(\omega)$, from the (experimentally accessible) generalized complex permittivity $\hat{\eta}(\omega)$:

$$\varepsilon'(\omega) = \eta'(\omega) \tag{1.30}$$

and

$$\varepsilon''(\omega) = \eta''(\omega) - \frac{\kappa'(0)}{\omega\varepsilon_0} \tag{1.31}$$

Using this approach $\hat{\varepsilon}(\omega)$ contains all contributions to the time dependent polarization, $\hat{\vec{P}}(t)$, that depend on frequency, irrespective of their rotational, vibrational, or translational character.
However, the theory of Debye and Falkenhagen[35] suggests some dispersion of the complex conductivity, $\hat{\kappa}$, of electrolyte solutions due to the relaxation of the ion cloud, i.e. the rearrangement of the ion cloud around an ion as a consequence of the translational movement of the ion. However, from an experimental point of view, this effect can be neglected[36] at frequencies relevant to this work and translational contributions to $\hat{\varepsilon}(\omega)$ should be negligible.

1.2 Dielectric relaxation

1.2.1 Polarization

The electric displacement field $\hat{\vec{D}}$ can be split into two contributions,

$$\hat{\vec{D}} = \hat{\varepsilon}\varepsilon_0\hat{\vec{E}} = \varepsilon_0\hat{\vec{E}} + \hat{\vec{P}} \tag{1.32}$$

with

$$\hat{\vec{P}} = (\hat{\varepsilon} - 1)\varepsilon_0\hat{\vec{E}} \tag{1.33}$$

where $\hat{\vec{P}}$ is the polarization describing the effect of an electric field on the medium, while $\varepsilon_0\hat{\vec{E}}$ is independent of the medium. The macroscopic definition[34] of $\hat{\vec{P}}$ can be microscopically divided into two contributions,

$$\hat{\vec{P}} = \hat{\vec{P}}_\mu + \hat{\vec{P}}_\alpha \tag{1.34}$$

the dipolar (orientational) polarization

$$\hat{\vec{P}}_\mu = \sum_k \rho_k \langle\vec{\mu}_k\rangle \tag{1.35}$$

and the induced polarization

$$\hat{\vec{P}}_\alpha = \sum_k \rho_k \alpha_k (\hat{\vec{E}}_\mathrm{i})_k \tag{1.36}$$

The orientational polarization (eq. 1.35) originates in the partial alignment of molecular dipoles of species k with dipole moment $\vec{\mu}_k$ and number density, ρ_k, as a consequence of the applied external field; the effect is countered by the thermal motion of the dipoles.
The induced polarization refers to the generation of an electrical dipole due to the molecular polarizability, α_k, of a particle originating in the displacement of electrons or atoms by the inner field, $(\hat{\vec{E}}_\mathrm{i})_k$, acting at the position of the particle.
Orientational polarization in liquids occurs at pico- to nanosecond timescales, corresponding to an approximate frequency scale of 1 MHz to 10 THz. Due to the coupling of the reorienting dipoles with the surrounding medium rather broad bands are observed. Nevertheless, determination of the frequency dependent complex permittivity can provide valuable insights into the dynamics of liquids.
The value of $\hat{\vec{P}}_\alpha$ is rather constant in the microwave frequency range although its frequency dependence at infrared frequencies yields information about the intramolecular dynamics of the system. Generally, it is a superposition of two contributions, atomic polarization at infrared frequencies (intramolecular vibrations) and electronic polarization in the ultraviolet range. The absorbtion peaks are in most cases more narrow compared to those at microwave frequencies.[37]

Due to the different time scales of $\hat{\vec{P}}_\mu$ and $\hat{\vec{P}}_\alpha$, both effects are generally well separated and can be regarded as linearly independent.[38] Thus the induced polarization can be incorporated into the infinite frequency permittivity, ε_∞:

$$\hat{\vec{P}}_\mu = \varepsilon_0(\hat{\varepsilon} - \varepsilon_\infty)\hat{\vec{E}} \tag{1.37}$$

$$\hat{\vec{P}}_\alpha = \varepsilon_0(\varepsilon_\infty - 1)\hat{\vec{E}} \tag{1.38}$$

Moreover, at THz and far infrared frequencies dielectric dispersion can occur due to librations (restricted rotations), which are often described as tumbling motions of the dipoles. The origin of these restricted rotations lies in the interactions (e.g. hydrogen bonding) with other molecules. Additional absorbtion can originate in intermolecular vibrations, of strongly bound systems. These contribution are generally observed at far infrared frequencies and are sometimes known as "liquid lattice" bands and the phenomenon is sometimes known as Poley-type librational absorbtion.[39]

For heterogeneous systems dielectric processes in the MHz frequency range can arise additionally from polarization at the interfaces of the system (interfacial polarization).[32,34,40]

1.2.2 Response functions of the orientational polarization

At sufficiently high frequencies the orientational polarization decreases, because the molecular dipoles cannot align parallel to the alternating field due to inertia and friction. Atomic polarization also occurs only close to its resonance frequencies. In the case of a linear medium, $\hat{\vec{P}}$ is related to $\hat{\vec{E}}$ via certain response functions.

A linear medium is characterized by the applicability of the superposition principle, i.e. if a field $\vec{E}_1$ creates a polarization $\vec{P}_1$ and field $\vec{E}_2$ a polarization $\vec{P}_2$, then the polarization $\vec{P}_1 + \vec{P}_2$ is generated by the field $\vec{E}_1 + \vec{E}_2$.

This can be illustrated by an isotropic linear dielectric material exposed to a static field $\vec{E}$ generating a polarization, $\vec{P}$. At a time $t = 0$, the field is switched off and a decay of the polarization is observed.

Assuming an instantaneous decay of the electronic polarization, $\vec{P}_\mathrm{e}$, without any delay, the remaining orientational polarization can be expressed as,

$$\hat{\vec{P}}(t) = \hat{\vec{P}}(0) \cdot F_P(t) \quad \text{with} \quad F_P(0) = 1, \quad F_P(\infty) = 0 \tag{1.39}$$

where $F_P(t)$ is the step response function defined as

$$F_P(t) = \frac{\langle \vec{P}(0) \cdot \vec{P}(t) \rangle}{\langle \vec{P}(0) \cdot \vec{P}(0) \rangle} \tag{1.40}$$

An experimental method utilizing this principle is time domain reflectometry (TDR).[41] In the case of a harmonic field of $\hat{\vec{E}}(t)$ $(= \hat{\vec{E}}_0 \exp(-\mathrm{i}\omega t))$ the polarization at any time t can be expressed as

$$\hat{\vec{P}}(\omega, t) = \varepsilon_0(\varepsilon - \varepsilon_\infty)\hat{\vec{E}}(t) \int_0^\infty \exp(-\mathrm{i}\omega t') f_P(t')\mathrm{d}t' \tag{1.41}$$

with

$$\int_0^\infty \exp(-\mathrm{i}\omega t') f_P(t')\mathrm{d}t' = \mathcal{L}_{\mathrm{i}\omega}[f_P(t')] \tag{1.42}$$

where $\mathcal{L}_{iw}[f_P(t')]$ is the Laplace transformed pulse response function of the orientational polarization. The latter can be obtained from the negative derivative of the normalized step response function

$$f_P(t') = -\frac{\partial F_P(t-t')}{\partial(t-t')} \quad \text{normalized with} \quad \int_0^\infty f_P(t')\mathrm{d}t' = 1 \tag{1.43}$$

Consequently, the complex permittivity, $\hat{\varepsilon}(\omega)$, can be calculated via[34]

$$\hat{\varepsilon}(\omega) = \varepsilon'(\omega) - \mathrm{i}\varepsilon''(\omega) = \varepsilon_\infty + (\varepsilon - \varepsilon_\infty) \cdot \mathcal{L}_{\mathrm{i}\omega}[f_P(t')] = \varepsilon_\infty + (\varepsilon - \varepsilon_\infty) \cdot F_j(\omega) \tag{1.44}$$

where $F_j(\omega)$ is the representation of the response function in the frequency domain.

1.3 Empirical description of dielectric relaxation

Various empirical and semi-empirical equations have been suggested in the literature for the description of dielectric relaxation phenomena. As the majority of the spectra represent a sum of various relaxation processes the best description of the spectra can be achieved by a superposition of various equations.

1.3.1 Debye equation

The simplest approach to model dielectric spectra of liquids is the Debye equation.[42] The basic assumption is a decrease of the orientational polarization in the absence of an external electric field directly proportional to the polarization itself[43] resulting in a time law of the first order,

$$\frac{\partial}{\partial t}\vec{P}_\mu(t) = -\frac{1}{\tau}\vec{P}_\mu(t) \tag{1.45}$$

where τ represents the relaxation time, characteristic for the dynamics of the system. Solution of the first order differential equation yields the step response function, $F_P(t) = \exp(-t/\tau)$:

$$\vec{P}_\mu(t) = \vec{P}_\mu(0)\exp\left(-\frac{t}{\tau}\right) \tag{1.46}$$

The pulse response function can be obtained according to eq. 1.43

$$f_P(t) = \frac{1}{\tau}\exp\left(-\frac{t}{\tau}\right) \tag{1.47}$$

By application of the Laplace transformation, the pulse response function in the time-domain is converted to the frequency domain according to eq. 1.44 yielding finally the response function of the Debye equation in its complex presentation

$$F_j(\omega) = \frac{1}{1 + \mathrm{i}\omega\tau} \tag{1.48}$$

The dispersion curve, $\varepsilon' = \varepsilon'(\ln(\omega))$, is a monotonically decreasing point-symmetric function and the absorption curve, $\varepsilon'' = \varepsilon''(\ln(\omega))$, an axis-symmetric band reaching its maximum at $\omega = 1/\tau$.

1.3.2 Extensions of the Debye equation

The dielectric spectra of a considerable number of condensed systems deviate from the mono-exponential relaxation of the Debye equation. Description of these spectra can be improved by assuming a continuous relaxation time distribution, $G(\tau)$.[34] For practical

reasons, a logarithmic distribution, $G(\ln\tau)$, is preferred. The complex permittivity can then be expressed as

$$F_j(\omega) = \int_0^\infty \frac{G(\ln\tau)}{(1+\mathrm{i}\omega\tau)}\mathrm{d}\ln\tau \quad \text{with} \quad \int_0^\infty G(\ln\tau)\mathrm{d}\ln\tau = 1 \tag{1.49}$$

Unfortunately, $G(\ln\tau)$ cannot be obtained from the experimental data in a straightforward manner. Nevertheless, empirical parameters can be introduced that account for the broadness and shape of the relaxation time distribution. Some of the common empirical equations yielding relaxation time distributions will be presented in the following section.

Cole-Cole equation

A symmetrical relaxation time distribution around a principal relaxation time τ_0 is modelled by introducing an additional empirical parameter $\alpha \in [0..1]$. Thus, the Cole-Cole equation[44,45] is

$$F_j = \frac{1}{1+(\mathrm{i}\omega\tau_0)^{1-\alpha}} \tag{1.50}$$

which results in flatter dispersion curves and broadened absorption spectra. For $\alpha = 0$, the Cole-Cole equation reduces to the Debye equation.

Cole-Davidson equation

The Cole-Davidson equation[46,47] with an empirical parameter $\beta \in [0..1]$, describes an asymmetric relaxation time distribution around the center of gravity τ_0

$$F_j = \frac{1}{(1+\mathrm{i}\omega\tau_0)^{\beta}} \tag{1.51}$$

The modification results in asymmetric dispersions and absorption curves. For $\beta = 1$, eq. 1.51 becomes equivalent to the Debye equation.

Havriliak-Negami equation

Introduction of both parameters $\alpha \in [0..1]$ and $\beta \in [0..1]$, yields the Havriliak-Negami equation describing a broad asymmetric relaxation time distribution:[48]

$$F_j = \frac{1}{(1+(\mathrm{i}\omega\tau_0)^{1-\alpha})^{\beta}} \tag{1.52}$$

Both the dispersion and absorption curves are asymmetric. For $\alpha = 0$ and $\beta = 1$ this equation simplifies to the Debye equation.
For time-domain dielectric data, the Kohlrausch-Williams-Watts[49] (KWW) model is generally preferred as it can be derived from mode coupling theory. There is no exact equivalent of KWW in the frequency domain but to a good approximation it corresponds to a Havriliak-Negami model with restrictions on the values of α and β.[34,50]

Modified Cole-Cole equation

Contributions of a relaxation function at frequencies where librational modes (see section below) occur are physically unreasonable, because a relaxation process evolves from librational fluctuations.[51] This means that the assumption of linearly independent processes is not valid anymore. The Debye equation, and even worse due to the broadening, the Cole-Cole and Cole-Davidson equations contribute considerably at THz and far-infrared frequencies. To avoid this unphysical behavior the relaxation equations have to be terminated at high frequencies by including an upper boundary. Following the approach suggested by Turton and Wynne,[52] this can be realized by subtracting a fast exponential decay characterized by an initial rise rate, γ_{lib}, determined by the librational frequencies, yielding:

$$F_j = \frac{1}{1-(1+\gamma_{\mathrm{lib}}\tau_0)^{-(1-\alpha)}} \cdot \left(\frac{1}{(1+(\mathrm{i}\omega\tau)^{1-\alpha}} - \frac{1}{1+(\mathrm{i}\omega\tau+\gamma_{\mathrm{lib}}\tau)^{1-\alpha}} \right) \tag{1.53}$$

According to Turton and Wynne,[52] γ_{lib} is higher than than the measured librational frequencies, because it represents a rise time rather than a full oscillation. Therefore, $\gamma_{\mathrm{lib}} \approx \langle\omega_{\mathrm{lib}}\rangle/(2\pi)$, where $\langle\omega_{\mathrm{lib}}\rangle$ is the average resonance angular frequency of the librational modes (see below).
If the relaxation process is dependent on a lower frequency mode, Turton and Wynne,[52] additionally introduced a low frequency termination, deduced from the relaxation behavior of glass forming liquids. This "α-termination" is described in detail elsewhere.[52]

1.3.3 Damped harmonic oscillator

Many vibrational dielectric processes (intermolecular and intramolecular vibrations as well as librations) can be modelled satisfactorily by harmonic oscillation.[39] Assuming a harmonic oscillator driven by a harmonically oscillating field $E(t) = E_0 e^{\mathrm{i}\omega t}$ which is subject to a damping force that is linearly dependent upon the velocity $\partial x(t)/\partial t$, the time-dependent motion $x(t)$ of an effective charge q can be obtained from the solution of the differential equation

$$m\frac{\partial^2}{\partial t^2}x(t) + m\gamma\frac{\partial}{\partial t}x(t) + kx(t) = qE(t) = qE_0 e^{\mathrm{i}\omega t} \tag{1.54}$$

derived from Newton's equation, eq. 1.5. With a characteristic angular resonance frequency $\omega_0 = \sqrt{k/m} = 2\pi\nu_0$ and a damping constant $\gamma = 1/(2\pi\tau_{\mathrm{D}})$, eq. 1.54 can be written as

$$\frac{\partial^2}{\partial t^2}x(t) + \tau_{\mathrm{D}}^{-1}\frac{\partial}{\partial t}x(t) + \omega_0^2 x(t) = \frac{qE_0}{m}e^{\mathrm{i}\omega t} = Ce^{\mathrm{i}\omega t} \tag{1.55}$$

where τ_{D} is the characteristic damping time and $C = qE_0/m$ a constant.

Solving eq. 1.55 yields

$$x(t) = \frac{C}{\omega_0^2 - \omega^2 + \mathrm{i}\omega\tau_\mathrm{D}^{-1}} e^{\mathrm{i}\omega t} \tag{1.56}$$

The oscillation of the effective charge q results in a time dependent polarization, defined by the total overall dipole moment per unit volume, $P(t) = \rho q x(t)$, where ρ is the resonator number density.
From an extension of eq. 1.37 to a polarization caused by a resonance type dielectric dispersion, the complex permittivity can be expressed by eq. 1.57.

$$\hat{\varepsilon}(\omega) - \varepsilon_\infty = \frac{P(t)}{\varepsilon_0 E(t)} = \frac{\rho q x(t)}{\varepsilon_0 E_0 e^{\mathrm{i}\omega t}} \tag{1.57}$$

Taking eq. 1.56 into account, the damped oscillation can be written in terms of complex permittivity $\hat{\varepsilon}(\omega)$:

$$\hat{\varepsilon}(\omega) - \varepsilon_\infty = \frac{P(t)}{\varepsilon_0 E(t)} = \frac{\rho q^2}{\varepsilon_0 m} \frac{1}{(\omega_0^2 - \omega^2 + \mathrm{i}\omega\tau_\mathrm{D}^{-1})} \tag{1.58}$$

For a static field (eq. 1.6) the low frequency limit,

$$\varepsilon = \hat{\varepsilon}(0) = \varepsilon_\infty + \frac{\rho q^2}{\varepsilon_0 m \omega_0^2} \tag{1.59}$$

is obtained. Combination of eq. 1.58 and 1.59 yields the frequency dependent response function of the system:

$$F_j(\omega) = \frac{\omega_0^2}{(\omega_0^2 - \omega^2) + \mathrm{i}\omega\tau_\mathrm{D}^{-1}} = \frac{\nu_0^2}{\nu_0^2 - \left(\frac{\omega}{2\pi}\right)^2 + \mathrm{i}\frac{\omega}{2\pi}\gamma} \tag{1.60}$$

In the limit of $\tau_\mathrm{D} \ll \omega_0^{-1}$, i.e. the damping time constant is much shorter than an oscillation period, the response reproduces the Debye equation.

1.3.4 Combination of models

For many real systems the complex permittivity spectrum is composed of several relaxation processes. In these cases the complex permittivity spectrum can be modelled by a superposition of n single relaxation processes:

$$\hat{\varepsilon}(\omega) = \varepsilon_\infty + \sum_{j=1}^{n} (\varepsilon_j - \varepsilon_{\infty,j}) F_j(\omega) \tag{1.61}$$

Each of the processes is treated as linearly independent with its own response function, $F_j(\omega)$, and dispersion amplitude, S_j:

$$\varepsilon - \varepsilon_\infty = \sum_{j=1}^{n} (\varepsilon_j - \varepsilon_{\infty,j}) = \sum_{j=1}^{n} S_j \tag{1.62}$$

where

$$\varepsilon_{\infty,j} = \varepsilon_{j+1} \tag{1.63}$$

1.4 Microscopic models of dielectric relaxation

In contrast to the previous sections, which described dielectric relaxation without considering the molecular structure of the system, now the macroscopic properties will be linked to microscopic properties.

1.4.1 Onsager equation

The Onsager model[34,53] describes the response of a single dipole embedded in a continuum, characterized by its macroscopic properties. Specific interactions and the anisotropy of the surrounding field are neglected.
Based on this approach, Onsager deduced following relation for the interpretation of dielectric properties

$$\varepsilon_0(\varepsilon - 1)\vec{E} = \vec{E}_\mathrm{h} \cdot \sum_j \frac{\rho_j}{1 - \alpha_j f_j} \left(\alpha_j + \frac{1}{3k_\mathrm{B}T} \cdot \frac{\mu_j^2}{1 - \alpha_j f_j} \right) \tag{1.64}$$

where ρ_j is the dipole density, α_j the polarizability, f_j the reaction field factor and μ_j the dipole moment of species j.
$\vec{E}_\mathrm{h}$ represents the cavity field which equals

$$\vec{E}_\mathrm{h} = \frac{3\varepsilon}{2\varepsilon + 1}\vec{E} \tag{1.65}$$

given the molecule is embedded in a spherical cavity in a continuum dielectric material of permittivity ε.
Combination of eq. 1.65 and eq. 1.64 yields the general form of the Onsager equation,

$$\frac{(\varepsilon - 1)(2\varepsilon + 1)\varepsilon_0}{3\varepsilon} = \sum_j \frac{\rho_j}{1 - \alpha_j f_j} \left(\alpha_j + \frac{1}{3k_\mathrm{B}T} \cdot \frac{\mu_j^2}{1 - \alpha_j f_j} \right) \tag{1.66}$$

In the case of a liquid, consisting of one dipolar component, that exhibits only one dielectric dispersion step, eq. 1.66 simplifies to

$$\frac{(\varepsilon - \varepsilon_\infty)(2\varepsilon + \varepsilon_\infty)}{\varepsilon(\varepsilon_\infty + 2)^2} = \frac{\rho\mu^2}{9\varepsilon_0 k_\mathrm{B}T} \tag{1.67}$$

1.4.2 Kirkwood-Fröhlich equation

Specific intermolecular interactions can be introduced with the help of statistical mechanics. The theory[54,55] is based on a model of a dipole whose orientation correlates with its neighboring dipoles resulting in the Kirkwood-Fröhlich equation,

$$\frac{(\varepsilon - \varepsilon_\infty)(2\varepsilon + \varepsilon_\infty)}{\varepsilon(\varepsilon_\infty + 2)^2} = \frac{\rho\mu^2}{9\varepsilon_0 k_\mathrm{B}T} \cdot g_\mathrm{K} \tag{1.68}$$

where g_K is the Kirkwood factor, which is a measure for the interactions among the particles. A value of $g_\mathrm{K} > 1$ represents preferentially parallel orientation of neighboring particles

whereas $g_K < 1$ indicates an antiparallel correlation. The value $g_K = 1$ is observed for statistical (i.e., fully random) alignment.

1.4.3 Cavell equation

The Cavell equation[56] is a more general expression describing systems with more than one dispersion step due to different dipolar species. It can be written as

$$\frac{\varepsilon + A_j(1-\varepsilon)}{\varepsilon} \cdot \Delta S_j = \frac{N_A c_j}{3 k_B T \varepsilon_0} \cdot \mu_{\mathrm{eff},j}^2 \tag{1.69}$$

This equation relates the amplitude S_j of such a mode to the effective dipole moment $\mu_{\mathrm{eff},j}$ of the molecular-level species j, of molar concentration c_j, responsible for that process. A_j is a shape factor for the molecule. The value of $\mu_{\mathrm{eff},j}$ (which can be calculated using eq. 1.69 if c_j is known) is related to $\mu_{\mathrm{ap},j}$, the apparent dipole moment of the species in solution in the absence of correlations, as

$$\mu_{\mathrm{eff},j} = \sqrt{g_j}\mu_{\mathrm{ap},j} \tag{1.70}$$

where

$$\mu_{\mathrm{ap},j} = \mu_j/(1 - f_j\alpha_j) \tag{1.71}$$

includes cavity- and reaction-field effects on μ_j, the dipole moment of the isolated (gas phase) species. These two effects depend on the field factor, f_j, and the polarizability, α_j, of the dipolar species j, while the factor g_j is a measure of their orientational correlations in the liquid. Note that in contrast to the well-known Kirkwood factor (eq. 1.68) for pure dipolar liquids, g_K, which can be directly traced to the molecular-level environment of the dipoles through statistical mechanics,[34] g_j is an empirical quantity that is defined through eqs. 1.69 - 1.71.
For a spherical cavity of radius a_j, the reaction field factor is given as[34]

$$f_j = \frac{1}{4\pi\varepsilon_0 a_j^3} \cdot \frac{2\varepsilon - 2}{2\varepsilon + 1} \tag{1.72}$$

and $A_j = 1/3$. For ellipsoidal particles with half-axes $a_j > b_j > c_j$ the reaction field factor and shape factor can be calculated from the geometry of the particle:[34,37]

$$f_j = \frac{3}{4\pi\varepsilon_0 a_j b_j c_j} \cdot \frac{A_j(1-A_j)(\varepsilon - 1)}{\varepsilon + (1-\varepsilon)A_j} \tag{1.73}$$

and

$$A_j = \frac{a_j b_j c_j}{2} \int_0^\infty \frac{\mathrm{d}s}{(s + a_j^2)^{3/2}(s + b_j^2)^{1/2}(s + c_j^2)^{1/2}} \tag{1.74}$$

1.4.4 Debye model of rotational diffusion

To relate the relaxation time to molecular properties, Debye assumed a simple system consisting of an aggregation of spherical inelastic dipoles which do not interact with each other. Microscopically, uncorrelated collisions of the dipolar particles results in a reorientation of dipoles. Therefore, this mechanism is called diffusion of dipolar orientation. [42]
However, as inertia effects and dipole-dipole interaction are neglected, this theory is limited to non-associated systems. Within these limitations and by describing the inner field with a Lorentz field, Debye obtained the dipole correlation function,

$$\gamma(t) = \exp\left(-\frac{t}{\tau_{\mathrm{rot}}}\right) \tag{1.75}$$

where the relaxation time, τ_{rot}, can be calculated from the friction factor, ζ,

$$\tau_{\mathrm{rot}} = \frac{\zeta}{2k_{\mathrm{B}}T} \tag{1.76}$$

Assuming a hydrodynamically controlled rotation of the sphere in a viscous media, the Stokes-Einstein-Debye equation

$$\tau_{\mathrm{rot}} = \frac{3V_{\mathrm{m}}\eta'}{k_{\mathrm{B}}T} \tag{1.77}$$

is obtained, where V_{m} represents the volume of the sphere and η' the dynamic viscosity of the environment of the sphere. However, the application of this theory is limited as the relation between macroscopic (measured) and microscopic viscosity is not clear. For example, the viscosity of water situated in the coordination sphere of solvated particles (microscopic viscosity) differs from the bulk-water value (macroscopic viscosity).
A more general expression for the microscopic relaxation time was derived by Dote *et al.* [57] by introducing an effective volume of rotation required by a particle, V_{eff}:

$$\tau_{\mathrm{rot}} = \frac{3V_{\mathrm{eff}}\eta}{k_{\mathrm{B}}T} + \tau^0_{\mathrm{rot}} \tag{1.78}$$

The empirical axis intercept, τ^0_{rot}, is occasionally interpreted as the correlation time of the freely rotating particle. V_{eff} accounts for the difference between macroscopic and microscopic viscosity by introducing a hydrodynamic friction factor, C, as well as for deviations from spherical shape, characterized by the shape factor f:

$$V_{\mathrm{eff}} = fCV_{\mathrm{m}} \tag{1.79}$$

where V_{m} is the molecular volume of the particle. C is generally treated as an empirical parameter, but its limiting values for *stick* ($C_{\mathrm{stick}} = 1$) and *slip* ($C_{\mathrm{slip}} = 1 - f^{-2/3}$) friction boundary conditions are known.

The shape parameter f can be calculated from the geometry of the molecule,

$$f = \frac{\frac{2}{3}[1-(\alpha^{\perp})^4]}{\frac{[2-(\alpha^{\perp})^2](\alpha^{\perp})^2}{[1-(\alpha^{\perp})^2]^{1/2}} \ln\left[\frac{1+[1-(\alpha^{\perp})^2]^{1/2}}{\alpha^{\perp}}\right] - (\alpha^{\perp})^2} \tag{1.80}$$

where where $\alpha^{\perp}$ represents the ratio between the volume of the particle and the volume swept out as the particle rotates about an axis perpendicular to the symmetry axis. For a prolate spheroid with major axis a and minor axis b, $\alpha^{\perp} = b/a$.[58]

1.4.5 Microscopic and macroscopic relaxation time

The experimentally accessible dielectric relaxation time, τ, is a collective property[34] and has to be converted into the corresponding rotational correlation time, τ_{rot}. There are various theoretical approaches that address this problem.
Debye suggested the relation[42]

$$\tau = \frac{\varepsilon + 2}{\varepsilon_{\infty} + 2} \cdot \tau_{\mathrm{rot}} \tag{1.81}$$

by assuming that the particle is exposed to a Lorentz field (inner field). However, this approach is not accurate enough for polar dielectrics and applies only to non-polar systems. Powles and Glarum[59,60] proposed following expression

$$\tau = \frac{3\varepsilon}{2\varepsilon + \varepsilon_{\infty}} \cdot \tau_{\mathrm{rot}} \tag{1.82}$$

for relating macroscopic and microscopic relaxation times, given that the underlying mechanism is due to rotational diffusion.
Allowing for dipole-dipole correlations, the Madden-Kivelson[61] equation has to be used to convert τ into τ_{rot}

$$\tau = \frac{3\varepsilon}{2\varepsilon + \varepsilon_{\infty}} \cdot \frac{g_{\mathrm{K}}}{\dot{g}} \cdot \tau_{\mathrm{rot}} \tag{1.83}$$

where g_{K} is the Kirkwood correlation factor and $\dot{g}$ the dynamic correlation factor. For the limit $g_{\mathrm{K}}/\dot{g} = 1$ eq. 1.83 reduces to the Powles-Glarum equation (eq. 1.82).

1.4.6 Comparison with other techniques

Comparison of τ with relaxation times from other experimental techniques allows conclusions to be drawn on the mechanism behind the observed dielectric relaxation. For rotational diffusion of a molecule, it is expected[34] that the molecular correlation times τ_L of rank L fulfill the relation

$$\tau_L = \frac{2\tau_{\mathrm{rot}}}{L(L+1)} \tag{1.84}$$

where $\tau_{\mathrm{rot}}\,(= \tau_{L=1})$ is the rotational correlation time of a probed intramolecular vector. Correlation times accessible with NMR, Optical-Kerr-Effect or Raman spectroscopy are single-particle relaxation times of rank $L = 2$. Dielectric and infrared spectroscopies probe correlations of rank $L = 1$.

eq. 1.84 is often successfully applied for large solute molecules in a solvent consisting of small solvent molecules and partly to solvents composed of small, rigid molecules. There is a fair number of cases where eq. 1.84 does not hold.[34] This observation can be explained by assuming a reorientation due to instantaneous jumps over considerable angles (non-continuous reorientation).
Assuming a distribution of jump angles, described by the function $K(\Theta)$ the correlation time of rank L can be expressed as:[34]

$$\tau_L = \frac{1}{k(1 - A_L)} \tag{1.85}$$

where k is the probability for a jump and A_L a factor defined as

$$A_L = 1/2 \int_0^{\pi} K(\Theta) \sin \Theta P_L(\cos \theta) \mathrm{d}\Theta \tag{1.86}$$

where P_L is the Legendre polynomial of degree L. The limiting cases are $A_L = 0$ for the absence of any correlation of angles and all correlation times become equal. If only jumps about one angle α occur

$$\tau_L = \frac{1}{k(1 - P_L(\cos \alpha))} \tag{1.87}$$

is obtained.
Consequently, for $\cos \alpha < -1/3$ (i.e. $\alpha > 109.5\,^{\circ}$) τ_1 is smaller than τ_2 meaning that the correlation time of rank $L = 2$ can be slower than the $L = 1$ correlation time. For small angles eq. 1.87 reduces to the relation observed for rotational diffusion (eq. 1.84).

1.5 Temperature dependence of relaxation times

1.5.1 Arrhenius equation

Besides the SED equation (eq. 1.78) temperature dependence of relaxation times can be described by the Arrhenius equation,[62] which represents one of the oldest methods for describing the temperature dependence of rate constants. For relaxation times, this equation typically has the form

$$\ln(\tau/\mathrm{s}) = \ln(\tau_0/\mathrm{s}) + \frac{E_\mathrm{a}}{RT} \tag{1.88}$$

It is based on the assumption that particles are excited by thermal fluctuations to a transition state between two stable energetic levels which are separated by a temperature dependent energetic barrier, E_a, the activation energy. The frequency factor, τ_0, represents the shortest possible relaxation time.

1.5.2 Eyring equation

The theory of Eyring[63] is based on transition state theory. The equation roughly resembles the Arrhenius equation, where $\Delta G^{\neq}$ is the Gibbs energy of activation, with its corresponding enthalpy, $\Delta H^{\neq}$ and entropy, $\Delta S^{\neq}$, components.

$$\tau^{-1} = \frac{k_\mathrm{B}T}{h} \cdot \exp\left(\frac{\Delta G^{\neq}}{RT}\right) \quad \text{with} \quad \Delta G^{\neq} = \Delta H^{\neq} - T\Delta S^{\neq} \tag{1.89}$$

Assuming a constant heat capacity for the transition state, i.e. $\Delta C_\mathrm{p}^{\neq} \neq \mathrm{f}(T)$, the entropy and enthalpy of activation can be expressed as a function of temperature according to thermodynamic laws:

$$\Delta H^{\neq} = \Delta H^{\neq}_{T^0} + \int_{T^0}^{T} \Delta C_\mathrm{p}^{\neq} \mathrm{d}T' \tag{1.90}$$

$$\Delta S^{\neq} = \Delta S^{\neq}_{T^0} + \int_{T^0}^{T} \Delta \frac{C_\mathrm{p}^{\neq}}{T'} \mathrm{d}T' \tag{1.91}$$

where T^0 ($= 298.15\,\mathrm{K}$) is the thermodynamic reference temperature. Introducing the heat capacity finally yields the extended Eyring theory:

$$\ln\tau = -\ln\left(\frac{k_\mathrm{B}\cdot T}{h}\right) + \frac{1}{R}\left[\frac{\Delta H^{\neq}_{T^0}}{T} - \Delta S^{\neq}_{T^0} + \Delta C_\mathrm{p}^{\neq}\left(1 + \ln\left(\frac{T^0}{T}\right) - \frac{T^0}{T}\right)\right] \tag{1.92}$$

1.5.3 Vogel-Fulcher-Tammann equation

For many glass-forming liquids, especially when the supercooled region is being considered, the Vogel-Fulcher-Tammann (VFT) equation[64–66] is commonly used to describe the rapid increase in viscosity at temperatures close to the glass transition temperature. Taking the difference between the macroscopic volume and the thermal volume of a particle into account[67] the William-Landel-Ferry (WLF) equation[68], which is equivalent to the VFT equation is derived for relaxation times. The WLF and VFT equation are connected via the time-temperature superposition principle. In the general representation[69]

$$\ln \tau = \ln \tau_0^{\mathrm{VFT}} + \frac{D_{\mathrm{VFT}} \cdot T_0^{\mathrm{VFT}}}{T - T_0^{\mathrm{VFT}}} \tag{1.93}$$

τ_0^{VFT} is the frequency factor and D_{VFT} the fragility parameter. The critical VFT temperature, T_0^{VFT}, is generally lower than the glass transition temperature[70] and equals the Kautzmann temperature, which is defined by the intersection of the entropy curve of the liquid and the solid.[71–73]

Chapter 2

Experimental

2.1 Materials

2.1.1 Molecular solvents

All molecular solvents used in this study were of analytical grade. Purified water using a Millipore MILLI-Q purification unit, yielding batches with specific resistivity $\geq 18\,\mathrm{M\Omega\,cm^{-1}}$ was used throughout. Propylene carbonate (PC, Sigma-Aldrich, 99.7 %), dimethylsulfoxide (DMSO, Merck, > 99.5 %), methanol (MeOH, Merck, > 99.9 %), *N*,*N*-dimethylacetamide (DMA, Fluka, > 99.8 %), acetonitrile (AN, Merck, > 99.9 %), benzonitrile (BN, Sigma-Aldrich, > 99.9 %), 1-propanol (Merck, > 99.8 %), 2-propanol (Merck, > 99.8 %), 1-butanol (Riedel-de Haën, > 99.5 %) and dichloromethane (DCM, Acros, > 99.9 %) were stored over activated 4 Å molecular sieves.
The purities of solvents used for the preparation of binary mixtures were additionally checked with gas chromatography, yielding > 99.94 % for PC and > 99.99 % for DMSO and DCM, respectively. The water content of PC, DMSO and DCM was always < 20 ppm prior to use as detected by coulometric Karl Fischer titration (Mitsubishi Moisturemeter MCI CA-02).

2.1.2 Ionic liquids

Properties of ionic liquids are very sensitive to various impurities[74] and several are also known to be very hygroscopic.[75] Moreover, there are some ILs that show hydrolysis[76] when in contact with water. The time constant for hydrolysis was investigated for a solution (10 % mass fraction of [bmim][BF_4] in water) yielding a half life time of $\tau \approx 1.2\,\mathrm{d}$ at 25 °C. After 24 h at 50 °C no BF_4^- was detectable with ion chromatography (for details see Ref. 76).
To avoid water impurities, synthesis and if possible measurements were performed under a dry N_2 atmosphere and compounds were stored in a N_2-filled glovebox. Water content and halide impurities were determined with coulometric Karl Fischer titration and potentiometric titration of an aqueous solution of the compound with a $AgNO_3$ standard solution (Carl Roth GmbH), respectively. All compounds were dried in high vacuum ($p < 10^{-8}$ bar)

yielding water contents of < 100 ppm. For all ionic liquids, no impurities were detectable with ^{1}H, ^{19}F, ^{11}B or ^{31}P-NMR, where applicable.

Starting materials For synthesis the of ionic liquids, the purity of the starting materials is crucial, because the compounds themselves are difficult to purify. Molecular solvents used for synthesis were of analytical grade and dried prior to use. For the synthesis of most of the ionic liquids, previously published routes were followed.[77–79]

N-methylimidazole (MI, Merck & Carl Roth, 99 %) as well as *N*-butylimidazole (BI, ABCR, 99 %) were distilled over KOH under reduced pressure and stored over activated molecular sieves (4 Å). Both imidazoles were filtered to remove the molecular sieve and then were distilled under reduced pressure immediately prior to use.

Samples of 1-bromoethane (Merck, $\geq$ 99 %), 1-chlorobutane (Merck, $\geq$ 99 %), 1-chlorohexane (Merck, $\geq$ 99 %) and methyl-2,2,2-trifluoroacetate (ABCR, 99 %) were distilled with a Vigreux fractionating column. The salts $AgBF_4$ (Fluorochem, 99 %), $NaBF_4$ (VWR Prolabo, 98.6 %) and KPF_6 (Fluorochem, 99 %) were used as received. Sodium dicyanamide (Fluka, $\geq$ 96 %) was recrystallized from MeOH. Methyl trifluoromethanesulfonate (Fluorochem, 98 %) was used without further purification.

Imidazolium halides *N*-ethyl-*N*-methylimidazolium bromide ([emim][Br]), *N*-butyl-*N*-methylimidazolium chloride ([bmim][Cl]) and *N*-hexyl-*N*-methylimidazolium chloride ([hmim][Cl]) were obtained by adding a slight molar excess ($n_{\mathrm{RHal}} \sim 1.1 n_{\mathrm{MI}}$) of the appropriate alkyl halide to a stirred solution of MI in AN. The mixtures were refluxed for an appropriate time (1 to 7 days) and conversion was verified with ^{1}H-NMR. The ILs [emim][Br] and [bmim][Cl] were recrystallized thrice from acetonitrile, whereas [hmim][Cl] was washed thrice with ethyl acetate. All imidazolium halides were dried in vacuo.

***N*-ethyl-*N*-methylimidazolium tertrafuoroborate ([emim][BF_4])** A sample of [emim][BF_4] was purchased from (IoLiTec, > 98 %). Although no halide impurities were detectable, an acidic proton of mole fraction < 0.01 was present in the ^{1}H-NMR spectrum, with a chemical shift of ~ 6.5 ppm.

Alternatively, a second batch of [emim][BF_4] was obtained via anion metathesis ([emim][Br] + $NaBF_4$) and subsequent precipitation of halide impurities with $AgBF_4$. A detailed description of the synthetic route was published previously.[76] Neither halide impurities nor methanolysis products were detectable.

***N*-butyl-*N*-methylimidazolium tertrafuoroborate ([bmim][BF_4])** This compound was obtained via anion metathesis from equimolar amounts of [bmim][Cl] and $NaBF_4$ dissolved in water. The solutions were cooled in an ice bath, to avoid hydrolysis of $[BF_4]^-$ and the resulting [bmim][BF_4] was extracted thrice with DCM. The organic phase was washed with water thrice to remove traces of NaCl and pre-dried over $MgSO_4$. DCM was removed under vacuum, yielding a colorless liquid with halide impurities of < 150 ppm.

***N*-hexyl-*N*-methylimidazolium tertrafuoroborate ([hmim][BF_4])** This salt was obtained from [hmim][Cl] and $NaBF_4$ according to the route described for [bmim][BF_4]. Halide impurities were found to be less than 10 ppm.

***N*-butyl-*N*-methylimidazolium hexafluorophosphate ([bmim][PF_6])** was synthesized from [bmim][Cl] and KPF_6 according to the route described for [bmim][BF_4]. Halide impurities of the colorless IL obtained were < 20 ppm.

***N*-ethyl-*N*-methylimidazolium dicyanamide ([emim][DCA])** The yellowish ionic liquid [emim][DCA] was purchased from (IoLiTec, $> 98\,\%$). Potentiometric titration indicated halide impurities of < 400 ppm.

***N*-butyl-*N*-methylimidazolium dicyanamide ([bmim][DCA])** was obtained by stirring equimolar amounts of [bmim][Cl] and NaDCA overnight. To separate the ionic liquid, an excess of DCM was added and the precipitating NaCl was filtered off. After evaporation of the solvent under vacuum, this procedure was repeated, yielding a slightly yellowish product. The first and second batch of [bmim][DCA] had Cl^- mass fractions of $< 0.5\,\%$ and $< 0.2\,\%$, respectively, as indicated by potentiometric titration.

***N*-butyl-*N*-methylimidazolium trifluoromethanesulfonate ([bmim][TfO])** was synthesized by slow addition of a slight molar excess of methyl trifluoromethanesulfonate to cooled BI. The exothermic reaction was completed by heating to $\sim 65\,°C$ overnight. Conversion was verified with ^{1}H-NMR and the excess methylating agent was evaporated in vacuo, yielding a slightly colored product with no detectable halide impurities.

***N*-butyl-*N*-methylimidazolium trifluoroacetate ([bmim][CF_3CO_2])** was synthesized by slow addition of a slight molar excess of methyl-2,2,2-trifluoroacetate to cooled BI. The exothermic reaction was completed by heating to $\sim 65\,°C$ overnight. Conversion was verified with ^{1}H-NMR and the excess methylating agent was evaporated in vacuo, yielding a slightly yellowish product with no detectable halide impurities.

***N*-ethyl-*N*-methylimidazolium ethylsulfate ([emim][$EtSO_4$])** was purchased from IoLiTec and had a stated purity of $> 99\,\%$. Industrial synthesis is performed via direct alkylation, thus no halide impurities are present.

***N*-ethyl-*N*-methylimidazolium bis(trifluoromethylsulfonyl)imide ([hmim][NTf_2])** was kindly provided by M. Muldoon (University of Notre Dame, USA). The compound has been chosen for the IUPAC standard ionic liquid.[80] The halide content was determined to be < 10 ppm.

***N*-methyl-*N*-ethylpyrrolidinium dicyanamide ([$p_{1,2}$][DCA])** was kindly provided by D. R. MacFarlane (Monash University, Australia). Stated halide impurities were less than $0.5\,\%$.[81]

2.2 Sample preparation and handling

All samples for measurements were prepared on an analytical balance without buoyancy corrections and thus were accurate to about $\pm 0.2\,\%$ relative. If preparation of samples under air was necessary, this was conducted in glass bottles sealed with a septum, to avoid uptake of water, otherwise samples were prepared in a glove box under a N_2 atmosphere. Due to the possible hydrolysis of $[BF_4]^-$ and $[PF_6]^-$, measurements on aqueous mixtures of compounds containing these anions were performed directly after sample preparation. All measurements on these systems were finished within $< 4\,\mathrm{h}$.
For samples containing DCM, the dry N_2 atmosphere of the more time-consuming interferometer measurements (which typically require 2-3 h) was presaturated with DCM.

2.3 Measurement of dielectric properties

2.3.1 Time-domain reflectometry

Time domain reflectometry (TDR) is capable of determining the dielectric properties of liquids at MHz to low GHz frequencies. The measurement cells consist of coaxial lines terminated by a coaxial line of different dimensions, where the insulating material is replaced by the sample. Ideally, the outer conductor is infinitely continued, while the inner conductor has a certain length, l. At the end of the inner conductor, a coaxial to circular waveguide transition is the electromagnetic boundary condition.[82] Due to a step in the impedance at the coaxial-line sample cell transition, an electromagnetic wave is partly reflected. The complex permittivity measurements are based on the determination of the complex reflection coefficients at this impedance step.[83]

Theory In the TDR experiment a fast rising voltage pulse, $V_0(t)$, is applied to the sample. The dielectric properties of the sample are reflected in the time evolution of the applied pulse $V_0(t)$ compared to the reflected signal, $V_r(t)$.
Application of a Fourier transformation to the time-dependent intensities of the signals yields the intensities in the frequency domain, $v_0(\omega)$ and $v_r(\omega)$:

$$v_0(\omega) = \mathcal{L}_{\mathrm{i}\omega}\left[\frac{\mathrm{d}}{\mathrm{d}t}V_0(t)\right] = \int_0^\infty \frac{\mathrm{d}}{\mathrm{d}t}V_0(t)\cdot\exp(\mathrm{i}\omega t)\mathrm{d}t \tag{2.1}$$

$$v_r(\omega) = \mathcal{L}_{\mathrm{i}\omega}\left[\frac{\mathrm{d}}{\mathrm{d}t}V_r(t)\right] = \int_0^\infty \frac{\mathrm{d}}{\mathrm{d}t}V_r(t)\cdot\exp(\mathrm{i}\omega t)\mathrm{d}t \tag{2.2}$$

These can be used to calculate the absolute complex reflection coefficient of the cell, $\hat{\rho}(\omega)$,

$$\hat{\rho}(\omega) = \frac{c_0}{\mathrm{i}\omega g l}\cdot\frac{\hat{v}_0(\omega)-\hat{v}_r(\omega)}{\hat{v}_0(\omega)+\hat{v}_r(\omega)} \tag{2.3}$$

where l is the pin-length of the inner conductor and g the ratio between the wave resistance of the empty cell and the feeding line. Note, that in the TDR experiment, the coaxial to waveguide transition is accounted for by inserting a slightly elongated, effective electrical pin-length l_{el} into eq. 2.3 (fringing field).
Within some approximations, the generalized complex dielectric permittivity, $\hat{\eta}(\omega)$, can be obtained from $\hat{\rho}(\omega)$ by numerical solution of,

$$\hat{\eta}(\omega) = \hat{\rho}(\omega)\cdot\hat{z}\cot\hat{z} \tag{2.4}$$

where

$$\hat{z} = \frac{\omega l}{c_0}\sqrt{\hat{\eta}(\omega)} \tag{2.5}$$

However, the incident wave is not easily accessible from the measurement. Therefore, a sample of known (and preferably similar) dielectric properties is used as reference, and the

relative reflection coefficient

$$\hat{\rho}_{xr}(\omega) = \frac{c}{\mathrm{i}\omega g l} \cdot \frac{\mathcal{L}_{\mathrm{i}\omega}\left[\frac{\mathrm{d}}{\mathrm{d}t}V_{rr}(t)\right] - \mathcal{L}_{\mathrm{i}\omega}\left[\frac{\mathrm{d}}{\mathrm{d}t}V_{rx}(t)\right]}{\mathcal{L}_{\mathrm{i}\omega}\left[\frac{\mathrm{d}}{\mathrm{d}t}V_{rr}(t)\right] + \mathcal{L}_{\mathrm{i}\omega}\left[\frac{\mathrm{d}}{\mathrm{d}t}V_{rx}(t)\right]} \tag{2.6}$$

is determined. $V_{rx}(t)$ and $V_{rr}(t)$ represent the relative time dependent reflection intensities of the sample and the reference, respectively.[84,85] The relative reflection coefficient is related to the dielectric properties by the working equation,

$$\hat{\rho}_{xr} = \frac{\hat{\eta}_x \cdot \hat{z}_r \cot(\hat{z}_r) - \hat{\eta}_r \cdot \hat{z}_x \cot(\hat{z}_x)}{\hat{z}_r \cot(\hat{z}_r)\hat{z}_x \cot(\hat{z}_x) + g^2 \cdot \hat{\eta}_x \hat{\eta}_r (\omega l/c)^2} \tag{2.7}$$

with

$$\hat{z}_x = \frac{\omega l}{c}\sqrt{\hat{\eta}_x} \quad \text{and} \quad \hat{z}_r = \frac{\omega l}{c}\sqrt{\hat{\eta}_r} \tag{2.8}$$

Numerical solution of eq. 2.7 with a Newton-Raphson procedure and Tailor series expansion of $\hat{z} \cdot \cot \hat{z}$ yields $\hat{\eta}_x(\omega)$.[86]

Instrumentation The experimental setup is sketched in fig. 2.1. The sampling scope (TEK 11802; Tektronix) is connected to sampling heads (SD24), which generate a square wave signal at 200 kHz with a fast rise time (typically 17.5 ps). Each sampling head has two independent channels which are used for the measurement of two cells of the cut-off type. One trace is used for the actual sample measurement, the other one as a time reference to account for drifts of the time base (e.g. due to thermal expansion of the cables). Traces are recorded with a resolution of 5120 points and averaged over 256 single measurements, to improve the signal to noise ratio. Several cells of different dimensions and pin-lengths are available, resulting in different impedances to optimize the signal for different frequency ranges and dielectric properties. Further details are described in detail elsewhere.[83,87,88] However, one has to keep in mind that TDR has some weaknesses with regards to low absorbing liquids[89] and electrolyte solutions[90] and is very sensitive to the pin-length, l. Moreover, imperfections of the feeding line result in further reflections, biasing the results.[90]

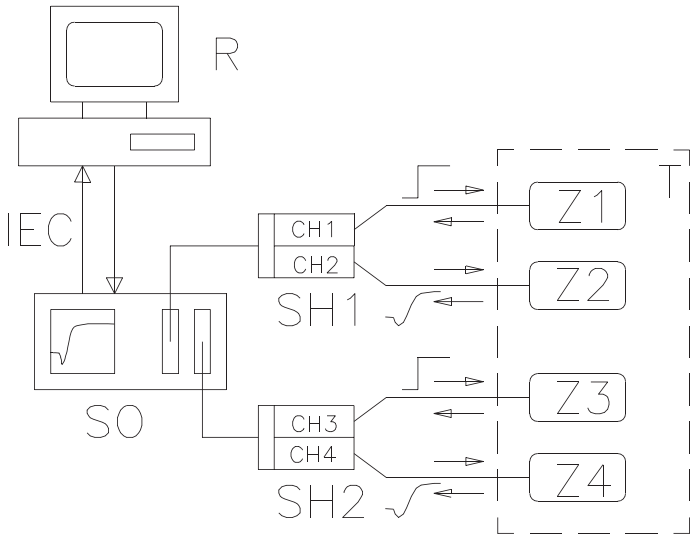

Figure 2.1: Schematic representation[83] of the time-domain reflectometer: **SO** digital sampling scope; **SH1,SH2** SD-24 sampling heads; **Z1-Z4** cutoff cells; **T** precision thermostat; **R** personal computer with access to other computers for data analysis.

2.3.2 Interferometry

At frequencies above $\sim 20\,\mathrm{GHz}$ waveguides become more efficient for the propagation of electromagnetic waves compared to coaxial lines. Therefore waveguide interferometers based on travelling waves are used at these frequencies. Unfortunately, the receivers of the current IFM setup are only capable of detecting the signal amplitude without any information about the phase. Thus, interferometry is required to determine the complex permittivity.
The equipment is based on the transmission principle. The travelling wave is split into a sample path and a reference path containing a phase shifter and a precision attenuator, respectively. The measuring cell itself is made up of a waveguide terminated by a window, containing the sample. A (position) variable, gold plated ceramic probe, acting as a waveguide itself, is immersed in the cell. By variation of the z position of the probe, the optical path length of the sample is altered.

Theory For each frequency, several steps are required to obtain both, the attenuation coefficient and the medium wavelength from a single data set, which is necessary for the determination of $\hat{\eta}(\nu)$. The first step of the procedure requires establishment of a fully destructive interference at an arbitrary probe position z_0' with the help of the attenuators and phase shifters.
Assuming harmonically oscillating fields, the time-dependent electric field propagating through the reference beam is given by

$$\hat{E}_1(t) = E_0 \exp(\mathrm{i}\omega t) \tag{2.9}$$

Assuming z_0 is the absolute optical path length of the transmission cell and x the relative distance from the interference minimum, $x = z_0 - z_0'$, the electromagnetic wave of the sample beam can be expressed as

$$\hat{E}_2(t, x) = E_0 \exp(-\alpha x) \exp\left[\mathrm{i}(\omega t + \pi - \beta x)\right] \tag{2.10}$$

where α is the absorbtion coefficient of the sample and $\beta = 2\pi/\lambda_\mathrm{m}$ the phase coefficient (λ_m is the wavelength in the medium). The term π of the second exponential term results from the condition of fully destructive interference, which requires a phase shift of $\Delta\varphi$ of the interfering waves:

$$\Delta\varphi = (2n + 1)\pi \quad \text{with } n \in \mathbb{Z} \tag{2.11}$$

At the receiver, the superposition of the fields propagating through the sample and reference beam,

$$\hat{E}(t, x) = \hat{E}_1(t) + \hat{E}_2(t, x) = \hat{E}_0 \exp(\mathrm{i}\omega t)\left[1 + \exp(-\alpha x) \exp(\mathrm{i}(\pi - \beta x))\right] \tag{2.12}$$

is detected. The magnitude of the detected signal, P, which is the experimentally accessible quantity, is defined by the squared amplitude of the electric field,

$$P = \hat{E} \cdot \hat{E}^* = E_0^2 \cdot I(x) \tag{2.13}$$

where $I(x)$ is the interference function,

$$\begin{aligned} I(x) &= \left[1 + \exp(-\alpha x) \exp(\mathrm{i}(\pi - \beta x))\right] \cdot \left[1 + \exp(-\alpha x) \exp(\mathrm{i}(\pi - \beta x))\right] && (2.14)\\ &= 1 + \exp(-2\alpha x) + \exp(-\alpha x) \cdot 2\cos(-\pi + \beta x) && (2.15) \end{aligned}$$

The quantity actually measured by the experiment is the relative attenuation of the signal on a logarithmic scale, $A(x)$, eq. 2.16.

$$A(x) = 10 \lg \frac{P(x)}{P_\mathrm{ref}} \tag{2.16}$$

P_ref is usually not known and consequently the measured attenuation is normalized by A_0 corresponding to $P_0 = E_0^2$:

$$\begin{aligned} A_\mathrm{rel}(x) &= A(x) - A_0 \\ &= 10 \lg \frac{P(x)}{P_\mathrm{ref}} - 10 \lg \frac{P_0}{P_\mathrm{ref}} \\ &= 10 \lg \frac{P(x)}{P_0} \\ &= 10 \lg \frac{E_0^2 \cdot I(x)}{E_0^2} \end{aligned} \tag{2.17}$$

The power attenuation coefficient, α_{dB} in dB/m, and the wavelength of the radiation within the sample, $\lambda_{\mathrm{M}} = 2\pi/\beta$ can be obtained from a fit of the recorded interference data $A(z_0 - z_0')$ by the expression[91]

$$\begin{aligned} A(z_0 - z_0') = A_0 + 10\lg\{1 + \exp\left[-2p\alpha_{\mathrm{dB}}(z_0 - z_0')\right] \\ - 2\cos\left(\frac{2\pi}{\lambda_M}(z_0 - z_0')\right) \cdot \exp\left[-2p\alpha_{\mathrm{dB}}(z_0 - z_0')\right]\Big\} \end{aligned} \tag{2.18}$$

with the conversion constant

$$p = \left(20\lg e \cdot \frac{dB}{Np}\right)^{-1} \tag{2.19}$$

The medium wavelength, λ_{M} and the absorbtion coefficient α are subsequently converted to permittivity data,

$$\eta'(\nu) = \left[\left(\frac{1}{\lambda_{\mathrm{c},10}^{\mathrm{vac}}}\right)^2 + \left(\frac{1}{\lambda_{\mathrm{M}}(\nu)}\right)^2 - \left(\frac{\alpha(\nu)}{2\pi}\right)^2\right]\left(\frac{c_0}{\nu}\right)^2 \tag{2.20}$$

$$\eta''(\nu) = \frac{\alpha(\nu)}{\pi\lambda_{\mathrm{M}}(\nu)}\left(\frac{c_0}{\nu}\right)^2 \tag{2.21}$$

where $\lambda_{\mathrm{c},10}^{\mathrm{vac}}$ is the limiting vacuum frequency, characteristic for the waveguide dimensions.

Instrumentation The double-beam interferometers with variable path-length transmission cells are described in detail elsewhere.[91] The IFMs are operated in a certain frequency range corresponding to microwave band nomenclature: X-band $8.5 \leq \nu/\mathrm{GHz} \leq 12$, Ku-band $12.5 \leq \nu/\mathrm{GHz} \leq 18$, A-band $27 \leq \nu/\mathrm{GHz} \leq 40$ and E-band $60 \leq \nu/\mathrm{GHz} \leq 89$, determined by the waveguide dimensions. Note that due to recent developments, interferometric measurements are only required at $60 \leq \nu/\mathrm{GHz} \leq 89$, while for the remaining bands transmission measurements with a vector network analyzer are performed (see below). The setup of the E-band interferometer is schematically shown in fig. 2.2. A frequency stabilized signal is split by a directional coupler into the measuring and reference path. The measuring path is composed of a phase shifter and the sample cell. The cell is composed of a piece of wave guide filled with the sample liquid and a waveguide probe with variable, motor-controlled position. A precision attenuator is located in the reference path. The relative amplitude of the recombined beams is measured by a precision attenuation measurement receiver, equipped with proper mixers for frequency conversion, as a function of optical path-length. The relative position of the probe is recorded with a precision gauge.

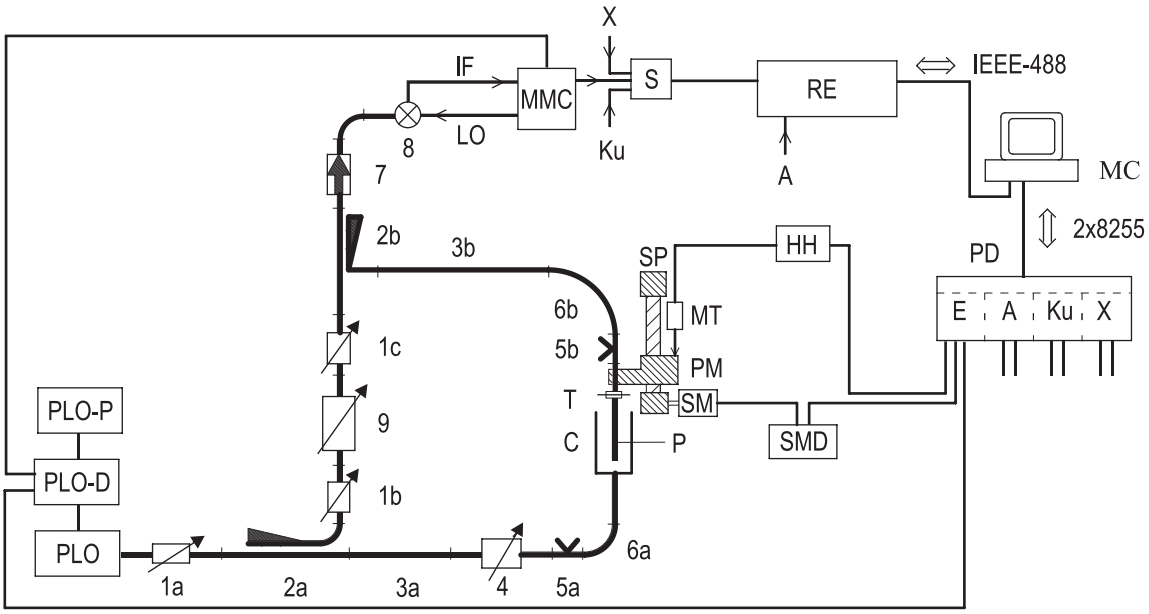

Figure 2.2: Block diagram of the E-band equipment:[91] **1a**, **b**, **c** represent variable attenuators; **2a**, **b** directional couplers; **3a**, **b** waveguide sections; **4** precision phase shifter; **5a**, **b** E/H tuners; **6a**, **b** flexible waveguides; **7** isolator; **8** harmonic mixer; **9** variable precision attenuator; **C** cell, **HH** bidirectional counter; **MC** microcomputer; **MMC** millimeter-wave to microwave converter; **MT** digital length gauge; **P** probe; **PD** parallel interface unit; **PLO** phase locked oscillators; **PLO-D** PLO-control unit; **PLO-P** PLO-power supply; **PM** probe mount; **RE** precision receiver; **S** electromechanical switch; **SM** stepping motor; **SMD** stepping motor control unit; **SP** spindle and spindle mount; **T** tapered transmission; double lines represent waveguides, thick lines semi-rigid microwave cables and normal lines symbolize data transfer connections (analog or digital).

2.3.3 Vector network analysis

Recent technological developments have enhanced the applicability of coaxal lines up to higher frequencies. Two-port instruments that can determine simultaneously the amplitude and phase of electromagnetic waves (vector network analyzers, VNAs) operating at frequencies up to 110 GHz are commercially available. An arbitrary electrical network is analyzed by determining the reflection and transmission of electrical signals, yielding the scattering parameter matrix, $\hat{S}$. For a two-port instrument, as is used in this work, $\hat{S}$ is defined as follows:

$$\begin{pmatrix} \hat{b}_1 \\ \hat{b}_2 \end{pmatrix} = \begin{pmatrix} \hat{S}_{11} & \hat{S}_{12} \\ \hat{S}_{21} & \hat{S}_{22} \end{pmatrix} \begin{pmatrix} \hat{a}_1 \\ \hat{a}_2 \end{pmatrix} \tag{2.22}$$

where $\hat{a}_j$ and $\hat{b}_j$ correspond to the incident and reflected power waves at port j, respectively. In the case of one-port measurements (i.e. measurement of $\hat{S}_{jj}$) the instrument has to be calibrated, correcting errors in directivity, $\hat{e}_\mathrm{d}$, frequency response, $\hat{e}_\mathrm{r}$ and source match,

$\hat{e}_\mathrm{s}$. The scattering parameter, measured by the VNA, $\hat{S}^\mathrm{m}_{jj}$ is then related to the actual scattering parameter at the plane of interest, $\hat{S}^\mathrm{a}_{jj}$, via

$$\hat{S}^\mathrm{m}_{jj} = \hat{e}_\mathrm{d} + \frac{\hat{e}_\mathrm{r}\hat{S}^\mathrm{a}_{jj}}{1 - \hat{e}_\mathrm{s}\hat{S}^\mathrm{a}_{jj}} \tag{2.23}$$

Thus, at least three references have to be measured to calibrate the instrument. For conventional electrical systems open, short and 50 Ω are often used.

In the case of a one-port reflection measurements on an electrical network, consisting of an impedance step from $\hat{Z}_1$ to $\hat{Z}_2$, the complex scattering parameter S_{11}, can be related to the normalized terminating impedance, $\hat{Y} = \hat{Z}_2/\hat{Z}_1$:

$$\hat{S}_{11} = \frac{1 - \hat{Y}}{1 + \hat{Y}}. \tag{2.24}$$

Open-ended coaxial probe

Experiments up to 20 GHz were performed with a Hewlett Packard HP85070B coaxial probe connected to a HP8720D vector network analyzer (VNA) at the institute of Prof. Glenn Hefter, Murdoch University (Western Australia).

Additionally, the dielectric properties up to 50 GHz were studied with a Agilent E8364B vector network analyzer connected to an electronic calibration module (ECal, Agilent N4693A) and a dielectric probe kit (85070E).

The latter setup has various advantages compared to the equipment at Murdoch University. First, the ECal module measures well known reflection standards during the measurement and thus systematic drifts, e.g. phase error due to the thermal expansion of the coaxial lines are compensated. Second, improved mechanical accuracy of coaxial lines and connectors enables reliable measurements up to 50 GHz.

For measurements up to 20 GHz and up to 50 GHz two open-ended coaxial probes are necessary. The sample is in contact with the open-ended coaxial probe. The 20 GHz (high temperature) probe is mounted in a temperature controlled cell as described by Schrödle.[87] A similar cell was designed for the 50 GHz (performance) probe. The low frequency limit of these probes is in principle 0, but due to the small aperture capacitances data were practically reproducible down to 200 MHz and 1 GHz for the high temperature and performance probe, respectively.

The temperature was controlled with a Huber CC505 thermostat and measured with a Agilent 34970A datalogger, by measuring the resistance of a platinum resistance thermometer (PRT, PT-100) in 4-wire configuration. Systematic errors in temperature determination are compensated by measuring the thermoelectric potential separately.

A simplified coaxial aperture opening model[92,93] was used to calculate the complex dielectric properties $\hat{\eta}_\mathrm{m}$ from the normalized aperture impedance of the probe head, $\hat{Y}$, by numerical solution of eq. 2.25,

$$\hat{Y} = \frac{\mathrm{i}\hat{k}_\mathrm{m}^2}{\pi\hat{k}_\mathrm{c}\ln(D/d)}\left[\mathrm{i}\left(I_1 - \frac{\hat{k}_\mathrm{m}^2 I_3}{2} + \frac{\hat{k}_\mathrm{m}^4 I_5}{24} - \frac{\hat{k}_\mathrm{m}^6 I_7}{720} + ...\right) + \left(I_2\hat{k}_\mathrm{m} - \frac{\hat{k}_\mathrm{m}^3 I_4}{6} + \frac{\hat{k}_\mathrm{m}^5 I_6}{120} - ...\right)\right] \tag{2.25}$$

where $\hat{k}_\mathrm{c} = \omega\sqrt{\hat{\eta}_\mathrm{c}\varepsilon_0\mu_0}$ is the propagation constant within the dielectric material of the coaxial probe head and $\hat{k}_\mathrm{m} = \omega\sqrt{\hat{\eta}_\mathrm{m}\varepsilon_0\mu_0}$ the propagation constant of the sample. The first 28 probe constants, I_i, are calculated from a theoretical approach and further optimized,[93] as implemented in the Agilent 85070C software package. The constants d and D are the radii of the inner and outer conductor of the coaxial line, respectively.

Calibration according to eq. 2.23 of the VNA with respect to the probe-sample interface was performed using a three point calibration: open, short and load, namely, air, purified mercury and a reference liquid, with dielectric properties similar to the sample properties. Water, DMA,[94,95] PC[94–96] and DMSO[95] were found to be suitable calibration standards.

If the dielectric properties of the sample deviate from the properties of the reference liquid a secondary calibration of $\hat{\varepsilon}(\nu)$ is necessary. Because systematic deviations are likely to be due to the model for the aperture impedance (eq. 2.25), a secondary calibration on the basis of $\hat{\varepsilon}(\nu)$ values is required. Therefore, a complex Padé approximation[97] was applied to correct raw spectra, $\hat{\varepsilon}_\mathrm{m}$:

$$\hat{\varepsilon}_\mathrm{m}^\mathrm{corr} = P_{n/m}\left[\hat{\varepsilon}_\mathrm{m}\right] = \frac{\hat{A}_0 + \hat{A}_1\hat{\varepsilon}_\mathrm{m} + ... + \hat{A}_n(\hat{\varepsilon}_\mathrm{m})^n}{1 + \hat{B}_1\hat{\varepsilon}_\mathrm{m} + ... + \hat{B}_m(\hat{\varepsilon}_\mathrm{m})^m} \tag{2.26}$$

The approximation constants, $\hat{A}_n(\omega)$ and $\hat{B}_m(\omega)$, required to calculate the corrected spectra, $\varepsilon_\mathrm{m}^\mathrm{corr}$, are obtained either analytically or by a complex linear fit algorithm[86] from a set of measurements of reference substances with known dielectric properties. Water,[87] PC,[94–96] DMA,[94,95] BN[96] and 1-butanol[98] were found to be suitable calibration standards, covering a range from low to high dielectric permittivities. This secondary calibration procedure is excellently suited to improve the accuracy of spectra for samples with low electrical conductivity.[87] A $P_{1/1}$ calibration was found to be sufficient for the samples investigated in this work.

In this work the Padé calibration was also applied to spectra of electrolyte solutions, by inserting the $\hat{\varepsilon}(\nu)$ spectra, already corrected for dc conductivity according to eq. 1.31, into eq. 2.26, but one has to bear in mind, that for electrolyte solutions the aperture impedance has a considerable resistive contribution, whereas for neat solvents the major part is capacitive. This means that the Padé calibration standards cover a different area of $\hat{S}_{11}$ values in the complex plane than the actual (electrolyte) sample. However, due to the lack of suitable electrolytes as calibration standards, this approach seems to be reasonable and systematic errors in the phase of $\hat{S}_{11}$ are corrected by it and the accuracy of the spectra improved. Thus, better agreement with other experimental techniques was achieved. Especially, experimental data of the 50 GHz (performance) probe improved considerably, as shown for an extreme case (aqueous electrolyte solution of high dc conductivity) in fig. 2.3.

However, suitable calibration standards with $\kappa \gg 0$ would be desirable and would probably improve the accuracy for electrolytes.

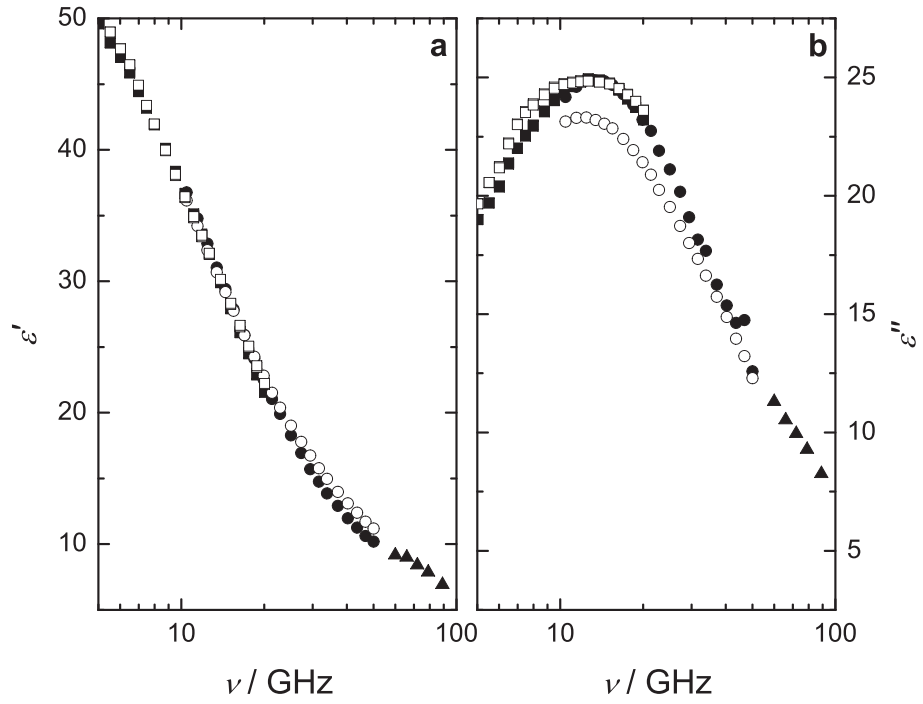

Figure 2.3: Dielectric permittivity (**a**) and loss (**b**) spectrum of $c = 1.21\,\mathrm{mol\,L^{-1}}$ [bmim][Cl] in water ($\kappa = 5.62\,\mathrm{S\,m^{-1}}$). Squares and circles correspond to results obtained with the 20 GHz and the 50 GHz probe head, respectively. Triangles represent results obtained with the E-band IFM. Open symbols correspond to raw data, filled symbols show data corrected with a complex Padé approximation (eq. 2.26) using water, PC and DMA as secondary calibration standards.

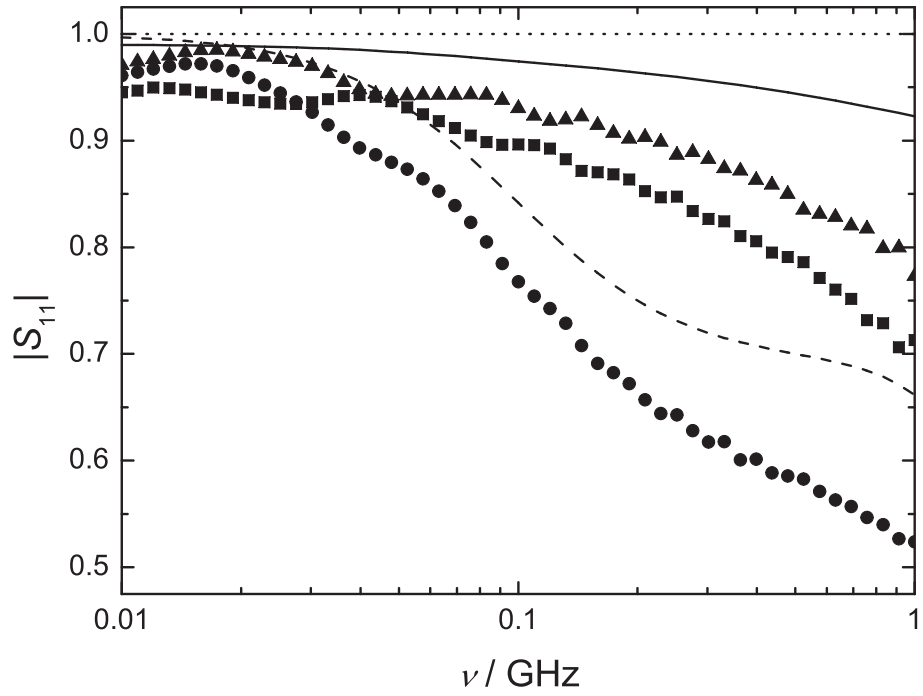

Figure 2.4: Modulus of the complex scattering parameter $|\hat{S}_{11}|$ of three representative references at 25 °C: air (▲, dotted line), 1-propanol[98] (●, dashed line) and NaCl(aq, $m \simeq 5\,\mathrm{mol\,kg^{-1}}$ (■, full line).[99] Symbols represent values at the connector plane, lines correspond to the theoretical values at the coaxial-sample interface (eqs. 2.24 and 2.27).

Cut-off type coaxial cells

As mentioned in section 2.3.1, the TDR equipment has some shortcomings with respect to electrolyte solutions and weakly absorbing liquids. Therefore, reflection coefficients of the cut-off type coaxial cells, as used in the TDR experiment, were measured with the Agilent E8364B vector network analyzer.
The normalized impedance of the cell is given by,[82]

$$\hat{Y} = \left[-2\pi Z_\mathrm{L} \ln\left(\frac{d}{D}\right) \sqrt{\frac{\varepsilon_0}{\mu_0} \cdot \hat{\eta}(\omega)} \tanh\left(\frac{\mathrm{i}\omega l}{c}\sqrt{\hat{\eta}(\omega)}\right) + \mathrm{i}\omega\hat{\eta}(\omega) Z_\mathrm{L} C_\mathrm{s} \right]^{-1} \tag{2.27}$$

where Z_L is the wave resistance of the feeding line (typically 50 Ω) and C_s the discontinuity capacity of the coaxial to circular waveguide transition. In the case of $C_\mathrm{s} = 0$ the electrical model becomes equal to the model used in the TDR experiment (section 2.3.1).[41,86] eqs. 2.24 and 2.27 are solved numerically to obtain the generalized complex permittivity of the sample, $\hat{\eta}(\nu)$.
It has been suggested in the literature[82] to calibrate the VNA by performing an open-short-load calibration of the cable at the connector plugged to the cell, and treat the remaining part (connector - sample plane) as an ideal coaxial line. However, as can be seen in fig. 2.4, the difference between the scattering parameter measured at the connector plane and the

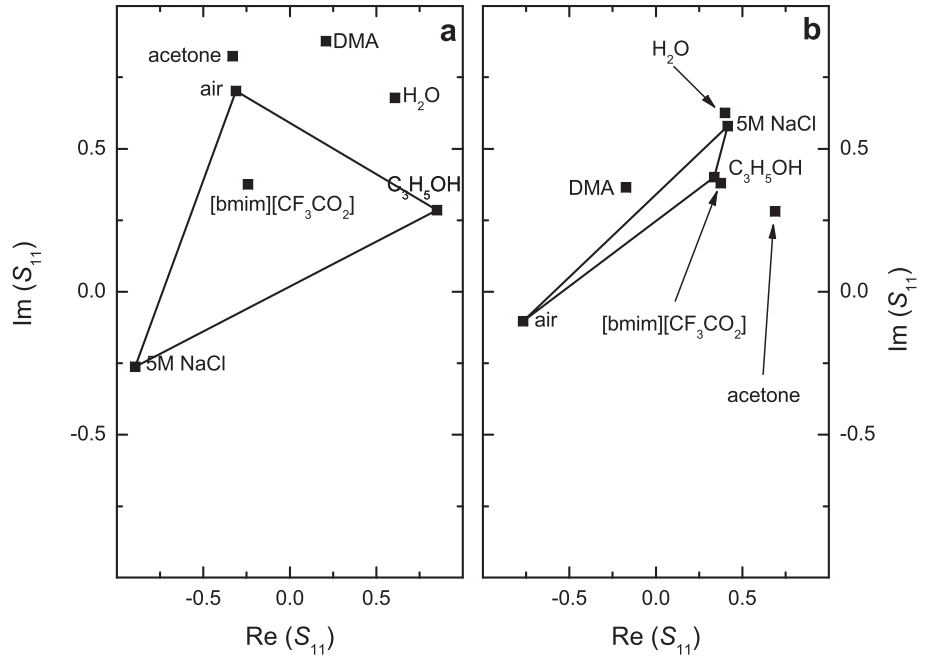

Figure 2.5: Complex scattering parameters $\hat{S}_{11}$ of some representative substances at 100 MHz (**a**) and 1 GHz (**b**) obtained with TS1 cell[100] at 25 °C. The value of C_s in eq. 2.27 was estimated from the cell geometry and literature values[82] to 40 fF. Lines represent the "calibration triangle" 1-Propanol-air-NaCl(aq, $m \simeq 5\,\mathrm{mol\,kg^{-1}}$).

calculated $\hat{S}_{11}$ values at the sample - coaxial line interface (eqs. 2.24 and 2.27) is far from being due to an ideal coaxial line.

Thus, it is essential to calibrate the VNA with respect to the sample - coaxial line interface with three reference materials. As a first approximation, the calibration standards should be roughly comparable to the short-load-open standards, to reliably obtain the three errors in directivity, frequency response and source match. For short calibration NaCl(aq, $m \sim 0.2\,\mathrm{mol\,kg^{-1}}$) or NaCl(aq, $m \sim 5\,\mathrm{mol\,kg^{-1}}$) were used.[99] Although the dielectric relaxation behavior is less accurately known,[99] the conductivity can be determined very accurately (see section 2.4.2), which is the main contribution to $\hat{\eta}(\nu)$ at the relevant frequencies. It was found that the dielectric parameters are not crucial as long as κ is sufficiently high and accurately determined (fig. 2.6). Air was used as second calibration standard, corresponding to the open calibration.

Unfortunately, to find a suitable third reference material $\hat{S}_{11}$ values in the complex plane must be considered. The prerequisite for the third material is that the "calibration triangle" (fig. 2.5) closely compromises the $\hat{S}_{11}$ value of the sample in the complex plane at all frequencies. As can be seen from fig. 2.5, for the ionic liquid [bmim][CF_3CO_2], 1-propanol[98] is an excellent reference material at 100 MHz and a good one at 1 GHz, whilst DMA[94,95] is a poor reference material at these frequencies. To obtain very accurate spectra, this condition has to be fulfilled, by variation of the reference substances and/or cell geometries.

Using this approach, it becomes possible to measure the dielectric spectrum of DCM, at $50\,\mathrm{MHz} \leq \nu \leq 300\,\mathrm{MHz}$ with an accuracy of better than 0.2 % (fig. 2.6) using air/1-

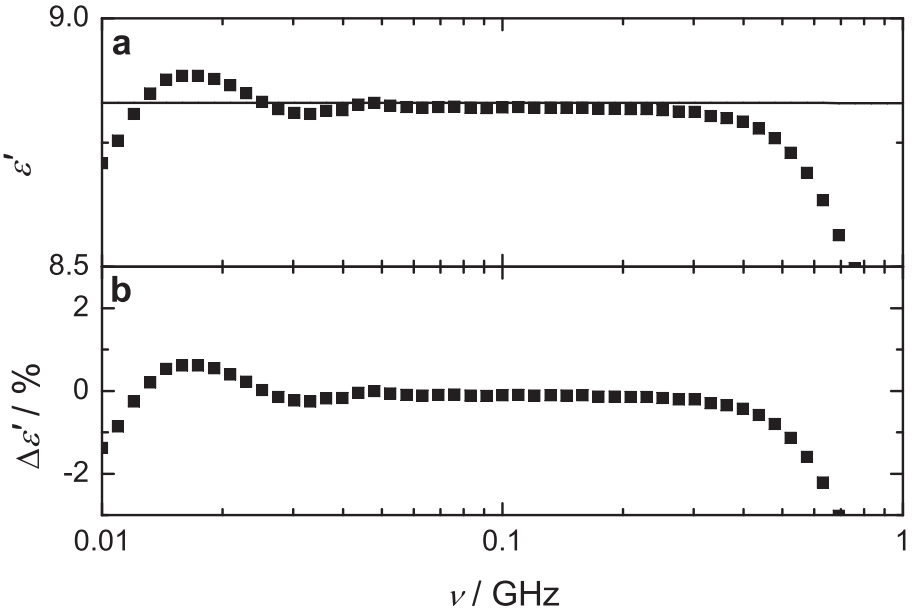

Figure 2.6: Dielectric permittivity spectrum (**a**) and deviations from a literature spectrum (**b**) of DCM at 25 °C. Symbols represent data obtained with an air/1-propanol[98]/NaCl(aq, $c \simeq 5\,\mathrm{mol\,kg^{-1}}$)[99] calibration of the TS1-cell.[100] The line represents literature spectrum.[101] The value of C_s in eq. 2.27 was estimated from the cell geometry and literature values[82] to 40 fF.

propanol/NaCl(aq, $m \sim 5\,\mathrm{mol\,kg^{-1}}$) as reference liquids. Deviations at even higher frequencies can be explained by the departure of the sample $\hat{S}_{11}$ values from the "calibration triangle" and the uncertainties in $\hat{\eta}(\nu)$ of the NaCl solutions. Most tested cells were not able to yield reliable data at $\nu < 50\,\mathrm{MHz}$, which is apparently the low frequency limit of the setup. This might also reflect decreasing accuracy of the vector network analyzer close to its low frequency limit of 10 MHz.

Nevertheless, using this technique reliable data at $50\,\mathrm{MHz} \leq \nu \leq 300\,\mathrm{MHz}$ for weakly absorbing liquids were obtained, where TDR-techniques usually fail.[89] Moreover, it was possible to investigate ionic liquids, which are experimentally difficult to access at low ν because of their mostly low permittivities and considerable conductivity. A representative example is shown in fig. 2.7, where it can be seen that a smooth dielectric permittivity spectrum is obtained, which also agreed with similar measurements with different cut-off type cells. Unfortunately, the dielectric loss spectrum scatters considerably at low frequencies, which is probably a reflection of the unfavorable $\eta'' - \varepsilon''$ (≈ 120 at 50 MHz) difference, meaning that the Ohmic loss is the dominating contribution at low ν.

Summarizing: connecting cut-off type cells to the VNA improved low frequency measurements considerably and the results are less sensitive to the pin-length of the cells than in the TDR experiments. Results improved additionally at high MHz to low GHz frequencies by introducing the discontinuity capacity C_s into the working equation (eq. 2.27). Although this quantity is not easily accessible, it can be obtained from modal analysis at the junction.[102] The value of C_s depends on the geometry of the cell and is weakly dependent

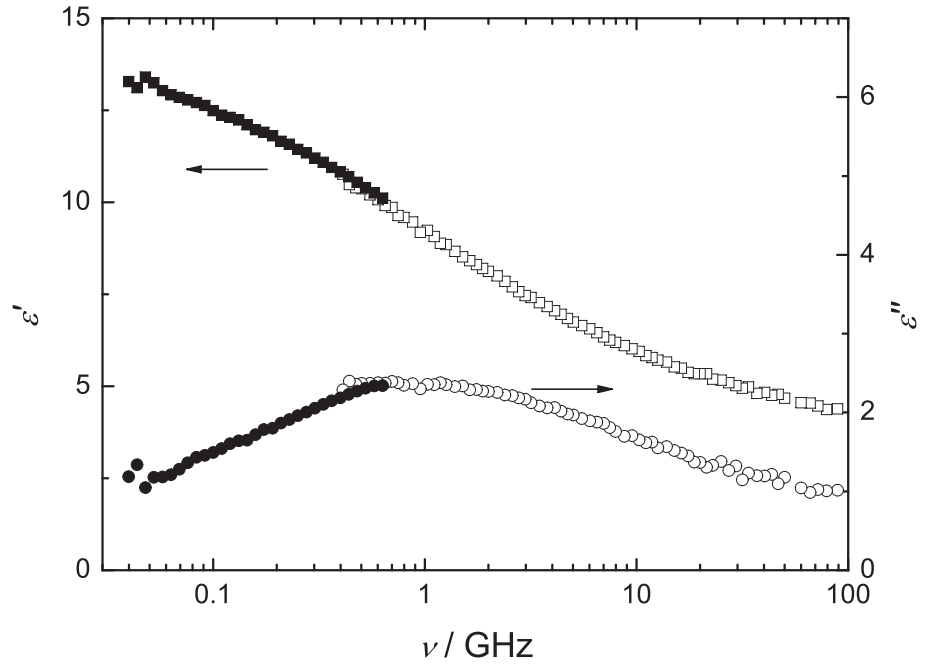

Figure 2.7: Dielectric permittivity, $\varepsilon'(\nu)$, and loss spectrum, $\varepsilon''(\nu)$, of [bmim][CF_3CO_2] at 25 °C. Open symbols correspond to data obtained with open-ended coaxial probe (section 2.3.3) and waveguide interferomenters (section 2.3.2). Filled symbols show results obtained with reflection measurements of cut-off type cells, using air/1-propanol[98]/NaCl(aq, $m \simeq 5\,\mathrm{mol\,kg^{-1}}$)[99] for calibration of the TS1 cell.[100] The value of C_s in eq. 2.27 was estimated from the cell geometry and literature values[82] to 40 fF.

on the frequency. For the TS1 cell[100] a value of $C_s = 40\,\mathrm{fF}$ was estimated by interpolating literature data.[82]

Wave guide transmission cells

As described above (section 2.3.3) the vector network analyzer is able to detect amplitude and phase simultaneously. Thus, it is not necessary to record interference curves at each frequency separately as described in section 2.3.2. Therefore, the waveguide-transmission cells of the IFMs (X-, Ku-, and A-band) were connected to the Agilent E8364B vector network analyzer. With this transmission setup the complex scattering parameter, $\hat{S}_{12}$, is recorded as a function of the relative optical path length at all relevant frequencies simultaneously.

Measurements were automated, by controlling the stepper motor, VNA and the precision gauge for the determination of the z position of the waveguide probe with a personal computer. Only the calibration of the VNA at the 2.4 mm connector planes has to be refreshed occasionally manually. Medium wavelength λ_M and absorbtion coefficient α_{dB} were obtained from the slopes of the linear regression of the phase and of the magnitude of $\hat{S}_{12}$. Regression coefficients R^2 were typically between 0.99998 and 0.999999. A typical measurement is displayed in fig. 2.8. λ_M and α_{dB} were converted to complex permittivity

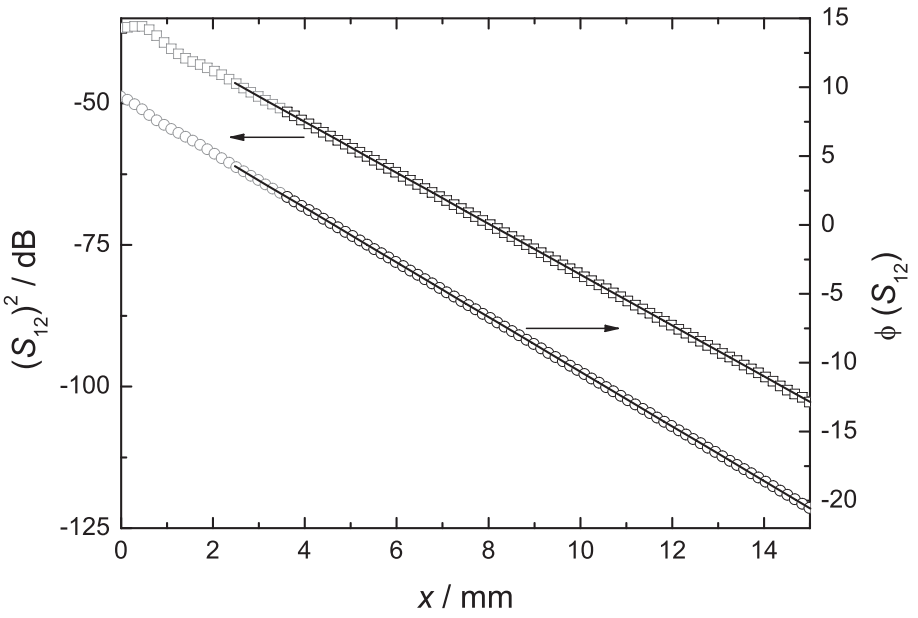

Figure 2.8: Magnitude $\hat{S}_{12}^2$ and phase $\phi(\hat{S}_{12})$ of the transmission experiment for H_2O at 25 °C at 12 GHz. Gray symbols represent omitted data due to multiple reflections at low optical path lengths x. Lines are linear regressions.

values via eqs. 2.20 and 2.21. Test measurements with a high permittivity (H_2O) and a low permittivity solvent (1-propanol) yielded a precision better than 0.5 % and 1 % in ε', respectively.

2.3.4 Time-domain THz-pulse spectroscopy

A standard THz time-domain spectrometer (THz-TDS) as described previously[87,103] (fig. 2.9) was used in cooperation with the group of Dr. Walther at the University of Freiburg (Germany). Pulses of $\sim 15 - 20$ fs duration from a Ti:sapphire oscillator at a repetition rate of 80 MHz with a center wavelength of ~ 800 nm and ~ 260 mW power (Femtolasers, Wien, Austria) were generated by a frequency-doubled Nd:YVO_4 solid state pump laser (4 W, 532 nm; VERDI, Coherent, USA). The pulse is split into two sections. A gallium arsenide (GaAs) dipole antenna, biased with a voltage (~ 35 V) applied between strips of 30 μm distance is excited with the first section of the laser pulses, yielding an estimated power incident on the transmitter chip of ~ 20 mW. The second part of the pulse acts as a gate pulse applied to a dipole receiver (silicon on sapphire, H structure with 5 μm gap). The photocurrent is measured with a lock-in amplifier connected to a mechanical chopper wheel operating at ~ 330 Hz.
With a delay line placed in the gate beam the time evolution of the electrical field strength of the THz pulse is recorded over 140 ps with time steps of 67 fs. Thus, the spectral resolution is ~ 30 GHz with a bandwidth ranging from 200 GHz to 4 THz ($7 - 130\,\mathrm{cm}^{-1}$). The whole THz beam path is located within a box filled with dry nitrogen (N_2) to avoid absorption induced by rotational transitions of water.

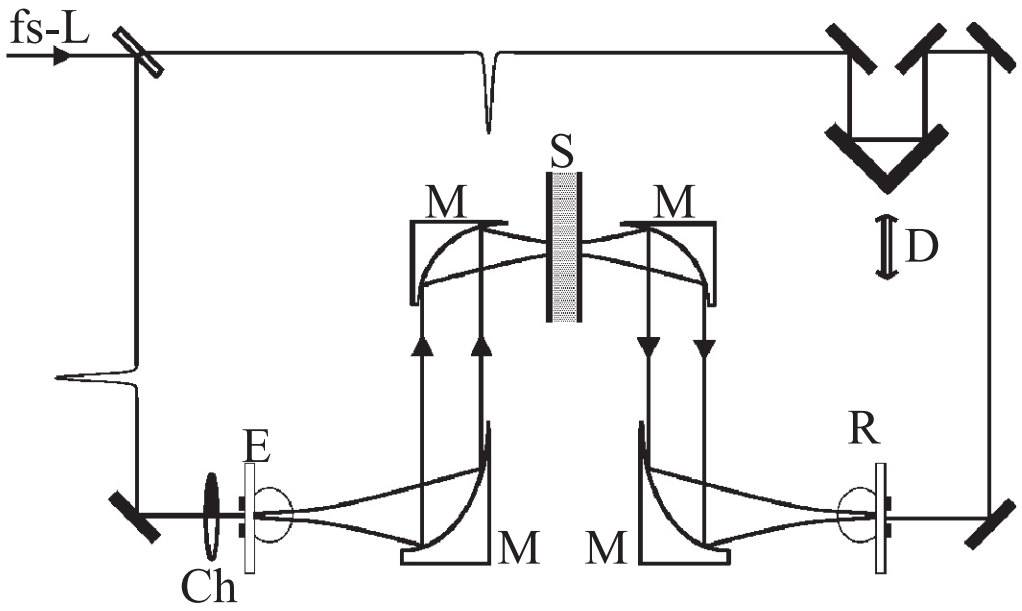

Figure 2.9: Schematic representation of the THz-TDS transmission setup consisting of **fs-L** fs-laser, **Ch** the chopper wheel, **M** parabolic mirrors, **S** liquid sample placed between two windows, **E** emitter antenna, **R** receiver antenna. **D** is a delay line in the gate beam.

A spherical silicon (Si) lens and two off-axis parabolic mirrors focus the THz beam to a spot of $\sim 3\,\mathrm{mm}$ diameter. Two additional mirrors and a Si lens guide the signal to the gated ultrafast antenna receiver.

Transmission geometry

For transmission measurements the sample was placed between two PTFE windows as described by Schrödle[87] and mounted on thermostatted metal blocks. The temperature is monitored with a calibrated platinum resistance temperature probe connected to a precision thermometer.
The time domain spectrum of the empty cell (reference pulse, $E_\mathrm{r}(t)$) is obtained in temporal proximity to the sample measurement (sample pulse, $E_\mathrm{s}(t)$). The time-domain data are transformed into the frequency domain by a Fourier integral:

$$\hat{E}_{\mathrm{r,s}}(\nu) = \frac{1}{2\pi} \int_{-\infty}^{+\infty} e^{-\mathrm{i}\,2\pi\nu t} E_{\mathrm{r,s}}(t) dt \tag{2.28}$$

From the ratio $\hat{R}(\nu)$ of the Fourier transforms of the sample pulse and the reference pulse,

$$\hat{R}(\nu) = \hat{E}_\mathrm{s}(\nu)/\hat{E}_\mathrm{r}(\nu) = A(\nu) \cdot e^{\mathrm{i}\,\Delta\phi(\nu)} \tag{2.29}$$

the refractive index of the sample is determined by the phase $\Delta\phi$ of $\hat{R}$ as $n_\mathrm{s} = n_\mathrm{air} + c\,\Delta\phi/2\pi\nu d$, where d is the optical path length and $n_\mathrm{air} = 1.00027$ the refractive index of

air. Assuming a weakly absorbing sample, the absorption coefficient is calculated from the amplitude, A, of $\hat{R}$ as $\alpha_s = -2\ln(f \cdot A)/d$, where

$$f = \frac{(n_w + n_s)^2}{n_s \cdot (n_w + 1)^2} \tag{2.30}$$

accounts for the reflection losses at the sample/PTFE interfaces. The refractive index of the PTFE window material was assumed to be constant $n_w = 1.433$[104] at the relevant frequencies.
From the calculated values of $n_s(\nu)$ and $\alpha_s(\nu)$ the complex frequency-dependent dielectric response of the sample liquid, $\hat{\eta}(\nu)$, can be obtained via,

$$\hat{\eta}(\nu) = \hat{n}^2 = [n_s(\nu) - ik(\nu)]^2 \tag{2.31}$$

where $k(\nu) = c\,\alpha_s/4\pi\nu$.

Reflection geometry

To increase the bandwidth for highly absorbing samples a reflection geometry is used. In the reflection setup the sample is placed on a Si disc and the pulse reflected at the Si-sample interface is recorded. Lenses and mirrors are similar to the transmission setup.[105]
The reflected pulse is defined by Fresnel's equation,

$$E_{refl} = -E_{inc}\frac{\hat{n}_s \cdot \hat{n}_w}{\hat{n}_s + \hat{n}_w} \tag{2.32}$$

where $\hat{n}_w$ is the complex index of refraction of the material where the field propagates (Si disc) and $\hat{n}_s$ of the material where the pulse is reflected. E_{inc} and E_{refl} are the incident and reflected electrical field pulses, respectively. The value of $\hat{\eta}$ for the sample is related to the complex index of refraction via eq. 2.31. To account for drifts due to changes in the mechanical dimensions, a relative signal E_s/E_{air} is analyzed, where E_s and E_{air} are the sample pulse and the pulse of the empty cell.

$$\frac{E_s}{E_{air}} = \frac{\hat{n}_w - \hat{n}_s}{n_w + \hat{n}_s} \cdot \frac{\hat{n}_{air} + \hat{n}_w}{\hat{n}_w - \hat{n}_{air}} \tag{2.33}$$

The indices of refraction for Si and air are assumed to be constant $\hat{n}_w = 3.42$ and $\hat{n}_{air} = 1.00027$.[87,105] Measurements were rejected if the signal from the silicon surface of the sample and the reference measurements did not match.

2.3.5 Far infrared spectroscopy

For some substances dispersion does not completely decay even at high frequencies and thus measurements at far infrared (FIR) frequencies are required. Most infrared spectrometers are based on (Michelson) interferometric measurements.[106] Unfortunately, interferometers where the sample is placed into the interferometer beam to allow determination of the complex index of refraction, $\hat{n}$, are unavailable. Commercial instruments, as used in this work, only determine the absorption coefficient, α defining the imaginary part of $\hat{n}_s$ (eq. 2.32).[107]

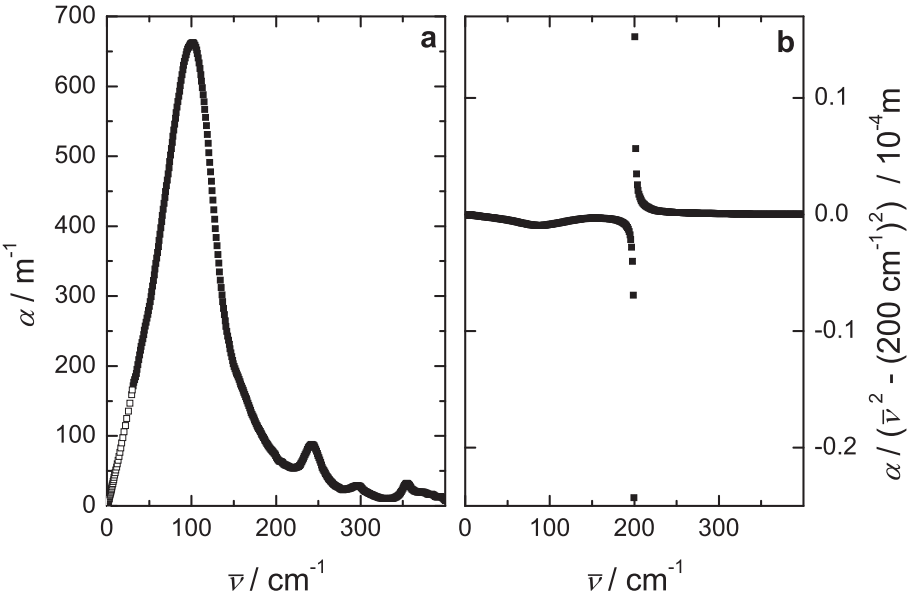

Figure 2.10: Far-infrared spectrum (**a**) of [emim][BF_4] at 25 °C. Closed symbols represent data obtained with a FIR spectrometer, open symbols correspond to data measured with THz-TDS, IFM and frequency domain reflectometer. Right figure (**b**) displays exemplarily the argument of the integral of eq. 2.34 for $\bar{\nu}_t = 200\,\mathrm{cm}^{-1}$.

The real part of $\hat{n}$ can be obtained with the help of the Kramers-Kronig (KK) relation[108]

$$n(\bar{\nu}_t) - n_\infty = \frac{1}{2\pi^2} \int_0^\infty \frac{\alpha(\bar{\nu})}{\bar{\nu}^2 - \bar{\nu}_t^2} \mathrm{d}\bar{\nu} \tag{2.34}$$

where n_∞ is the index of refraction at infinite frequency and $\bar{\nu} = 1/\lambda$ is the wave number. A prerequisite for this transformation is the integration from 0 to ∞, which in practice is not achievable. Thus, it is necessary that α has decayed to zero at the upper and lower integration limit. However, if data of all previously described experimental techniques are combined with the FIR data and subsequently transformed (according to eq. 2.31), this requirement is met (fig. 2.10a). Moreover, contributions to the integral where $\bar{\nu}$ is far from $\bar{\nu}_t$ are very small. This means that for the determination of $n(\bar{\nu}_t)$ at FIR frequencies, the condition $\alpha = 0$ is less important at the low frequency limit than at the high frequency limit.

The transformation was conducted according to following procedure: Dielectric spectra, obtained with the techniques described above, were fitted with a mathematical model and converted to the complex refractive index scale (eq. 2.31). FIR spectra, equidistant on a linear scale, were re-scaled by multiplying with a constant scaling factor in order to match the α values obtained with the THz-TDS experiment over a $\bar{\nu}$-range of a few cm^{-1} (fig. 2.10a). This scaling factor results from the uncertainty in the optical path length of the FIR cell (e.g. cell dilation due to filling).

The resulting combined spectrum, ranging from ~ 0.003 to $400\,\mathrm{cm}^{-1}$ (fig. 2.10a), is subsequently converted with eq. 2.34 numerically with the trapezoidal method. Note that

the integral in eq. 2.34 is an improper integral with a discontinuity at $\bar{\nu} = \bar{\nu}_t$ (fig. 2.10b). Thus, for the numerical treatment $\bar{\nu}_t$ has to be different from the measured frequencies $\bar{\nu}_i$. To keep the contribution at the discontinuity small, transformations were conducted at $\bar{\nu}_t = (\bar{\nu}_i + \bar{\nu}_{i+1})/2$ (Cauchy principle value $\to 0$).[109] To obtain n and α values at the same frequencies, calculated $n(\bar{\nu}_t)$ values were linearly interpolated to $n(\bar{\nu}_i)$.
The value of n_∞ was adjusted to minimize deviations from the n values obtained from the THz-TDS experiment. Resultant complex indices of refraction were converted to the permittivity scale (eq. 2.31) and combined with the experimental data at lower frequencies.
Far-infrared spectra from $25 - 450\,\mathrm{cm}^{-1}$ were measured with a resolution of $4\,\mathrm{cm}^{-1}$ on a Bruker Vertex 70. The measurements were performed by Dr. Turton (University of Strathclyde, Glasgow, UK). The liquids were held between polymethylpentene (TPX) windows with a $20\,\mu$m path length in a thermostatted assembly. An average of about 4000 scans was taken for each sample and a background spectrum taken from the windows alone was subtracted. Spectra measured with attenuated total reflection cells were found to be not suitable for this procedure.
The main sources of error, are due to uncertainties in the FIR spectra (optical path length, reflection losses at window-sample interface are not regarded) and the described uncertainties of the KK-transformation.

2.3.6 Data processing

To link the dielectric spectra to physical properties a frequency-continuous description has to be found. In principle $\hat{\eta}(\nu)$ spectra can be processed, but to avoid biasing of the resulting parameters, due to the large values of η'' at low ν (higher weights at low ν than at high ν), only $\hat{\varepsilon}(\nu)$ data (corrected for the dc conductivity, eq. 1.31) are analyzed. Therefore, the spectra were corrected for the measured conductivity, κ, as a starting approximation. Then κ was varied slightly in order to improve the fit quality (eq. 2.35). The difference between the experimental and adjusted κ values reflects errors in the measurement setup and/or in the mathematical model for the equipment.[110,111]
Subsequently, the measured data triples (ν_i, ε'_i, ε''_i) have to be fitted by the relaxation models (or superpositions) presented in section 1.3. Due to the broadness of relaxation modes in the condensed phase finding the right model is not trivial, and it should be kept in mind, that a successful formal description does not automatically imply that the resolved modes have a physical meaning or that they are independent of each other. Thus, some basic rules should be obeyed:
First, the variance of the fit, χ^2_r:

$$\chi^2_r = \frac{1}{2N - m - 1}\left[\sum_{i=1}^{N} w_{\varepsilon'}(\nu_i)\delta\varepsilon'(\nu_i)^2 + \sum_{i=1}^{N} w_{\varepsilon''}(\nu_i)\delta\varepsilon''(\nu_i)^2\right] \tag{2.35}$$

should be small. In eq. 2.35 $\delta\varepsilon'(\nu_i)$ and $\delta\varepsilon''(\nu_i)$ are the residuals, N is the number of data triples (ν_i, $\varepsilon'(\nu_i)$, $\varepsilon''(\nu_i)$), and m the number of the adjustable parameters, while $w_{\varepsilon'}(\nu_i)$ and $w_{\varepsilon''}(\nu_i)$ are the weights.

Second, the number of the relaxation processes should be reasonably small and the obtained fitting parameters have to be physically reasonable (e.g. no negative relaxation times or amplitudes; the extrapolated ε_∞ cannot become lower than the squared refractive index at optical frequencies, n_D^2). Furthermore, the relaxation model should not change within a concentration or a temperature series, except for specific physical reasons. Additional input from other techniques (if available), e.g. computer simulations, can be considered for finding the right description.
The model can depend on the measured frequency range as well as on the precision and the "density" of the data. Special care should be taken regarding the density, meaning that the data density should be comparable over the whole frequency range.
According to the Kramers-Kronig relation (eq. 2.34) the real and imaginary parts of $\hat{\varepsilon}(\nu)$ are not independent. Thus, $\varepsilon'(\nu)$ and $\varepsilon''(\nu)$ are fitted simultaneously with the MWFIT program, based on the method of Levenberg and Marquardt.[112] For the purpose of this study, the program was extended by the modified Cole-Cole equation (eq. 1.53). Note that due to the nonlinear nature of the fitting process, it is not possible to assign statistically meaningful standard uncertainties to the individual fit parameters. However, the square root of the diagonal elements of the covariance matrix can be used as a measure for the certainty of the resulting parameters.[112,113]

2.4 Auxiliary measurements

2.4.1 Densimetry

To determine molar concentrations, sample densities, ρ, were obtained with a vibrating tube densimeter (Anton Paar DMA60/601 HT), which measures the period of vibration, τ, of a glass tube filled with the sample. The value of τ is related to the sample density according to eq. 2.36:

$$\rho = A(\tau^2 - B) \tag{2.36}$$

The instrument-specific constants A and B were determined via calibration using water and N_2(g), assuming densities from standard sources.[114] The temperature was kept constant to $\pm\,4\,\mathrm{mK}$ with a circulating thermostat (Julabo F33 SD) and results are accurate to $\sim 5 \cdot 10^{-2}\,\mathrm{kg\,m^{-3}}$.

2.4.2 Conductometry

For the determination of electrical conductivities, κ, the resistance of capillary cells was measured at frequencies ranging from $\sim 100\,\mathrm{Hz}$ to $\sim 11\,\mathrm{kHz}$ with a variable frequency AC bridge. The capillary cells with varying cell constants, C, were filled with the sample and held in a high precision thermostat, which is stable to $\pm 0.001\,\mathrm{K}$. To account for the electrical double layer at the electrodes, the exact resistance was obtained by extrapolation of the frequency-dependent resistance $R(\nu \to \infty)$.[115,116] Electrical conductivities, κ ($=C/R_\infty$) were obtained with a precision of $\pm 0.2\,\%$ and an estimated accuracy of $\pm 0.5\,\%$. The experimental setup is described in detail elsewhere.[115–117]

2.5 Quantum mechanical calculations

For validation of the experimental results for molecular properties semiempirical calculations for various conformers of the ions as well as of the ion-pairs have been performed using MOPAC2009[118] and the PM6 Hamiltonian. Dipole moments were calculated assuming the geometric center (i.e. the center of the longest axis of the molecule/ion-pair) as the pivot. DFT (BP86/TZVP) calculations with Turbomole[119] for selected conformations suggested that the choice of the theoretical method is not critical for the value of the dipole momentand geometric properties and thus that the semiempirical PM6 Hamiltonian is sufficient. Molecular diameters, $d_{\max}$ were obtained by taking the longest distance between two atoms and adding the van der Waals radii of the atoms.[120] These diameters were used to calculate the maximum molecular volumes of reorientation, $V_{\max}$, by assuming a spherical particle. To account for solvent effects (e.g. polarization in the condensed phase) the COSMO[121] technique was applied assuming the appropriate static permittivity. Van der Waals volumes, V_{vdW}, were determined from the optimized geometry with WINMOSTAR.[122]

Chapter 3

Neat ionic liquids

3.1 Introduction

Understanding the dynamic characteristics of ILs is a major focus of current IL research. Recent investigations include studies using optical heterodyne-detected Raman-induced Kerr-effect spectroscopy (OHD-RIKES),[123–127] NMR-relaxation,[128–133] time-resolved infrared,[134] and emission[135–139] spectroscopies, quasi-elastic neutron scattering,[140–142] terahertz spectroscopy,[26,143,144] and dielectric relaxation spectroscopy (DRS).[27–30,145–151]
Detailed knowledge of the dielectric behaviour of RTILs is particularly important since such properties are essential for understanding their solvation dynamics.[135,137,138] Unfortunately, the picture that has emerged from dynamics studies to date has been unsatisfactory.[135–137] For example, it has been found that dielectric continuum models, which successfully describe the frequency-dependent dielectric response of polar molecular liquids,[152] miss a considerable part of the fast solvation dynamics of RTILs.[135,137] This discrepancy resulted, at least in part, from the limited frequency range of the then available dielectric spectra, which were measured only up to 20[30] or 40[25] GHz. Apparently, dielectric spectra with a broader frequency range[146] improve the accuracy of the continuum models.[139]
Moreover, it is essential to understand the liquid structure of ILs, their microscopic dynamics, and the way in which pertinent macroscopic properties, such as viscosity, thermal conductivity, ionic diffusion, and solvation dynamics depend on these properties, to fully exploit their possible applications as solvents.
In addition to extending the frequency window, further insights into the dynamics of RTILs can be gained by studying the effects of temperature on their dielectric response. In particular, such data yield activation energies for the relaxation processes, which in turn provide clues as to the nature of these processes and the species producing them. While there are a few low-frequency dielectric studies focusing on the conductivity response,[149–151] with some notable exceptions,[29,145] almost nothing is known about the dielectric properties of RTILs in the microwave region at temperatures other than ambient.

3.2 Dielectric properties at 0.2 GHz $\leq \nu \leq$ 89 GHz and 5 °C $\leq \theta \leq$ 65 °C

3.2.1 Ionic liquids with dipolar cations and weakly dipolar anions

The material presented in this chapter forms the basis of the paper:

Johannes Hunger, Alexander Stoppa, Simon Schrödle, Glenn Hefter, and Richard Buchner *"Temperature Dependence of the Dielectric Properties and Dynamics of Ionic Liquids" ChemPhysChem* **2009**, *10*, 723-733.

In this section results at microwave frequencies for a selected range of mostly imidazolium-based RTILs are presented. To disentangle cation and anion effects, dielectric spectra were recorded for the 1-*N*-butyl-3-*N*-methylimidazolium cation with varying anions, namely tetrafluoroborate ([bmim][BF_4]), hexafluorophosphate ([bmim][PF_6]) and dicyanamide ([bmim][DCA]). Viscosity and cation side-chain length effects were investigated using the $[BF_4]^-$ and $[NTf_2]^-$ (bis(trifluoromethylsulfonyl)imide) salts of 1-*N*-hexyl-3-*N*-methylimidazolium ($[hmim]^+$) along with the $[BF_4]^-$ and $[DCA]^-$ salts of 1-*N*-ethyl-3-*N*-methylimidazolium ($[emim]^+$) and [$p_{1,2}$][DCA]. With the exception of *cis*-$[NTf_2]^-$ ($\mu = 5.7$ D)[153] the present anions have zero or low dipole moments. Thus, only minor contributions of the anions to the dielectric spectra are expected.
For all samples, $\hat{\varepsilon}(\nu)$ was determined in the frequency range $0.2 \lesssim \nu/\text{GHz} \leq 89$ (HP8720D VNA setup + A & E-band interferometers, section 2.3) at intervals of 10 °C over the range $5 \leq \theta/°\text{C} \leq 65$, except for [bmim][$PF_6$] (15-65°C) due to its high melting point ($\theta_{\text{fus}} \approx 11$ °C). For [$p_{1,2}$][DCA], previously measured VNA spectra[29] recorded at $15 \leq \theta/°\text{C} \leq 55$ were supplemented with IFM data over the same temperature range and reanalyzed. For secondary calibration (see section 2.3.3) purified DMA, BN and 1-butanol were used. Where possible conductivity data were taken from literature.[154–157] If such data were not available, κ was measured. For convenience all κ values used are listed in table 3.1 and 3.2. Densities, ρ, required for the calculation of molar (mol L^{-1}) concentrations, c, were taken from literature sources,[78,155,157–165] interpolated or extrapolated if necessary. For [$p_{1,2}$][DCA] the density was only available at 20°C,[157] therefore this value was also used for the calculation of c at 15 °C and 25 °C. The dielectric and related data obtained for the eight RTILs studied are summarized in tables 3.1 and 3.2. Typical spectra obtained by combination of the VNA and IFM data are shown in figs. 3.1 and 3.2.

Choice of Relaxation Model.

Accurate description and decomposition of DR spectra is rarely trivial due to the extremely broad nature of DR modes and current technological limitations on the precision and bandwidth (frequency limits) of DR instrumentation. For conducting solutions there is an additional problem resulting from the difference between $\eta''(\nu)$ and $\varepsilon''(\nu)$, which increases with decreasing ν (eq. 1.31). This makes it difficult to determine $\hat{\varepsilon}(\nu)$ to the required accuracy at low frequencies. This situation is exacerbated for the present RTILs because their dielectric loss is small and their dc conductivity relatively high. This is especially

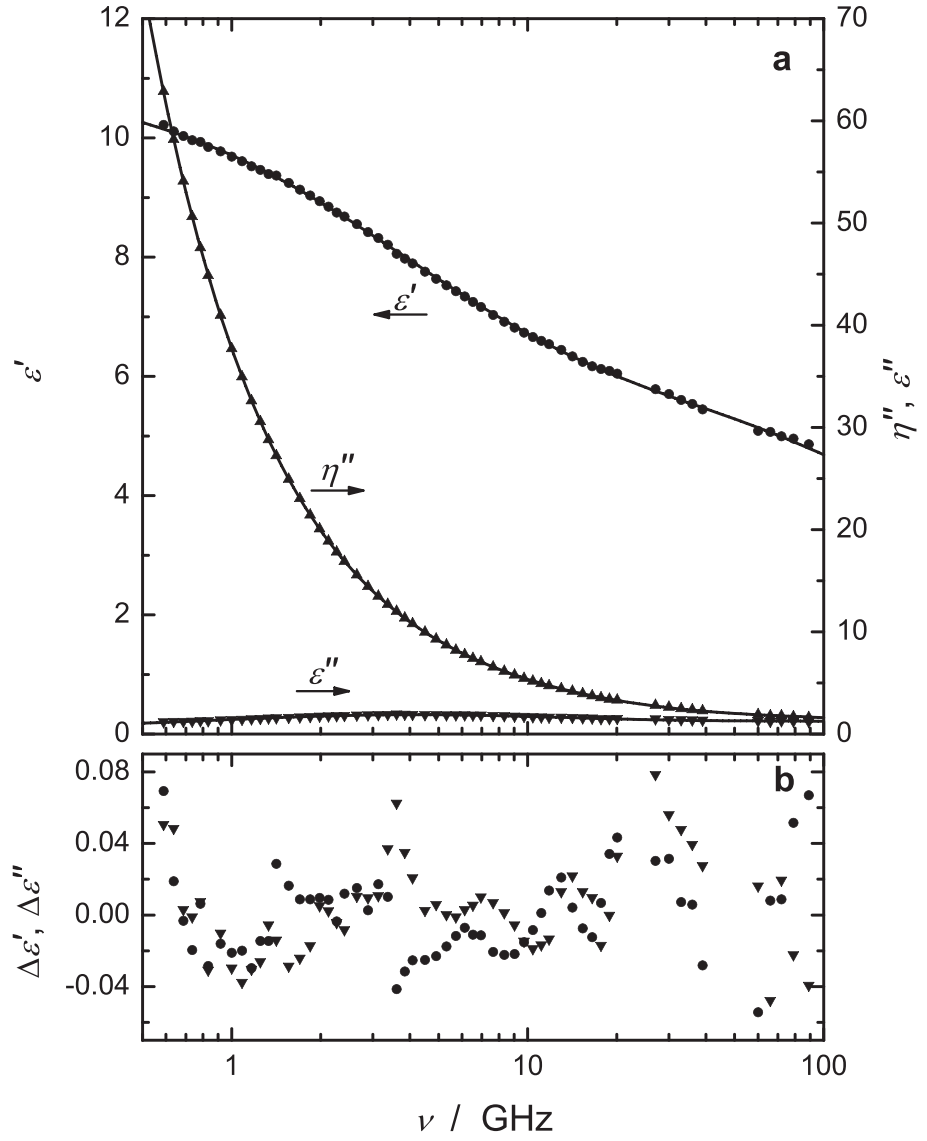

Figure 3.1: (**a**) Dielectric permittivity, $\varepsilon'(\nu)$, total loss, $\eta''(\nu)$, and dielectric loss, $\varepsilon''(\nu)$, spectra of [bmim][DCA] at 45 °C; symbols show experimental data, lines represent the CC+D fit. (**b**) Absolute deviations $\Delta\varepsilon'$ (●) and $\Delta\varepsilon''$ (▼) of $\varepsilon'(\nu)$ and $\varepsilon''(\nu)$ values from the CC+D fit at $\nu \geq 0.6$ GHz.

true for the more viscous RTILs whose dominant relaxation mode occurs at rather low frequencies. The net effect is that the uncertainty in the conductivity correction ultimately swamps the dielectric response at low ν (fig. 3.1).

Low frequency modes of the DR spectra of highly viscous molecular liquids are usually described in the ***frequency*** domain using a Havriliak-Negami (eq. 1.52) or Cole-Davidson model (eq. 1.51), which corresponds to an asymmetric Lorentzian.[166] For ***time*** domain dielectric data, the Kohlrausch-Williams-Watts (KWW) model is generally preferred as it can be derived from mode coupling theory. There is no exact equivalent of KWW in

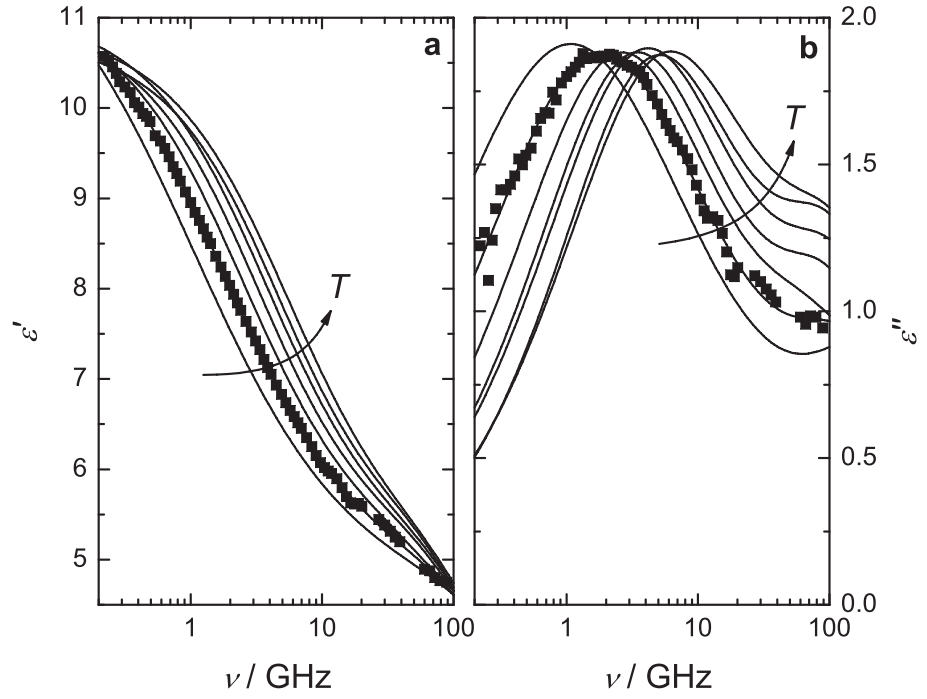

Figure 3.2: (**a**) Dielectric permittivity, $\varepsilon'(\nu)$, and (**b**) dielectric loss, $\varepsilon''(\nu)$, spectra of [bmim][DCA] at temperatures from 5 °C to 65 °C. Symbols show typical experimental data (others omitted for visual clarity), lines represent the CC+D fit. Arrows indicate increasing temperature.

the frequency domain but to a good approximation it corresponds to a HN model with restrictions on the values of α_j and β_j.[34,50] For experimental dielectric spectra of viscous molecular liquids, it is often found that $\alpha_j \approx 0$ so that a CD model is sufficient to fit the data.[166] However, it should be kept in mind that the empirical CD equation for the frequency domain is not fully equivalent to the (*a posteriori*) theoretically-based KWW model in the time domain.

Informed by these standard treatments, the CD model was used by Weingärtner *et al.*[27,147] and Stoppa *et al.*[146] to describe the dielectric behaviour of several RTILs. For example, the DR spectrum of the viscous RTIL [bmim][PF_6], for which data were available over an unusually wide frequency range of $0.1 \leq \nu/\text{ GHz} \leq 2000$, was satisfactorily fitted[146] using a model that consisted of a CD equation for the dominant lowest frequency process centred at ~ 0.2 GHz, plus two low-amplitude Debye processes at 5 and 150 GHz, and a damped harmonic oscillation (DHO, eq. 1.60) at 1.5 THz. For spectra recorded up to 89 GHz this description is effectively reduced to a CD+D+D model because the contribution of the DHO mode is relatively small at $\nu \leq 89$ GHz. For reasons that will become apparent below it is emphasized that the CD mode for [bmim][PF_6] occurs at the lower limit of the experimentally accessible frequency range.

Table 3.1: Temperature dependence of the dielectric relaxation parameters of [$p_{1,2}$][DCA], [emim][DCA], [emim][BF_4], and [bmim][DCA]: static permittivity, ε, relaxation amplitudes S_j, relaxation times, τ_j, Cole-Cole parameter, α, infinite frequency permittivity, ε_∞; electrical conductivity, κ, and variance of fit, χ^2_r, assuming a CC+D model.[a]

T	ε	S_1	τ_1	α	S_2	τ_2	ε_∞	κ^b	$\chi^2_r/10^{-5}$
					[$p_{1,2}$][DCA]				
288.15	14.5	8.69	31.1	0.18	2.42	1.16	3.36	1.62	281
298.15	14.0	7.88	25.7	0.15	2.11	1.70	3.98	2.12	184
308.15	13.8	7.85	20.8	0.14	2.28	1.30	3.65	2.67	33
318.15	13.6	7.77	17.7	0.15	2.51	1.08	3.32	3.30	110
328.15	13.0	6.99	14.8	0.11	2.73	1.11	3.28	4.01	87
					[emim][DCA]				
278.15	11.7	5.95	46.4	0.23	1.49	1.88	4.30	1.77[c]	40
288.15	11.3	5.28	34.5	0.18	1.69	2.14	4.37	2.27[c]	86
298.15	11.0	4.97	30.7	0.16	1.90	1.84	4.18	2.84[d]	42
308.15	10.5	4.25	25.2	0.13	1.95	2.08	4.33	3.56[d]	34
318.15	10.0	3.55	18.9	0.08	2.11	2.11	4.31	4.33[d]	75
328.15	10.1	3.74	16.7	0.10	2.06	2.11	4.32	5.15[d]	76
338.15	10.0	3.17	16.1	0.03	2.38	2.49	4.42	6.41[d]	91
					[emim][BF_4]				
278.15	16.3	11.0	99.3	0.46	1.85	1.00	3.41	0.735[e]	111
288.15	15.6	10.2	60.7	0.44	1.65	1.26	3.69	1.091[e]	76
298.15	14.5	8.70	46.6	0.36	2.05	1.22	3.75	1.571[e]	79
308.15	13.6	7.42	36.6	0.31	2.13	1.60	4.07	2.02[e]	48
318.15	13.0	7.31	21.9	0.34	1.91	1.30	3.75	2.55[e]	47
328.15	12.6	6.51	18.4	0.26	2.41	1.24	3.64	3.22[e]	156
338.15	12.1	5.84	15.5	0.20	2.48	1.29	3.79	3.95[e]	135
					[bmim][DCA]				
278.15	12.4	7.93	150	0.43	1.20	0.73	3.24	0.4821	161
288.15	11.7	7.14	89.3	0.39	1.12	1.06	3.48	0.7675	82
298.15[f]	11.3	6.42	63.0	0.33	0.75	2.09	4.11	1.139	89
308.15	11.0	6.04	49.1	0.30	1.41	1.39	3.58	1.592	88
318.15	11.1	6.24	41.4	0.32	1.47	1.25	3.42	2.124	70
328.15	10.8	5.75	34.6	0.29	1.66	1.32	3.40	2.729	95
338.15	11.0	6.14	28.9	0.32	1.46	1.21	3.36	3.400	97

[a]Units: T in K; τ_1 and τ_2 in 10^{-12}s; κ in $\Omega^{-1}m^{-1}$. [b]Measured values unless otherwise specified. [c]Extrapolated from data in Ref. 157. [d]From Ref. 157. [e] From Ref. 156. [f]Ref. 146.

Table 3.2: Temperature dependence of the dielectric relaxation parameters of [bmim][BF_4], [bmim][PF_6], [hmim][NTf_2], and [hmim][BF_4]: static permittivity, ε, relaxation amplitudes S_j, relaxation times, τ_j, Cole-Cole parameter, α, infinite frequency permittivity, ε_∞; electrical conductivity, κ, and variance of fit, χ^2_r, assuming a CC+D model.[a]

T	ε	S_1	τ_1	α	S_2	τ_2	ε_∞	κ^b	$\chi^2_r/10^{-5}$
					[bmim][BF_4]				
278.15	14.4	10.1	670	0.59	3.24	0.26	1.10	0.1124	284
288.15	14.1	9.64	351	0.54	2.78	0.40	1.72	0.2134	200
298.15	14.6	10.0	284	0.52	2.04	0.62	2.57	0.3601	199
308.15	13.8	9.09	140	0.49	1.68	0.80	2.98	0.5574	47
318.15	13.3	8.43	93.7	0.45	1.71	0.94	3.11	0.8100	55
328.15	12.5	7.56	59.4	0.40	1.76	0.97	3.17	1.1227	67
338.15	12.5	7.34	52.5	0.39	1.58	1.42	3.56	1.5003	90
					[bmim][PF_6]				
288.15	16.7	12.8	2625	0.61	1.32	0.50[c]	2.55	0.0790[d]	503
298.15	16.1	12.0	1178	0.57	1.86	0.47	2.24	0.1495[d]	87
308.15	17.2	13.2	905	0.58	1.61	0.48	2.30	0.2481[d]	75
318.15	16.8	12.9	535	0.56	1.39	0.64	2.56	0.3822[d]	67
328.15	13.9	9.8	166	0.50	1.71	0.61	2.39	0.5561[d]	68
338.15	13.0	8.5	106	0.43	1.23	1.39	3.27	0.7795[d]	59
					[hmim][NTf_2]				
278.15	13.8	10.6	925	0.55	0.43	0.80[c]	2.77	0.06997[e]	180
288.15	12.1	8.72	299	0.47	0.65	0.80[c]	2.71	0.1307[e]	162
298.15	12.7	9.40	233	0.47	0.68	0.80[c]	2.58	0.2179[e]	126
308.15	11.6	8.11	128	0.40	1.09	0.69	2.40	0.3314[e]	68
318.15	11.9	8.40	107	0.39	0.97	0.80	2.52	0.4714[e]	124
328.15	11.3	7.68	73.1	0.34	1.19	0.80	2.38	0.6378[e]	61
338.15	11.2	7.56	64.0	0.33	1.03	1.2	2.66	0.8307[e]	74
					[hmim][BF_4]				
278.15	11.0	7.03	1048	0.60	1.33	0.50[c]	2.68	0.03329	333
288.15	12.3	8.27	893	0.58	1.52	0.50[c]	2.51	0.06688	364
298.15	12.0	7.87	451	0.54	1.95	0.44	2.18	0.1226	162
308.15	12.2	8.09	283	0.53	1.91	0.46	2.20	0.2071	86
318.15	12.8	8.70	240	0.52	1.63	0.58	2.49	0.3256	69
328.15	12.5	8.47	151	0.50	2.14	0.44	1.93	0.4838	78
338.15	12.6	8.29	121	0.48	1.22	0.98	3.06	0.6894	103

[a]Units: T in K; τ_1 and τ_2 in 10^{-12}s; κ in $\Omega^{-1}m^{-1}$. [b]Measured values unless otherwise specified. [c]Parameter fixed during fit procedure. [d]Interpolated from Refs. 154,155. [e]Interpolated and extrapolated from Ref. 155.

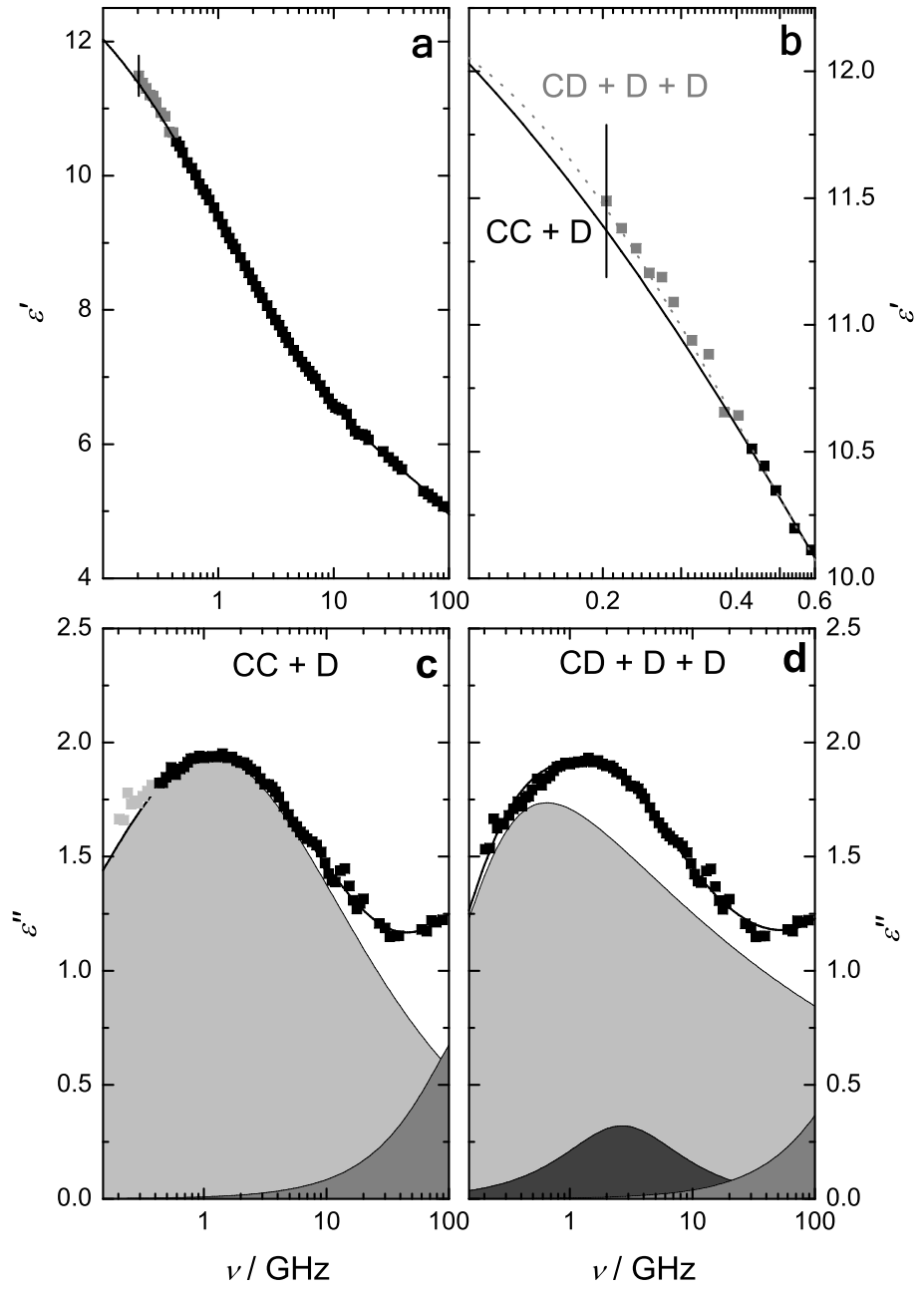

Figure 3.3: (**a**) Overall and (**b**) expanded views of the dielectric permittivity, $\varepsilon'(\nu)$, for [bmim][BF_4] at 35 °C, along with the dielectric loss spectra, $\varepsilon''(\nu)$, using (**c**) the CC+D model excluding data at $\nu \leq 0.4$ GHz ($\chi^2_r = 4.7 \times 10^{-4}$) and (**d**) the CD+D+D model including all data at $\nu \geq 0.2$ GHz ($\chi^2_r = 8.6 \times 10^{-4}$). Black symbols show accepted experimental points, grey symbols show data disregarded in the CC+D model and shaded areas indicate the contributions of the individual processes.

Consistent with previous dielectric studies of RTILs,[146,147] analysis of the present spectra commenced by adopting a CD+D+D model throughout. Such fits (fig. 3.3) showed good

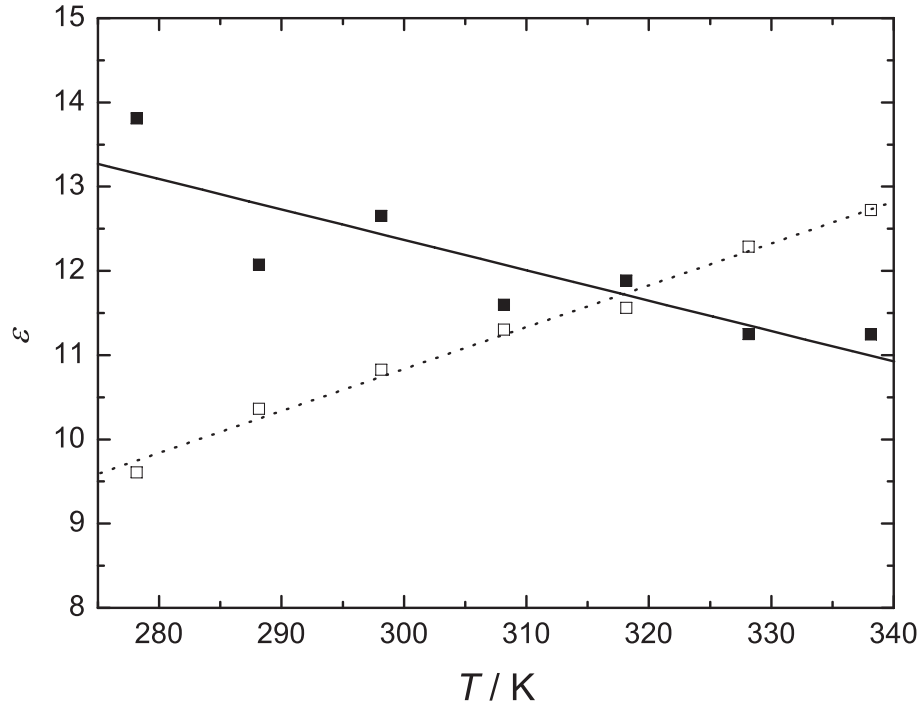

Figure 3.4: Static permittivity, $\varepsilon = \lim_{\nu \to 0} \varepsilon'(\nu)$, as a function of temperature, for [hmim][NTf_2] derived from the dielectric data at $\nu \geq 0.2$ GHz with the CD+D+D model (open symbols) and the CC+D model (filled symbols) with $0.35 \lesssim \nu_{\min}/\text{GHz} \lesssim 1.03$.

statistics ($\chi^2_r \leq 0.02$) at all temperatures and gave values of the static permittivity, ε, at 25 °C similar to those reported previously[28,146] with acceptable estimated uncertainties (ca. ±0.5 to ±2.5, depending on viscosity, i.e., the position of $\nu_{\max}$). However, a detailed consideration of the results obtained with this model revealed a number of difficulties.

First, the DR spectra for all the less viscous RTILs ([emim][DCA], [emim][BF_4] and [bmim][DCA],[146] fig. 3.2) were clearly better fitted (χ^2_r decreased by ca. 10 %) using a Cole-Cole equation for the low frequency mode plus one faster Debye process, i.e., a CC+D model. This is significant because the low frequency mode in the less viscous RTILs occurs at much higher frequencies (e.g., at 25 °C, $\nu_{1,\max} \approx 2.5$ GHz for [bmim][DCA], $\eta = 29$ mPa s;[157] cf. $\nu_{1,\max} \approx 0.14$ GHz for [bmim][PF_6], $\eta = 218$ mPa s).[167] This means that its band-shape at frequencies $\nu < \nu_{1,\max}$ is much better defined and less subject to errors than the corresponding mode in the more viscous RTILs.

Second, the CD+D+D model produced ε values that increased with increasing temperature, i.e., gave ***positive*** values of $d\varepsilon/dT$. A typical result is shown in fig. 3.4 (dotted line). While molecular-level explanations of this putative phenomenon are possible, for instance: the break-up of an antiparallel arrangement of dipoles, as occurs for some neat liquid carboxylic acids,[168] such behaviour is extremely unusual. Virtually all molecular liquids have negative $d\varepsilon/dT$ values;[168] this is because the decrease in the number density of their dipoles with increasing T, which also occurs for RTILs, predominates over the temperature-induced decrease in antiparallel dipole-dipole correlations, where present, as

for example in acetonitrile. Whilst there are indeed indications for some antiparallel alignment of the cation dipoles (see discussion below on the effective dipole moments) there is no evidence from simulations or from structural studies that the forces producing these correlations are comparable to the strong hydrogen bonds that create the antiparallel dimers in the liquid carboxylic acids, the only known common substances to have positive $d\varepsilon/dT$ values.

Table 3.3: Temperature coefficient of the static permittivity, $d\varepsilon/dT$, effective dipole moment, μ_{eff} (eq. 1.69), effective volume, V_{eff} (eq. 1.78), and Arrhenius activation energies, $E_a(x)$, of: the dielectric relaxation time, $x = \tau_1$, electrical conductivity, $x = \kappa$, and viscous flow, $x = \eta$, for the investigated RTILs.[a]

	$d\varepsilon/dT$[b]	μ_{eff}	V_{eff}[b]	$E_a(\tau_1)$[b]	$E_a(\kappa)$	$E_a(\eta)$
[$p_{1,2}$][DCA]	-0.034 ± 0.004	3.9 ± 0.1	0.46 ± 0.02	14.6 ± 0.2	17.8 ± 0.3	22.6 ± 0.1[c]
[emim][DCA]	-0.030 ± 0.004	2.9 ± 0.2	0.73 ± 0.05	14.4 ± 0.9	16.4 ± 0.3	24.1 ± 0.7[c]
[emim][BF_4]	-0.067 ± 0.006	3.8 ± 0.3	0.81 ± 0.03	24.1 ± 1.3	21.5 ± 0.5	27.5 ± 0.4[d]
[bmim][DCA]	-0.020 ± 0.006	3.9 ± 0.3	2.7 ± 0.3	19.0 ± 1.4	25.4 ± 0.8	27.4 ± 0.4[c]
[bmim][BF_4]	-0.041 ± 0.007	4.4 ± 0.9	1.4 ± 0.2	32.0 ± 3.1	33.5 ± 1.3	34.6 ± 1.2[e]
[bmim][PF_6]	-0.094 ± 0.027	5.3 ± 1.9	5.3 ± 0.6	38.4 ± 9.1	38.5 ± 1.6	43.5 ± 0.1[f]
[hmim][NTf_2]	-0.030 ± 0.009	5.7 ± 0.9	2.2 ± 0.3	25.4 ± 2.6	30.4 ± 1.4	31.6 ± 0.8[e]
[hmim][BF_4]	0.02 ± 0.01	4.6 ± 1.8	1.4 ± 0.2	28.7 ± 1.8	39.4 ± 1.1	39.2 ± 0.6[g]

[a]Units: $d\varepsilon/dT$ in K^{-1}, μ in D ($1\,D = 3.336 \cdot 10^{-30}\,C\,m$), V in 10^{-30} m^3, E_a in $kJ\,mol^{-1}$. [b]Error estimates in ε and τ_1 of the non-linear least-squares routine were used as weights for the linear regressions. Errors given for $d\varepsilon/dT$, V_{eff} and $E_a(\tau_1)$ are standard values from the linear regressions; real errors may be substantially higher. $E_a(\eta)$ calculated from the data of [c]Ref.[157], [d]Ref.[169], [e]Ref.[155], [f]Ref.[167], [g]Ref.[161].

Third, the small values of the relaxation-time distribution parameter obtained with the CD+D+D model, $\beta_1 \approx 0.2$ to 0.3, predict that the slowest (CD) process will contribute significantly to the DR spectrum even up to THz frequencies. This is physically unreasonable because it implies that part of the diffusive reorientation of dipoles is faster than the randomizing intermolecular collisions creating diffusive motion.[51,52]
Fourth, use of the CD equation for the dominant low frequency mode requires the presence of a small amplitude Debye mode at ~ 3 GHz (fig. 3.3b). No satisfactory explanation of the origin of such a mode has been possible to date.[30,146]
Fifth, a study of [bmim][BF_4] + dichloromethane (DCM) mixtures[111] suggests, that the ionic liquid retains its "character" up to relatively high dilutions in DCM, $x_{\text{DCM}} \lesssim 0.7$.[111] In this region, starting from the smallest DCM content investigated ($x_{\text{DCM}} = 0.089$), CC+D is clearly superior to all other fit models tested and the obtained parameters (ε, S_1, τ_1, α, S_2, τ_2, ε_∞) extrapolate smoothly to the corresponding values obtained with CC+D for the pure IL (tables 3.1 and 3.2).
Last but not least, the CD+D+D model gave $E_a(\tau_1) \approx 0$ for the activation energy of the lowest frequency DR process for most of the RTILs studied. Such values of $E_a(\tau_1)$

contrast markedly with the corresponding activation energies for electrical conductivity or viscous flow ($E_a(\kappa)$ and $E_a(\eta)$, table 3.3). Additionally, values of $E_a(\tau_1) \approx 0$ contradict the assumption necessary to explain the positive $d\varepsilon/dT$ obtained with the CD+D+D model, namely that strong intermolecular forces induce a pronounced antiparallel alignment of cation dipole moments (see above).

The strong case made collectively against the CD+D+D model by these factors led us to re-analyse all the DR spectra using the CC+D model.* For the more viscous RTILs (but not the dicyanamides, see above) fits using the CC+D model were worse (χ^2_r increased by ca. 10 %) than those obtained with the CD+D+D model, when all the data at $0.2 \leq \nu/\text{GHz} \leq 89$ were included. Inspection of the CC+D fits indicated that this was almost entirely due to a ***systematic*** divergence between the model and the observed values at low frequencies (figs. 3.3 and 3.4). When data at $\nu \lesssim 0.6\,\text{GHz}$ (the exact value depended on the relative magnitudes of $\varepsilon''(\nu)$ and $\eta''(\nu)$) were excluded from the fit, χ^2_r decreased by ca. 25 %. More importantly, fitting of the spectra with the CC+D model (even without exclusion of the data at $\nu \lesssim 0.6\,\text{GHz}$ for the more viscous RTILs) resulted in ***negative*** values of $d\varepsilon/dT$ for all of the present RTILs (except the most viscous [hmim][BF_4]), albeit with somewhat greater scatter in the ε values (fig. 3.4, full line). The CC+D model also produced $E_a(\tau_1)$ values that were similar to and correlated well with $E_a(\kappa$ or $\eta)$ values (see below).

It is emphasized that the systematic departures between the CC+D model and the observed dielectric data for the more viscous RTILs at $\nu \lesssim 0.6\,\text{GHz}$ (fig. 3.3) are well within the probable experimental errors of ca. ± 2 % in $\hat{\varepsilon}(\nu)$. However, unambiguous resolution of this issue requires more accurate measurements than are possible with the present apparatus. Such improvements in accuracy are potentially obtainable through the ongoing improvements in commercial instrumentation and the development of better VNA calibration procedures. The latter will not be easy to achieve because they will require a better mathematical model for VNA probe heads and much higher quality "absolute" (non-VNA) dielectric data for the VNA calibration materials than are currently available.

It should be noted, that none of these findings proves that the CC+D model is "more correct" than the CD+D+D model for the present RTILs. In particular it is stressed that both models are only mathematical descriptions of $\hat{\varepsilon}(\nu)$ in the investigated frequency range. Nevertheless, by considering all findings, it is reasonable to conclude that the present data are best analyzed in terms of the CC+D model, excluding data at $\nu \lesssim 0.6\,\text{GHz}$ (depending on the viscosity and conductivity of the sample).

Higher frequency Debye process

As will be shown below, the dominant lower-frequency relaxation is mainly due to the reorientation of the dipolar cations. The faster process observed for the present RTILs, centred at ca. 100 GHz (depending on the RTIL, see for example fig. 3.3c), is a superposition of several high frequency modes, as will become apparent in section 3.3. These modes arise

*We also tested a HN+D and CD+D model. For the first model the fits did not usually converge or yielded physically meaningless parameters. Fits with CD+D produced values of χ^2_r that were significantly larger than those for CC+D and CD+D+D.

from intermolecular vibrations, librational modes and cross-correlation of the latter with vibrational modes.[111,170] Conformational changes of the alkyl side chains of the cations may also contribute. However, because this faster process lies only partly within the upper frequency limit of the present spectra ($\nu \leq 89$ GHz) and because of the presence of several overlapping modes at THz frequencies it is inadvisable to attempt a quantitative analysis of this process using only the existing data. Hence, all subsequent discussion in this section refers only to the dominant lower frequency mode, treated as a Cole-Cole process.

Static permittivities

The static permittivity (dielectric constant, ε) of a liquid is one of its most important physical characteristics.[168] At present, DRS is the only technique available that can directly measure the permittivities of electrically conducting liquids, although its accuracy is usually about an order of magnitude lower than traditional methods (which are not applicable to conducting liquids).[22] The magnitude of ε is determined from DRS as $\lim_{\nu\to 0} \varepsilon'(\nu)$ by fitting an appropriate model to the $\varepsilon'(\nu)$ data. The validity of the values so obtained depends on the absence of any relaxation modes below $\nu_{\min}$, the low frequency limit of the measurements. Dielectric constants of a variety of RTILs have been measured by DRS.[11,27,28,146,147,171] These studies have shown, despite earlier expectations to the contrary,[172,173] that typical RTILs have only modest permittivities: mostly within the range $10 \lesssim \varepsilon \lesssim 30$, which are about the same as those of medium chain length ketones or ethers. Exceptions are strongly hydrogen-bonded ILs (protic ionic liquids), which have rather high dielectric constants.[174]

Table 3.4: Comparison of reported experimental static permittivities, ε, of [bmim][BF_4] at temperatures near 25 °C.

	Ref. 27	Ref. 146	this work	Ref. 143	Ref. 172	Ref. 175
ε	11.7 ± 0.6	12.2 ± 1.4	14.6	6.7[a]	68.89 ± 0.67[b]	1600[b]
ν / GHz	0.2-20	0.1-3000	0.2-89	100-1200	$50 \cdot 10^{-5}$	$(1\text{-}3)\cdot 10^{-3}$
Exp.[c]	DRS	DRS	DRS	TTS	Volt	Cap
Model	CD	CD+D+D+DHO	CC+D	D+D	-	-

[a]Ambient temperature. [b]20 °C. [c]DRS – dielectric relaxation spectroscopy; TTS – terahertz transmission spectroscopy; Volt – voltammetric measurements; Cap – capacitance measurements.

Reliable measurements of ε for RTILs using DRS are rather complicated due to the problems mentioned above: the choice of relaxation model, the uncertainties in the data, and the location of the dominant relaxation process at low ν. Note that these complications exist not only for the present measurements but for all DRS studies. The choice of the fitting model (CC+D vs. CD+D+D) has a relatively small but systematic effect on the values of ε because of the differing curvatures of the two plots at low ν (fig. 3.3b). In general, the ε values obtained assuming a CC model for the dominant slow process are

higher by ca. 10 % than those obtained with a CD model (table 3.4). The relatively small differences among the DRS studies confirm that the high values of ε obtained by inappropriate electrochemical methods (table 3.4) are simply incorrect as they neglect electrode polarization, etc.[151]

The location of the lower frequency process, which is largely governed by the RTIL viscosity, is more critical in fixing ε than is the choice of fitting model. This is illustrated in fig. 3.5, which demonstrates that the value of ε for [bmim][PF_6] ($\eta = 218\,\mathrm{mPa\,s}$;[167] $\nu_{1,\max} = 0.14\,\mathrm{GHz}$ at 25 °C) is much less well defined than that of the less viscous [$p_{1,2}$][DCA] ($\eta = 25.8\,\mathrm{mPa\,s}$;[157] $\nu_{1,\max} = 6.2\,\mathrm{GHz}$ at 25 °C). In essence this is because the plateau in $\varepsilon'(\nu)$, which is critical for fixing the value of ε, occurs at $\nu \ll \nu_{\min}$ for [bmim][PF_6].

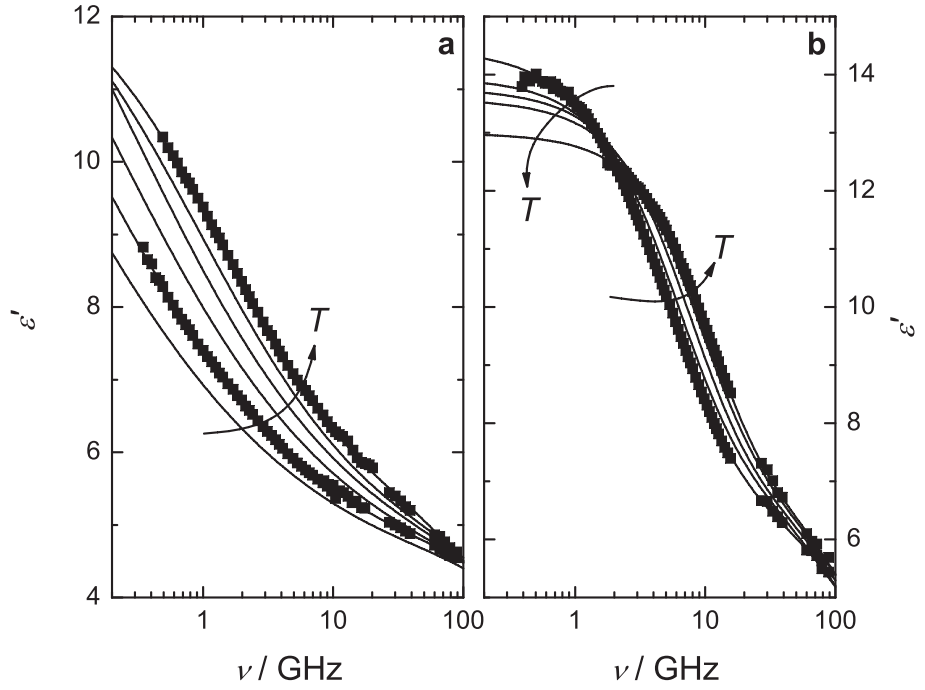

Figure 3.5: Dielectric permittivity spectra, $\varepsilon'(\nu)$, of: (**a**) [bmim][PF_6] and (**b**) [$p_{1,2}$][DCA] at temperatures from 15 °C to 65 °C and to 55 °C, respectively. Symbols show experimental data (mostly omitted for visual clarity), lines represent the CC+D fit, arrows indicate increasing temperature.

Estimated uncertainties in ε

As noted earlier, non-zero off-diagonal elements in the sensitivity matrix for the simultaneous non-linear fits of $\varepsilon'(\nu)$ and $\varepsilon''(\nu)$ preclude calculation of standard errors for the static permittivities of all the present RTILs.[112] However, for the less viscous compounds, where the low frequency process is better defined, estimated errors in ε were ≤ 1.0, with many ≤ 0.5. These uncertainties are similar to those previously reported for RTILs using VNA measurements alone.[28] For the more viscous RTILs, while the uncertainties are undoubtedly higher, the self-consistency of the $\varepsilon(T)$ values suggests that they are probably $\lesssim 2.5$.

As already noted, the uncertainty in ε is larger for the CC+D model because of the longer extrapolation due to the exclusion of the data at $\nu \lesssim 0.6$ GHz and the sensitivity of α_1 and thus ε on experimental errors at $\nu > \nu_{1,\max}$ as a consequence of the symmetrical CC band shape.

Temperature coefficients

The uncertainties in $\varepsilon(T)$ inevitably mean that the temperature coefficients, $\mathrm{d}\varepsilon/\mathrm{d}T$ (table 3.3), derived from the linear regression of $\varepsilon(T)$ vs. T are only approximate. Their small negative values (ca. $-0.04\,\mathrm{K}^{-1}$) are broadly comparable with those of medium sized ketones and ethers[168] and indicate that the present RTILs do not exhibit any unusual structural effects, at least over the temperature range studied. The only exception is [hmim][BF_4], for which the $\mathrm{d}\varepsilon/\mathrm{d}T$ value is slightly positive. However, for this very viscous compound ($\eta_{25} = 240\,\mathrm{mPa\,s}$), $\nu_{1,\max}$ is very low ($\sim 0.35\,\mathrm{GHz}$), so that the uncertainty in ε is large. There is no obvious reason why it should differ markedly from the other RTILs studied.

Dipole moments

Insight into RTIL structure can be obtained using Cavell's equation (eq. 1.69) to calculate the effective dipole moment μ_{eff} of the relaxing species. The values of μ_{eff} calculated for the dominant slower process ($j = 1$) using eq. 1.69 were found to be independent of T within the likely experimental errors, therefore only average values are listed in table 3.3. The constancy of μ_{eff} suggests, consistent with the $\mathrm{d}\varepsilon/\mathrm{d}T$ values, that there are no unusual structural changes occurring in the present RTILs over the temperature range studied. In other words, the variation of dipole density with T is sufficient to explain the observed temperature coefficients $\mathrm{d}\varepsilon/\mathrm{d}T$.
Given that — with the exception of *cis*-[NTf_2]$^-$ ($\mu = 5.7\,\mathrm{D}$[153]) — the present anions have zero or low dipole moments, it would be expected that the "experimental" values of μ_{eff} derived via eq. 1.69 should correlate well with the values derived from semiempirical MOPAC[118] calculations, which gave for [emim]$^+$, [bmim]$^+$, and [hmim]$^+$, $\mu = (3.5 \pm 0.5)\,\mathrm{D}$, $(7.0 \pm 1.7)\,\mathrm{D}$ and $(10.2 \pm 4.5)\,\mathrm{D}$, respectively (see section 2.5), where the uncertainties correspond to different conformations of the 1-alkyl side chains. While the trend in the gas phase dipole moments of these three cations parallels the μ_{eff} values of their [BF_4]$^-$ salts (table 3.2), the latter show very much smaller variation. These findings suggest that process 1 is not due ***solely*** to the rotational diffusion of individual dipolar imidazolium cations, as has been supposed.[129] Further measurements using a wider range of salts will be required to identify these other possible contributions but some input from antiparallel orientational correlations (see section 3.2.2) among the constituent ions (or larger aggregates) and their resulting cooperative motions seems likely. Consistent with recent computer simulations[176–178] this is almost certainly the case for [hmim][NTf_2].
More important, molecular dynamics simulation[179] and comparison[180] of dielectric relaxation with optical Kerr effect spectroscopy (see section 3.3) yield strong indications for non diffusion-controlled rotation of the constituting ions of the RTILs, but reorientation via large angle jumps. Thus, the observed μ_{eff} can be different from the molecular dipole moment because the dipole vectors are not randomly aligned, but there are some preferred orientations.

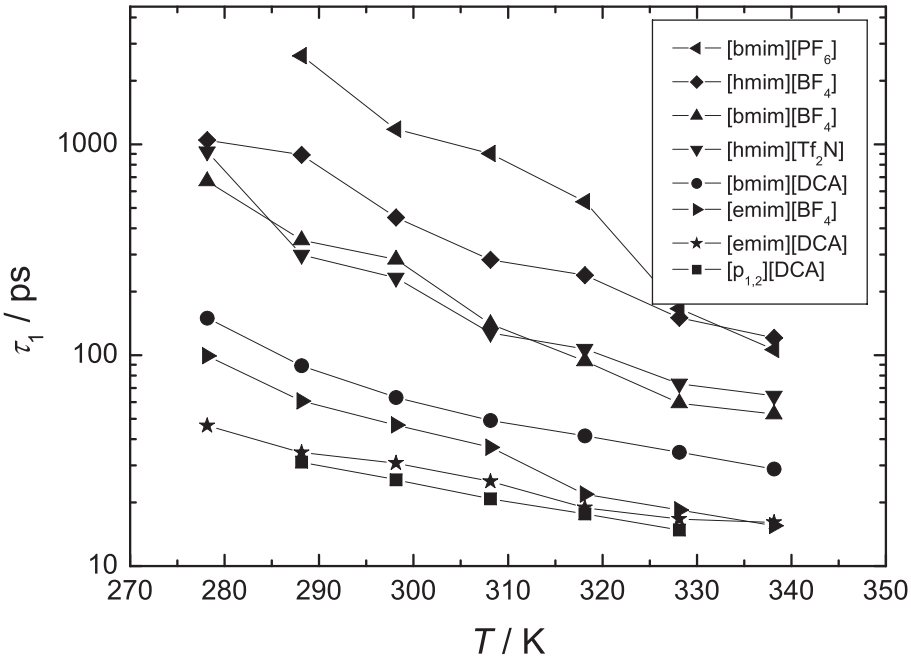

Figure 3.6: Relaxation time of the first (CC) process, τ_1, as function of temperature, T. Lines are included as visual aids.

Activation energies

Observed relaxation times for the dominant first process, τ_1, are plotted against temperature in fig. 3.6. All decrease more or less monotonically with increasing T, with departures probably reflecting experimental errors. The relatively larger decrease for the upper four curves in fig. 3.6 reflect the greater effect of T on their viscosities ([emim][BF_4] is an exception). More importantly, the reasonably smooth decrease in $\tau_1(T)$ with increasing T again shows that there are no unusual or aprupt structural changes in any of the present RTILs over the temperature range studied, contrary to what has been claimed in a recent NMR study.[131]

Due to the experimental uncertainties in τ_1 it was considered sufficient to employ only the simple Arrhenius model (eq. 1.88) used previously,[29] to analyze the present relaxation times as a function of temperature. Activation energies (table 3.3) for the dominant low frequency dielectric relaxation, $E_a(\tau_1)$, were obtained by a linear regression against T of the relaxation times, τ_1, weighted using $\delta\tau_1$ from the non-linear least-squares routine. The values of $E_a(\tau_1)$ are similar to those observed for the cooperative relaxation processes of strongly H-bonded liquids such as water, methanol, ethanol, 1-propanol and 1-butanol for which $E_a(\tau_1)$ =15.9,[181] 13.0[98], 19.9[98], 26.0[98] and 28.6[98] $kJ\,mol^{-1}$, respectively. This again suggests that the slow (τ_1) process in imidazolium-based RTILs may reflect not only rotation of the dipolar cation[129] but also cooperative motions of the IL.

The values of $E_a(\tau_1)$ are quite large but of similar magnitude to, and correlate reasonably well (table 3.3, fig. 3.7) with, the activation energies for electrical conductivity and viscous flow, $E_a(\kappa$ or $\eta)$. Comparison of $E_a(\tau_1)$ for the $[BF_4]^-$ salts of $[emim]^+$, $[bmim]^+$ and

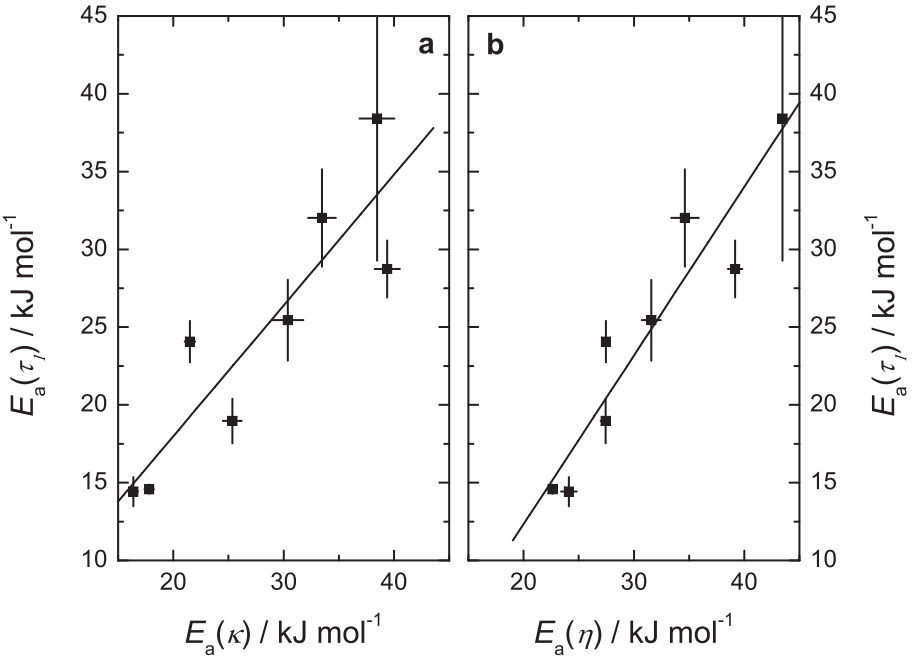

Figure 3.7: Relationship of Arrhenius activation energies for process 1, $E_a(\tau_1)$, as a function of the activation energies for (**a**) electrical conductivity, $E_a(\kappa)$, $R^2 = 0.80$ and (**b**) viscosity, $E_a(\eta)$, $R^2 = 0.89$.

$[hmim]^+$ suggests that, in contrast to $E_a(\kappa$ or $\eta)$, increasing the carbon chain length on the imidazolium cation does not systematically affect $E_a(\tau_1)$. However, this may be a reflection of the greater uncertainties in $E_a(\tau_1)$ for the more viscous RTILs since $E_a(\tau_1)$ values for the less viscous [emim][DCA] and [bmim][DCA] do parallel $E_a(\kappa$ or $\eta)$. Substitution of $[BF_4]^-$ ($r = 274$ pm[182]) for the chemically similar but larger $[PF_6]^-$ ($r = 295$ pm[182]) results in a surprisingly large increase in $E_a(\tau_1)$ which is partly reflected in $E_a(\kappa$ or $\eta)$: compare [bmim][BF_4] and [bmim][PF_6]. On the other hand, substitution of $[BF_4]^-$ by the larger but chemically dissimilar $[NTf_2]^-$ results in a relatively small decrease in $E_a(\tau_1)$ but much larger decreases in $E_a(\kappa$ or $\eta)$.

Volumes of rotation

Provided the reorientation of a molecular-level species is governed by isotropic rotational diffusion, its effective volume of rotation, V_{eff}, can be calculated using the Stokes-Einstein-Debye (SED) theory, which connects (eq. 1.78) the vector-based ($L = 1$, eq. 1.84) rotational correlation time of the species, τ_r, with temperature T and dynamic viscosity η.
The observed dielectric relaxation times, τ, are converted to the corresponding molecular relaxation time via the Powles-Glarum[59,60] equation (eq. 1.82): For this analysis the necessary dynamic viscosities were interpolated or extrapolated from literature data.[155,157,161,167,169] The effective volume of the relaxing species was obtained by a linear regression of the weighted $\tau_{r,DRS}$ values against η/T, *cf.* eq. 1.78. Although such plots were reasonably linear ($0.815 \leq R^2 \leq 0.999$) the values of V_{eff} derived from them (table 3.3) were ex-

traordinarily small compared to the maximum volumes of rotation of $V_{\max} = 510\,\text{Å}^3$ for $[\text{emim}]^+$, $750\,\text{Å}^3$ for $[\text{bmim}]^+$, and $1060\,\text{Å}^3$ for $[\text{hmim}]^+$ or compared to their van der Waals volumes ($V_{\text{vdW}} = 120\,\text{Å}^3$ for $[\text{emim}]^+$; $150\,\text{Å}^3$ for $[\text{bmim}]^+$; $190\,\text{Å}^3$ for $[\text{hmim}]^+$) estimated from semiempirical calculations (see section 2.5). Similar differences have been reported by others.[30,129,183] Even allowing for the difficulties in deciding the boundary conditions (slip or stick), and in defining the volume of rotation of a highly non-symmetrical cation, these small values of V_{eff} suggest that process 1 involves more than just rotational diffusion of the cations.

As already mentioned above, molecular dynamics simulations[179] and comparison[180] of dielectric relaxation with optical Kerr effect spectroscopy (see section 3.3) yield strong indications jump reorientation as the underlying relaxation mechanism. Thus, application of eq. 1.78 is inappropriate and hence the obtained values for V_{eff} do not directly reflect molecular properties.

One possible explanation is that the V_{eff} values might reflect the presence of a strongly inhomogeneous environment around the rotating cation, arising from the proximity of other charged species and leading to anisotropic reorientation, as suggested by NMR measurements[132] and computer simulations.[179,183] This notion is consistent with the decrease with increasing T (tables 3.1 and 3.2), of the Cole-Cole parameter, α, which is a measure of the range of environments experienced by the relaxing species.[184] The decrease in α, which is observed for all the investigated RTILs, reflects the increasing randomization of the environment of the relaxing species, associated with increased thermal motion of the RTIL "particles".

Comparisons of relaxation times

Data for molecular-level relaxation times in RTILs obtained with other techniques are limited.[124,129–131,134,140] Furthermore, before comparing results obtained using different experimental techniques, the rank, L, of the correlation function has to be taken into account (eq. 1.84). For DRS and IR spectroscopy $L = 1$, whereas for Raman, OHD-RIKES and NMR spectroscopies, $L = 2$ (see section 1.4.6).[129,184] This yields $\tau_{\text{r,DRS}} = \tau_{\text{r,IR}} = 3\tau_{\text{r,NMR}} = 3\tau_{\text{r,Raman}} = 3\tau_{\text{r,OHD-RIKES}}$, provided the reorientation of the molecular-level species can be considered as isotropic rotational diffusion in a homogeneous medium of viscosity η,

Discussion of the present relaxation times is best commenced by considering the low viscosity salts as their low-frequency relaxation process is better defined ($\nu_{1,\max} > \nu_{\min}$). In this context, Wulf *et al.*[129] observed the expected ratio (eq. 1.84) between their dielectric and NMR relaxation times for $[\text{emim}][\text{NTf}_2]$. However, their value for $\tau_{\text{r,NMR}} = 39.4\,\text{ps}$ for $[\text{emim}]^+$ in [emim][DCA] is much larger than the $\tau_{\text{r,DRS}}/3 \approx 10\,\text{ps}$ observed in the present study. This difference might arise from anisotropic reorientation of the cation because the H-C2 vector measured by NMR[129] is almost perpendicular to the dipole vector probed by DRS. Nevertheless, the shorter molecular dimensions along the H-C2 vector *cf.* the dipole vector should make $\tau_{\text{r,NMR}}$ smaller, not larger, than $\tau_{\text{r,DRS}}/3$. This implies, consistent with the observed V_{eff} values, that mechanisms other than simple rotational diffusion, *e.g.* cooperative motions, may be present in these RTILs. Similarly, the average ^{13}C-NMR correlation time, $\tau_{\text{r,NMR}} \approx 25\,\text{ps}$, reported for $[\text{emim}]^+$ in $[\text{emim}][\text{BF}_4]$ at $\sim 335\,\text{K}$[131] is also

considerably higher than the present value of $\tau_r/3 \approx 5$ ps at this temperature (table 3.1). More importantly, the NMR value[131] is inconsistent with the relaxation time of $[emim]^+$ determined by OHD-RIKES measurements on $[emim][NO_3]$.[124] The latter gave a relaxation time ~ 15 times slower than the NMR result, which cannot be accounted for by differences in viscosity ($\eta([emim][NO_3]) \approx 70$ mPa s cf. $\eta([emim][BF_4]) \approx 37$ mPa s at 298 K). It should also be noted that the claimed transition of $[emim][BF_4]$ from discrete ion pairs to individual ions above 335 K[131] is inconsistent with the present results and also with the much broader bandwidth dielectric spectrum reported by Sangoro *et al.*[151] for $[bmim][BF_4]$. The latter study excludes the presence of any discrete ion pairs with a sufficient life-time to be detected by DRS in the neat IL.

For the more viscous RTILs, not only are the τ_r values obtained by DRS less well defined (because $\nu_{1,max} < \nu_{min}$) but also the differences between the orientational relaxation of the aromatic imidazolium ring and the flexible alkyl side-chain increase. Both NMR[130] and quasi-elastic neutron scattering[140] studies of $[bmim]^+$ in $[bmim][PF_6]$ were able to separate the orientational dynamics into these two contributions. The results ($\tau_{r,NMR} \approx 2$ ns at 25 °C)[130] obtained for the slower rotation of the cation ring are also a factor of 5 greater than the present result of $\tau_{r,DRS}/3 \approx 0.4$ ns. This again suggests that cooperative effects may be important in RTIL dynamics.

Clearly, the available data imply that the reorientational dynamics of the cations in these RTILs cannot be viewed as isotropic rotational diffusion. This is in line with the recent simulation results of Shim and Kim[185] who not only found that the relaxation of $[emim]^+$ was markedly anisotropic but also that the reorientation was characterized by large-angle ($> 90°$) "hopping" motions (see sections 1.4.6 and 3.3). This observation is supported by comparing the dielectric spectra with optical Kerr effect spectra of related compounds (see section 3.3).[180]

3.2.2 [emim][$EtSO_4$] — An ionic liquid with dipolar cation and anion

Parts of the material presented in this chapter form the basis of the paper:

Johannes Hunger, Alexander Stoppa, Richard Buchner, and Glenn Hefter *"Dipole Correlations in the Ionic Liquid 1-N-Ethyl-3-N-methylimidazolium Ethylsulfate and Its Binary Mixtures with Dichloromethane" J. Phys. Chem. B* **2009**, *113*, 9527-9537.

One of the most promising RTILs for industrial application is 1-*N*-ethyl-3-*N*-methylimidazolium ethylsulfate ([emim][$EtSO_4$]), since it is commercially available on a large scale and cheap.[186] This compound has an unusually high dielectric constant,[28] a relatively large electrochemical window,[8] is useful as a reaction medium[187,188] and has applications in separation technology.[189–191] Surprisingly, in spite of the potential utility of [emim][$EtSO_4$], few of its physicochemical properties have been reported,[192–195] and almost nothing is known about its dynamics.
Interestingly, the dielectric constant for [emim][$EtSO_4$] is almost three times higher than for other imidazolium-based RTILs.[11,28,147] No convincing explanation has yet been given for this observation and empirical correlations used for predicting dielectric constants fail for this compound.[196]
The main difference of [emim][$EtSO_4$] compared to the RTILs presented in the previous section is, that in addition to the dipolar $[emim]^+$, the $[EtSO_4]^-$ has a remarkably high dipole moment of $\mu = 11.2$ to 13.2 D (from semiempirical calculations, see section 2.5) depending on the conformation of the anion. The influence of the dipolar anion on the dynamical as well as static properties of this IL and the conclusions that can be drawn from these will be presented in the following section.
The dielectric spectra over a broad range of frequencies ($0.2 \leq \nu/\mathrm{GHz} \leq 89$) for neat [emim][$EtSO_4$] over the temperature range of $5 \leq \theta/\,^\circ\mathrm{C} \leq 65$ were obtained by combining data at $0.2 \lesssim \nu/\mathrm{GHz} \leq 20$ from a frequency-domain reflectometer (HP8720D VNA, see section 2.3.3) and two waveguide interferometers operating at $27 \leq \nu/\mathrm{GHz} \leq 89$ (see section 2.3.2). Raw VNA data were obtained using air, mercury and purified DMA as primary calibration standards. For secondary calibration purified BN and 1-butanol were used (section 2.3.3) Typical experimental spectra for the neat IL are displayed in fig. 3.8.

Relaxation model

The spectra of neat [emim][$EtSO_4$] show that the maximum in $\varepsilon''(\nu)$ shifts to higher frequencies with increasing temperature (fig. 3.8b) in accordance with a decrease in viscosity[192,195] and consequently accelerated dynamics. After extensive testing of alternatives it was found that a CC+D+D model provided the best description of the observed spectra at all temperatures (fig. 3.9, table 3.5). This model is analogous to that reported recently for seven related imidazolium-based RTILs[11] (section 3.2.1) except for the presence of an additional Debye process at ~ 8 GHz in the present spectra (see below). It should be noted that, while the three modes in the dielectric spectrum of neat [emim][$EtSO_4$] are well defined within the present frequency range at $\theta > 35\,^\circ\mathrm{C}$, at lower temperatures the dominant

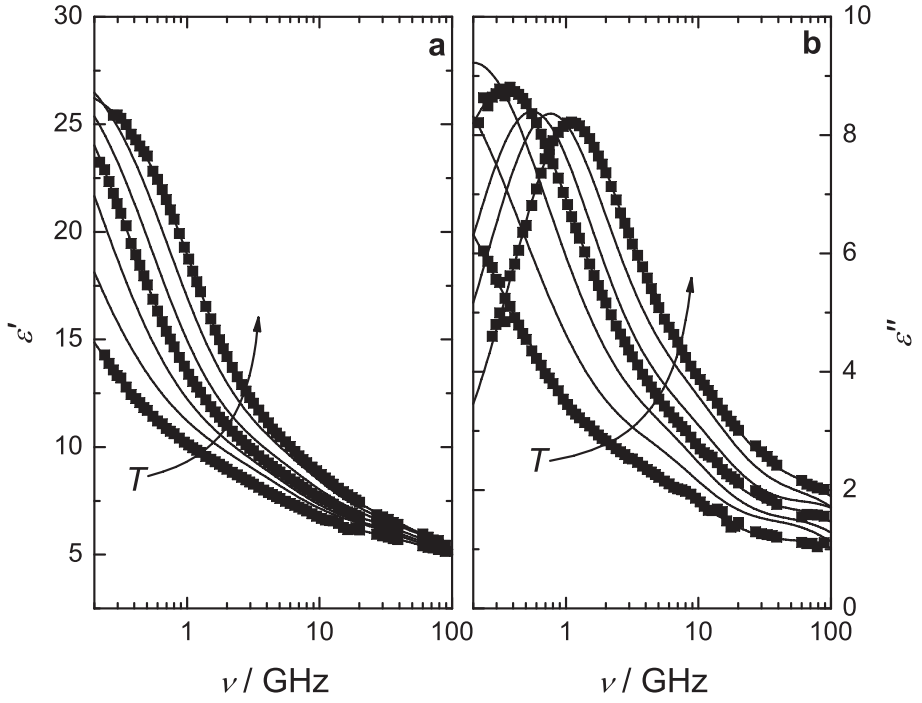

Figure 3.8: Dielectric permittivity (**a**), $\varepsilon'(\nu)$, and dielectric loss (**b**), $\varepsilon''(\nu)$, spectra of neat [emim][$EtSO_4$] at $5 \leq \theta/\,°C \leq 65$. Symbols show typical experimental data (others are omitted for visual clarity); lines represent the CC+D+D fit; arrows indicate increasing T.

Table 3.5: Fit parameters of eq. 1.61 for the observed dielectric spectra of neat [emim][$EtSO_4$] in the temperature range $278.15 \leq T/\mathrm{K} \leq 338.15$ assuming a CC+D+D model: static permittivities, ε; relaxation times, τ_j, and amplitudes, S_j, of process j; Cole-Cole shape parameter, α of the first (lowest frequency) process; infinite frequency permittivity, ε_∞, and reduced error function of the overall fit, χ^2_r.[a]

T	ε	τ_1	α	S_1	τ_2	S_2	τ_3	S_3	ε_∞	$\chi^2_\mathrm{r}/10^{-5}$
278.15	39.16	3770	0.40	32.0	26.7	1.59	1.85	1.37	4.22	175
288.15	36.95	1530	0.30	28.8	27.0	2.02	2.45	1.76	4.36	247
298.15	35.20	806	0.24	26.9	24.0	2.22	2.03	1.89	4.24	265
308.15	32.51	476	0.21	24.1	20.2	2.14	1.87	2.13	4.12	268
318.15	29.42	297	0.13	20.3	17.5	2.70	1.54	2.49	3.89	247
328.15	29.17	218	0.13	19.8	16.0	2.90	1.77	2.35	4.10	340
338.15	27.33	149	0.072	17.6	14.4	3.16	1.76	2.59	3.98	357

[a]Units: T in K; τ_j in ps.

CC process is located close to the lower frequency limit (fig. 3.8), which increases the uncertainties in the derived relaxation parameters. This problem was also encountered with other imidazolium-based RTILs and has been discussed at length in the previous section.

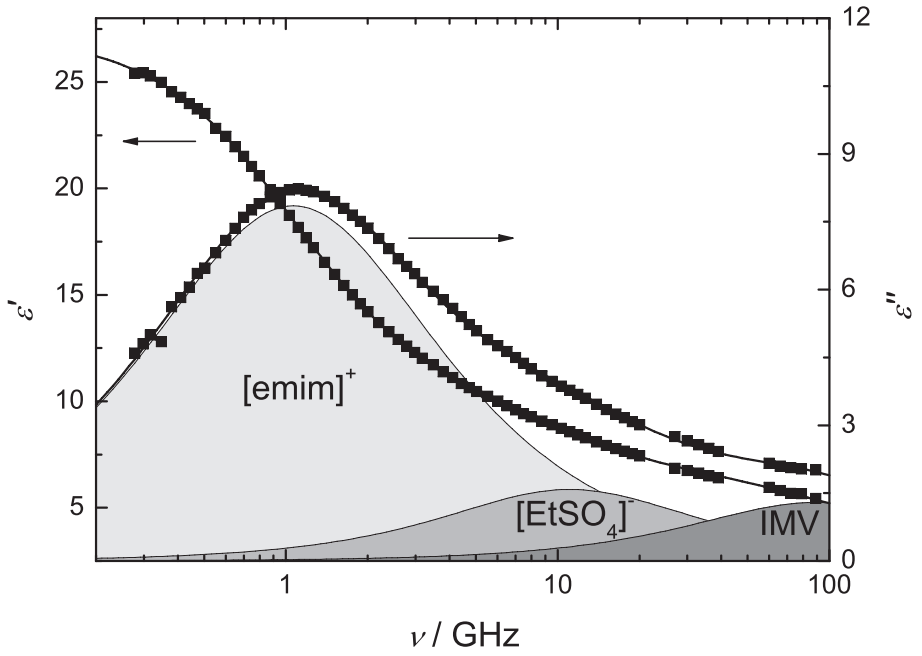

Figure 3.9: Dielectric permittivity, $\varepsilon'(\nu)$, and loss, $\varepsilon''(\nu)$, spectrum of neat [emim][$EtSO_4$] at 65 °C. Symbols represent experimental data, lines show the CC+D+D fit, and shaded areas indicate the contributions of the cation ($[emim]^+$), the anion ($[EtSO_4]^-$), and intermolecular vibrations (IMV).

Assignment of dielectric relaxation modes

The highest frequency mode centered at $\sim$ 80 GHz (corresponding to a relaxation time of $\sim$ 2 ps) is observed for all imidazolium-based RTILs investigated to date[11,26,143,144,146] and occurs also in time-resolved Kerr spectra[124,127,133,197] of related compounds at THz frequencies (see section 3.3). As will become apparent in section 3.3, it is dominated by intermolecular vibrations. However, due to its location close to the high frequency limit (89 GHz) of the present spectra and because the observed mode is overlapped by additional higher frequency modes[146,180] (see section 3.3) detailed analysis of mode 3 is not appropriate on the basis of the present frequency range.

In contrast to the spectra of previously-studied neat imidazolium-based ionic liquids[11] and of [bmim][BF_4] + DCM mixtures,[111] the intermediate Debye mode centred at $\sim$ 8 GHz occurs only in the present spectra, both for neat [emim][$EtSO_4$] and its mixtures with DCM. Accordingly, this mode can be assigned unequivocally to the reorientation of dipolar $[EtSO_4]^-$ anions. Whereas $[BF_4]^-$ has no dipole moment, semiempirical MOPAC[118] calculations yield a value of $\mu_{ap,-} = 11.2$ to 13.2 D for $[EtSO_4]^-$, depending on its conformation (see section 2.5). This assignment is in accordance with MD simulations of the dielectric spectrum of 1-*N*-butyl-3-*N*-methylimidazolium trifluoroacetate, [bmim][CF_3CO_2].[178] This compound also contains a dipolar anion, which simulations predict to contribute to the dielectric spectrum between the translational and cation reorientation modes.

The low frequency Cole-Cole mode, centred at 0.04 to 1 GHz depending on temperature, is also observed for other imidazolium-based RTILs[11,30,111,146,147] and is assigned to the reorientation of the dipolar cations.† The MD simulations of [bmim][CF_3CO_2][178] suggest that anion and cation reorientations overlap, and that there is a cross correlation between them. Even though both of these effects are small, contributing $< 10\,\%$ to the amplitude of each mode,[178] the simulations imply that the low frequency mode observed for [emim][$EtSO_4$] is not exclusively due to $[emim]^+$ reorientation.

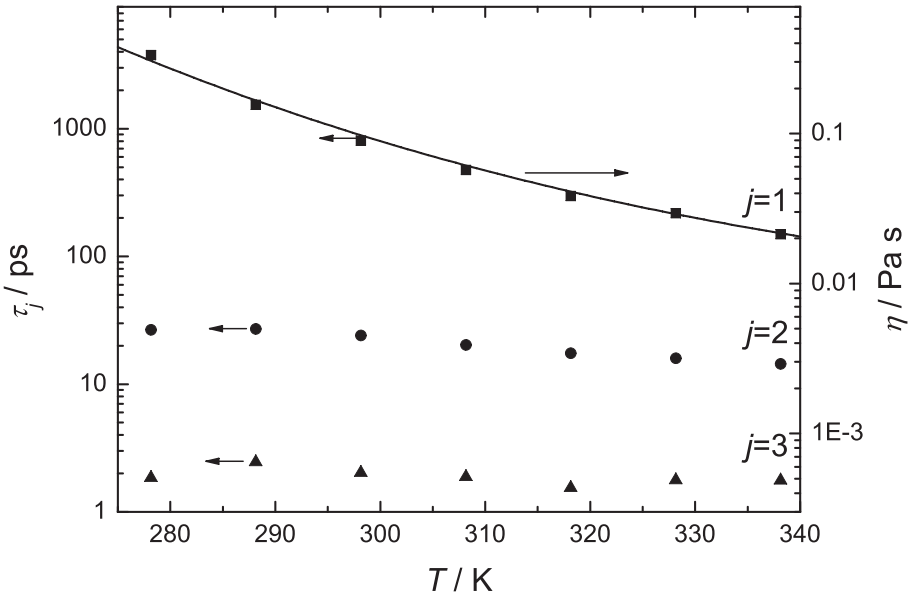

Figure 3.10: Relaxation times, τ_j, (left-hand axis, symbols) of the three observed relaxation processes and viscosity, η, (right-hand axis, full line)[192,195] of neat [emim][$EtSO_4$], as function of temperature, T.

Relaxation Times

The location of the maximum in $\varepsilon''(\nu)$ for neat [emim][$EtSO_4$] is largely a reflection of the relaxation time τ_1, since process 1 is the main dispersion step (fig. 3.8). The large decrease in τ_1 with increasing T correlates well with changes in viscosity, η (fig. 3.10, uppermost curve). The relaxation time τ_2 associated with the second mode centred at $\sim$ 8 GHz, also decreases as T increases (fig. 3.10, middle curve), but to a much lesser extent. The relaxation time for process 3 scatters somewhat, but is almost independent of T (fig. 3.10, lowest curve).

The temperature dependence of τ_j (table 3.5) can be analysed in terms of the Arrhenius equation[11,29] (eq. 1.88) which yields activation energies of $E_a(\tau_1) = (41 \pm 2)\,\mathrm{kJ\,mol^{-1}}$ and $E_a(\tau_2) = (8.9 \pm 0.8)\,\mathrm{kJ\,mol^{-1}}$. The value of $E_a(\tau_1)$ is approximately twice that observed

†It is not clear at present whether the mechanism of reorientation is solely due to single particle (cation) rotation. A recent study[11] suggests that cooperative motions may also be significant and reorientation via large angle jumps are likely.[179,180]

for other RTILs containing $[emim]^+$ but is broadly comparable to the activation energies shown by [emim][$EtSO_4$] for viscous flow ($E_a(\eta) = 34.4 \pm 0.7\,kJ\,mol^{-1}$) and for electrical conductivity ($E_a(\kappa) = 34.9 \pm 1.3\,kJ\,mol^{-1}$).[‡] The large values of these activation energies probably reflect an unusually large energetic barrier for the reorientation of the cation due to dipole-dipole correlations. The very much smaller value of $E_a(\tau_2)$ cf. $E_a(\tau_1)$ is partially due to the smaller volume of rotation of $[EtSO_4]^-$ (see below) and probably to the "stacking" (and hence correlation) of $[emim]^+$ suggested by MD simulations.[177,198] Also different mechanisms of reorientation (e.g. jump reorientation as suggested by MD simulations)[179] might be reflected in the different activation energies. The scatter in $\tau_3(T)$ does not permit a meaningful analysis, but the resulting activation energy of $E_a(\tau_3) \simeq 0$, is consistent with this process arising from intermolecular vibrations.

Although experimental relaxation times often scale with viscosity, as for τ_1 in [emim][$EtSO_4$], there is mounting evidence[11,111,179,183] that the reorientation of the ions in imidazolium RTILs cannot be described as either isotropic or rotational diffusion. Thus, application of the Stokes-Einstein-Debye equation (eq. 1.78), which is strictly valid only for isotropic rotational diffusion, to relate the corresponding microscopic relaxation times, τ'_j, to the solution viscosity, η, and the effective volume of rotation of the relaxing species, $V_{\mathrm{eff},j}$, should be considered with caution. This is especially true for dielectric experiments because the obtained macroscopic τ_j, which reflects self- *and* cross-correlations of the dipoles, has to be converted into τ'_j via the Madden-Kivelson equation (eq. 1.83) Unfortunately, application of eq. 1.83 to the present dipole mixtures is problematic as it was derived for pure liquids consisting of a single dipole species. Additionally, the value for the dynamic correlation factor, $\dot{g}$ (which, by analogy with the substitution $g_K \to g_j$, is replaced by $\dot{g}_j$ for each relaxation), which accounts for possibly correlated motions of the tagged dipole and its neighbours, is not independently accessible.[61] For RTILs, where ion shapes often deviate significantly from spherical, the usual assumption of $\dot{g} \approx 1$ seems questionable. In the present case, combination of eqs. 1.78 and 1.83 will thus only allow a check of whether isotropic rotational diffusion represents a reasonable relaxation mechanism for a given process.

If we follow the commonly used Powles-Glarum approach (eq. 1.82) and assume negligible static and dynamic correlations for relaxations $j = 1$ & 2, *i.e.* $g_j/\dot{g}_j = 1$, we obtain effective volumes of $V_{\mathrm{eff},1} = (7 \pm 1)\,Å^3$ and $V_{\mathrm{eff},2} = (0.3 \pm 0.2)\,Å^3$ for the cations and the anions, respectively. These values are much smaller than the corresponding maximum volumes of reorientation ($V_{\mathrm{max},+} = 510\,Å^3$ and $V_{\mathrm{max},-} = 310\,Å^3$) and the van-der-Waals volumes ($V_{\mathrm{vdW},+} = 120\,Å^3$ and $V_{\mathrm{vdW},-} = 90\,Å^3$) (see section 2.5). Such a discrepancy has been noted for other RTILs[11,30,111] and was taken as an argument against rotational diffusion of the ions being a realistic explanation for the observed dielectric process. This argument remains unchanged even if the strong orientational correlations among the ions suggested by our results (fig. 3.11) are taken into account and $\dot{g} \approx 1$ is assumed. Since $g_+ > 1$ (see below) $V_{\mathrm{eff},1}$ becomes even smaller, whereas $V_{\mathrm{eff},2}$ is still, by an order of magnitude, too small despite $g_- \approx 0.02$. In the framework of isotropic rotational diffusion, effective and molecular volumes could only be reconciled by assuming that the $\dot{g}_j$ are vastly different

[‡] $E_a(\eta$ or $\kappa)$ were obtained by application of eq. 1.88 to appropiate literature data.[156,192,195]

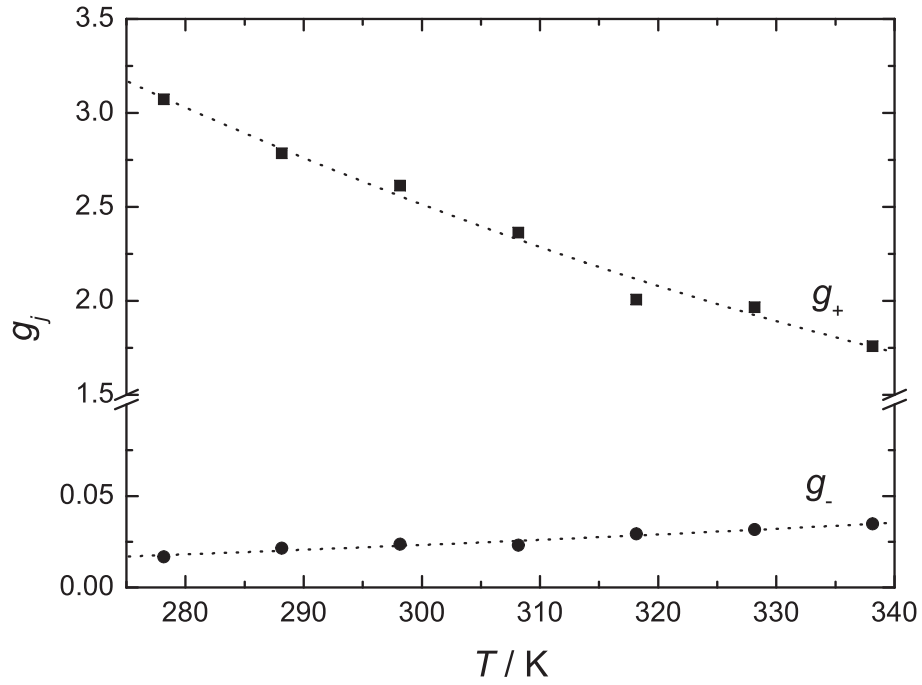

Figure 3.11: Orientational correlation factors of $[emim]^+$, g_+, (■) and $[EtSO_4]^-$, g_-, (●) in neat $[emim][EtSO_4]$ as a function of temperature, T.

from unity, which seems unlikely. The most straightforward interpretation of the present results is that in the pure RTIL (and RTIL-rich mixtures, see section 4.2.2) cations and anions do **not** reorient via uncorrelated isotropic rotational diffusion.
This explains the relatively large separation between the cation and anion modes (processes 1 and 2; table 3.5; fig. 3.9), which is at variance with recent MD simulations.[199] The latter suggested that the rotational correlation times for these two ions should be rather similar, although the values predicted are much larger than τ_1 and τ_2 (table 3.5, fig. 3.10). The observed difference between the present values of τ_1 and τ_2 reflects differences in the anisotropy and the "jump" angle for the reorientation of the cation and anion, as has been proposed for $[emim]^+$ in $[emim][PF_6]$ on the basis of MD simulations.[179] Such hindered rotation would be even more likely for $[emim][EtSO_4]$ because of its non-spherical anion. This interpretation is strongly supported by the E_a values discussed above and the g_j factors (see below), which indicate strong orientational correlations of both the cation and anion.

Static Permittivity

The present estimate of the static permittivitiy of $[emim][EtSO_4]$, $\varepsilon = 35.20$ at 25 °C (table 3.5), is considerably higher than the value of $\varepsilon = 27.9$ reported by Weingärtner[28] and, more importantly, than those observed for other imidazolium-based RTILs.[11,28,147] There are several explanations for these differences. First, Weingärtner's value was derived from data measured over a more limited frequency range[28] and is therefore less certain than the present result. Second, as discussed at length elsewhere (see section 3.2.1),[11] the static permittivity of imidazolium-based RTILs is sensitive to the model adopted for the dominant

low frequency process. The Cole-Davidson model used previously by Weingärtner[28,147] and Stoppa *et al.*[146] to describe this process gives systematically lower values of ε *cf.* the CC model adopted here.[11] This effect is exacerbated for [emim][$EtSO_4$] by the relatively high dielectric loss at low ν (fig. 3.8). Third, the uncertainty in ε is larger than is usual for DRS measurements because of the location of the low frequency process close to the lower frequency limit of the present instrumentation. Fourth, and probably most significant with respect to comparison with other RTILs, it is likely that the $[emim]^+$ cations in the neat [emim][$EtSO_4$] are strongly parallel correlated, as is observed in its mixtures with DCM (see section 4.2.2). This last point is consistent with the value of the temperature derivative of the static permittivity ($d\varepsilon/dT = -0.20$), which is about an order of magnitude larger than those observed for other imidazolium-based ionic liquids (section 3.2.1).[11]

Amplitudes

The amplitude (peak area) of the first process, S_1, decreases with increasing T, whereas S_2 and S_3 increase (table 3.5). Utilizing the uncorrelated dipole moments of the cation $\mu_{ap,+} = 4.46\,D$ and the anion $\mu_{ap,-} = 14.0\,D$ in solution obtained from the measurements on the IL + DCM mixtures (see section 4.2.2 below) and the analytical RTIL concentration for both ions, *i.e.* $c = c_+ = c_-$, the temperature dependence of the correlation factors of the cations, g_+, and of the anions, g_-, can be calculated from S_1 and S_2 via eqs. 1.69 and 1.70. As can be seen from fig. 3.11, g_+ is significantly larger than unity, whereas g_- is considerably smaller. This indicates strong intermolecular interactions, with cations experiencing an environment where the surrounding dipoles are mostly parallel to the tagged dipole, whereas the anion dipoles are largely antiparallel to adjacent dipoles. As expected, the intermolecular interactions decrease with increasing temperature, as both the antiparallel correlation of the anions and the parallel correlation of the cations are weakened (g_- increases, g_+ decreases). As indicated in section 1.4.3, the derived correlation factors g_+ and g_- are only an indirect measure of the local environments of the cations and anions as these empirical quantities cannot be split into the relative contributions arising from correlations among like and unlike species on the basis of dielectric data alone. Here scattering experiments and/or computer simulations using the present correlation factors as a benchmark might help to obtain a more detailed view of the [emim][$EtSO_4$] structure. At present, it can only be inferred that the very small values of g_- and the corresponding large values of g_+ are not so much a result of pronounced antiparallel alignment anions relative to each other but more likely an indication of strong anion-cation interactions which slow down the dynamics of *some* anions to the timescale of the cation relaxation. In other words, the motions of cations and anions partly synchronize, with the slowest partner (the cation) determining the pace. As a consequence, the concentration of slow dipoles (relaxing with τ_1) would be larger than the concentration of cations, c_+, and that of fast dipoles (relaxing with τ_2) smaller than c_-. In the present analysis of S_1 and S_2 with eq. 1.69 such deviations would be included in the correlation factors, leading to $g_+ > 1$ and $g_- < 1$. Note that this (partial) synchronization of cation and anion dynamics has to be distinguished from the situation for an ion pair (as found in dilute solutions in DCM, see section 4.2.2), because in the latter the constituting anions and cations move together in a fixed relative orientation. Nevertheless, there is a considerable degree of dipole-dipole correlations in [emim][$EtSO_4$]

since the effective dipole moment obtained from the combined amplitudes $S_1 + S_2$ is not constant.
The slight increase of S_3 with increasing T (table 3.5) might reflect an enhancement of intermolecular vibrations, due to the decreasing correlation of the ions but, as this mode is close to the present high frequency limit where other modes contribute (see section 3.3) a more detailed analysis is not appropriate here.

3.3 Broadband spectra at 0.2 GHz $\leq \nu \leq$ 10 THz at 25 °C

As is apparent from the previous sections, the frequency range up to 89 GHz is not covering all relevant modes in RTILs and the dielectric loss has not yet decayed to zero at THz frequencies.[26,143,144,146] These higher frequency modes in RTILs range up to far-infrared frequencies[200,201] and originate in translational modes as found by MD simulations.[170] Some of these intermolecular vibrations at far-infrared frequencies are occasionally attributed to hydrogen-bonds via the C2-H atom in imidazolium based ionic liquids.[131,200,201]

Most of the studies published in the literature focus on restricted frequency ranges (i.e. microwave frequencies,[27–30,145,147–151] THz frequencies[26,143,144] or far-infrared frequencies[200,201]) and thus the accessible information on the intermolecular modes in RTILs is limited, since these high frequency modes overlap and stretch out over very wide frequency ranges. To disentangle all contributions the spectra presented in the previous section at $0.2 \lesssim \nu/\mathrm{GHz} \leq 89$ were supplemented by THz and far infrared spectra at 25 °C to cover all relevant modes present in RTILs.

Spectra were obtained by a combination of data recorded with a frequency-domain reflectometer (HP8720D VNA, section 2.3.3, $0.2 \lesssim \nu/\mathrm{GHz} < 20$) two waveguide interferometers ($27 \leq \nu/\mathrm{GHz} \leq 89$, section 2.3.2) and a transmission/reflection THz-time-domain spectrometer ($0.3 \leq \nu/\mathrm{THz} \leq 3$, section 2.3.4). All measurements were conducted at (25.00 ± 0.05) °C, except for the THz-TDS spectra which were recorded at (25.0 ± 0.5) °C. Data were supplemented by far-infrared absorption data ($25 - 450\,\mathrm{cm^{-1}}$; $0.75 - 13.5$ THz) converted to complex permittivity spectra via the Kramers-Kronig transformation (section 2.3.5). Spectra were recorded for the $[BF_4]^-$ salts of $[emim]^+$, $[bmim]^+$ and $[hmim]^+$ as well as for the $[DCA]^-$ containing RTILs of $[emim]^+$ and $[bmim]^+$. To investigate effects due to the anion the $[CF_3CO_2]^-$ and $[PF_6]^-$ salts of the $[bmim]^+$ cation were studied. Due to the reasonably high viscosity of $[bmim][CF_3CO_2]$ ($\eta^{30\,°C} = 58\,\mathrm{mPa\,s}$)[155] this RTIL exhibits a considerable dispersion below 200 MHz. Thus, the spectrum was extended with cut-off type coaxial cells (section 2.3.3) to ≈ 50 MHz using TS1 cell[100] and a (1-propanol, air, NaCl(aq, $m \simeq 5\,\mathrm{mol\,kg^{-1}}$) calibration.

The spectra of the investigated compounds are displayed in figs. 3.12 and 3.13 emphasizing effects due to the cations and the anions, respectively. All the present spectra show broad peaks in $\varepsilon''(\nu)$ in the low GHz and THz regions and a reasonably distinct plateau in $\varepsilon'(\nu)$ at high GHz frequencies. $\varepsilon'(\nu)$ has almost reached a constant value and $\varepsilon''(\nu)$ has declined close to zero at the high frequency limit, thus all THz and far-infrared modes below 10 THz ($334\,\mathrm{cm^{-1}}$) are properly defined within the current spectral range. However, for the highly viscous $[bmim][PF_6]$, the maximum in $\varepsilon''(\nu)$ is close to the edge of the spectral range at low frequencies and thus the uncertainties for the slow modes are higher than for the less viscous compounds (eg. [emim][DCA] and $[emim][BF_4]$). From qualitative consideration of the spectra it becomes apparent, that increasing chain length of the imidazolium cation results in a red-shift of the peaks in the GHz range — in accordance with the increasing viscosity[146] — whereas the higher-frequency modes vary mainly in intensity. The variation in the amplitude of the main (low-frequency) DR mode is in accordance with the variation in the dipole moment and dipole density (as discussed in section 3.2.1). It is noteworthy, that variation of the anion has no pronounced effect on the lower-frequency modes (apart from

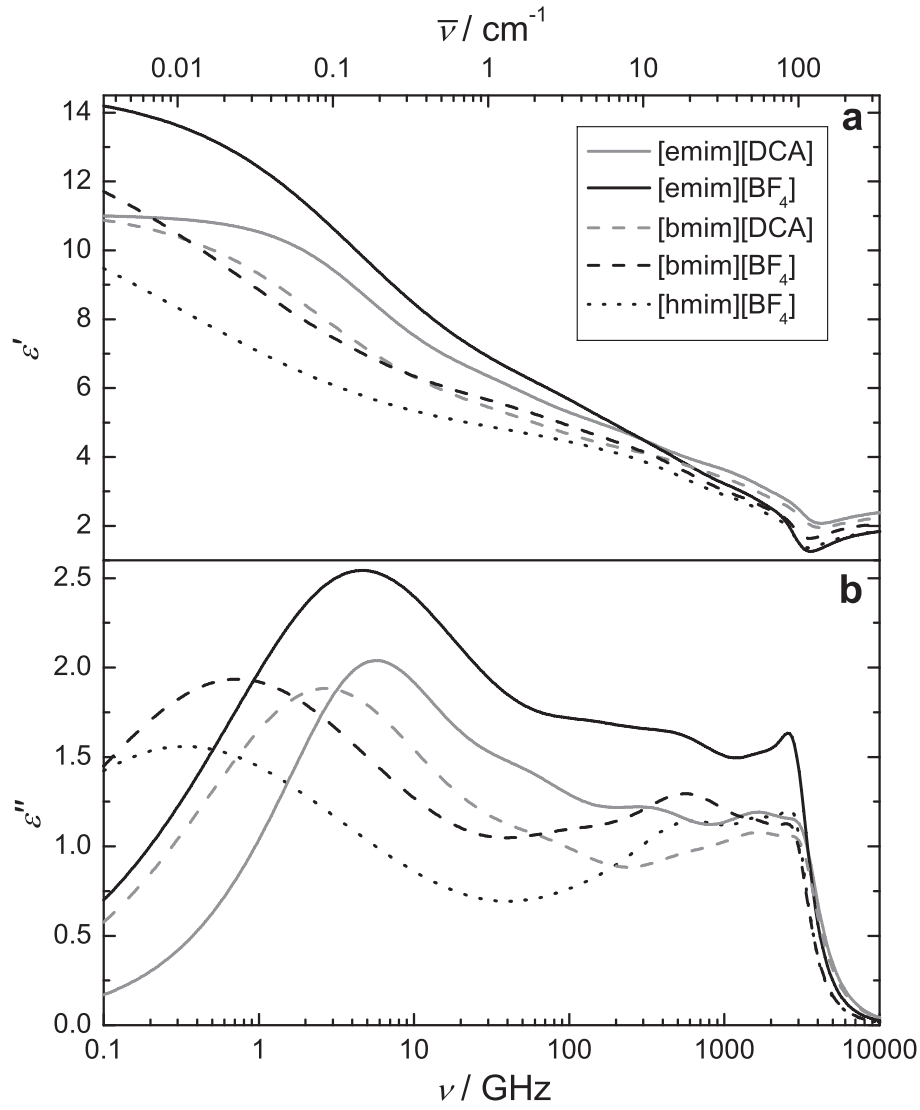

Figure 3.12: (**a**) Dielectric permittivity, $\varepsilon'(\nu)$, and (**b**) dielectric loss, $\varepsilon''(\nu)$ spectra of $[BF_4]^-$ and $[DCA]^-$ salts at 25 °C including THz and far-infrared data. For visual clarity only the fits are displayed.

the described change in viscosity and dipole density, fig. 3.13) except for [bmim][CF_3CO_2] where the main low-frequency mode is much slower than for the other salts (in spite of its medium viscosity).[155] This suggests that the highly asymmetrical and dipolar anion has a major impact on the structural and dynamical properties of the RTIL, similar to $[EtSO_4]^-$ (see section 3.2.2).

3.3.1 Comparison with MD simulations

Recently, the DR spectra of [emim][DCA] and [bmim][CF_3CO_2] were MD simulated by Schröder *et al.*[170] at frequencies ranging from ∼ 1 MHz to ∼ 8 THz. In contrast to sim-

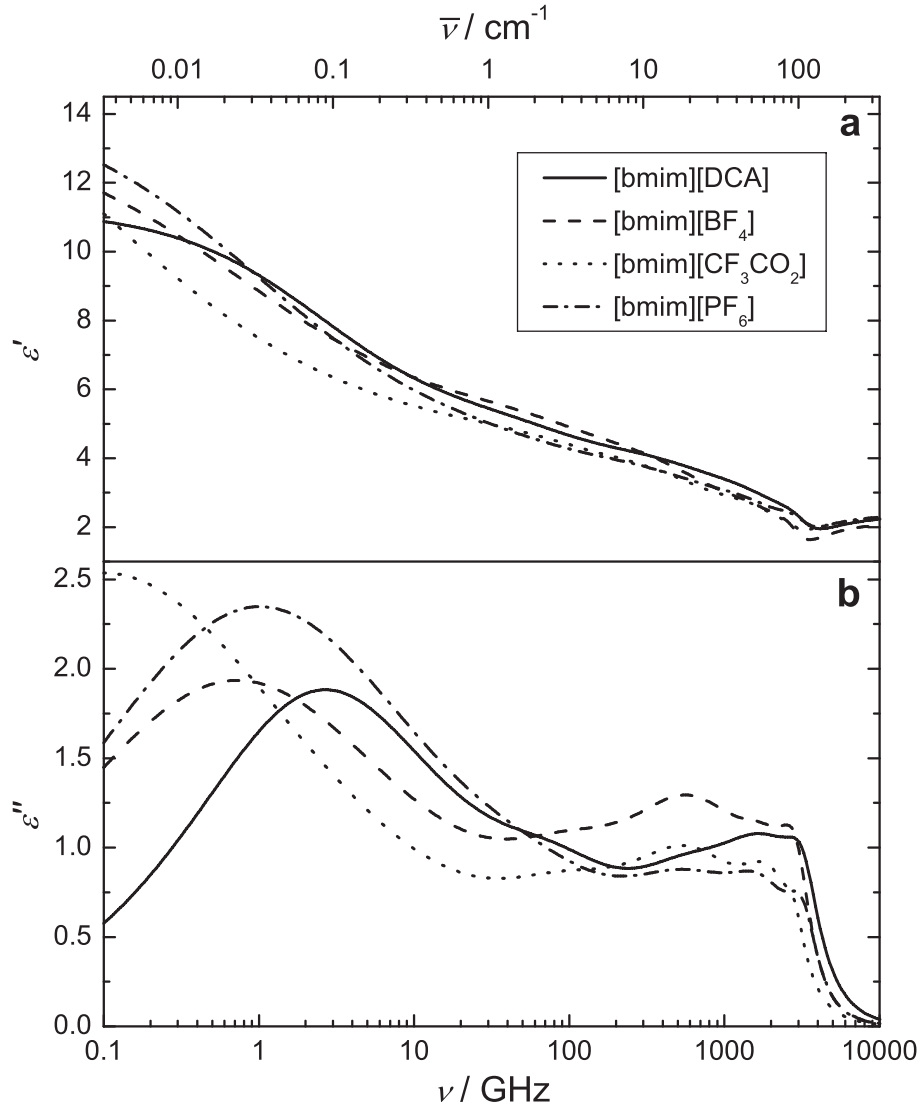

Figure 3.13: (**a**) Dielectric permittivity, $\varepsilon'(\nu)$, and (**b**) dielectric loss, $\varepsilon''(\nu)$ spectra of the $[BF_4]^-$, $[DCA]^-$, $[CF_3CO_2]^-$ and $[PF_6]^-$ salts of the $[bmim]^+$ cation at 25 °C including THz and far-infrared data. For visual clarity only the fits are displayed.

ulations of aqueous [bmim][BF_4] solutions,[202] the simulated and measured spectra agree poorly for the neat ILs (fig. 3.14). Nevertheless, the MD simulation can give insights into the underlying relaxation mechanism. Especially the possible splitting into rotational and translational contributions provides valuable insight into the systems.

The static permittivity is slightly underestimated for [emim[DCA] and considerably overestimated for [bmim][CF_3CO_2] (fig. 3.14) by the simulations. Interestingly, the simulations predict translational contributions at relatively low frequencies (down to ~ 1 GHz), which is a very important observation for the analysis and interpretation of the experimental spectra.

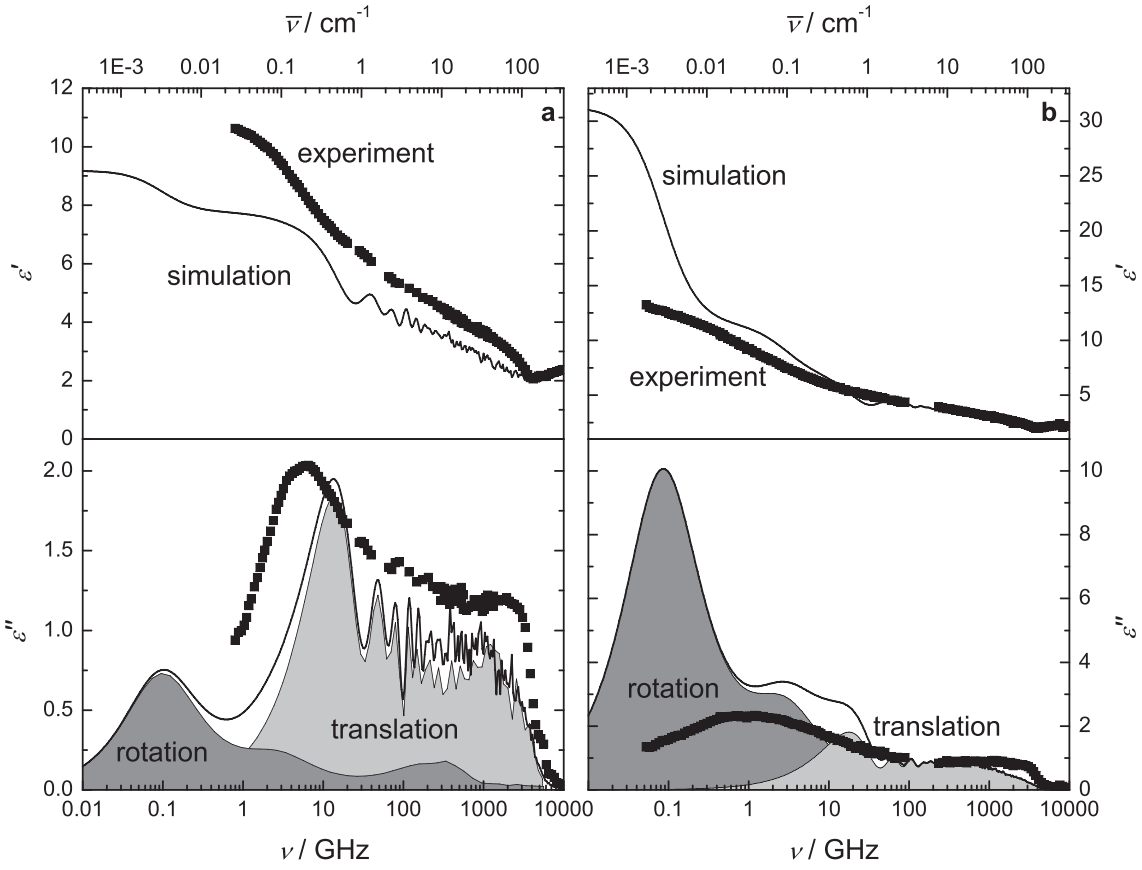

Figure 3.14: Comparison of experimental (symbols) dielectric dispersion, $\varepsilon'(\nu)$, and dielectric loss, $\varepsilon'(\nu)$, spectra at 25 °C with results from MD simulations[170] (lines) for (**a**) [emim][DCA] and (**b**) [bmim][CF_3CO_2]. Simulations were performed at 300 K. Shaded areas indicate rotational and translational contributions, as predicted by the computer simulations.

Detailed comparison of theory and experiment reveals that the simulation reproduces the high frequency onset excellently (fig. 3.14), i.e., the highest-frequency translational contributions (intermolecular vibrations) are predicted very well by the MD simulation. In contrast the simulation cannot fully reproduce intramolecular modes, since the bond-lengths are fixed during the simulation and thus stretching vibrations can not be rendered and other intramolecular modes involving a change in the bond angles are biased. Moreover, the high frequency part of the simulation differs in the amplitude from the experiment and also the statistics appear to be not sufficient to quantitatively reproduce the experiment since the computer simulation produce considerable oscillations of the translational modes.

The rotational contributions of the simulation are much slower compared to the experiment. This is at least partly a reflection of the overestimated by a factor of ~ 3 viscosity of the simulation for [emim][DCA].[203] However, the difference in viscosity cannot account completely, for the differences in the timescales of the experiment compared to the simulation. Moreover, for [bmim][CF_3CO_2] the simulation reproduces the experimental value for

η pretty well,[178] thus the slow rotational dynamics as predicted by MD simulations cannot be solely due to viscosity effects.
Attempts to scale the rotational part of the simulation in order to match the experimental curve for [emim][DCA] suggested that the rotational dynamics of the simulation have to be faster by a factor ~ 10 to reproduce the experiment roughly. For [emim][DCA] the amplitude of the rotational modes appears to be slightly lower compared to the experiment. This might be explained by the negligence of the polarizability of the ions by the force field used for the MD simulation.[204] However, the computation of dielectric spectra requires already very long simulation times (100 ns)[178] and proper treatment of polarizability for slow dynamical processes, like dipole rotation is quite time consuming with current computer equipment.
For [bmim][CF_3CO_2] the simulation deviates considerably from the experiment, i.e. the simulation predicts a huge rotational contribution at low frequencies, that is experimentally not observed. This results in the considerable overestimation of the static permittivity. It is likely that these findings are a reflection of problems in the parameterization of the $[CF_3CO_2]^-$ anion, since theory and experiment agree reasonably for another [bmim][BF_4].[148] The problem might arise especially from the lower symmetry of the $[CF_3CO_2]^-$ anion and possibly the applied force field overestimates the specific interactions (e.g. dipole correlations).
For [emim][DCA] as well as for [bmim][CF_3CO_2] the rotational modes are more narrow in the simulation than observed with DRS. This might be a result of the finite box size of the simulation, that cannot reproduce heterogeneities, or to be more specific, the statistics of the simulation might be not sufficient to reproduce a relaxation time distribution, as observed in the experiment (Cole-Cole equation, see section 3.2.1).
To summarize, for [emim][DCA] the simulated spectra are already close to the experimental results. Application of a polarizable force-field would be able to mimic the stabilized charge separation in the condensed phase and thus better agreement, especially for the amplitudes, is expected. For the dipolar $[CF_3CO_2]^-$ anion of low symmetry comparison between simulation and experiment reveals major differences and suggest that the force-field for the anion requires considerable improvement. Enlarging the box-size might be able to better simulate the heterogeneity within the RTILs.

3.3.2 Fitting model

To fit the experimental spectra, various relaxation models based on up to 6 individual contributions were tested.[205] Best fits were obtained by superimposing five processes. However, fits that included more modes, as has been performed successfully on the basis of data obtained from two experimental techniques (OKE and DR spectroscopy, see below) did not converge on the basis of DR data alone. As already discussed (section 3.2.1), modelling the low frequency modes centered at $\sim 0.2 - 10$ GHz (depending on the compound) with a Cole-Cole equation yielded lower values of the reduced error function, χ^2_r, than an asymmetric Cole-Davidson equation. Best fit qualities were achieved be superposing an additional Debye equation at ~ 80 GHz and three damped harmonic oscillators (DHOs) at THz frequencies. However, the classical Cole-Cole and Debye equations contribute sig-

nificantly at high frequencies, which is known to be physically unreasonable.[51,52] Thus the modified Cole-Cole and Debye equations accounting for the inertial rise were used (section 1.3.2) because the extended frequency range covers several high frequency modes and makes it necessary to terminate the low frequency modes at their high frequency onset. The terminated Debye and Cole-Cole equations additionally improve χ^2_r values while the number of adjustable parameters essentially stays constant. The parameter accounting for the inertial rise, $\gamma_{lib} = 2$ THz, was fixed at the average resonance frequency of the DHOs as discussed elsewhere.[52,101] The fit parameters obtained are summarized in table 3.3.2, the corresponding fits are shown in figs. 3.12 and 3.13. An experimental spectrum together with the fitted curve and the contributions of the single modes is displayed in fig. 3.15.

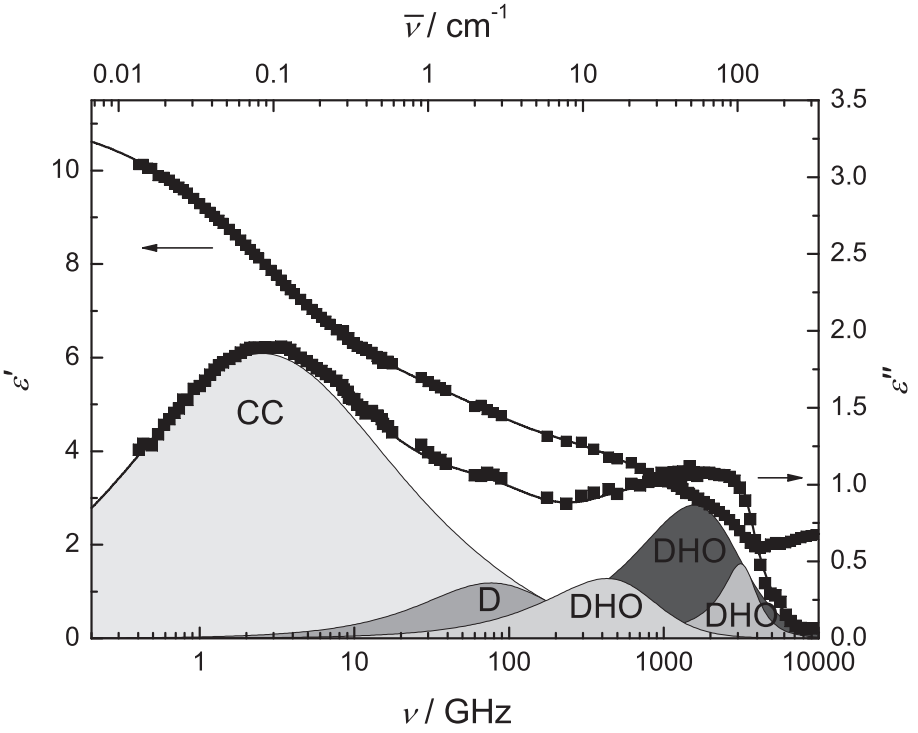

Figure 3.15: Dielectric permittivity, $\varepsilon'(\nu)$, and loss, $\varepsilon''(\nu)$, spectra of [bmim][DCA] at 25 °C. Symbols represent experimental data, lines the fit with a modified Cole-Cole (CC), Debye (D) and three DHOs (see text). Shaded areas indicate the contributions of the individual processes to $\varepsilon''(\nu)$.

In the raw far-infrared spectra for some RTILs $\alpha(\bar{\nu})$ exhibits sharp absorption bands (fig. 3.16) that are attributed to intramolecular vibrations of the anion. These intramolecular modes are pronounced for the $[DCA]^-$ anion (5.5 THz, 180 cm^{-1}) and especially for the $[CF_3CO_2]^-$ anion (8 THz, 270 cm^{-1}). However, since ε'' roughly scales with $\alpha(\bar{\nu})/\bar{\nu}$, they are very weak in $\hat{\varepsilon}(\nu)$ and appear only as rather small shoulders in ε'' at the high frequency onset of the spectra (fig. 3.15). Thus, the amplitude in the complex permittivity spectra of these modes is too small for them to be to reliably resolved.
As can be seen in table 3.3.2, the ε_∞ values obtained are slightly higher than the squared refractive indices, n^2_D for all of the compounds studied. This means that minor contribu-

tions (almost certainly due to intramolecular vibrations) are present at infrared and optical frequencies, that are not covered by the present frequency range.

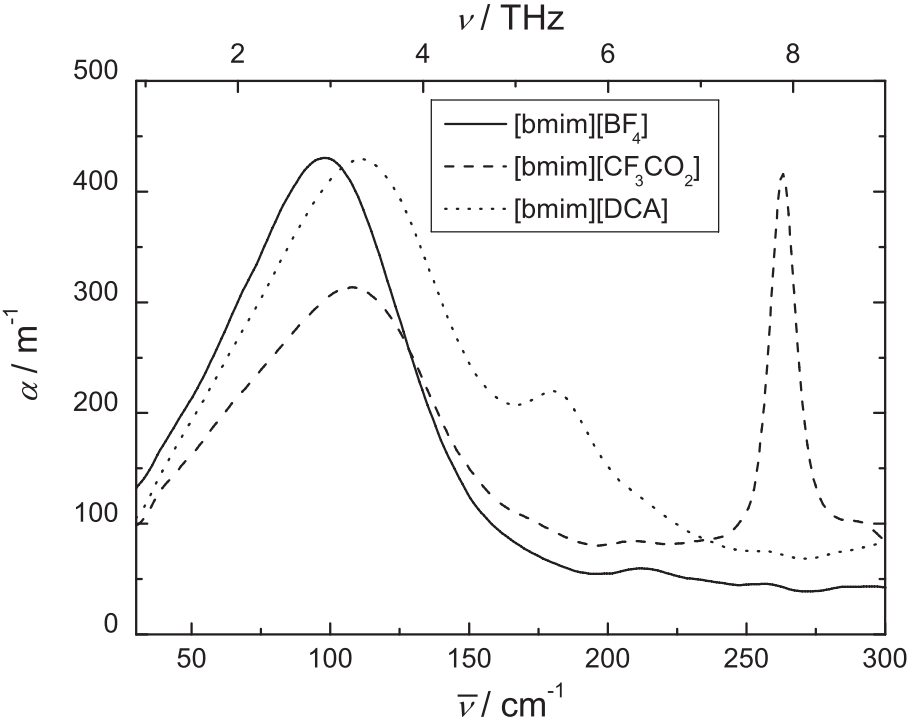

Figure 3.16: Far-infrared absorption spectra, $\alpha(\bar{\nu})$ for [bmim][BF_4], [bmim][CF_3CO_2] and [bmim][DCA] at 25 °C.

3.3.3 Results and Discussion

Low frequency modes

The low frequency mode, modelled with a Cole-Cole equation (fig. 3.15), is readily assigned to the reorientation of the dipolar cations as extensively discussed previously (see section 3.2.1). This assignment is also in concordance with the MD simulations (fig. 3.14). More importantly, the parameters of the low-frequency mode agree within the likely experimental errors with those obtained over the restricted frequency range at $0.2 \lesssim \nu/\mathrm{GHz} \leq 89$ (section 3.2.1). Although significant differences between the present parameters for this mode and those derived from the more limited frequency range (section 3.2.1) are apparent for the more viscous compounds, the uncertainties in the determination of the relaxation parameters are also higher in these cases because of the location of the mode close to the low-frequency limit of the instrumentation (as discussed at length in section 3.2.1).
On the other hand, the origin of the Debye mode at ∼80 GHz, which was already reported previously[11,145,146] (see also section 3.2.1), is not obvious. The simulated spectra (fig. 3.14) suggest indeed that there are considerable contributions of the translational modes (intermolecular vibrations) and translational-rotational cross-correlation at these frequencies.

Table 3.6: Static permittivities, ε, relaxation times, τ_j, amplitudes, S_j, Cole-Cole parameter, α, resonance frequencies $\nu_{0,j}$ and damping constants γ_j obtained by fitting a superposition of a modified Cole-Cole, a modified Debye and three damped harmonic oscillators to the experimental spectra of seven RTILs at 25 °C. χ^2_r represents the reduced error function and n^2_D the squared refractive index at $\lambda = 589.6\,\mathrm{nm}$. The inertial rise constant of the Cole-Cole and Debye mode was fixed to $\gamma_\mathrm{lib} = 2\,\mathrm{THz}$.[a]

RTIL	ε	S_1	τ_1	α	S_2	τ_2	S_3	$\nu_{0,3}$	γ_3	S_4	$\nu_{0,4}$	γ_4	S_5	$\nu_{0,5}$	γ_5	ε_∞	n^2_D	$\chi^2_\mathrm{r} \cdot 10^5$
[emim][BF_4]	14.77	8.94	37.1	0.387	0.733	1.07	1.87	1.18	2.94	0.598	1.95	2.15	0.686	2.92	1.84	2.63	1.994[b]	386
[bmim][BF_4]	13.79	8.58	225	0.482	0.576	1.59	1.54	1.03	2.29	0.558	2.01	2.28	0.408	2.95	1.75	2.54	2.016[c]	196
[hmim][BF_4]	12.20	7.66	481	0.525	0.252	1.39	1.28	0.952	2.07	0.655	1.95	2.15	0.441	2.92	1.62	2.35	2.027[d]	278
[emim][DCA]	11.05	4.70	31.8	0.152	1.06	2.76	1.07	0.562	1.16	1.39	2.43	4.29	0.325	3.34	2.11	2.82	2.292[e]	163
[bmim][DCA]	11.29	6.20	62.7	0.336	0.621	1.93	0.579	0.698	1.31	1.25	2.44	4.36	0.298	3.29	2.07	2.63	2.277[e]	72.5
[bmim][PF_6]	17.81	13.2	1560	0.542	0.487	1.67	1.09	0.879	1.75	0.702	2.18	2.39	0.0905	2.87	1.08	2.38	1.985[c]	664
[bmim][CF_3CO_2]	15.24	10.3	160	0.481	0.254	0.481	0.891	0.962	2.17	0.548	1.93	2.28	0.308	3.26	2.03	2.66	2.079[b]	139

[a]Units: τ_j in ps, γ_j, $\nu_{0,j}$ in THz; [b]Ref. 206; [c]Ref. 207; [d]Ref. 208; [e]Ref. 209.

However, due to the rather broad and featureless spectra of the present RTILs an unambiguous splitting into rotational and translational contributions is not possible at this stage although consistent with the MD simulations (fig. 3.14), intermolecular vibrations appear to be the main contribution.
As can be seen in table 3.3.2, the damping constants of the higher-frequency DHO modes do not vary much. Therefore, assuming that mode 2 arises from intermolecular vibrations (i.e. a resonance phenomenon) the band-shape of mode 2 is expected to be close to a Debye band-shape if the damping constant has about the same value as for the other DHO modes observed, because of the similarity of the Debye equation and the DHO in the case of $\gamma \gg \nu_0$. At such low frequencies (for vibrations) the differences between a Debye and DHO band-shape are too small to distinguish reliably between the two models. On the other hand, an interaction-induced rotation, as observed for many systems,[184,210] would conform with the observed Debye shape.

THz modes

The high frequency (DHO) modes are mainly due to intermolecular vibrations and to some extent to librations, as indicated by MD simulations[170] (see above). The presence of the three DHO modes for all investigated compounds at similar resonance frequencies suggests, that they are characteristic of cation-anion interactions rather than for the specific ions. Although these modes are occasionally interpreted in terms of hydrogen bonding,[200,201] the presence of far-infrared modes doesn't prove the existence of a directional hydrogen-bond but is indicative of strong interactions in these RTILs. This assignment is in broad concordance with *ab initio* calculations that yield several cation-anion bending and torsion modes at these frequencies.[211]
There are some studies that investigate fragments of the present frequency range (far-infrared[200,201], THz[26,143,144]), but their limited ranges prevent the authors from more detailed conclusions.
A complementary technique, Optical-Kerr-Effect (OKE) spectroscopy, that is sensitive to the time correlations of the anisotropic part of the polarizability tensor, can access the same broad frequency range as the present measurements (see below). Due to the asymmetry of the cations (and some anions) and also because modes occurring at these frequencies are mainly interaction induced, the intermolecular modes of this study are expected to be OKE (Raman) active. Comparison with studies literature studies[123,124,127,133] reveals that the DHOs observed in this study are in good agreement with the OKE results.[124,127] The authors of these studies assume out-of-plane librations of the cation with different environments, caused by different positions of the closest counterions as molecular origin for these modes.
From fig. 3.17 it can be seen that there is no simple dependence of S_j or $\nu_{0,j}$ on the cation or anion. On the other hand if the cation is substituted, while the anion remains the same, the parameters vary smoothly with the alkyl chain length, n, of the side chain. This observation is in accordance with the assignments to intermolecular vibrations, since the main cation-anion interaction side is at the C2-H position of the imidazolium ring.[200] Accordingly, the side chain of the imidazolium ring has only a minor effect onto the cation-

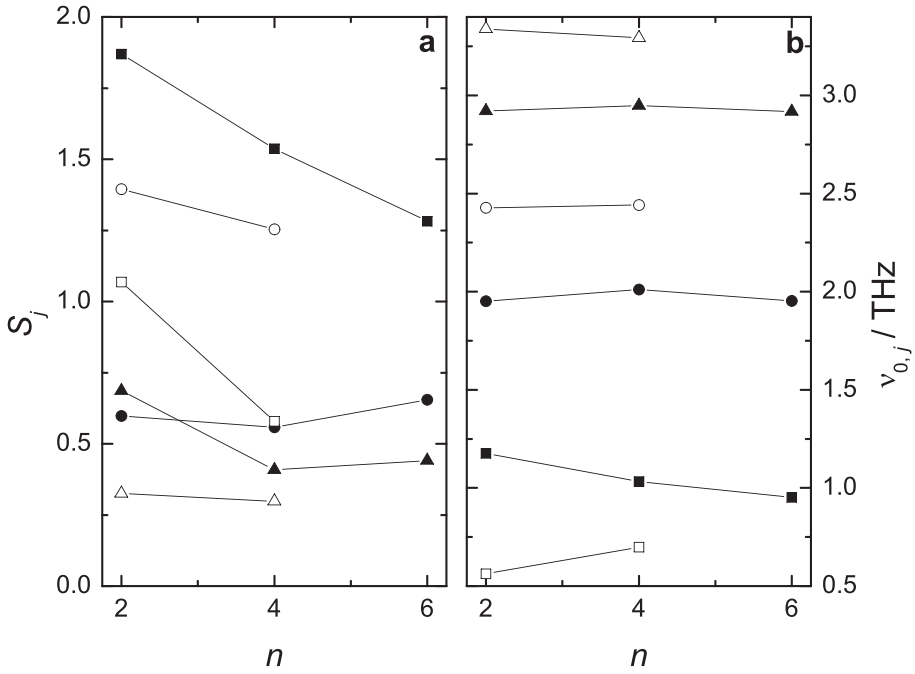

Figure 3.17: (**a**) Amplitudes, S_j and resonance frequencies, $\nu_{0,j}$, of the three DHO modes as a function of the alkyl side chain length of the cation, n (squares: $j = 3$, circles: $j = 4$, triangles: $j = 5$; closed and open symbols represent $[BF_4]^-$ and $[DCA]^-$ containing RTILs, respectively).

anion interaction. Variation of the anion changes the resonance frequencies as well as the amplitudes considerably (fig. 3.17), meaning that the interaction energy is strongly affected by the nature of the anion.
The parameters defining mode 3 (S_3 and $\nu_{0,3}$) are most sensitive to variation of the cation (fig. 3.17). Interestingly, $\nu_{0,3}$ decreases with increasing alkyl side-chain length for $[BF_4]^-$ salts while it increases for RTILs with $[DCA]^-$ as the counterion. This suggests, that the interaction energy is affected differently by the alkyl chain length for the two anions. On the other hand modes 4 and 5 show only little variation with the side-chain length.

3.3.4 Comparison with optical Kerr effect spectroscopy

As already mentioned above, comparison with other experimental techniques can gain valuable insight into the dynamics of liquids.[34,184] In the framework of the broadband dielectric studies the results were compared to optical Kerr effect (OKE) spectra. Where dielectric spectroscopy is sensitive to the time derivative of the correlation function of the macroscopic dipole moment ($\propto \frac{\mathrm{d}}{\mathrm{d}t}\langle\mu(t)\mu(0)\rangle$) OKE spectroscopy measures the time derivative of the correlation function of the anisotropic part of the polarizability tensor, Π, (($\propto \frac{\mathrm{d}}{\mathrm{d}t}\langle\Pi(t)\Pi(0)\rangle$)) Both techniques are sensitive to rotational motions and only weakly sensitive to translational motions.[52,184] In principle, the two experiments are complementary for intramolecular vibrations (OKE: Raman active; DR: IR-active). However, at

low (infrared) frequencies in the condensed phase, the modes arise from multiple particle motions, and will be present in spectra obtained with both techniques. Consequently, comparison of DR and OKE spectra allows better resolution of the broad and overlapping bands.
Detailed discussion of the results from the comparison of OKE and DR spectra for three imidazolium-based RTILs ([emim][DCA], [emim][BF_4] and [bmim][DCA]) can be found in the following publication:

David A. Turton, Johannes Hunger, Alexander Stoppa, Glenn Hefter, Andreas Thoman, Markus Walther, Richard Buchner, and Klaas Wynne *"Dynamics of Imidazolium Ionic Liquids from a Combined Dielectric Relaxation and Optical Kerr Effect Study: Evidence for Mesoscopic Aggregation" J. Am. Chem. Soc.* **2009**, *131*, 11140-11146.

but some salient aspects will be presented here. Comparison of both spectra obtained with the two complementary techniques is exemplarily displayed for [emim][DCA] in fig. 3.18.

Results and Analysis

The great advantage of this concerted approach is the high signal to noise ratio of OKE spectroscopy at high frequencies and for DR at low frequencies (fig. 3.18). Although spectra obtained with both techniques are still rather broad and featureless at frequencies ranging from ca. 100 GHz to 6 THz, the OKE results allow a better resolution of the various modes at these frequencies. Thus, the OKE data show that four DHOs and one Gaussian oscillator are required to model the intermolecular modes. Consistent with computer simulations,[170] these modes are dominated by many-particle interactions and are thus OKE and DR active. At higher frequencies the intramolecular modes, which are OKE active but only weakly DR active, are described by another two underdamped DHOs. These modes are the $[DCA]^-$ bending vibration at $\sim 5.5\,\mathrm{THz}$ ($184\,\mathrm{cm}^{-1}$) and intramolecular modes of the $[emim]^+$ cation at $\sim 4.75\,\mathrm{THz}$ and $\sim 7.2\,\mathrm{THz}$ ($158\,\mathrm{cm}^{-1}$ and $240\,\mathrm{cm}^{-1}$).
Although the fitting model at THz frequencies is still somewhat uncertain due to the broad nature of the spectra, the combined analysis allows preclusion of inappropriate models.
The most surprising feature of these spectra is that the maximum in the OKE imaginary part is at lower frequencies than observed for the dielectric loss. Usually modes occurring at GHz frequencies arise from rotational relaxation. However, for single molecule rotational diffusion the relaxation time is determined by the macroscopic shear viscosity and the effective volume according to the SED equation (eq. 1.78, section 1.4.4). If the principal axis of the polarizability tensor, Π coincides with the dipole vector, μ, of the molecule the $2nd$ rank relaxation time of the OKE signal should be three times faster than the DR (1st rank) relaxation. In the case of the investigated RTILs qualitative comparison of the lower-frequency peak maxima would suggest that the OKE relaxation time is approximately five times *slower* than the DR relaxation time.
With no additional information it is not possible to fit the low frequency OKE mode unambiguously and studies of similar RTILs have employed a Cole-Davidson mode which is well established for the description of the so-called α relaxation in glass-forming and

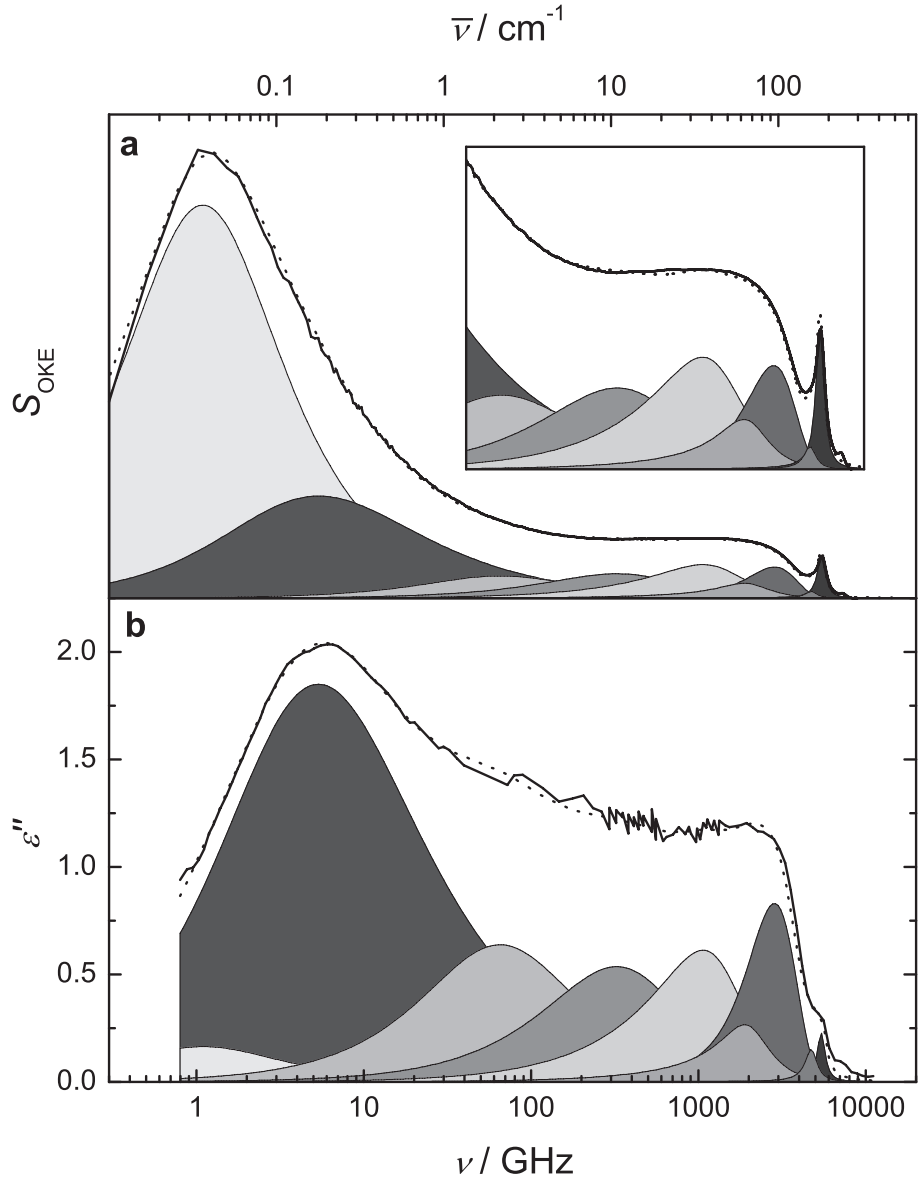

Figure 3.18: Spectra for [emim][DCA] at 25 °C showing the total fit (dashed) and its component parts (shaded areas): (**a**) OKE imaginary part with inset, a vertical expansion and (**b**) dielectric loss, ε''. Solid lines correspond to experimental spectra.

supercooled liquids.[212,213] For several systems this mode resolves into a Debye and a Cole-Cole mode, when the glass transition is approached.[212,213] For the present low frequency modes the combination of a Debye equation with a Cole-Cole mode modelled the low frequency OKE part excellently, and resulted in a meaningful physical interpretation.

The second interesting feature is that the OKE Cole-Cole mode occurs at similar frequencies to those of the DR spectra. In contrast to the previous fits (sections 3.2.1, 3.2.2 and 3.3; Refs. 11,171) the low frequency Debye mode is also fitted to the DR spectra, although it is very weak in its amplitude. From DR spectra alone it is not possible to resolve this

weak mode, but with the concerted approach it is possible to model the spectra with this low-frequency Cole-Cole (α) and the sub-α (Debye) mode, with the latter terminating the α relaxation (this is necessary because the alpha mode cannot become slower than the sub-α relaxation (see section 1.3.2 and Ref. 52)).

Discussion

The most remarkable feature of the combined analysis is the large-amplitude mode appearing in the OKE spectra at low frequencies (lower than the DR Cole-Cole mode). This is surprising because simple theories (see section 1.4.6) predict that OKE relaxation times should be faster than the DR relaxation time. Although the dipole vector and the principal axis of the polarizability tensor are very likely aligned differently in the dipolar cations, this can be eliminated on the basis of low frequency studies[151] that this sub-α mode occurs at lower frequencies, not covered by the investigated frequency range of the DR experiment. The large difference in intensity of the sub-α mode in OKE and DR spectra implies that this process must be due to a motion that corresponds to a considerable change in polarizability, while the macroscopic dipole moment is only weakly affected. Computer simulations[198] and a recent DR study of RTIL mixtures[214] suggest the formation of π-stacked cation clusters in the RTILs, especially for [emim][BF_4]. On the other hand, cation dimers sandwiched by two anions, as found for [emim][$AlCl_4$] by computer simulations[198] and by NMR-spectroscopy for [emim]$^+$ halides[215] appear to be more likely for [emim][DCA].[214] The position of the sub-α mode and its strong OKE activity suggests it is due to a motion of high symmetry such as a simple breathing mode of cation-stacked or micelle-like clusters. MD simulations also show strong contributions of translational modes at quite low frequencies,[170,176,179] which might be a reflection of inhibited rotation by this clustering.
Recent MD simulations[216] and a X-ray scattering study[217] suggest a pronounced aggregation of the alkyl substituents of the imidazolium ring with increasing chain-length. Due to bandwidth limitations RTILs with longer side-chains cannot be studied at present with OKE. However, the present results suggest considerable structuring already in RTILs with small cations, in accordance with the simulations.[198] Such large scale aggregates have already been postulated previously on the basis of dynamic light scattering (DLS) measurements, where time correlations of density fluctuations are recorded.[218] The vast difference in timescales (DLS correlation time: $\sim 1\,\mathrm{s}$) can be explained by assuming that the present results involve infracluster motions.
The coincidence α Cole-Cole mode in the OKE and DR spectra can be explained by recent MD simulations,[179] suggesting that the cations in [emim][PF_6] reorient via large angle jumps. For jump reorientation the OKE/DR relaxation time ratio is less than 3 and for large angle jumps ($> 109\,^\circ$) DR relaxation time can even become faster than the corresponding 2nd rank (OKE) relaxation time. Indeed, the simulations[179] predict that the $2nd$ rank correlation time can be up to two times slower than the $1st$ rank decay. Therefore jump orientation in combination with the asymmetry of the constituting ions of the RTILs can explain the observed similar relaxation times in the OKE and DR experiments. This relaxation mechanism can also explain the observation of the extraordinarily small volumes of rotation obtained with the Stokes-Einstein-Debye theory (see section 1.4.4) as observed

previously[11,30,111,129,171,183] (i.e. rotational diffusion is not the underlying relaxation mechanism).
To summarize, the combination of DR and OKE spectroscopy allows fitting of the spectra more accurately and reliably than previously possible. At THz frequencies has been shown that there is a greater number of librational/intermolecular modes than detected previously, mainly due to the high signal-to-noise ratio of the OKE experiment. However, the degree of overlap of the individual modes still prevents a more detailed analysis.[§] The presence of an intense low-frequency mode in the OKE spectra can be explained by a mesoscale structure. This means that there is a certain degree of heterogeneity in the liquids, resulting in a broadening of the α relaxation. The underlying mechanism of the α relaxation is due to large angle jumps, as suggested by computer simulations.[179]

3.4 Conclusions

More detailed insights into the dynamical as well as the structural and static properties of RTILs can be obtained by combination of optical Kerr effect and dielectric spectra over a very broad frequency range. This concerted analysis allowed the resolution of nine modes at $0.2 \lesssim \nu/\mathrm{GHz} \lesssim 10000$, including intramolecular modes. The most interesting feature is the large-amplitude low-frequency mode in the OKE spectra due to the meso-scale structure. It was not possible to resolve this mode just on the basis of DR data due to its low DR amplitude.
Based on only DR data, five modes were sufficient to model the experimental spectra. Nevertheless, the parameters obtained agree well with the parameters obtained from the concerted analysis. Thus, it is possible to infer the dynamical and structural properties — connected with these processes — on the basis of just DR data. However, especially at THz frequencies, the low signal-to-noise ratio prevents a more detailed analysis.
Covering only frequencies up to 89 GHz allows a reliable characterization of the microwave modes. The parameters determining these low frequency modes agree well with the broadband studies and allow an analysis of the rotational modes, even though the high frequency modes are not properly resolved. The effect of temperature on these modes enabled the derivation of activation parameters and gave additional insight into the relaxation mechanisms. Due to current limitations of the THz apparatus the temperature dependence can only be studied at frequencies of $\nu \leq 89\,\mathrm{GHz}$. Ongoing improvements of the THz setup will allow more insight into the structural and dynamical properties as function of temperature to be gained in them.

[§]One may doubt the presence of well-defined individual modes. A continuum of intermolecular vibrations and librations can also be a plausible origin of the observed THz spectra.

Chapter 4

Binary mixtures

4.1 Introduction

While most of the earlier papers about RTILs were naturally focused on synthesis and the use of RTILs as reaction media,[219,220] there has been growing interest in their physical, dynamical and structural properties.[31,221] Because the information that can be gained from a physicochemical study of a single RTIL is necessarily limited, most current studies either report data on sensibly-related series of salts[222–224] or on the effects of other variables, such as temperature.[225,226] Another way of gaining insights into the nature of RTILs is to study their mixtures with co-solvents whose properties are well known. Such investigations are particularly pertinent to potential technical applications of RTILs, as reaction media for industrial-scale syntheses or in batteries, where they would not normally be present in neat form.

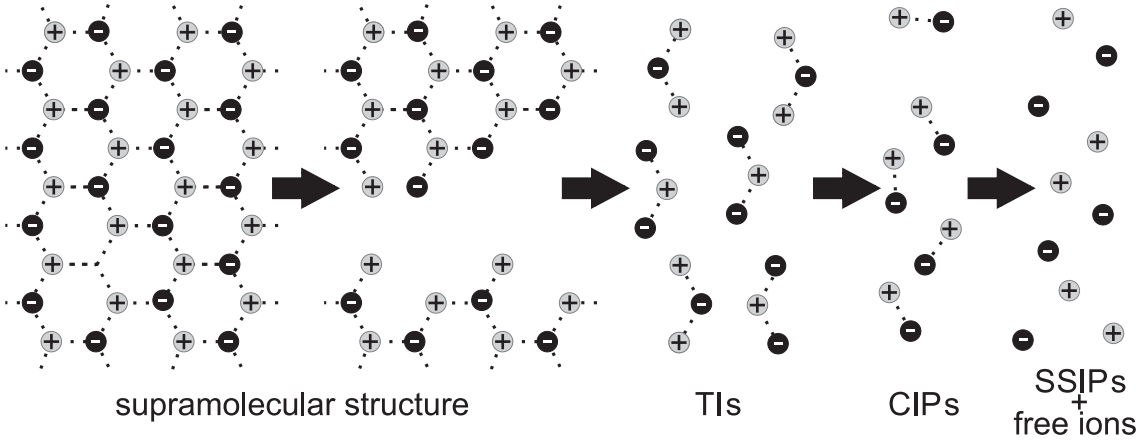

Figure 4.1: The scheme of Dupont[227] for the dilution of an ionic liquid by a co-solvent; the arrows represent increasing co-solvent content.

Of the vast range of RTILs currently available, those containing substituted imidazolium cations have been the most intensively studied,[31] but relatively few of these investigations have focused on their mixtures with co-solvents. According to Dupont,[227] neat

imidazolium-based RTILs form an extended hydrogen-bond network that strongly resembles the corresponding solid structures.[228] Upon addition of a polar co-solvent, Dupont has proposed that this network breaks up, initially forming "supramolecular" aggregates of the constituent ions of the RTIL (fig. 4.1). With increasing dilution such aggregates are succeeded in turn by triple ions (TIs), contact ion pairs (CIPs) and, ultimately, solvent-separated ion pairs (SSIPs) and free ions.[227] This scheme has intuitive appeal since, except perhaps for the first step, it is essentially the mirror image of what is known to occur in conventional electrolyte solutions with increasing concentration.[229,230] However, while some of the features of Dupont's scheme have been verified for some RTIL/co-solvent mixtures[29,231,232] others remain speculative.

The range of techniques available to study the structure and dynamics of RTILs and their mixtures is limited. Thermodynamic (solubility, excess volume, etc.) and transport (conductivity, viscosity, etc.) measurements are useful but provide only indirect insights into the nature of solutions at the molecular level. The powerful spectroscopic techniques (NMR, Raman, etc.) on the other hand, generally provide information only about short range (bonding) interactions, and have a specific weakness with respect to the detection of SSIPs.[233]

Dielectric relaxation spectroscopy (DRS) is particularly suited for the investigation of the long and medium range ordering[234] that is implied, at least in RTIL-rich solutions, by Dupont's scheme.[227] DRS also has unique abilities to detect and quantify the formation of all ion pair types in solution.[229,230] A modest number of papers have reported the dielectric properties of neat RTILs,[28–30,145–147] including some containing imidazolium cations.[28,30,146] However, studies investigating RTIL/co-solvent mixtures are scarce and have been limited with respect to the range of frequencies and/or compositions investigated.[29]

4.2 Binary mixtures RTIL + dichloromethane

4.2.1 [bmim][BF_4] + DCM

The material presented in this chapter forms the basis of the paper:

Johannes Hunger, Alexander Stoppa, Richard Buchner, and Glenn Hefter *"From Ionic Liquid to Electrolyte Solution: Dynamics of 1-N-Butyl-3-N-methylimidazolium Tetrafluoroborate + Dichloromethane Mixtures" J. Phys. Chem. B* **2008**, *112*, 12913-12919.

One of the most frequently studied RTILs is 1-*N*-butyl-3-*N*-methylimidazolium tetrafluoroborate ([bmim][BF_4]) because it is stable (in the absence of water) and can readily be prepared in high purity.[76] In this section dielectric spectra of mixtures of [bmim][BF_4] with dichloromethane (DCM) over a broad range of frequencies ($0.2 \leq \nu/\mathrm{GHz} \leq 89$) and at closely spaced intervals over the whole composition range are reported. The imidazolium salt was chosen as a representative RTIL because some of its other properties (both neat and in mixtures with DCM) relevant to the present investigation have been reported.[11,76,235] DCM was selected as the co-solvent because it is fully miscible with [bmim][BF_4] at 25 °C[235] yet sufficiently polar to support the formation of ion pairs and (to some extent) free ions.[29] In addition, the dynamics of DCM are fast on the DRS timescale and it has a low static permittivity, which means its contribution over the frequency range of interest should be relatively small.

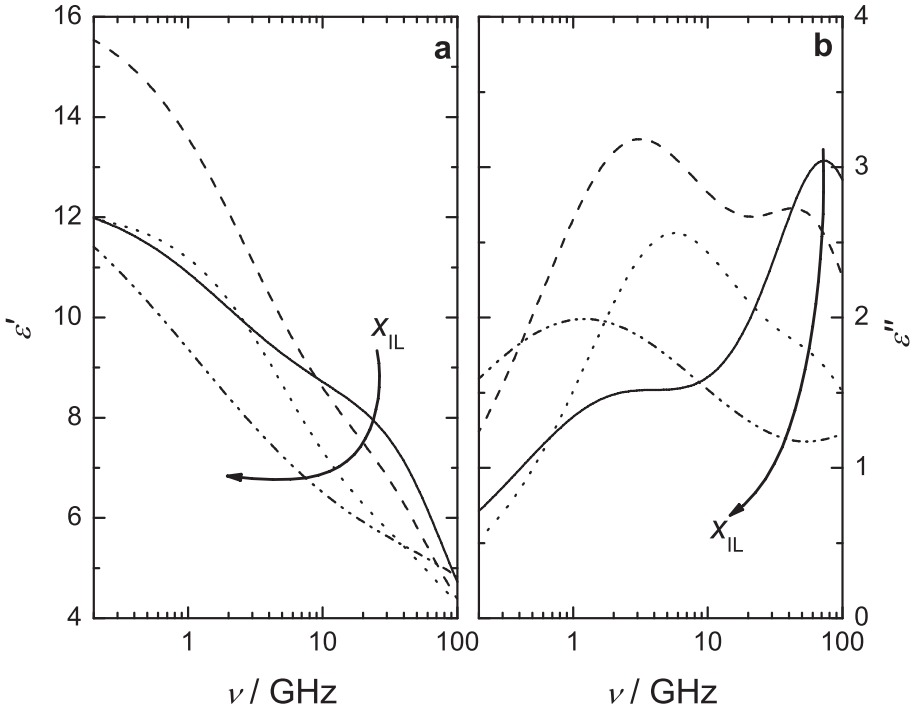

Figure 4.2: Dielectric permittivity (**a**), ε', and dielectric loss (**b**), ε'', spectra of representative [bmim][BF_4] + DCM mixtures ($x_{\mathrm{IL}} = 0.00755$, 0.0799, 0.355 and 0.850) at 25 °C.

For all solutions, $\hat{\varepsilon}(\nu)$ was determined in the frequency range $0.2 \lesssim \nu/\mathrm{GHz} \leq 89$ (HP8720D VNA setup + A & E-band interferometer, section 2.3). Raw VNA data were obtained using air, mercury and purified benzonitrile as primary calibration standards. Calibration errors were corrected with a Padé approximation using pure dimethylacetamide and 1-butanol as secondary standards (see section 2.3.3). All dielectric measurements were performed at $(25.00 \pm 0.05)\,^{\circ}\mathrm{C}$. Typical experimental spectra with a precision of 1-2 % are displayed in Figure 4.2.
Mixture densities, ρ, and electrical conductivities, κ, required for data analysis were additionally determined (see section 2.4) and are summarized in table 4.1.

Table 4.1: Weight fraction, w_{IL}, mole fraction, x_{IL}, and molar concentration, c_{IL}, of [bmim][BF_4] in binary mixtures with DCM and their measured densities, ρ, electrical conductivities, κ, and molar conductivities, Λ, at 25 °C.[a]

w_{IL}	x_{IL}	c_{IL}	ρ	κ	$\Lambda/10^{-4}$
0	0	0	1316.98[b]	-	-
0.01984	0.007550	0.1156	1316.60	0.0602	5.21
0.04955	0.01921	0.2882	1314.92	0.200	6.92
0.06912	0.02714	0.4016	1313.40	0.310	7.72
0.09695	0.03878	0.5626	1311.80	0.436	7.76
0.1877	0.07987	1.083	1304.97	0.980	9.05
0.3014	0.1395	1.726	1294.06	1.427	8.27
0.3905	0.1940	2.219	1284.29	1.550	6.99
0.4928	0.2674	2.773	1271.96	1.607	5.80
0.5733	0.3355	3.199	1261.43	1.530	4.78
0.7096	0.4787	3.902	1242.95	1.209	3.10
0.8010	0.6019	4.360	1230.33	0.930	2.13
0.9006	0.7730	4.846	1216.18	0.620	1.278
0.9376	0.8496	5.024	1211.19	0.511	1.018
0.9645	0.9107	5.152	1207.46	0.441	0.856
1	1	5.319	1202.19	0.353	0.664

[a] Units: ρ in $\mathrm{kg\,m^{-3}}$; c_{IL} in $\mathrm{mol\,L^{-1}}$; κ in $\mathrm{S\,m^{-1}}$; $\Lambda(=\kappa/c_{\mathrm{IL}})$ in $\mathrm{S\,m^2\,mol^{-1}}$. [b] Ref. 114.

Relaxation model

The fitting of dielectric spectra is not trivial and must be done with care due to the broadness of DR modes. A full description of the fitting procedure is given in section 2.3.6 so only some salient aspects are presented here. In addition to the overall quality of the fits (eq. 2.35), it is essential that models are physically meaningful and that the derived parameters are realistic and vary smoothly as functions of concentration. All plausible (HN, CD, CC and D) models for the various processes were investigated.

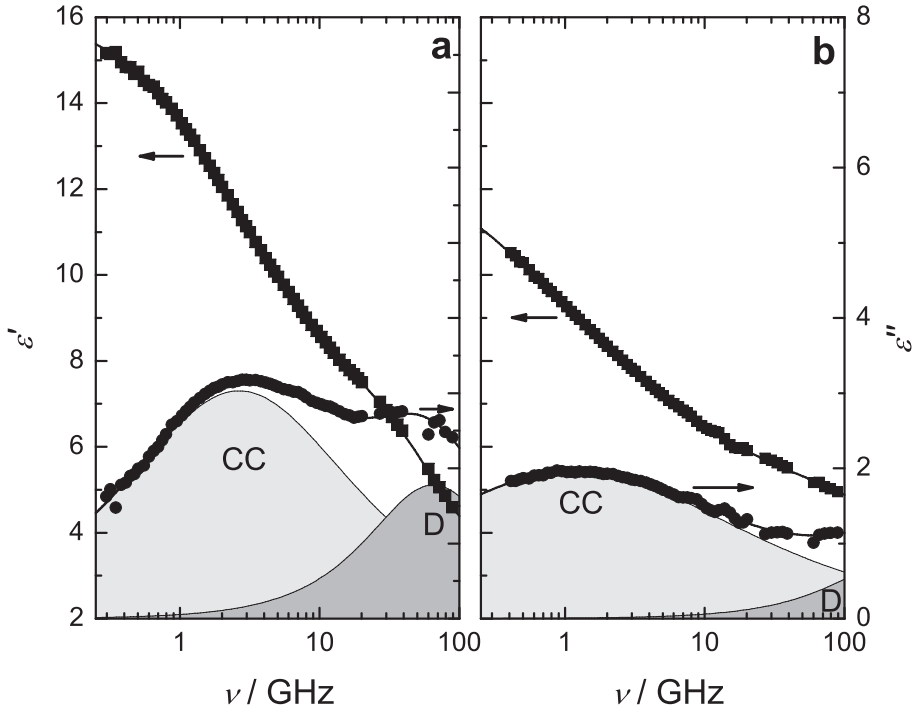

Figure 4.3: Dielectric permittivity, ε', and loss, ε'', spectra of representative IL + DCM mixtures at (**a**) $x_{\mathrm{IL}} = 0.07987$ and (**b**) $x_{\mathrm{IL}} = 0.9107$ at 25 °C. Symbols represent experimental data, lines show the CC+D fit, and shaded areas indicate the contributions of the individual processes.

The simplest model that could adequately describe the experimental spectra (fig. 4.2) involved superposition of just two processes. These were a lower frequency Cole-Cole relaxation centred between 0.6 and 5 GHz and a faster Debye process centred between 70 and 260 GHz (the CC+D model), with the exact location of both processes depending on solution composition (fig. 4.2). The contributions made by these two processes to representative spectra at high and low x_{IL} are presented in fig. 4.3. As will be shown below, however, this apparent simplicity is misleading. The underlying complexity of the DR behavior of these mixtures is illustrated (fig. 4.4) by the presence of two extrema in the static permittivity and the variation of the CC α-parameter as a function of the solution composition. The parameters derived from their detailed analysis (see below) are summarized in table 4.2.

Lower frequency Cole-Cole process

The generally dominant mode in the DR spectra of DCM + [bmim][BF_4] mixtures (figs. 4.2 and 4.3), centred between 0.6 and 5 GHz, is satisfactorily modelled over the whole composition range by a CC distribution of relaxation times. Further consideration of this mode will for convenience be subdivided in terms of mixture composition.

Table 4.2: Fit parameters of eq. 1.61 for the observed DR spectra of mixtures of [bmim][BF_4] with DCM at 25 °C assuming the CC+D model (see text): static permittivities, ε; relaxation times, τ_j, and amplitudes, S_j, of process j; Cole-Cole shape parameter, α of the first (lower frequency) process; infinite frequency permittivity, ε_∞, and reduced error function of the overall fit, χ^2_r.[a]

x_{IL}	ε	τ_1	α	S_1	τ_2	S_2	ε_∞	$\chi^2_r/10^{-5}$
0[b]	8.81	-	-	-	2.23	4.92	3.89	150
0.00755	12.55	84.1	0.33	4.60	2.03	5.47	2.47	163
0.0192	15.43	109	0.34	7.88	2.13	4.97	2.58	144
0.0271	16.64	109	0.35	9.32	2.23	4.81	2.51	212
0.0388	16.85	93.3	0.32	9.65	2.23	4.54	2.65	133
0.0799	16.38	60.0	0.30	9.88	2.44	3.56	2.94	185
0.140	14.74	40.6	0.26	8.83	2.51	2.82	3.09	81
0.194	13.67	34.4	0.25	8.14	2.31	2.42	3.12	81
0.267	12.57	32.3	0.22	7.12	2.42	2.14	3.31	74
0.335	12.21	31.8	0.23	7.08	2.01	1.83	3.30	65
0.479	11.97	39.2	0.28	7.06	1.72	1.50	3.40	59
0.602	12.33	52.2	0.37	7.71	1.12	1.54	3.08	52
0.773	13.44	97.1	0.47	9.06	0.79	1.48	2.89	48
0.850	13.93	135	0.50	9.58	0.69	1.63	2.73	66
0.911	13.81	136	0.50	9.43	0.61	1.57	2.81	76
1[c]	13.79	225	0.48	8.58	1.59	0.576	4.63	196

[a] Units: τ_j in ps; [b] Parameters taken from Ref. 101; [c] Parameters taken from section 3.3.*

IL-rich solutions As for the neat IL (see section 3.2.1), the CC process in the low GHz region in IL-rich mixtures is reasonably ascribed to the reorientation of the dipolar $[bmim]^+$ cations. Ion pairs with $[BF_4]^-$, with or without intervening solvent molecules, may also contribute (see below), albeit not for the pure IL.[151] At $x_{IL} \gtrsim 0.5$ the value of the effective dipole moment of the relaxing species, calculated via eq. 1.69 using the analytical concentration of IL, is essentially constant: $\mu_{eff,1} = 4.6\,D$ ($1\,D = 3.33564 \cdot 10^{-30}\,C\,m$), and is the same as that observed for the neat IL (fig. 4.5). This result is also in broad agreement with the values of $\mu = (5.3 - 7.8)\,D$ (depending on the conformation) obtained for $[bmim]^+$ from semiempirical MOPAC[118] calculations (see section 2.5). Also at $x_{IL} \gtrsim 0.5$ the microscopic relaxation time, τ_1', correlates strongly with the mixture viscosity (fig. 4.6), consistent with eq. 1.78, and the static permittivity shows a simple dependence on composition (fig. 4.4a).

These observations collectively argue for an essentially random (homogeneous) dilution of the "particles" of the neat IL by DCM molecules at $x_{IL} \gtrsim 0.5$. It seems that the chemical "character" of IL + DCM mixtures, at least as detected by DRS, remains "IL-like" even

*Note that these studies are based on a broader frequency range and use a modified Debye or Cole-Cole equation terminated at high frequencies

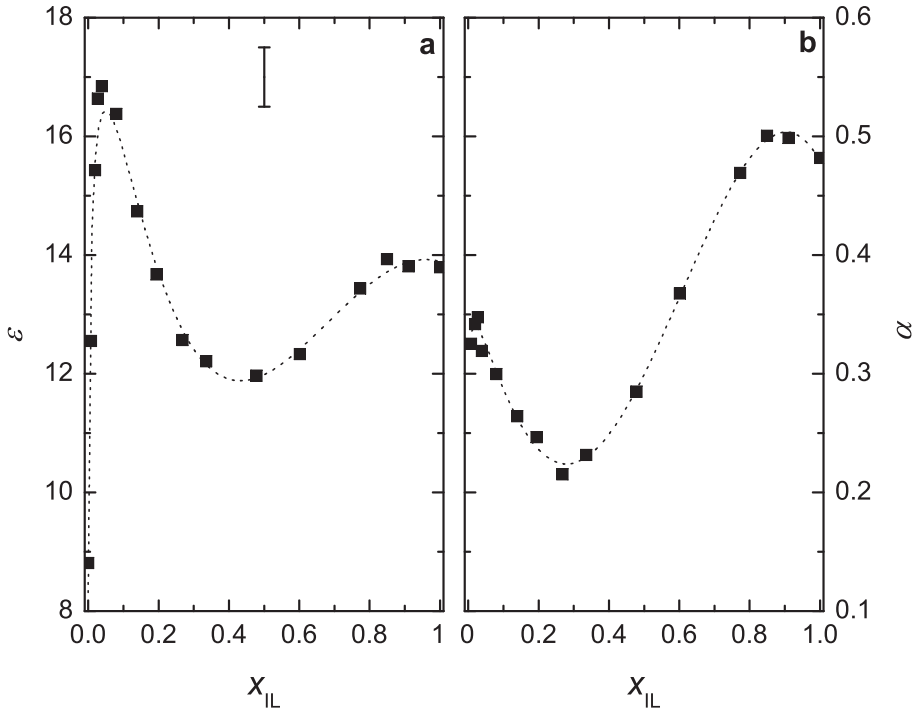

Figure 4.4: (**a**) Extrapolated static permittivity, ε, and (**b**) Cole-Cole parameter, α, of the first process for IL + DCM mixtures at 25 °C. Dotted lines are included only as a visual aid. Error bar is an estimated typical value.

at dilutions down to $x_{\mathrm{IL}} \simeq 0.5$. A similar result was inferred, from much more limited data, for mixtures of the RTIL *N*-methyl-*N*-ethylpyrrolidinium dicyanamide with DCM at even higher dilutions.[29] This finding has potentially significant technical implications. For example, it opens up the possibility of modifying an undesirable physical property (such as a high viscosity or low electrical conductivity) while retaining the desirable chemical characteristics of the RTIL. Similarly, for a RTILs used as a reaction medium it is useful to know at what level of dilution its dynamics cease to be RTIL-like.

The large value of the CC α-parameter at high x_{IL} (table 4.2, fig. 4.4b) indicates a diversity of molecular-level environments for the relaxing species, $[\mathrm{bmim}]^+$, and the probable co-existence of different conformations for these cations. This is consistent with the recent *ab initio* QM calculations of Zahn *et. al.* for [mmim][Cl] which show that the interaction energy is characterized by a broad and shallow minimum.[236] Addition of DCM to the IL significantly decreases the value of α (fig. 4.4b), consistent with a decrease in the spread of environments (as a consequence of the reduced viscosity and thus accelerated overall dynamics) and/or the development of a preferred conformation for the cation. The constancy of $\mu_{\mathrm{eff},1}$ at high x_{IL} (fig. 4.5) indicates the latter is unlikely so it appears that the major effect of the DCM molecules is simply to dilute the IL particles. This reduces the strong Coulombic interactions between the ions (or larger-scale collections of them)[227] and lowers the energy barriers between the different environments, thereby lowering the value of α. It may be noted in passing that the value of $V_{\mathrm{eff}} \simeq 2.5\,\mathrm{Å}^3$ at high x_{IL} calculated from

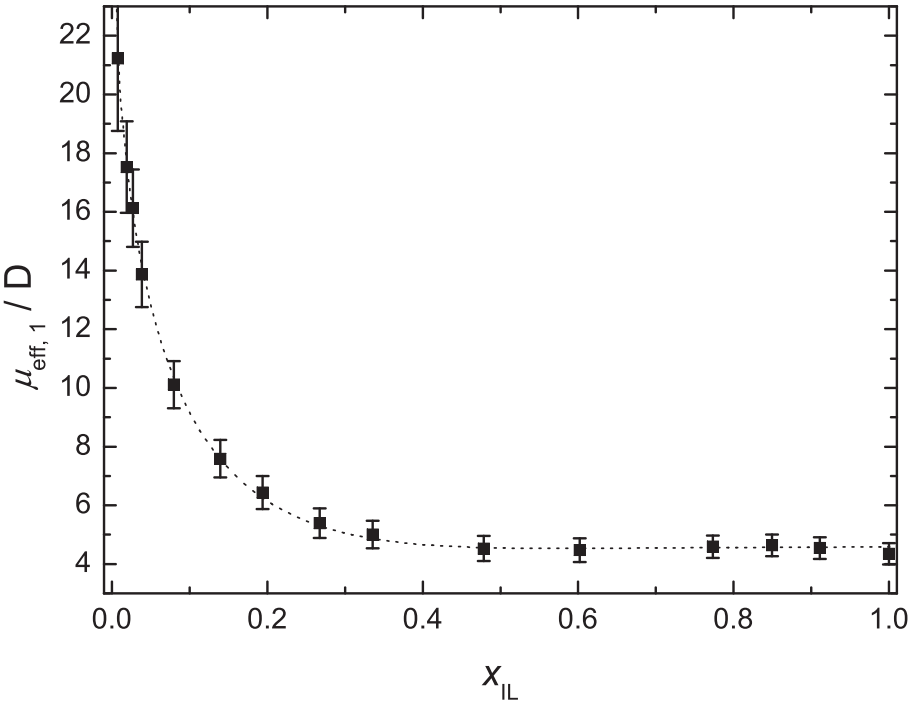

Figure 4.5: Effective dipole moment of species causing process 1, $\mu_{\mathrm{eff},1}$, in IL + DCM mixtures at 25 °C. Dotted line is included only as a visual aid; error bars correspond to an estimated error of $\delta S_1 = 0.5$.

eq. 1.78 is about two to three orders of magnitude smaller than the maximum volume of rotation of $V_{\max} \sim 1060\,\text{Å}^3$ or the van-der-Waals volume of $V_{\mathrm{vdW}} \sim 150\,\text{Å}^3$ for $[\mathrm{bmim}]^+$ (see section 2.5). This indicates that rotation of the cation (and other species if present) does not conform to a simple SED model, as has been found for some other RTILs.[129]

DCM-rich solutions At $x_{\mathrm{IL}} \lesssim 0.3$ there is an increase in the amplitude of process 1 (S_1 in table 4.2), which reaches a maximum at $x_{\mathrm{IL}} \simeq 0.08$ before dropping to zero as $x_{\mathrm{IL}} \to 0$. There is also a rapid increase in $\mu_{\mathrm{eff},1}$ (fig. 4.5, calculated assuming a single CC mode). These two effects strongly suggest the presence of a new relaxing species with a reasonably large dipole moment, almost certainly ion pairs. This is consistent with recent conductivity measurements in dilute solutions.[237] The existence of such species is also in agreement with the sharp increase in the static permittivity at $x_{\mathrm{IL}} \lesssim 0.08$ (fig. 4.4a). Inclusion of an additional Debye process for these mixtures produced better fits (χ^2_{r} decreased by $\sim 10\,\%$, keeping in mind that χ^2_{r} is adjusted for any extra parameters) but its overlap with the dominant cation reorientation (CC) mode was too strong to allow reliable separation. Because of this the exact nature of the ion pairs formed in the DCM rich mixtures can only be inferred, although SSIPs can probably be ruled out on the basis of the relatively weakly coordinating nature of DCM and the known strength of association.[237] Given that the value of $\mu_{\mathrm{eff},1}$ extrapolated to $x_{\mathrm{IL}} = 0$ (fig. 4.5) agrees well with the values of $\mu = 17 - 25\,\mathrm{D}$ (see

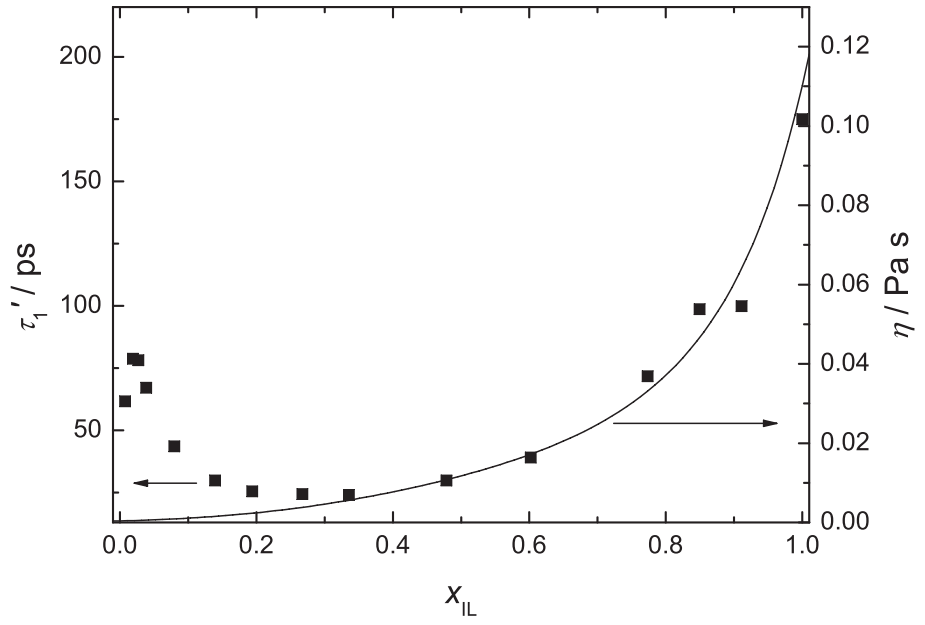

Figure 4.6: Microscopic relaxation time of process 1, τ_1' (■, left-hand axis), and dynamic viscosity, η (line, right-hand axis),[235] for DCM + IL mixtures at 25 °C.

section 2.5) obtained by semiempirical MOPAC[118] calculations for the contact ion pair,[†] this species seems most likely. Additional support for the formation of CIPs comes from the values of $V_{\text{eff}} \approx 260\,\text{Å}^3$ calculated via eq. 1.78 at these compositions, which approach the volume of rotation expected for the CIP rather than the much larger values expected for S-SIPs ($V_{\text{vdW}} \approx 250\,\text{Å}^3$, see section 2.5).

By assuming for simplicity that only free $[\text{bmim}]^+$ and CIPs contribute to the CC mode, that is $S_1 = S([\text{bmim}]^+) + S(\text{CIP})$, their concentrations can be estimated with the help of eq. 1.69. Taking the limits of $\mu_{\text{eff},1}$ (fig. 4.5) as 4.6 D at $x_{\text{IL}} = 1$ and 22 D at $x_{\text{IL}} \to 0$ as the effective dipole moments of $[\text{bmim}]^+$ and the CIP, respectively, the data shown in fig. 4.7 are obtained. Clearly, CIPs are present at significant concentrations only at $x_{\text{IL}} < 0.3$ and only at $x_{\text{IL}} \lesssim 0.03$ are they the dominant species (note that at ***very*** low IL concentrations free ions should again prevail).[237]

The rapid increase of the fraction of free cations at the expense of CIPs (fig. 4.7a), probably reflecting the redissociation of the ion pairs and/or the formation of higher (charged) aggregates triggered by the increasing ion-CIP interactions, explains the marked maximum at $x_{\text{IL}} \approx 0.03$ for the relaxation time of this process (fig. 4.6) and the less well-defined peak in the CC α-parameter (fig. 4.4b). This is because τ_1' is a weighted average of the (viscosity-dependent) relaxation times of both $[\text{bmim}]^+$ and the CIP, with possible contributions from the kinetics of ion-pair formation and decay and of other species.[238] It is noteworthy that semiempirical calculations (see section 2.5) indicate that the effective volumes required for the reorientation of the free cations ($d_{\text{max}} \approx 10.0\,\text{Å}$, see section 2.5) and their CIPs

[†]Solvent-shared ion pairs (with one intervening solvent molecule between the ions) have an approximate dipole moment of > 30 D and are unlikely on the basis of the relatively weakly coordinating nature of DCM. Double-solvent-separated ion pairs are even less plausible.

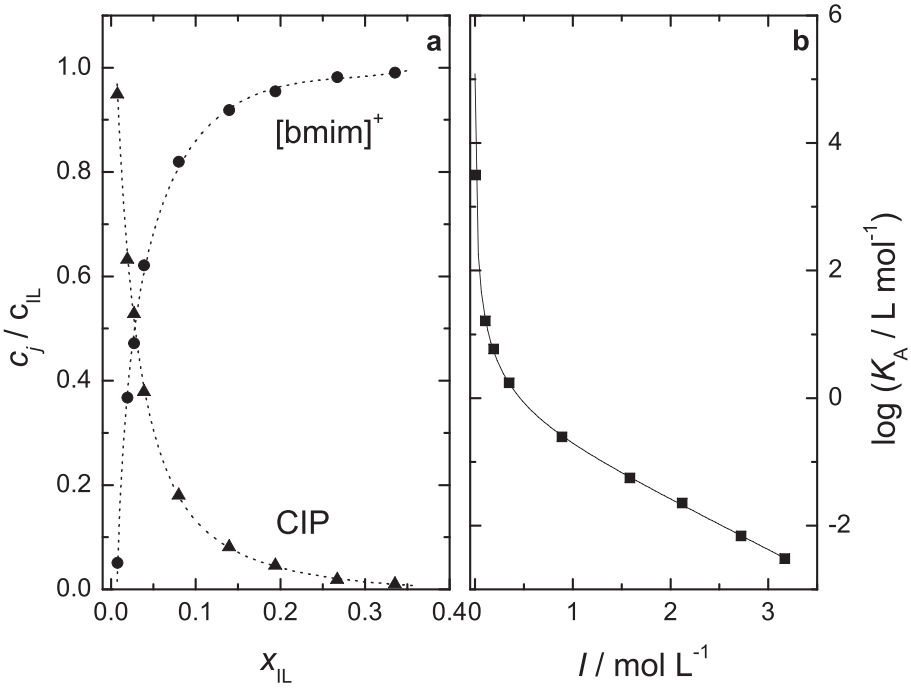

Figure 4.7: (**a**) Concentration fractions, c_i/c_{IL}, of free $[\mathrm{bmim}]^+$ cations and contact ion pairs (CIPs) for IL + DCM mixtures at 25 °C. Dotted lines are included only as a visual aid. (**b**) Overall association constant, $\log K_{\mathrm{A}}$ of $[\mathrm{bmim}][\mathrm{BF_4}]$ in DCM at 25 °C as function of ionic strength, I. Lines represent fits according to eq. 4.1.

($d_{\max} \approx 11.5$) are very similar because the anion sits on the plane of the imidazolium ring. This is consistent with these two species having similar relaxation times, which makes them difficult to distinguish by DRS.

To estimate the standard (infinite dilution) association constant of the CIPs , K_{A}°, the association constant measured at finite ionic strengths, $K_{\mathrm{A}} = c_{\mathrm{IP}}/(c_{\mathrm{IL}} - c_{\mathrm{IP}})^2$, can be extrapolated using a Guggenheim-type equation:[24]

$$\log K_{\mathrm{A}} = \log K_{\mathrm{A}}^{\circ} - \frac{2A_{\mathrm{DH}}\sqrt{I}}{1 + A_{\mathrm{K}}\sqrt{I}} + B_{\mathrm{K}}I + C_{\mathrm{K}}I^{3/2} \tag{4.1}$$

where $I(= c_{\mathrm{IL}} - c_{\mathrm{IP}})$ is the ionic strength, $A_{\mathrm{DH}} = 13.555\,\mathrm{L}^{1/2}\mathrm{mol}^{-1/2}$ the Debye-Hückel constant for activity coefficients and Y_{K} ($Y = A$, B, or C) are adjustable parameters. This fit (fig. 4.7b) shows good statistics ($R^2 > 0.999$) although the extrapolated value of $\log K_{\mathrm{A}}^{\circ} = 5.08 \pm 0.03$ is somewhat lower than that obtained from conductance methods ($\log K_{\mathrm{A}}^{\circ} = 5.58 \pm 0.01$).[237] Nevertheless, it indicates strong ion association in this system.

Higher-Frequency Mode

The faster mode in the present spectra, process 2, centred at ca. 70 to 260 GHz depending on x_{IL} (figs. 4.2 and 4.3), is satisfactorily described by a single Debye equation over the whole composition range. However, as became apparent in section 3.3, the observed inten-

sity in this frequency region arises from at least two strongly overlapping modes associated with IL and, a mode due to rotational diffusion of DCM.[101] Again the following discussion is divided into two parts based on solution composition.

DCM-rich solutions At low x_{IL} process 2 is readily assigned to the rotational diffusion of CH_2Cl_2 molecules with a relaxation time $\tau_2 \approx 2.3\,\mathrm{ps}$ (table 4.2, fig. 4.2) comparable to that of the the neat solvent ($\tau = 2.23\,\mathrm{ps}$;[101] table 4.2). At $x_{\mathrm{IL}} \lesssim 0.15$, τ_2 correlates with mixture viscosities (compare figs. 4.6 and 4.8). However, for reasons that will become apparent, τ_2 decreases as x_{IL} increases from 0.15 to 0.9, before rising again to the neat IL value of 1.59 ps (fig. 4.8).
In spite of the contribution of IL modes, it is still possible to compare (fig. 4.8) the experimental values of S_2 with S_{DCM}, the amplitude estimated from eq. 1.69 assuming all DCM molecules contribute to the spectrum and that their dipole moment, $\mu_{\mathrm{eff,DCM}}$, has the same value as in neat DCM.[101] fig. 4.8 shows that S_3 and S_{DCM} agree well at low x_{IL}. The slight discrepancies are probably due to the the fact that S_{DCM} is estimated on the basis of a study[101] covering a broader frequency range. Additionally, mode 2 is located near the high-frequency limit of the present instrumentation (fig. 4.2). Thus, it is not fully defined and may contain contributions from even higher frequency modes, which are known to exist for neat ionic liquids in the THz and far IR region (see section 3.3, Ref. 146). To disentangle these higher frequency contributions the experimental frequency range would have to be extended to THz-frequencies.

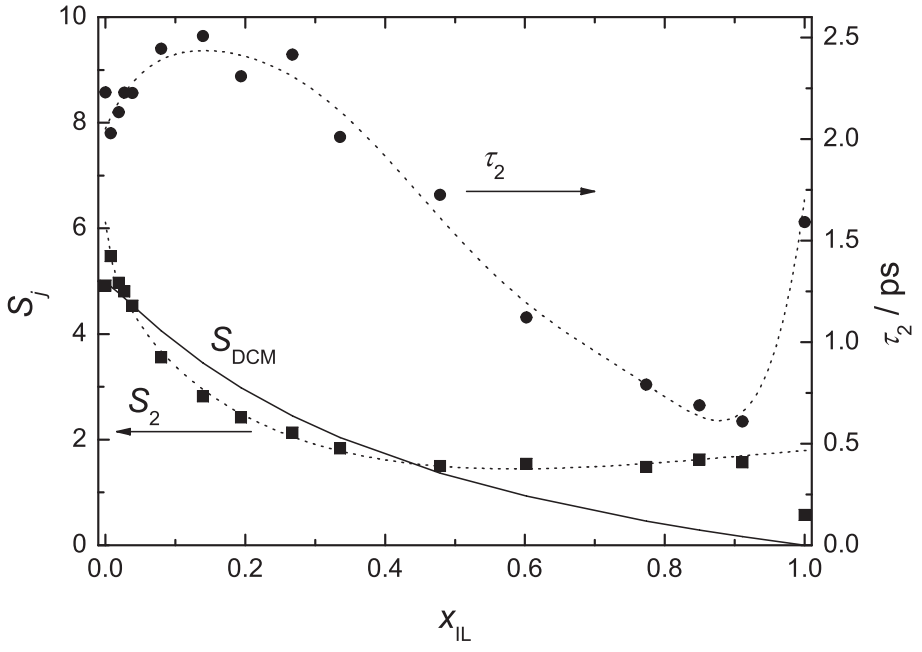

Figure 4.8: Observed amplitude of process 2, S_2 (■, left-hand axis), DCM amplitude estimated from the Cavell equation, S_{DCM} (eq. 1.69, full line, left-hand axis), and relaxation time of the Debye process, τ_2 (●, right hand axis), in IL + DCM mixtures at 25 °C. Dotted lines are included only as a visual aid.

IL-rich solutions At $x_{\mathrm{IL}} \gtrsim 0.5$ the observed values of S_2 are greater than S_{DCM} (fig. 4.8). Since this is physically impossible this must mean that there is another (IL-related) process contributing to the observed spectra at these frequencies. This is consistent with the presence of one or more processes in neat IL (see section 3.3) centred at ∼100 GHz (τ = 1.59 ps) and ∼1 THz (corresponding to $\tau = 0.2$ ps if it was a relaxation). The origins of these modes in the neat IL were discussed in section 3.3. The substantial decrease in τ_2 with increasing x_{IL} (fig. 4.8) suggests that it is the faster intermolecular vibration rather than the 100 GHz relaxation that largely determines the effective relaxation time obtained in the mixtures. This is consistent with the spectrum for the pure IL which, if the fit is limited to $0.2 \leq \nu/\mathrm{GHz} \leq 89$, yields $\tau_2 = 0.6$ ps in accordance with the mixture results (fig. 4.8).

Concluding Remarks

The present DR spectra of [bmim][BF_4] + DCM can be satisfactorily fitted over the entire composition range by assuming just two relaxation modes: a Cole-Cole process at lower frequencies and a faster Debye process. However, detailed consideration of these spectra indicates that both of these processes include additional modes, which could not be resolved because of spectral overlaps.

The observed spectra are broadly consistent with the model suggested by Dupont[227] for mixtures of ILs with co-solvents but differ in detail (fig. 4.1). For example, no direct information is provided by the present measurements as to the "supramolecular" structure of the neat IL or its postulated break up upon dilution with a co-solvent. This may be because such large structures would have relatively low dipole moments and/or slow dynamics and therefore do not contribute significantly to the DR spectra. There is also no dielectric evidence for the successive formation, with increasing IL dilution, of TIs, CIPs, SSIPs and free ions, even though such species are usually readily detected by DRS.[229] The conductivity data (table 4.1) indicate a high level of ion association at low x_{IL} which the DRS data suggest is due to the formation of CIPs. All of these observations are consistent with the rather low dielectric constant of DCM (table 4.2) and its relatively weak ionizing properties (with donor and acceptor numbers of 2 and 20 respectively).[239]

Probably the most interesting feature is that the IL appears to retains its chemical character (insofar as these are reflected in dielectric properties) to surprisingly high levels of dilution ($x_{\mathrm{IL}} \gtrsim 0.5$) with DCM. At even higher dilutions ($x_{\mathrm{IL}} \lesssim 0.3$) the data suggest that the IL acts as a conventional but rather strongly associated electrolyte. At $x_{\mathrm{IL}} \lesssim 0.03$, consistent with recent conductivity studies,[237] CIPs are probably the dominant species (fig. 4.7). However, as the IL content increases, ion-ion pair interactions lead to their break-up and/or replacement by other charged species such as triple ions. In effect the present work shows that IL + DCM mixtures can be divided into two regions. At $x_{\mathrm{IL}} \lesssim 0.5$ the dynamics are in essence those of an electrolyte solution showing strong association at low concentrations and subsequent redissociation and/or other processes at intermediate ($0.03 \lesssim x_{\mathrm{IL}} \lesssim 0.5$) IL concentrations. At $x_{\mathrm{IL}} \gtrsim 0.5$ the behaviour is essentially that of an ionic liquid. These finding are in broad accordance with data from other techniques. For example, Wang *et al.*[235] have reported that both excess molar volumes and viscosities of IL + DCM mixtures exhibit extrema at $x_{\mathrm{IL}} \simeq 0.3$.

4.2.2 [emim][EtSO$_4$] + DCM

Parts of the material presented in this chapter form the basis of the paper:

Johannes Hunger, Alexander Stoppa, Richard Buchner, and Glenn Hefter *"Dipole Correlations in the Ionic Liquid 1-N-Ethyl-3-N-methylimidazolium Ethylsulfate and Its Binary Mixtures with Dichloromethane" J. Phys. Chem. B* **2009**, *113*, 9527-9537.

The RTIL 1-*N*-ethyl-3-*N*-methylimidazolium ethylsulfate ([emim][EtSO$_4$]) has potentially a great significance for industrial applications, since it is commercially available on a large scale and cheap[186] as already mentioned in section 3.2.2. In contrast to [bmim][BF$_4$], [emim][EtSO$_4$] is contains dipolar anion. The influence of the the dipole-dipole interaction between anions and cations — in addition to the Coulombic and cation-cation dipolar interactions (present in [bmim][BF$_4$]) — on the structure and dynamics is investigated by studying dielectric spectra of its mixtures with DCM at 25 °C at closely spaced intervals over the whole composition range.
The dielectric spectra over frequencies ranging from (0.2 to 89) GHz for [emim][EtSO$_4$] + DCM mixtures were obtained by combining data at $0.2 \lesssim \nu/\mathrm{GHz} \leq 20$ from a frequency-domain reflectometer (HP8720D VNA, see section 2.3.3) and two waveguide interferometers operating at $27 \leq \nu/\mathrm{GHz} \leq 89$ (see section 2.3.2). Raw VNA data were obtained using air, mercury and purified DMA as primary calibration standards. For secondary calibration purified BN and 1-butanol were used (section 2.3.3). Typical experimental spectra for [emim][EtSO$_4$] + DCM mixtures are displayed in fig. 4.9.
Electrical conductivities of the mixtures, κ, and mixture densities, ρ, required for the calculation of molar concentrations, $c/\mathrm{mol\,L^{-1}}$, were measured according to the procedure described in section 2.4. All of these data together with the compositions at 25 °C are collected in table 4.3.

Relaxation model

The two neat components, IL and DCM, possess very different dielectric spectra. As discussed in section 3.2.2, [emim][EtSO$_4$] exhibits three modes (CC + D + D) over the present frequency range. On the other hand, the dielectric spectrum of DCM is rather simple, being dominated by a single Debye process with relaxation time $\tau_{\mathrm{DCM}} = 2.2\,\mathrm{ps}$ ($\nu \approx 70\,\mathrm{GHz}$), which is readily assigned to the rotational diffusion of the dipolar DCM molecules.[101,111‡]
Various plausible superpositions of different band-shapes (eq. 1.61) were tested to model the dielectric spectra of the [emim][EtSO$_4$] + DCM mixtures. As for the neat IL, a superposition of a low-frequency Cole-Cole process and two Debye modes at higher frequencies (i.e., a CC+D+D-model, table 3.5) yielded the lowest values for χ^2_{r}. The contributions of the three relaxation processes and the quality of the overall fit for a representative mixture

‡Note that the spectra of DCM exhibit additional high frequency contributions in the THz region due to librational modes.[101,241] Although these modes do not contribute significantly in the present spectral range, the relaxation parameters are taken from broadband spectra[101] and thus might be slightly biased by the different frequency ranges.

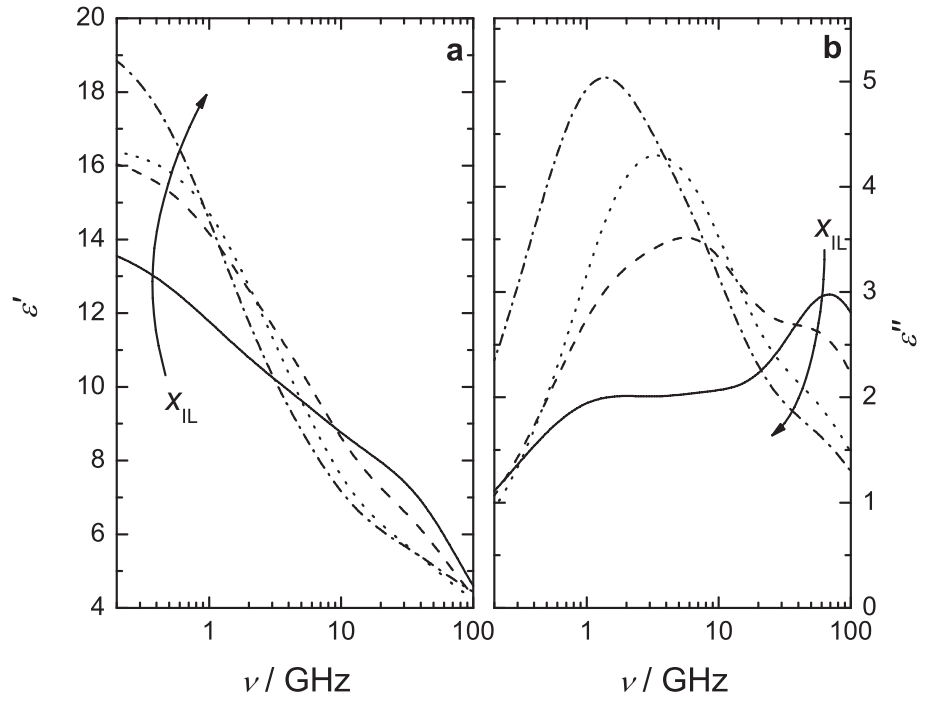

Figure 4.9: Dielectric permittivity (**a**), $\varepsilon'(\nu)$, and dielectric loss (**b**), $\varepsilon''(\nu)$, spectra of representative [emim][$EtSO_4$] + DCM mixtures at 25 °C. Arrows indicate increasing IL content (x_{IL} = 0.0186, 0.0823, 0.265 and 0.449).

are illustrated in fig. 4.10. As will become apparent below, contact ion pairs (CIPs) also contribute to the low frequency CC process at high dilutions of IL in DCM. This is reflected in the fact that at low concentrations ($x_{IL} < 0.2$) there are indications of an additional low frequency process, which could not be resolved properly due to spectral overlap (see below).

Use of the same (CC+D+D) model for both neat [emim][$EtSO_4$] and the [emim][$EtSO_4$] + DCM mixtures implies that no separate DCM contribution could be resolved at high frequencies. This occurs because the broad high frequency IL mode (centered at ∼80 GHz) and the main DCM relaxation (at ∼ 70 GHz) overlap too closely to be separated.

Relaxation times and band shape

Lowest frequency process The relaxation time for the lowest-frequency process, τ_1, exhibits a minimum at $x_{IL} \approx 0.2$ and increases strongly at higher IL concentrations (table 4.4). The shape of this curve is similar to that of the corresponding process in [bmim][BF_4] + DCM mixtures (fig. 4.11a). Unfortunately, no experimental viscosity data for the present mixtures are available and thus the relaxation times can only be discussed qualitatively. On the basis of the [bmim][BF_4] + DCM data (section 4.2.1),[111] it is probable that the increase in τ_1 at $x_{IL} > 0.2$ reflects increasing mixture viscosity, which in itself reflects the transition from electrolyte-solution like behaviour at high DCM content to IL-like structure and dynamics when approaching the pure IL. It is interesting to note

Table 4.3: Weight fraction, w_{IL}, mole fraction, x_{IL}, and molar concentration, c_{IL}, of [emim][$EtSO_4$] in binary mixtures with DCM and the measured densities, ρ, electrical conductivities, κ, and molar conductivities, Λ of those mixtures at 25 °C.[a]

w_{IL}	x_{IL}	c_{IL}	ρ	κ	$\Lambda/10^{-4}$
0	0	0	1316.98[b]	-	-
0.02479	0.009055	0.1382	1317.42	0.06340	4.587
0.05011	0.01861	0.2793	1317.25	0.1366	4.889
0.09979	0.03832	0.5560	1316.44	0.3103	5.580
0.1997	0.08232	1.110	1313.25	0.6636	5.978
0.3002	0.1336	1.662	1307.67	0.9352	5.628
0.3995	0.1930	2.195	1298.30	1.085	4.942
0.5007	0.2650	2.737	1291.58	1.112	4.062
0.6031	0.3532	3.270	1281.25	1.027	3.140
0.6936	0.4487	3.734	1272.16	0.8935	2.393
0.7936	0.5802	4.235	1261.09	0.7280	1.719
0.8973	0.7584	4.748	1250.30	0.5558	1.171
0.9694	0.9194	5.097	1242.23	0.4362	0.8559
1	1	5.237	1242.3[c]	0.3820[d]	0.7295

[a] Units: ρ in $\mathrm{kg\,m^{-3}}$; c_{IL} in $\mathrm{mol\,L^{-1}}$; κ in $\mathrm{S\,m^{-1}}$; $\Lambda(=\kappa/c_{\mathrm{IL}})$ in $\mathrm{S\,m^2\,mol^{-1}}$. [b] Ref. 114; [c] Ref. 240; [d] Ref. 156.

that although the molecular volume of $[emim]^+$ ($V_{\max} = 510\,\text{Å}^3$, $V_{\mathrm{vdW}} = 120\,\text{Å}^3$) is smaller than that of $[bmim]^+$ ($V_{\max} = 750\,\text{Å}^3$, $V_{\mathrm{vdW}} = 150\,\text{Å}^3$, see section 2.5), the present τ_1 values are larger than in [bmim][BF_4] + DCM mixtures (fig. 4.11a). This is compatible with a strong orientational correlation hindering the reorientation of $[emim]^+$. At $x_{\mathrm{IL}} \lesssim 0.2$ the increase in τ_1 (fig. 4.11a) is almost certainly related to the presence of two overlapping modes: one due to CIPs and the other to cation reorientation. The relative contributions of these two processes varies with x_{IL} as discussed previously for [bmim][BF_4] + DCM mixtures (see section 4.2.1).[111] At $x_{\mathrm{IL}} \to 0$, free ions are dominant but as x_{IL} increases some ions associate to form CIPs. At even higher x_{IL} there appears to be re-dissociation of the CIPs,[242] resulting in the maximum in τ_1 at $x_{\mathrm{IL}} \approx 0.03$. Attempts to separate these two processes were not successful but the presence of ion pairs at low x_{IL} accords with the decrease in the CC broadness-parameter α (table 4.4, fig. 4.11b) at $0.03 \leq x_{\mathrm{IL}} \leq 0.2$. Similar behaviour was also found for [bmim][BF_4] + DCM mixtures (see section 4.2.1).[111]

With regard to the dominant low frequency process there are two obvious differences between the mixtures of DCM with [bmim][BF_4][111] and with [emim][$EtSO_4$]. First (fig. 4.11), the minima in τ_1 and α for the latter mixtures are at slightly lower x_{IL} suggesting that [emim][$EtSO_4$] keeps its molten-salt-like character up to even higher dilutions in DCM than does [bmim][BF_4]. Second (fig. 4.11b), the values of α for [emim][$EtSO_4$] + DCM mixtures are systematically lower than the corresponding mixtures with [bmim][BF_4]. As has been noted previously (see section 4.2.1),[111] molecular explanation of the variation of

Table 4.4: Fit parameters of eq. 1.61 for the observed dielectric spectra of mixtures of [emim][$EtSO_4$] with DCM at 25 °C assuming a CC+D+D model (see text): static permittivities, ε; relaxation times, τ_j, and amplitudes, S_j, of process j; Cole-Cole shape parameter, α of the first (lowest frequency) process; infinite frequency permittivity, ε_∞, and reduced error function of the overall fit, χ^2_r.[a]

x_{IL}	ε	τ_1	α	S_1	τ_2	S_2	τ_3	S_3	ε_∞	$\chi^2_r/10^{-5}$
0[b]	8.81	-	-	-	-	-	2.23	4.92	3.89	-
0.00906	12.23	117	0.24	3.22	19.8	0.877	2.13	5.47	2.66	206
0.0186	14.33	155	0.25	5.15	19.1	1.33	2.08	5.27	2.58	157
0.0383	15.97	151	0.19	6.03	19.8	2.42	2.15	4.80	2.72	142
0.0823	16.46	112	0.15	5.85	20.4	3.76	2.29	3.81	3.04	180
0.134	16.29	80.5	0.15	6.08	20.6	3.91	2.29	3.18	3.13	218
0.193	16.13	81.3	0.084	5.54	22.7	4.41	2.72	2.72	3.46	206
0.265	16.61	80.8	0.091	7.14	21.9	3.59	2.62	2.31	3.56	285
0.353	17.99	101	0.13	9.32	22.5	2.95	2.56	2.03	3.69	193
0.449	19.99	139	0.16	11.9	21.7	2.47	2.37	1.83	3.78	196
0.580	22.97	225	0.18	14.8	23.2	2.41	2.41	1.86	3.92	229
0.758	28.77	431	0.24	20.8	23.0	2.11	2.23	1.79	4.06	179
0.919	34.06	706	0.26	26.1	22.3	2.10	1.88	1.83	4.06	234
1	35.20	806	0.24	26.9	24.0	2.22	2.03	1.89	4.24	265

[a] Units: τ_j in ps; [b] Parameters taken from Ref. 101.

α values in such mixtures is not straightforward. The increase in α between [emim][$EtSO_4$] and [bmim][BF_4] probably reflects an increase in the heterogeneity of the molecular-level environment of the relaxing species. This is consistent with the enhanced nano-scale segregation with increasing imidazolium side-chain length found from MD simulations[216] and from X-ray scattering experiments.[217] Some of the changes in α might also arise from changes in the conformation of the alkyl side chain of the imidazolium cation because a distribution of relaxation times occurs from variations in the volumes of rotation (eq. 1.78) of the different conformers, whose maximum diameters range from (990 to 1007) pm for $[emim]^+$ and from (1012 to 1236) pm for $[bmim]^+$ (see section 2.5). However, $[EtSO_4]^-$ may also adopt different conformations with a similar variation in diameter (829 pm to 850 pm) to that of $[emim]^+$ yet the anion mode exhibits Debye behaviour ($\alpha = 0$). This suggests that, as for [bmim][BF_4],[111] it is not the variation of conformer distribution that dominates the bandwidth, and thus the heterogeneity of cation and anion relaxation(s) in [emim][$EtSO_4$] and its mixtures with DCM but more likely molecular-level environmental effects. At high x_{IL} the decrease of α with decreasing x_{IL} (fig. 4.11b) indicates that the environment of the cation becomes more homogeneous upon addition of DCM.

Intermediate and highest frequency processes The relaxation time of the second (intermediate frequency) process, τ_2, appears to increase with the expected increase in viscosity, *i.e.*, with increasing x_{IL} (table 4.4). Again, due to the lack of viscosity data such

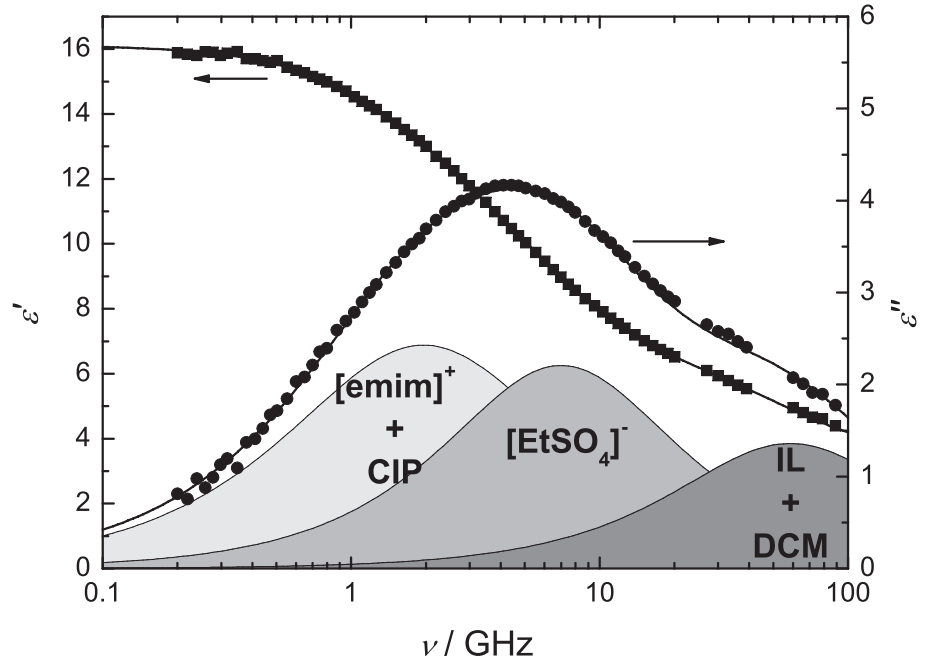

Figure 4.10: Dielectric permittivity, $\varepsilon'(\nu)$, and loss, $\varepsilon''(\nu)$, spectrum of a representative [emim][$EtSO_4$] + DCM mixture ($x_{IL} = 0.193$) at 25 °C. Symbols represent experimental data, lines show the CC+D+D fit, and shaded areas indicate the contributions of the individual processes.

effects will be not discussed in detail. The observed spectra at intermediate frequencies were well fitted by a single Debye process corresponding to a single relaxation time. For the fastest process observed in the present spectra the relaxation time, τ_3, is ~ 2.2 ps for the diluted mixtures and passes through a maximum at intermediate x_{IL} before dropping to ~ 2 ps for the neat IL (table 4.4). This behaviour is not related in any simple way to mixture properties such as viscosity (which would be expected to vary smoothly with composition).[111] This is not surprising because, as already noted, the highest frequency mode is a superposition of the rotational diffusion of DCM and one or possibly more high frequency modes of the IL, dominated by intermolecular vibrations (see section 3.3).[170]

Static permittivities and amplitudes

The extrapolated static permittivities, ε, of [emim][$EtSO_4$] + DCM mixtures (table 4.4) are not a simple function of composition, exhibiting a steep increase at low x_{IL} followed by a shallow minimum at $x_{IL} \approx 0.2$. At higher IL concentrations, ε increases monotonically to the value of neat [emim][$EtSO_4$]. Insights into this complex behaviour can be obtained from a detailed consideration of the amplitudes of the individual processes.

Lower frequency modes For reasons that will become apparent below, only processes 1 and 2, assigned to reorientation of the cations and anions respectively, will be discussed. With the analytical (total) IL concentration, c_{IL}, and the measured relaxation amplitudes,

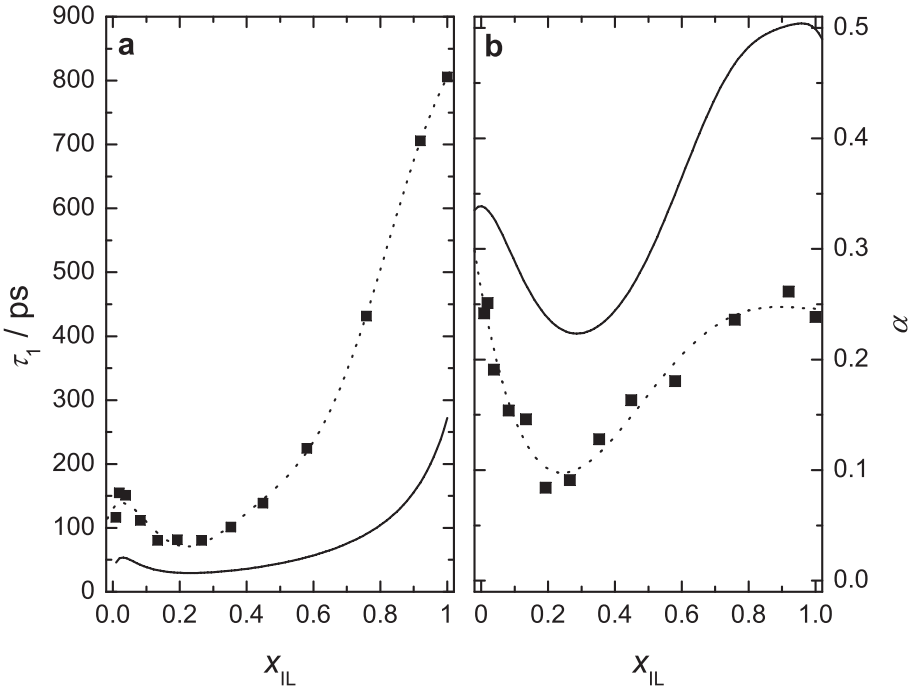

Figure 4.11: (**a**) Relaxation time, τ_1, and (**b**) Cole-Cole parameter, α, of the first (lowest-frequency) process for [emim][$EtSO_4$] + DCM mixtures (points and dotted lines) and for [bmim][BF_4] + DCM mixtures (full lines) at 25 °C.[111]

S_j, it is possible to use eq. 1.69 to calculate the effective molecular dipole moment, $\mu_{\mathrm{eff},j}$, of the species responsible for a relaxation process. Note that to obtain the value of $\mu_{\mathrm{eff},2}$ the concentration of "free" IL

$$c_{\mathrm{IL}}^{\mathrm{free}} = c_{\mathrm{IL}} - c_{\mathrm{CIP}} \tag{4.2}$$

was used since anions that are bound in an ion pair can reasonably be assumed not to contribute to this process. Because *a priori* we have no information about dipole correlations within the samples, only the effective dipole moment, $\mu_{\mathrm{eff},j}$, which incorporates orientational correlations, is accessible.

Neither of the $\mu_{\mathrm{eff},j}$ values calculated via eq. 1.69 is a simple function of composition (fig. 4.12). Thus, $\mu_{\mathrm{eff},1}$ shows a pronounced decrease with increasing x_{IL} at low x_{IL} before passing through a minimum at $x_{\mathrm{IL}} \approx 0.2$ followed by a more or less linear increase at higher x_{IL}. The behaviour at low x_{IL} also occurs in the [bmim][BF_4] + DCM system, and was attributed to the formation of contact ion pairs, however, the linear increase in $\mu_{\mathrm{eff},1}$ at higher x_{IL} was not observed previously.[111] On the other hand, the values of $\mu_{\mathrm{eff},2}$ decrease monotonically from infinite dilution to the pure IL. The variation of $\mu_{\mathrm{eff},j}$ with x_{IL} may be due to spectral overlap *e.g.* of the cation and anion modes,[178] as discussed above. However, attempts to analyse the combined amplitudes S_1+S_2 or even $S_1+S_2+S_3$ yielded no simple composition dependence and so this possibility can be ruled out.

There are two other plausible explanations for the variations in $\mu_{\mathrm{eff},j}$ with composition. First, it is possible that not all the "particles" of the ionic liquid are contributing to the

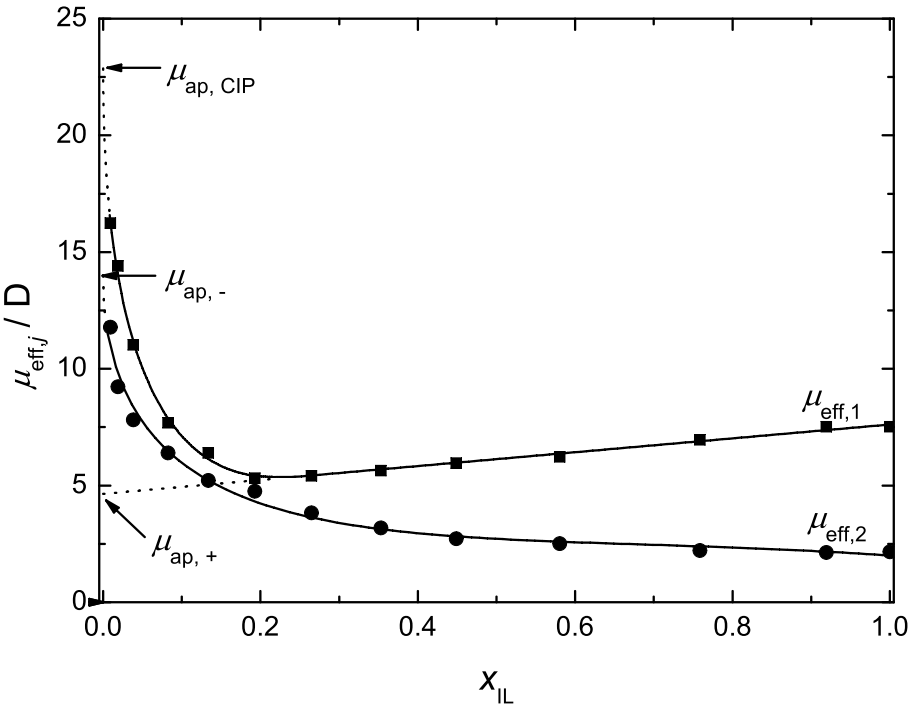

Figure 4.12: Effective dipole moments $\mu_{\mathrm{eff},j}$ of relaxation processes 1 ($j = 1$, ■) and 2 ($j = 2$, ●) of [emim][$EtSO_4$] + DCM mixtures at 25 °C. Dotted lines represent the extrapolations to obtain the apparent dipole moments of the cation ($\mu_{\mathrm{ap},+}$), anion ($\mu_{\mathrm{ap},-}$) and ion pair ($\mu_{\mathrm{ap,CIP}}$) at infinite dilution.

observed dielectric process because the concentration of the relaxing species is lower than the analytical concentration, c_{IL}. This possibility can be excluded since it does not occur for [bmim][BF_4] + DCM mixtures and there is no obvious reason why it should be different for the present mixtures. Additionally, since $\mu_{\mathrm{eff},1}$ increases at $x_{\mathrm{IL}} > 0.2$, this interpretation would imply that the concentration of "frozen" IL particles would decrease with increasing x_{IL} (strong interaction would be weakened as x_{IL} increases).

Second, the change in $\mu_{\mathrm{eff},j}$ in the mixtures could be a consequence of enhanced correlations of the relaxing dipoles. This interpretation is consistent with MD simulations of neat RTILs that suggest pronounced dipole correlation and collective dipole reorientations.[176,178,179] For example, Schröder *et al.*[178] found for [bmim][CF_3CO_2], where the anion has a relatively large dipole moment, that the dielectric response is mainly of a collective nature. Additionally, they found a very pronounced parallel correlation of the cations, whereas the contribution of the anions to the dielectric spectra was relatively small. In the present work, both cations and anions have a dipole moment, hence it seems reasonable to assume that dipolar correlation is responsible for the observed variation in $\mu_{\mathrm{eff},j}$. These dipole-dipole correlations might explain the strong anion dependence of aggregate formation in binary mixtures of ionic liquids with molecular solvents, obtained with mass spectrometry.[243] Consideration of these dipole-dipole correlations inferred from the mix-

ture studies also allows a consistent interpretation of the temperature dependence of the spectra of the pure IL (see section 3.2.2).

Apparent dipole moments As already mentioned, process 1, which is mainly due to cation reorientation, overlaps with an ion pair relaxation process at $x_{\mathrm{IL}} \leq 0.2$. At even higher x_{IL} values the linear variation of $\mu_{\mathrm{eff},1}$ suggests that no ion pairs are present in this composition range, as observed previously for [bmim][BF_4] + DCM mixtures[111] (section 4.2.1). Assuming $\mu_{\mathrm{ap},+}$ is independent of composition, $\mu_{\mathrm{eff},1}$ values at $x_{\mathrm{IL}} > 0.20$ can be extrapolated to $x_{\mathrm{IL}} = 0$ (fig. 4.12) to obtain an estimate of $\mu_{\mathrm{ap},+}$, since the limiting value of g_+ is by definition unity at infinite dilution. The value of $\mu_{\mathrm{ap},+} = 4.64\,\mathrm{D}$ so obtained is in reasonable agreement with the dipole moments obtained from DRS measurements of neat RTILs containing $[\mathrm{emim}]^+$[11] but is somewhat higher than the semiempirical MOPAC[118] value ($\mu_{\mathrm{ap},+} = 2.95$ to $4.00\,\mathrm{D}$, see section 2.5). An estimate of $\mu_{\mathrm{ap,CIP}}$ can also be obtained from $\mu_{\mathrm{eff},1}$ by recognizing that CIPs become dominant at very low x_{IL}.[111] The value so obtained (fig. 4.12), $\mu_{\mathrm{ap,CIP}} = 22.9\,\mathrm{D}$, is broadly consistent with the semiempirical MOPAC[118] estimates of $\mu_{\mathrm{ap,CIP}}$, which range from $16.6\,\mathrm{D}$ to $19.7\,\mathrm{D}$ (see section 2.5) and with the experimental value for [bmim][BF_4] in DCM.[111]
Because process 2 is associated only with anion re-orientation, extrapolation of $\mu_{\mathrm{eff},2}$ to $x_{\mathrm{IL}} \to 0$ (where $g_- = 1$) gives a value for the apparent dipole moment of the anion of $\mu_{\mathrm{ap},-} = 14.0$ D (fig. 4.12). This is in reasonable agreement with the liquid-phase dipole moments obtained from MOPAC,[118] of between $11.2\,\mathrm{D}$ and $13.2\,\mathrm{D}$, depending on the anion conformation (see section 2.5).

Dipole-dipole correlation The apparent dipole moments for the cation, $\mu_{\mathrm{ap},+}$, and the anion, $\mu_{\mathrm{ap},-}$, can be used to estimate the corresponding correlation factors g_+ and g_- from the effective dipole moments $\mu_{\mathrm{eff},1}$ (at $x_{\mathrm{IL}} > 0.2$ where no CIPs exist) and $\mu_{\mathrm{eff},2}$ using eq. 1.70. Because $g_+ = 1$ at infinite dilution, it is possible to interpolate the values of g_+ at $0 \leq x_{\mathrm{IL}} \leq 0.2$ (fig. 4.12). The correlation factors so obtained are displayed in fig. 4.13. The value of g_- drops remarkably with increasing x_{IL} ultimately reaching ~ 0.024 for the neat IL. In contrast g_+ increases monotonically to ~ 2.6 in the neat IL. This suggests that DCM breaks up the IL structure and weakens the correlations among the dipoles by increasing the distance between the ions, as the IL "particles" are diluted.

Ion pairing The concentration of CIPs can be calculated by assuming that only CIPs and ions are present at $x_{\mathrm{IL}} < 0.2$. If so, it follows that

$$c_{\mathrm{IL}}\mu_{\mathrm{eff},1}^2 = c_{\mathrm{IL}}^{\mathrm{free}} g_+ \mu_{\mathrm{ap},+}^2 + c_{\mathrm{CIP}} g_{\mathrm{CIP}} \mu_{\mathrm{ap,CIP}}^2 \tag{4.3}$$

The term on the left-hand side of eq. 4.3 is obtained from the experimental data via eq. 1.69. As c_{CIP} is reasonably small, orientational correlation of the CIPs can be neglected (i.e., $g_{\mathrm{CIP}} = 1$),[24] while g_+, at low x_{IL} can be obtained by interpolation of the g_+ values at $x_{\mathrm{IL}} > 0.2$ (fig. 4.13). Combination of eqs. 4.2 and 4.3 then yields the concentrations $c_{\mathrm{IL}}^{\mathrm{free}}$ and c_{CIP}. The results so obtained are plotted in fig. 4.14 along with the corresponding values for [bmim][BF_4]+DCM mixtures.[111]

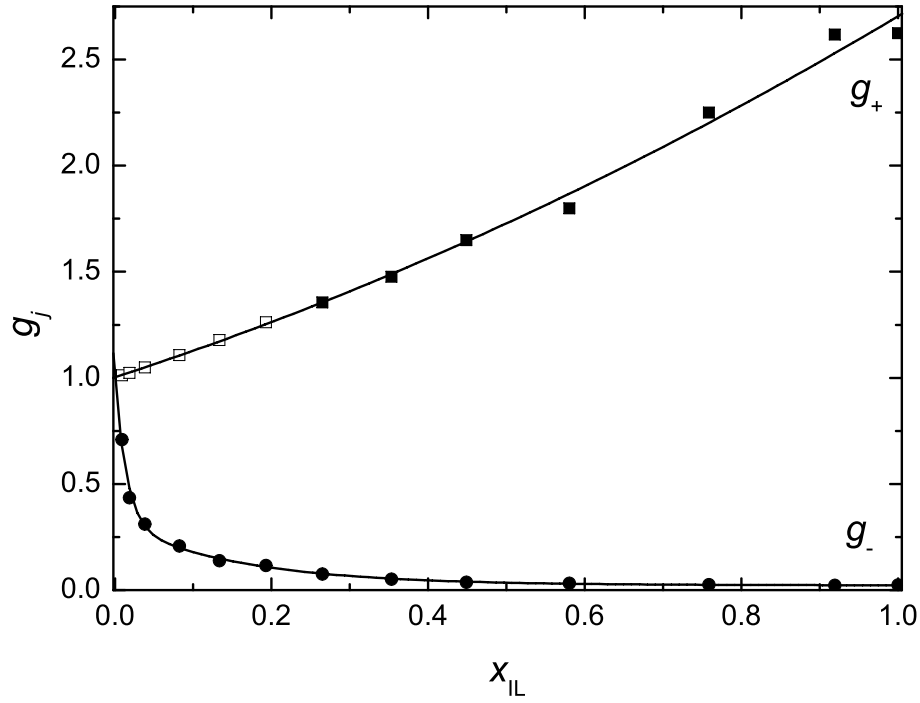

Figure 4.13: Kirkwood correlation factors of $[emim]^+$, g_+ (■) and of $[EtSO_4]^-$, g_- (●) for [emim][$EtSO_4$] + DCM mixtures at 25 °C as a function of composition. Open symols represent interpolated values for mixtures were ion pairing contributes to process 1 (see text). Lines are included only as a visual aid.

Both [bmim][BF_4][111] and [emim][$EtSO_4$] are relatively strongly associated at high dilutions in DCM. The presence of [emim][$EtSO_4$] ion pairs in DCM mixtures is consistent with the equivalent conductance, Λ, which peaks at $x_{IL} \approx 0.13$ (table 4.3), since DCM has a relatively low dielectric constant and weak ionizing properties.[168] This means that in the composition range $0.009 \leq x_{IL} \leq 0.13$ for which conductivities were measured, the effective number of charge carriers rises sufficiently to overcome the increasing viscosity of the mixtures. The decrease in c_{CIP}/c_{IL} over this composition range (fig. 4.14) suggests that this is due to so-called re-dissociation of the CIPs.[242] The formation of triple ions can be excluded, since the irregular shape of the cations and the anions make it likely that any triple ions formed would have a finite dipole moment and therefore would be distinguishable in the dielectric spectra. On the other hand, formation of larger, more symmetric aggregates, like ion quadruples (pairs of ion pairs), cannot be excluded as such species would have negligible dipole moments and thus would not contribute to $\hat{\varepsilon}(\nu)$. The marked deviations of g_+ and especially g_- from unity even at low IL content may hint at such clusters. Interestingly, the maximum in $\Lambda(c_{IL})$ is observed only in mixtures with DCM: in binary mixtures of RTILs with solvents like acetonitrile, dimethylsulfoxide, propylene carbonate or water $\Lambda(c_{IL})$ decreases monotonically with increasing c_{IL}[76] consistent with their more strongly ionizing nature.

To estimate the standard (infinite dilution) association constant of the CIPs , K_A°, the association constant measured at finite ionic strengths, $K_A = c_{IP}/(c_{IL} - c_{IP})^2$, can be

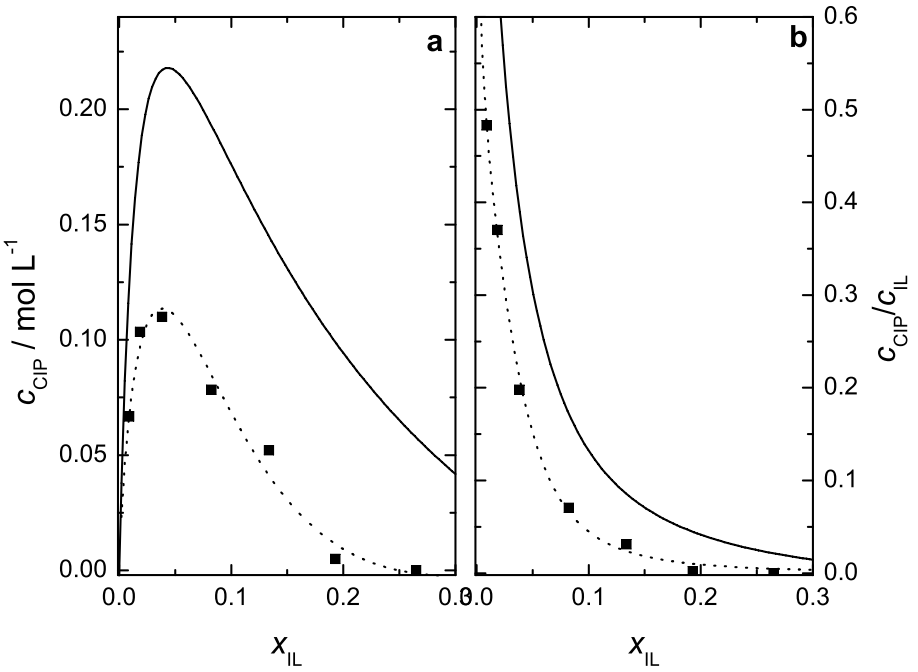

Figure 4.14: (**a**) Total, c_{CIP}, and (**b**) relative, $c_{\mathrm{CIP}}/c_{\mathrm{IL}}$, ion pair concentrations in [emim][$EtSO_4$] + DCM mixtures at 25 °C. Symbols show the experimental values, dotted lines are included only as a visual aid. Full lines represent the values observed for [bmim][BF_4] + DCM mixtures at 25 °C.[111]

extrapolated using eq. 4.1. While for [bmim][BF_4] in DCM[111] (section 4.2.1, fig. 4.7) this fit shows good statistics ($R^2 > 0.999$) for [emim][$EtSO_4$] in DCM, the extrapolation (fig. 4.15) is more uncertain because the ion pairing occurs in a more restricted composition range and the data scatter considerably. The obtained value of $\log K_{\mathrm{A}}^{\circ} = 4.8 \pm 0.6$ is thus only a rough estimate, but indicates strong ion association in this system, although it is less than for [bmim][BF_4] in DCM.[111]

Highest-frequency mode As the highest frequency mode, process 3, is a superposition of intermolecular vibrations due to the IL (see section 3.3) and the rotational diffusion of DCM molecules,[101] a simple analysis of its relaxation amplitude, S_3, is not possible. In addition, because this process is located near the high frequency limit of the present instrumentation (fig. 4.10) it is not fully defined and may contain contributions from even higher frequency modes, that are known to exist for neat ionic liquids in the THz and far IR region (see section 3.3, Ref. 146) In spite of these difficulties, it is still possible to compare (fig. 4.16) the experimental values of S_3 with S_{DCM}, the amplitude estimated from eq. 1.69 assuming all DCM molecules contribute to the spectrum and that their dipole moment, $\mu_{\mathrm{eff,DCM}}$, has the same value as in neat DCM.[101] fig. 4.16 shows that S_3 and S_{DCM} agree well at low x_{IL}. At $x_{\mathrm{IL}} > 0.3$, however, $S_3 > S_{\mathrm{DCM}}$ because the contributions from the high frequency modes of the IL begin to dominate. The slight discrepancies at low x_{IL} are

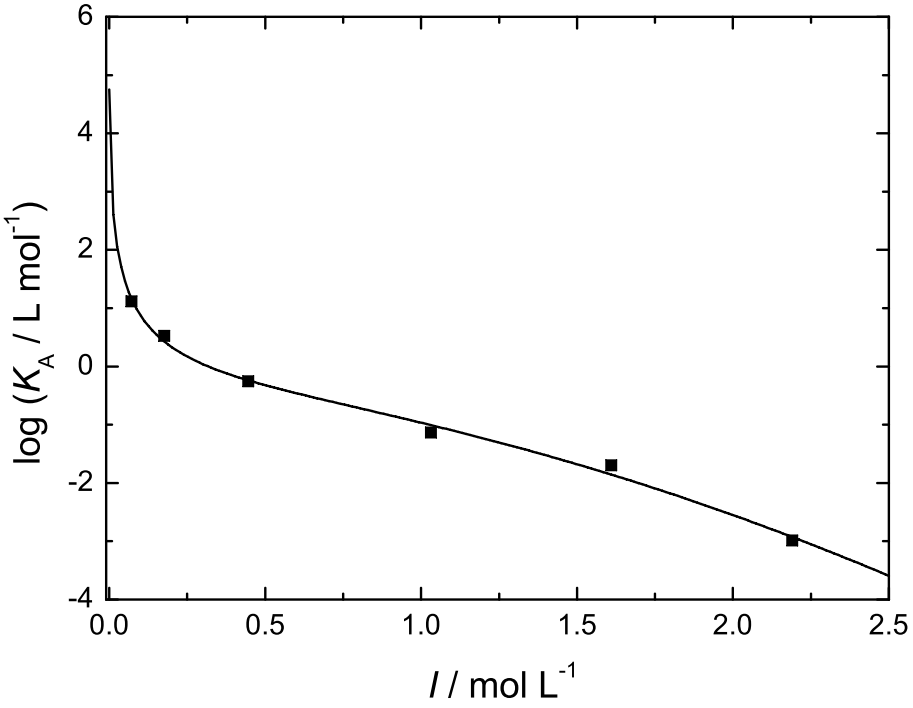

Figure 4.15: Overall association constant, $\log K_{\mathrm{A}}$ of [emim][$EtSO_4$] in DCM at 25 °C as function of ionic strength, I. Lines represent fits according to eq. 4.1.

probably because S_{DCM} is estimated using parameters obtained from a study[101] covering a broader frequency range.
More detailed analysis of this process is not justified using the present data alone but it is possibly noteworthy that the contribution from IL to S_3 disappears at $x_{\mathrm{IL}} \approx 0.3$ (fig. 4.16), which is about the same composition where ion pairs begin to form (fig. 4.14) and α exhibits its minimum (fig. 4.11). This suggests that the high-frequency IL modes that are characteristic of an ionic-liquid-like structure persist to quite high levels of dilution in these mixtures.

Concluding remarks

The dielectric spectra of [emim][$EtSO_4$] + DCM mixtures can be satisfactorily fitted by a Cole-Cole process at lower frequencies, a Debye mode at intermediate frequencies and a faster Debye process. Detailed consideration of the spectra of the binary mixtures indicates that both the CC process and the higher frequency Debye process include additional modes that could not be resolved because of spectral overlaps.
Consistent with the molar conductivities, Λ, (table 4.3) the CC mode associated with the reorientation of $[emim]^+$ is overlapped at $x_{\mathrm{IL}} < 0.2$ by a contribution from the reorientation of contact ion pairs while the highest frequency Debye mode includes contributions from the IL and DCM. It appears that [emim][$EtSO_4$] retains its molten-salt-like character, as far as this is reflected by its dielectric properties, up to relatively high dilutions ($x_{\mathrm{IL}} \approx 0.2$) in DCM.

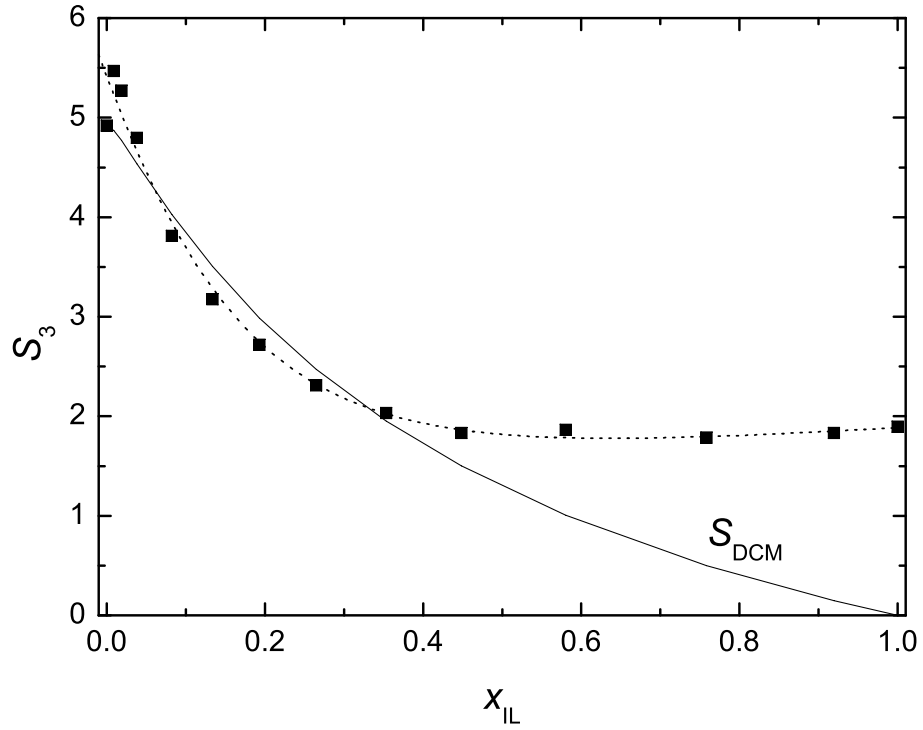

Figure 4.16: Amplitudes of relaxation process 3, S_3, (symbols) and the DCM relaxation estimated from the Cavell equation, S_{DCM} (eq. 1.69, full line), of [emim][$EtSO_4$] + DCM mixtures at 25 °C as a function of composition.

In contrast to the [bmim][BF_4] + DCM system, the [emim][$EtSO_4$] + DCM mixtures exhibit strong dipole-dipole correlations. These correlations are almost certainly the molecular origin of the unusually high dielectric constant of [emim][$EtSO_4$] having the largest dielectric constant among "conventional" imidazolium-based RTILs reported to date.[11,28,146,147] The strongly antiparallel correlations of the dipolar anions and the strongly parallel correlations of the dipolar cations are consistent with recent molecular dynamics simulations of neat ionic liquids.[176,178] The dipole-dipole correlation is weakened, as the IL is diluted with DCM or as the temperature (and thus thermal motion) is increased.

4.3 Binary mixtures RTIL + water

Several studies can be found in the literature that reprot the potential application of ionic liquids in fuel cells. For example proton conducting ILs can be used as starting materials for fabrication of proton conducting membranes.[19,244] These membranes find applications in polymer-electrolyte membrane fuel cells that can be operated at room temperature.[245] However, proton conducting ILs are often based on acid/base neutralization reactions that are accompanied by the loss of desired properties like negligible vapor pressure.[246,247]

Another approach is based on conventional alkaline fuel cells (AFCs), which use concentrated KOH solutions as the electrolyte. These AFCs have good efficiencies at 60 °C - 90 °C, but require pure (CO_2 free) hydrogen and oxygen to prevent carbonate formation from the presence of carbon dioxide.[245]

Recently, de Souza *et al.*[248] replaced the KOH electrolyte in a conventional AFC by an ionic liquid, yielding a fuel cell operating at ambient temperature and working with air instead of pure oxygen. However, the water content of the IL has significant influence on the performance. Because water, being the only product of the conversion of hydrogen with oxygen in hydrogen fuel cells, will always be present in such systems, it is desirable to gain knowledge about the state of water in ILs and its influence on the properties of ILs.

These questions have been addressed in the present work by studying several ILs mixed with water by dielectric spectroscopy.

4.3.1 [bmim][Cl] + H_2O

The ionic liquid [bmim][Cl] is not strictly a RTIL as it has a melting point of approximately $T_{\mathrm{fus}} \approx 340\,\mathrm{K}$.[249]

Therefore, dielectric spectra of dilute solutions of [bmim][Cl] in water ($c_{\mathrm{IL}} < 1.3\,\mathrm{mol\,L^{-1}}$) were recorded at 25 °C at frequencies ranging from 0.2 to 89 GHz. Analysis of the spectra revealed that there are at least two modes present. Beside the water relaxation at $\sim$ 20 GHz, a lower frequency mode is detected and assigned to contact ion-pairs.

Experimental details

For all solutions, $\hat{\varepsilon}(\nu)$ was determined in the frequency range $0.2 \lesssim \nu/\mathrm{GHz} \leq 89$ (Agilent E8364B VNA + 85070E dielectric probe kit + E-band interferometer, section 2.3).

Raw VNA data were obtained using air, mercury and degassed Millipore (Milli-Q) water as primary calibration standards. Calibration errors were corrected with a Padé approximation using pure propylene carbonate and dimethylacetamide as secondary standards (see section 2.3.3). All dielectric measurements were performed at (25.00 ± 0.05). Typical experimental spectra with a precision of 1-2 % are displayed in fig. 4.17.

Mixture densities, ρ, and electrical conductivities, κ, required for data analysis were additionally determined (see section 2.4) and are summarized in table 4.5.

Table 4.5: Mole fraction, x_{IL}, molar concentration, c_{IL}, measured densities, ρ, and electrical conductivities, κ, of [bmim][Cl] in water at 25 °C together with the fit parameters obatined assuming a D + CC model: static permittivity, ε, relaxation amplitudes, S_j, and relaxation times, τ_j. α is the broadness parameter of the second (CC) mode and χ^2_{r} the reduced error function.[a]

x_{IL}	c_{IL}	ρ	κ	ε	S_1	τ_1	S_2	τ_2	α	ε_∞	χ^2_{r}
0[b]	0	997.05	-	78.37	-	-	72.27	8.25	0	6.10	-
0.000901	0.0495	997.65	0.459	77.76	0.32	521	71.98	8.47	0.0036	5.46	885
0.001797	0.0980	998.28	0.849	77.36	0.70	328	71.38	8.51	0.0083	5.28	713
0.004466	0.2386	1000.15	1.816	75.45	1.49	166	68.58	8.92	0.0094	5.38	1079
0.008938	0.4618	1003.30	3.062	72.38	1.46	165	66.21	9.56	0.0308	4.72	765
0.01311	0.6569	1006.20	3.933	69.61	1.68	155	63.15	10.25	0.0380	4.78	941
0.01769	0.8587	1009.38	4.666	66.74	1.66	167	60.30	11.07	0.0474	4.79	1181
0.02647	1.2124	1015.29	5.622	61.86	1.66	206	55.31	12.68	0.0631	4.90	1148

[a] Units: c_{IL} in $\mathrm{mol\,L^{-1}}$; ρ in $\mathrm{kg\,m^{-3}}$; κ in $\mathrm{S\,m^{-1}}$; τ_j in ps. [b] Parameter taken from appendix A.2.

Relaxation model and assignment

A superposition of up to four separate modes was tested to model the experimental spectra. However, following the criteria presented in section 2.3.6, only a superposition of a lower frequency Debye and a higher frequency Cole-Cole process yielded a consistent set of parameters and lowest values in the reduced error function. The parameters obtained assuming a D + CC model are summarized in table 4.5. Note that for 3 out of 7 investigated mixtures an equally good description of the experimental spectra was obtained by assuming 3 Debye modes. Assuming the D + CC model the Cole-Cole mode is split into a 8 ps and a 15 ps process. However, these relaxation times are too similar to be reliably separated, but might indicate a newly emerging mode.

The large-amplitude (CC) mode at $\sim$ 20 GHz is mainly due to the collective dynamics of the hydrogen-bonded water structure.[250] However, as will become apparent below, it may contain contributions from $[\mathrm{bmim}]^+$ cations. The lower frequency (D) mode is assigned to contact ion-pairs of [bmim][Cl]. A fast water relaxation, as found for neat water (see appendix A.2) could not be resolved because this fast water mode ($\tau \approx 0.5$ ps) is occurring close to the high frequency limit of this study and is probably subsumed by the symmetrically broadened Cole-Cole equation.

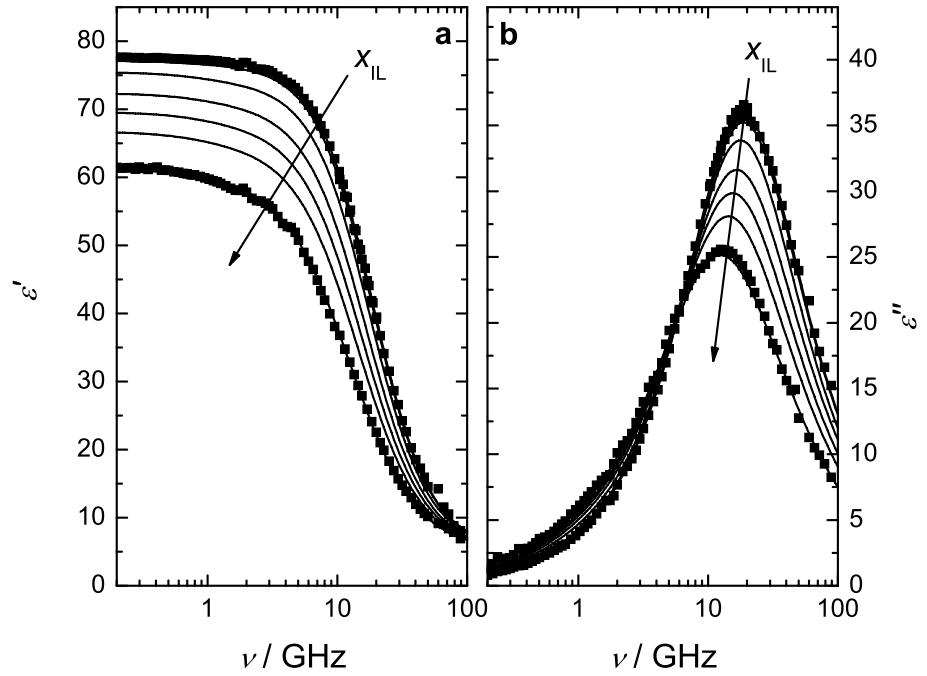

Figure 4.17: (**a**) Dielectric permittivity, ε', and (**b**) dielectric loss, ε'', spectra of [bmim][Cl](aq) solutions at 25 °C. Symbols correspond to selected experimental data (other data points are omitted for visual clarity); lines represent the D + CC fit. Arrows indicate increasing IL concentration.

Results and discussion

Higher frequency Cole-Cole mode The main water relaxation centered at $\sim 20\,\mathrm{GHz}$[250] decreases considerably in amplitude and the relaxation time slows down (table 4.5 and fig. 4.17b) upon addition of [bmim][Cl]. While for inorganic solutes an increase in relaxation time of the water mode is frequently observed,[24] organic solutes (e.g. tetraalkylammonium salts)[251] are found to decelerate water dynamics. The present [bmim][Cl](aq) solutions follow the latter trend, which can be explained by the hydrophobic character of the $[\mathrm{bmim}]^+$ cation. This deceleration of the water dynamics is rather an effect of the decreasing number density of hydrogen-bond acceptor sites than an enhancement of the water structure,[251] because water reorientation is catalyzed by an additional water molecule acting as hydrogen-bond acceptor.[251,252] The decreasing values for τ_2 as function of concentration are comparable to the bulk water relaxation times observed for aqueous tetraalkylammonium salts.[251] However, for the latter salts an additional slow water process is observed, hence the two systems are not directly comparable. On the other hand, as noted above, there are indications for the presence of such a slow water process in the present mixtures. The symmetrical broadening (Cole-Cole α parameter) might be due to an unresolved slow water process, that is also observed for aqueous solutions of terafluoroborate RTILs (see below).
For the analysis of the amplitude the apparent (i.e., the DRS-detected) concentration of H_2O, $c^{\mathrm{app}}_{H_2O}$, is calculated by inserting $S_{H_2O}(c)$ (see below) into the Cavell-equation (eq. 1.69).

Therefore, $\mu_{\mathrm{eff,H_2O}}$ is assumed to be the same as in neat water (and thus can be calculated from the relaxation parameters of neat water, given in appendix A.2). Note that for analysis with eq. 1.69 both water relaxation processes, as observed in neat water (see appendix A.2), were taken into account, by assuming $\varepsilon_\infty = 4.08$ throughout. Since water has a high relaxation amplitude and only a moderately-fast relaxation time, kinetic polarization effects[253,254] cannot be neglected in aqueous electrolyte solutions.[99] These were accounted for by assuming slip boundary conditions for the correction of the relaxation amplitudes:

$$S_{\mathrm{H_2O}}(c) = (\varepsilon_2(c) - \varepsilon_\infty^{\mathrm{H_2O}}) + \frac{2}{3} \cdot \frac{\varepsilon^{\mathrm{H_2O}} - \varepsilon_\infty^{\mathrm{H_2O}}}{\varepsilon^{\mathrm{H_2O}}} \cdot \frac{\tau^{\mathrm{H_2O}}}{\varepsilon_0} \tag{4.4}$$

where $\varepsilon_\infty^{\mathrm{H_2O}} = 4.08$, $\varepsilon^{\mathrm{H_2O}} = 78.368$ and $\tau^{\mathrm{H_2O}} = 8.25\,\mathrm{ps}$ are the static permittivity, the infinite frequency permittivity and the relaxation time of neat water, respectively (see appendix A.2). The quantity $\varepsilon_2(c)$ $(= \varepsilon - S_1)$ is the limiting permittivity of the main relaxation of this study (table 4.5).

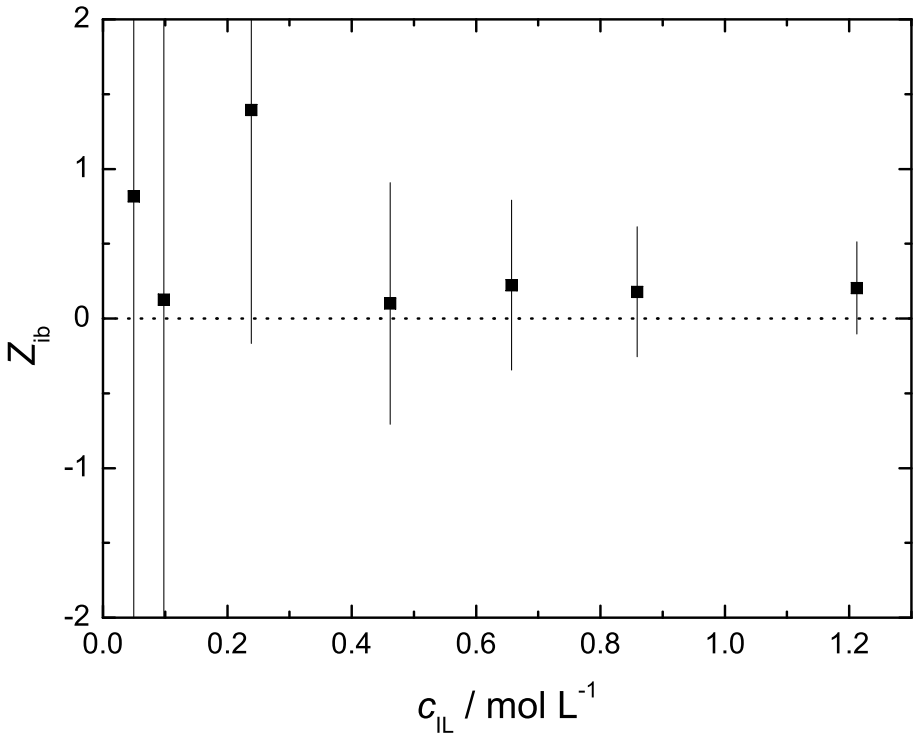

Figure 4.18: Solvation numbers, Z_{ib}, of [bmim][Cl](aq) at 25 °C. Error bars correspond to an estimated error of $\delta S_{\mathrm{H_2O}} = 0.5$, dotted line equals zero.

From the difference between the observed apparent concentration and the analytical concentration, $c_{\mathrm{H_2O}}$, effective hydration numbers, Z_{ib}, corresponding to the number of water

molecules irrotationally bound (ib) on the DRS timescale per unit of concentration, can be obtained:

$$Z_{\mathrm{ib}} = \frac{c_{\mathrm{H_2O}} - c^{\mathrm{app}}_{\mathrm{H2O}}}{c_{\mathrm{IL}}} \tag{4.5}$$

As can be seen in fig. 4.18, Z_{ib} values obtained according to eq. 4.5 are slightly positive but are essentially equal to zero within the likely experimental errors. It is well known, that Cl^- has no stable hydration shell on the DRS time scale.[99] The present results (fig. 4.18) suggest that hydration of $[bmim]^+$ is also not strong enough to irrotationally bind solvent molecules so that they disappear from the dielectric spectra, presumably because of the highly delocalized charge on the imidazolium cation.

Lower frequency Debye mode There are two plausible explanations for the origin of the lower frequency Debye mode. This mode might be due to the dipolar $[bmim]^+$ cations, but in that case a more or less linear increase of the amplitude S_1 with increasing concentration would be expected, which is not the case (see table 4.5). The observed variation of S_1 is rather typical for ion-pair formation, namely an increase in S_1 at low c_{IL} and a decrease at high c_{IL} due to the re-dissociation of the ion-pairs.[24] Moreover, the assignment of mode 1 to ion-pairs is supported by the relaxation times τ_1. At $c_{\mathrm{IL}} > 0.2\,\mathrm{mol\,L^{-1}}$, where S_1 is sufficiently high to reliably determine τ_1, the corresponding microscopic relaxation time $\tau_{\mathrm{rot},1}$ is determined to $(120 \pm 10)\,\mathrm{ps}$ (table 4.5, eq. 1.82).
The estimated value for $\tau_{\mathrm{rot},1} \approx 114\,\mathrm{ps}$ (from eq. 1.78 and the molecular volume of a [bmim][Cl] contact ion-pair in water, $V_{\mathrm{vdW}} \approx 175\,\mathrm{Å}^3$, see section 2.5) is in good agreement with the experimental value. Hence, it is reasonable to assume CIPs as the underlying species of mode 1, which is additionally supported by the mixture studies of ionic liquids + dichloromethane (see section 4.2.1). Moreover, the presence of long-lived contact ion pairs is supported by a recent *ab initio* simulation[255] of [emim][Cl] in water, where strong association of the (contact) ion pair at a given concentration ($x_{\mathrm{IL}} = 0.017$) is found. Additionally, there are several studies finding indications for ion pairing in aqueous solutions of related ILs. For instance Jeon *et al.*[256] observe structural changes in the infrared spectra of $[bmim][BF_4]$ + H_2O mixtures at $c_{\mathrm{H_2O}} \approx 45\,\mathrm{mol\,L^{-1}}$, which is about the highest concentration of the present study. From analysis of MD simulations Raju and Balasubramanian[257] conclude that 13 % of $[bmim][PF_6]$ in water are associated as ion pairs.
For quantitative analysis of S_1, in contrast to the IL + DCM studies, the dipole moment of the CIPs cannot be extrapolated from the experimental μ_{eff} values, because water has very strong ionizing properties[239] and CIPs cannot be assumed to be the dominating species at low c_{IL}. Therefore, effective dipole moments, necessary for the quantitative analysis of S_1 were obtained with semiempirical MOPAC[118] calculations (see section 2.5) yielding $\mu_{\mathrm{eff,CIP}} = (19.1 \pm 0.4)\,\mathrm{D}$ where the uncertainty corresponds to different conformations of the ion pair. This value is somewhat lower than in the case of $[bmim][BF_4]$ (see section 4.2.1), which can be attributed to the smaller radius of the anion, compared to $[BF_4]^-$. Thus, the effective cation-anion distance is shorter, resulting in a lower dipole moment. Simultaneously, the difference in the ionizing properties of the solvent results in a stabilization of the

charge separation (i.e. for the same ion-pair μ_{eff} is higher for high permittivity solvents than for lower permittivity solvents).[258]

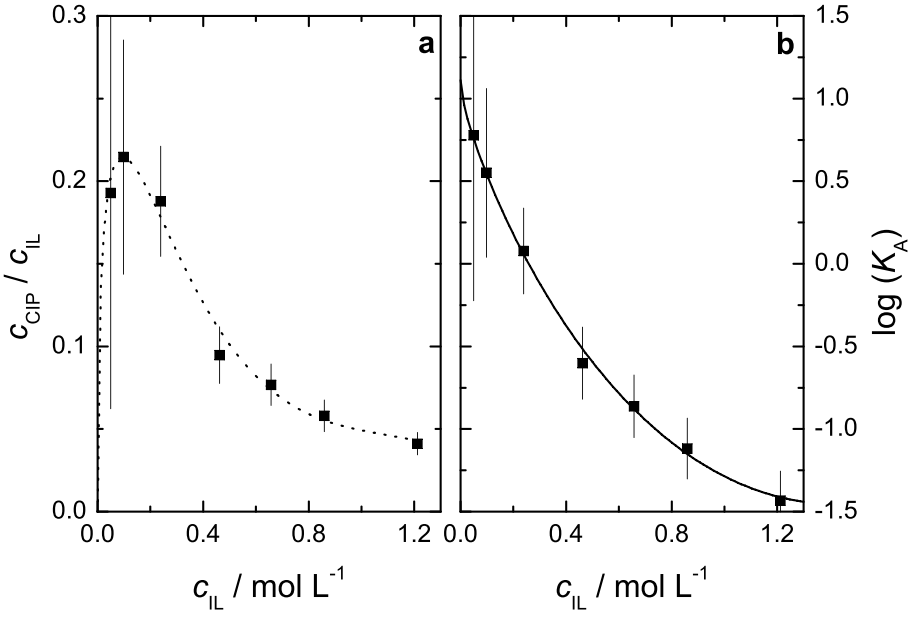

Figure 4.19: (**a**) Relative ion-pair concentration, $c_{\text{CIP}}/c_{\text{IL}}$, and (**b**) overall association constant, K_{A} as function of IL concentration c_{IL} of [bmim][Cl](aq) at 25 °C. Solid line corresponds to a fit with a Guggenheim-type equation (eq. 4.1), dotted line is included as a visual aid. Error bars are obtained assuming $\delta S_1 = 0.2$ and $\delta\mu_{\text{eff,CIP}} = 0.4\,\text{D}$.

Insertion of $\mu_{\text{eff,CIP}} = 19.1\,\text{D}$ into eq. 1.69 yields the total ion-pair concentration. As can be seen in fig. 4.19, after an initial increase in $c_{\text{CIP}}/c_{\text{IL}}$ the CIPs re-dissociate at higher concentration, as frequently found for electrolyte solutions.[24] According to section 4.2.1, the association constants, K_{A} ($= c_{\text{CIP}}/(c_{\text{IL}} - c_{\text{CIP}})^2$), are calculated and extrapolated with an Guggenheim-type equation (eq. 4.1) to infinite dilution to obtain the standard association constant, K_{A}^0.

In eq. 4.1 the Debye-Hückel coefficient $A_{\text{DH}} = 0.511\,\text{L}^{1/2}\,\text{mol}^{-1/2}$ was fixed to the value for neat water at 25 °C. The parameter A_{K} equals according to the Debye-Hückel theory $B_{\text{DH}} \cdot R_{ij}$, where B_{DH} ($= 3.301 \cdot 10^9\,\text{L}^{1/2}\,\text{mol}^{-1/2}\,\text{m}^{-1}$ for water at 25 °C) is the second Debye-Hückel coefficient, which is a characteristic parameter for the solvent and R_{ij} is the association distance. The association distance was fixed to $R_{ij} = 7.86\,\text{Å}$, which is composed of the radius of Cl^- ($r_{\text{Cl}^-} = 1.81\,\text{Å}$)[259], the radius of the cation ($r_{[\text{bmim}]^+} = 3.25\,\text{Å}$, being the dimension along the C2-H axis, obtained from MOPAC[118] calculations; see section 2.5) and the length of an oriented water molecule ($d_{\text{H}_2\text{O}} = 2.8\,\text{Å}$).[260] This approach regards two ions as associated, when less than one water molecule is separating them. As confirmed by a recent Car-Parrinello simulation,[255] coordination of the anion via the C2-H hydrogen atom of $[\text{bmim}]^+$ is assumed.

The parameters B_{K} and C_{K} in eq. 4.1 are adjusted during fitting procedure. For better comparability with other experimental techniques the ionic strength, I, was assumed to

equal the analytical concentration, c_{IL}.[§] Taking all these considerations into account a standard association constant of $K_{\mathrm{A}}^{0} = (12.9 \pm 2.3)\,\mathrm{L\,mol^{-1}}$ is obtained. Thus the system can be classified as weakly associated, compared to the [bmim][BF_4] + DCM and [emim][$EtSO_4$] + DCM systems (see sections 4.2.1 and 4.2.2). The observed value is slightly higher than observed with conductance methods ($K_{\mathrm{A}}^{0} = 6.2\,\mathrm{L\,mol^{-1}}$),[258] but since association of [bmim][Cl] is very weak in water, the K_{A}^{0} values obtained with both experimental techniques most likely have higher uncertainties than the statistical errors.
In general, [bmim][Cl] is less associated than the corresponding Br^- salt.[261] The present results might contradict the interpretation by Koga *et al.*,[262,263] who conclude from thermodynamic measurements on $[bmim]^+$-containing ionic liquids in water that cations and anions start to interact at $x_{\mathrm{IL}} \gtrsim 0.015$. The present study rather suggests that most of the ion-pairs are re-dissociated at this threshold. Interestingly, the same group observes increasing diffusion coefficients up to $x_{\mathrm{IL}} = 0.0019$ and a decrease at higher IL concentrations for [bmim][Br] in water.[264] This observation is in line with the present observations that at $x_{\mathrm{IL}} \gtrsim 0.015$ less association to discrete ion-pairs is detected.

Concluding remarks

Dielectric spectra of dilute [bmim][Cl](aq) solutions were recorded at frequencies ranging from 200 MHz to 89 GHz. Detailed analysis revealed two different contributions to the spectra, a lower-frequency contact ion pair mode and the main water relaxation at ~ 20 GHz. Quantitative analysis yielded the total ion pair concentration, c_{CIP}. The extrapolated association constant at infinite dilution is in reasonable agreement with values obtained from conductance measurements.
The apparent water concentration obtained from analysis of the main relaxation mode reproduces the analytical water concentration almost perfectly. Consequently, no stable hydration shells for the $[bmim]^+$ as well as for Cl^- can be detected by means of DRS, i.e. the residence time of a water molecule in the hydration shell of an ion is shorter than ~ 10 ps. This finding is verfied by a recent MD simulation,[265] observing a mean residence time of ~ 2.5 ps for water in the hydration shell of $[bmim]^+$. Nevertheless, water dynamics are slightly decelerated, as x_{IL} increases.
Although the cation has a dipole moment, no separate relaxation process due to free $[bmim]^+$ was observed. Assuming $\mu_{\mathrm{eff},[bmim]^+} = 4.4$ D, similar to the dipole moment observed in section 3.2.1, the amplitude of the free cations can be estimated with eq. 1.69. The resulting amplitude of this hypothetical mode increases linearly from 0 to ≈ 2 at the highest concentration of this study. Thus, the cation mode will be difficult to detect, if the contribution to the dielectric spectra due to the cation are overlapped by other modes. Nevertheless, contributions of free cations to the ion-pair amplitude S_1 of the present study could possibly be the reason for the somewhat higher K_{A}^{0} values of this work compared to results from a conductance study.[258] Also the presence of an unresolved "slow water" mode (see below) might bias the association constants slightly.

[§]Because other experimental techniques cannot directly access c_{CIP}, extrapolation is performed based on the nominal ionic strength, $I = c_{\mathrm{IL}}$, and not on basis of the exact ionic strength $I = c_{\mathrm{IL}} - c_{\mathrm{CIP}}$.

4.3.2 [Rmim][BF_4] + H_2O

Probably the most frequently studied aqueous systems are BF_4^--containing RTILs mixed with water, despite some undesirable properties of these systems, like e.g. hydrolysis of the anion (see section 2.1.2).[76]
Beside a fair number of spectroscopy studies,[256,266–270] insight into these systems has been gained by scattering techniques.[267,271] One of the latter studies found structural inhomogeneities from small angle neutron scattering,[271] which is supported by surface tension measurements,[272] observing aggregation of IL in water above a critical aggregation concentration. Infrared studies indicate the aggregation of the alkyl chain, while the stretching vibrations related to the imidazolium ring are mainly affected by D_2O in [bmim][BF_4]+D_2O.[270] Interestingly, Jeon *et al.*[256] come to the exactly opposite conclusion for [bmim][BF_4]+H_2O, namely that the peak positions of the terminal CH_3 vibrations are shifted considerably, while the other C-H modes remain rather unaffected. However, in the latter study the system [bmim][BF_4]+H_2O is investigated. Since it is unlikely that the different findings are due to the substitution of H_2O for D_2O, it is probably an effect of overlapping bands for the [bmim][BF_4]+H_2O system. As can be seen in Ref. 256, the C-H stretching vibrations are strongly overlapped by the O-H stretching mode which makes the determination of the peak position more uncertain.
Studies of the water libration bands[266] indicate a strong anion dependence on the peak position. The authors interpret their results in terms of a less hindered libration of the water molecule in ILs. However, this effect might arise as well from different weighting of the two librational modes of water in ILs, which was not accounted for in this study (cf. Ref. 266 and appendix A.2). On the other hand the finding of freer water rotation at $0. \leq x_{H_2O} \leq 0.3$ is supported by activation energy of rotational correlation times obtained from a ^{2}H-NMR relaxation study,[267] although the correlation times are much slower than for neat water. However, the molecular origin of libration and rotational diffusion is different and the observed effects do not necessarily coincide.
To gain more insight into the dynamics and structural properties of these mixtures, dielectric spectra in the frequency range $0.2 \lesssim \nu/\mathrm{GHz} \leq 89$ at 25 °C of the tetrafluoroborate (BF_4^-) salts of 1-*N*-ethyl-3-methylimidazolium ([emim]$^+$), 1-*N*-butyl-3-methylimidazolium ([bmim]$^+$), and 1-*N*-hexyl-3-methylimidazolium, ([hmim]$^+$) mixed with water are reported in this section.

Experimental details

It is well known, that BF_4^- is prone to hydrolysis[273,274] with one of the reaction products being HF. As mentioned in section 2.1.2, the half-life time of the pseudo first-order reaction was determined to $\tau \approx 1.2$ d. Therefore special care was taken, and measurements were always performed within ~ 2 h after sample preparation.
While [emim][BF_4] and [bmim][BF_4] are miscible with water over the whole composition range at room temperature ([bmim][BF_4]+ water shows a upper critical solution temperature of ~ 5 °C),[274,275] the [hmim][BF_4]+water system exhibits a considerable miscibility gap at 25 °C.[274] In order to accurately determine the solubility limits at 25 °C, conductivities of a series of compositions at closely spaced intervalls were determined. Subsequently, the

conductivities of the saturated water-rich and IL-rich phases were determined and extrapolated to the equilibrium compositions, yielding separation compositions of $x_{\mathrm{IL}} = 0.0050$ and $x_{\mathrm{IL}} = 0.2750$. The procedure is described in detail elsewhere.[76]
For all mixtures, $\hat{\varepsilon}(\nu)$ was determined in the frequency range $0.2 \lesssim \nu/\mathrm{GHz} \leq 89$ (HP8720D VNA setup + A & E-band interferometer, section 2.3). For [emim][BF_4] + water and [bmim][BF_4] + water raw VNA data were obtained using air, mercury and water as primary calibration standards. Calibration errors were corrected with a Padé approximation using pure propylenecarbonate, dimethylacetamide, benzonitrile, and 1-butanol as secondary standards (see section 2.3.3). In the case of [hmim][BF_4] + water the water rich solutions were measured using water, mercury and air as primary calibration standards. Since the dielectric properties of the samples were close to that of water no secondary calibration was performed. For the IL-rich samples, DMA was used for primary and additionally benzonitrile and 1-butanol for secondary calibration. All dielectric measurements were performed at $(25.00 \pm 0.05)\,^{\circ}\mathrm{C}$. Typical experimental spectra with a precision of 1-2 % are displayed in Figure 4.20.
Mixture densities, ρ, and electrical conductivities, κ, required for data analysis were additionally determined (see section 2.4) and are summarized in table 4.6.

[emim][BF_4] + water and [bmim][BF_4] + water

Superpositions of up to five modes were tested to model the experimental spectra of the two systems exhibiting no miscibility gap. A superposition of four Debye equations yielded the lowest χ^2_{r} values and a smooth variation of the parameters with composition. All other models tested, including asymmetrical (Cole-Davidson) or symmetrical (Cole-Cole) broadened modes resulted in physical meaningless parameters (e.g. $\alpha < 0$).

Table 4.6: Mole fraction, x_{IL}, molar concentration, c_{IL}, measured densities, ρ, and electrical conductivities, κ, of [Rmim][BF_4] + water mixtures at 25 °C.[a]

x_{IL}	c_{IL}	ρ	κ	x_{IL}	c_{IL}	ρ	κ	x_{IL}	c_{IL}	ρ	κ
[emim][BF_4] + water				[bmim][BF_4] + water				[hmim][BF_4] + water			
0	0	997.05[b]	-	0	0	997.05[b]	-	0	0	997.05[b]	-
0.004747	0.2534	1007.69	1.874	0.005055	0.2669	1007.00	1.720	0.001429	0.07778	999.52	0.5671
0.01001	0.5144	1018.31	3.259	0.008753	0.4471	1013.47	2.467	0.002927	0.1568	1002.63	1.049
0.02227	1.052	1040.22	5.347	0.01927	0.9018	1030.78	3.592	0.004471	0.2356	1005.24	1.411
0.03638	1.572	1061.36	6.805	0.03304	1.391	1047.81	4.464	0.3141	3.806	1116.76	1.829
0.05734	2.200	1087.31	8.078	0.04970	1.867	1065.19	4.900	0.3813	3.962	1122.43	1.456
0.08104	2.761	1110.93	8.839	0.07387	2.400	1084.47	5.165	0.5139	4.170	1130.58	0.8984
0.1150	3.376	1136.45	9.240	0.1053	2.910	1103.47	5.214	1	4.512	1146.34	0.1228
0.1740	4.122	1168.60	9.075	0.1567	3.482	1124.77	4.926				
0.2565	4.790	1198.61	8.132	0.1991	3.810	1137.31	4.548				
0.4190	5.532	1233.28	5.987	0.2825	4.247	1154.46	3.710				
1	6.484	1283.70	1.553	0.4141	4.656	1171.08	2.566				
				0.4960	4.815	1177.86	2.036				
				0.5757	4.946	1183.94	1.574				
				0.6845	5.078	1190.14	1.098				
				0.7613	5.150	1193.53	0.846				
				0.8954	5.253	1198.74	0.527				
				1	5.319	1202.19	0.353				

[a] Units: c_{IL} in $mol\,L^{-1}$; ρ in $kg\,m^{-3}$; κ in $S\,m^{-1}$. [b] Taken from Ref. 114.

As became apparent from the previous sections (neat ILs, section 3; IL + DCM, sections 4.2.1 and 4.2.2), the main relaxation in the neat ILs is described by a symmetrically broadened Cole-Cole equation. Therefore, the finding that for IL mixtures with water a four Debye model was always superior to others containing a Cole-Cole mode is surprising. This means that no smooth transition in the dielectric relaxation parameters to the pure IL is observed. This might be a reflection of the quality of the data, since it is an experimental challenge to measure accurate spectra for such an large range in dielectric properties (e.g. the static permittivity is ranging from ~ 15 to ~ 78). Additionally, the high conductivities decrease the accuracy of the spectra. The parameters obtained with the 4 Debye (4D) fit are summarized in table 4.7. Typical dielectric permittivity and loss spectra of [bmim][BF_4] + water spectra are displayed in fig. 4.20.

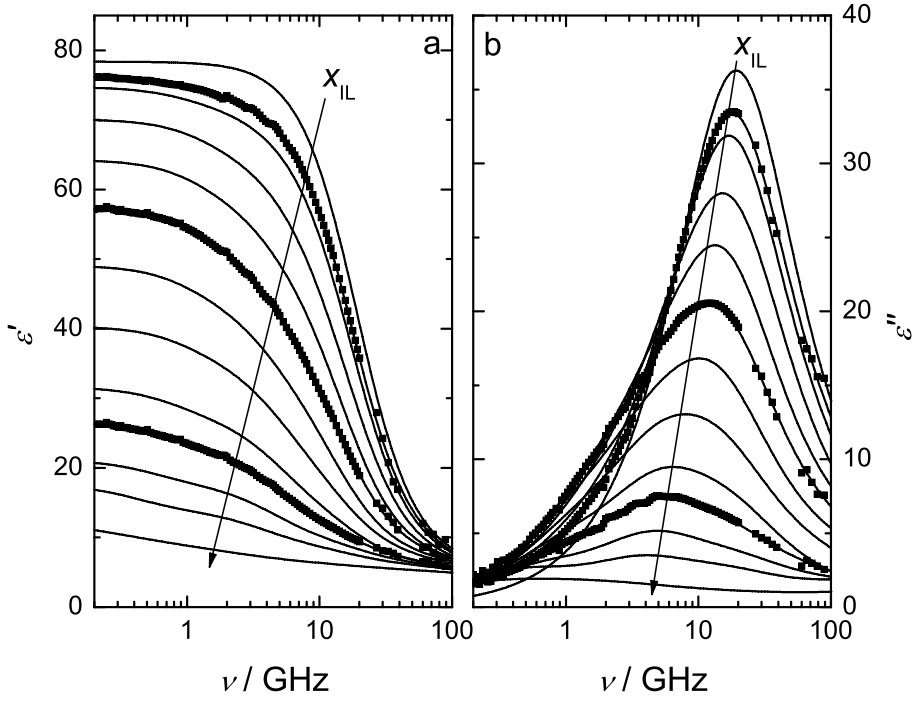

Figure 4.20: Dielectric permittivity (**a**), ε', and dielectric loss (**b**), ε'', spectra of [bmim][BF_4] + H_2O mixtures at 25 °C. Lines correspond to fit with a 4D model, symbols represent experimental data (other omitted for visual clarity. Arrows indicate increasing x_{IL})

Water relaxation As mentioned above, no smooth transition in relaxation parameters from RTIL to aqueous solutions can be observed, which is probably a reflection of closely overlapping bands and experimental problems in covering such a large range of dielectric properties. Nevertheless, the relaxation parameters obtained where water is the dominant species can be interpreted.

Water exhibits at room temperature two relaxation contribution to its spectrum at $\nu \leq 89\,\mathrm{GHz}$ (see appendix A.2). The main relaxation ($\tau \approx 8.3\,\mathrm{ps}$) is associated with the

Table 4.7: Fit parameters of eq. 1.61 for the observed DR spectra of mixtures of [Rmim][BF_4] with water at 25 °C assuming a superposition of 4 Debye equations: static permittivities, ε; relaxation times, τ_j, and amplitudes, S_j, of process j, and reduced error function of the overall fit, χ^2_r.[a]

x_{IL}	ε	τ_1	S_1	τ_2	S_2	τ_3	S_3	τ_4	S_4	$\chi^2_r \cdot 10^4$
[emim][BF_4] + H_2O										
0[b]	78.37	-	-	-	-	8.25	72.27	0.50	2.02	-
0.004747	76.42	178	2.07	41.8	0.86	8.62	67.32	0.27	5.69	780
0.01001	74.14	165	2.43	38.7	2.69	9.06	61.84	0.50[c]	6.89	546
0.02227	68.95	203	2.61	29.2	8.32	9.32	51.20	0.69	3.70	500
0.03638	62.79	243	2.38	28.5	11.04	9.88	42.07	1.41	2.50	418
0.05734	54.98	279	2.31	24.4	16.54	9.51	29.22	0.81	3.62	477
0.08104	47.72	378	2.49	25.3	15.56	10.22	22.50	0.91	3.79	249
0.1150	38.75	332	1.61	24.3	15.85	10.26	13.62	1.66	3.07	407
0.1740	30.03	455	1.90	24.0	14.94	7.33	6.55	1.22	2.06	249
0.2565	21.85	505	0.70	27.0	10.11	6.59	4.72	1.00	1.62	210
0.4190	15.92	471	0.58	30.6	5.92	5.02	3.52	0.53	2.12	128
[bmim][BF_4] + H_2O										
0[b]	78.37	-	-	-	-	8.25	72.27	0.50	2.02	-
0.005055	76.34	284	1.38	68.5	2.57	8.96	65.39	1.00[c]	3.42	700
0.008753	74.73	153	3.03	38.6	3.83	9.16	61.07	1.10	2.45	368
0.01927	70.08	109	5.47	24.1	11.46	9.12	46.57	1.00[c]	2.18	526
0.03304	64.25	124	5.57	36.2	10.07	10.49	41.72	0.87	3.54	391
0.04970	57.34	116	6.57	30.4	13.59	10.36	30.09	1.00[c]	3.30	242
0.07387	49.09	145	5.47	37.0	12.33	11.54	24.29	1.01	3.23	361
0.1053	40.33	147	5.14	32.0	14.15	10.54	14.15	1.35	2.35	173
0.1567	31.61	190	4.65	31.6	12.77	8.82	8.39	1.00[c]	0.60	232
0.1991	26.58	217	3.99	33.1	10.83	8.63	5.73	1.36	1.58	112
0.2825	21.15	280	3.76	35.4	7.84	7.36	3.51	1.06	2.07	73
0.4141	17.62	384	3.96	42.0	4.94	8.51	2.81	0.83	2.83	49
0.4920	16.26	431	3.98	43.7	4.29	7.37	2.16	1.03	2.22	18
0.5750	14.86	418	3.41	47.7	3.71	8.03	1.90	1.12	2.15	14
0.6839	13.45	369	2.87	52.8	3.13	8.96	1.63	1.12	2.24	11
0.7594	12.70	333	2.73	53.8	2.81	8.36	1.50	1.02	2.20	9
0.8931	12.10	355	2.90	58.2	2.39	8.60	1.26	1.05	2.10	11

[a] Units: τ_j in ps. [b] Parameters taken from appendix A.2. [c] Parameter fixed during fitting procedure.

collective rearrangements of the three dimensional hydrogen-bonded network of water, while the fast component ($\tau \approx 0.5$ ps) has considerable translational contributions (see appendix A.2). The main relaxation is also observed for [emim][BF_4] + H_2O and [bmim][BF_4] + H_2O (τ_3, S_3 in table 4.7). As for pure water, a fast component is observed (τ_4, S_4 in

table 4.7), that is obviously dominated by the fast component of water at low x_{IL}, while contributions from the ILs can be expected for high x_{IL} (see section 3).
The relaxation time of the fast water component, τ_4, is rather unaffected by the IL (table 4.7) and also the amplitude is essentially constant, given that this mode is occurring close to the high frequency limit of the present study. Hence, this mode will not be discussed in detail. However, studies of neat ILs (see section 3) show several high frequency modes, which will contribute to the observed mode 4, especially at high x_{IL}.
As becomes apparent from table 4.7, for both IL + H_2O systems the relaxation time of the main water dispersion τ_3 increases from 8.25 ps in pure water to $\sim$ 10.5 ps at $x_{\mathrm{IL}} \approx 0.1$. Increasing the IL concentration further, the relaxation time drops to the value of pure water and remains rather constant. Interestingly, the abrupt decrease in relaxation time coincides with the composition of $w_{\mathrm{IL}} \approx 0.5$ where the upper critical solution temperature for [bmim][BF_4] + water is observed[275] indicating structural changes within the mixtures. Quantitative analysis of the amplitude S_3 using the solvent normalized[¶] Cavell equation (eq. 1.69) reveals that mode 3 cannot reproduce the analytical concentration of water. However, assuming mode 2 also to be due to water, i.e. taking S_2+S_3 to be the total water amplitude, gives almost exactly the analytical water concentration (fig. 4.21a) at $x_{\mathrm{IL}} \lesssim 0.3$. At even higher IL content this is not the case, suggesting contributions from other (IL-related) modes. This means that in the present mixtures two water species are present, namely bulk-like water (mode 3) and slow water (mode 2). A separation of the water process has already been observed in other systems,[251,276,277] mainly for solutes with hydrophobic moieties. The slowing down of certain water dynamics seems to be more pronounced in the present mixtures than in the [bmim][Cl] + H_2O system, where a slow water process could not be resolved, suggesting that the hydration of the anion is also relevant for this process.
As can be seen in fig. 4.21 the relative amplitude of mode 2, $S_2/(S_2 + S_3)$, corresponding to the fraction of slow water, increases considerably until $x_{\mathrm{IL}} \approx 0.3$, suggesting that at this mole fraction more than 2/3 of water is present as slow water molecules. At higher IL concentrations this ratio remains constant. However, as mentioned above, here other IL-related modes are contributing, and the relative amplitude is not representing the fraction of slow water molecules anymore. The relaxation time of the slow water molecules $\tau_2 \approx 40$ ps is roughly comparable to that observed for tetraalkylammonium salts.[251] The apparent concentration of slow water molecules, $c_{\mathrm{app}}^{\mathrm{slow}}$, can be obtained by inserting S_2 into the solvent normalized Cavell equation (eq. 1.69). In analogy to the irrotationally bound hydration numbers, Z_{ib} (eq. 4.5), a slow hydration number, $Z_{\mathrm{slow}} = c_{\mathrm{app}}^{\mathrm{slow}}/c_{\mathrm{IL}}$, can be obtained. These Z_{slow} values are not a simple function of composition and are decreasing from $\sim$ 10 at infinite dilution to $\sim$ 2 at $x_{\mathrm{IL}} = 0.2$. This strong decrease in combination with the absence of such a process for [bmim][Cl] in H_2O (see above) may hint at the formation of water clusters rather than weak solvation of the ions. The presence of water clusters was also inferred from MD simulations and NMR measurements.[278] However, the formation of structured water around the alkyl chain[270] might also be the origin of the slow water mode.

[¶] μ_{eff} for water is obtained from the relaxation parameter of pure water given in appendix A.2. Slip boundary conditions for kinetic depolarization are assumed.[253,254]

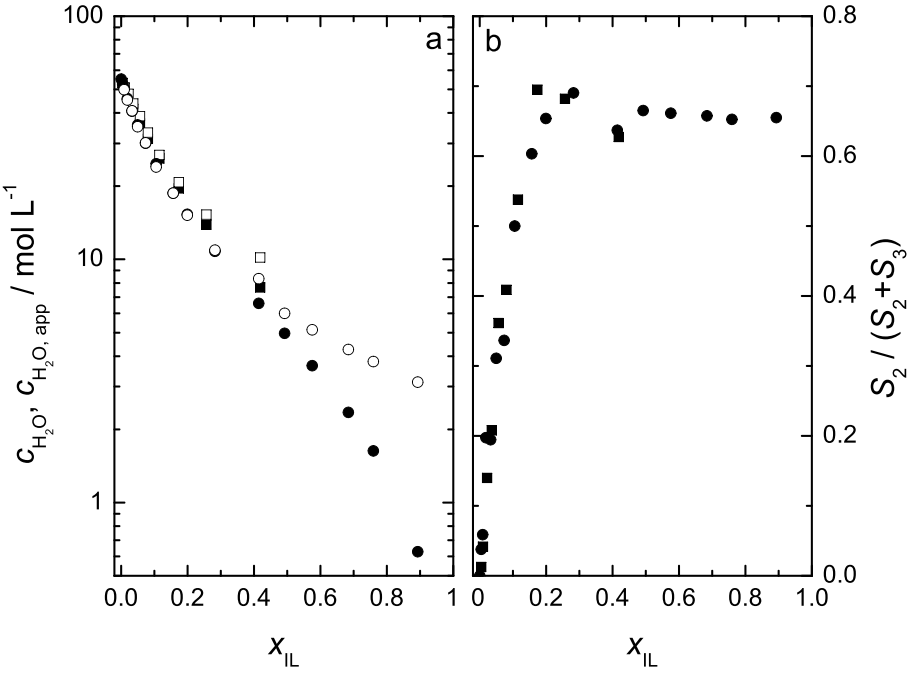

Figure 4.21: (**a**) Analytical water concentration, c_{H_2O} (closed symbols), and apparent water concentration, $c_{H_2O,app}$ obtained by inserting $S_2 + S_3$ into eq. 1.69 for [emim][BF_4] + H_2O (squares) and [bmim][BF_4] + H_2O (circles) at 25 °C. (**b**) Relative amplitude, $S_2/(S_2 + S_3)$ corresponding to the fraction of slow water in [emim][BF_4] + H_2O (■) and [bmim][BF_4] + H_2O (●).

On the other hand, inserting the slow water amplitude S_2 into eq. 1.69 at $x_{IL} \approx 0.4$ produces values of $c_{H_2O,app}$ that are only slightly higher than the analytical water concentration, c_{H_2O}. Hence, it is very likely that above this threshold mode 2 is dominated by slow water and has few IL-related contributions, while mode 3 is mainly due to IL relaxations.

These findings collectively suggest that in the range $0.2 \leq x_{IL} \leq 0.4$ major changes in the water structure, and thus most likely in the mixture structure are occurring. These structural changes might indicate that the system is in the vicinity of phase separation, which is supported by large concentration fluctuations for the [bmim][BF_4] + H_2O system observed with neutron scattering.[271] The observation of relatively slow water dynamics (compared to bulk water) are also supported by ^{2}H-NMR rotational correlation times.[267]

Ionic liquid relaxations As became apparent above, for most of the compositions the four relaxation processes cannot be assign unambiguously to either IL relaxation or water relaxation. Nevertheless, at low x_{IL} only the lowest-frequency mode (1) seems to be due to the IL. Its amplitude exhibits a steep increase up to $x_{IL} \approx 0.04$, where it reaches a maximum for both systems (table 4.7), but is much less pronounced for [emim][BF_4] + H_2O. At higher IL concentrations S_1 decreases again with indications of a plateau at $x_{IL} > 0.4$, but with considerable scatter.

At $x_{\mathrm{IL}} < 0.1$ the variation in S_1 is pretty similar to the observations for [bmim][Cl] + H_2O, where it could be interpreted in terms of ion-pair formation. Also the relaxation times suggest a similar molecular origin at low IL concentration. However, especially for [emim][BF_4] + H_2O the relaxation strength S_1 is very weak, and the IL appears to be less associated than in [bmim][BF_4] + H_2O. It cannot be excluded that free cations contribute to the lowest frequency mode at low x_{IL}. Additionally, the relaxation parameters of mode 1 exhibit some scatter and therefore a more detailed analysis of this mode is not performed. Attempts to analyze this mode in terms of ion-pairing (CIP) for the dilute solutions of IL in water yielded very weak association ($K_{\mathrm{A}}^0 = 1 \ldots 10\,\mathrm{L\,mol^{-1}}$), but due to the strong overlap of the different bands this value is just a rough estimate.

At higher x_{IL} it appears that only mode 2 is dominated by water relaxation and the remaining modes (1, 3, and 4) are IL-related. Since it is rather unlikely, that the relaxation mechanism in these mixtures in the IL-rich region is different from that observed in the pure IL, this might be a reflection of problems in resolving the IL modes properly. One might speculate that this model is mimicking a broadened IL relaxation, with a contribution of water with $\tau \approx 40\,\mathrm{ps}$. Again, detailed analysis of these modes at high x_{IL} is not justified due to these uncertainties.

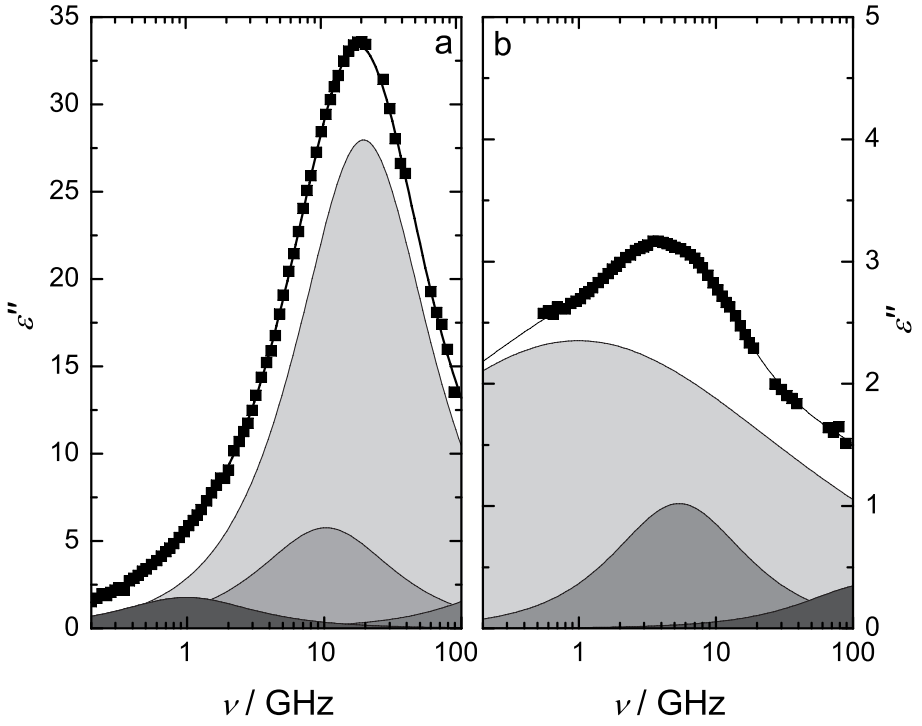

Figure 4.22: Dielectric loss spectra, ε'' of a water-rich (**a**, $x_{\mathrm{IL}} = 0.004471$) and a IL-rich (**b**, $x_{\mathrm{IL}} = 0.3813$) [hmim][BF_4] + water mixture at 25 °C. Symbols correspond to experimental data, lines represent fits with the 4 Debye and CC + D + D models, respectively. Shaded areas correspond to the individual process contributions.

[hmim][BF_4] + water

For the system [hmim][BF_4] + H_2O, a relatively broad mixing gap is observed at 25 °C. Hence, the structural features, inferred from the studies of [bmim][BF_4] and [emim][BF_4] in water (that probably lead to the phase separation) might be more pronounced than in the systems with an upper critical solution temperature below ambient temperature. Because of this and the slower dynamics of pure [hmim][BF_4] compared to [bmim][BF_4] a more reliable resolution of the overlapping bands can be expected.

Table 4.8: Fit parameters of eq. 1.61 for the observed DR spectra of mixtures of [hmim][BF_4] with water at 25 °C assuming a superposition of 4 Debye equations for the water-rich mixtures and a CC + D + D model for the IL-rich mixtures: static permittivities, ε; relaxation times, τ_j, Cole-Cole shape parameter, α, amplitudes, S_j, of process j, and reduced error function of the overall fit, χ^2_r.[a]

x_{IL}	ε	τ_1	α	S_1	τ_2	S_2	τ_3	S_3	τ_4	S_4	$\chi^2_r \cdot 10^4$
0[b]	78.37	-	-	-	-	-	8.25	72.27	0.49	2.02	-
0.001429	78.00	197	-	1.36	26.2	0.54	8.63	69.35	0.68	3.50	763
0.002927	77.76	177	-	2.54	17.5	3.52	8.80	62.46	3.76	3.85	262
0.004471	77.37	161	-	3.54	15.4	11.52	8.21	55.93	0.51	5.31	509
0.3141	26.63	359	0.68	21.46	27.6	2.89	-	-	2.49	0.32	3.70
0.3813	19.98	160	0.60	14.50	29.5	2.04	-	-	1.18	0.72	4.39
0.5139	14.37	101	0.45	9.03	29.1	0.75	-	-	1.17	1.31	2.99
1[c]	12.00	451	0.54	7.87	-	-	-	-	0.44	1.95	-

[a] Units: τ_j in ps; [b] Parameters taken from appendix A.2. [c] Parameters taken from section 3.2.1.

Water-rich solutions The spectra of water-rich [hmim][BF_4] + H_2O mixtures were best described by a superposition of four Debye processes, in accordance with the aqueous [emim][BF_4] and [bmim][BF_4] solutions. The parameters obtained are listed in table 4.8. The four processes can be assigned in the same way as for the previous systems (fig. 4.22a). The lowest frequency process (τ_1, S_1) is due to an IL-related relaxation, because the relaxation times correspond to the observed τ_1 values of the previous systems. Inserting the analytical IL concentration, c_{IL}, and the amplitude S_1 into the Cavell equation (eq. 1.69) yields a rather constant effective dipole moment of $\mu_{eff,1} = (13.3 \pm 0.5)$ D, close to the value of the [hmim]$^+$-cation obtained from semiempirical MOPAC calculations ($\mu = (10.2 \pm 4.5)$ D, see section 2.5). However, the experimental value appears to be higher than just the cation dipole moment and the presence of ion-pairs might explain this discrepancy. Additionally, the slow relaxation times $\tau_1 \approx 200$ ps might indicate ion-pair contributions, which in turn can cause the discrepancy in the dipole moments. It is interesting to note that τ_1 is decreasing with increasing x_{IL}. On the one hand, the kinetics of the ion-pair formation can lead to a decrease in τ_1 if the relaxation time and the life-time of an ion-pair are similar.[279] On the other hand, because in this case two species (cations and ion-pairs) might contribute to

the observed relaxation process, the variation in τ_1 can also originate in different relative contributions of these two species. Based on the restricted concentration range, limited by the solubility of [hmim][BF_4] in water, more detailed conclusions cannot be drawn from the lowest frequency mode.
The remaining modes are assigned to water relaxations. According to the previous systems, a slow water mode can be separated ($\tau_3 \approx 20\,\mathrm{ps}$). Combination of the slow water mode and the bulk water mode (mode 3) can again reproduce the analytical water concentration (using the solvent-normalized Cavell equation and assuming slip boundary conditions for kinetic depolarization[253,254]). As observed for [bmim][BF_4] + H_2O, the fraction of slow water, represented by $(S_2/(S_2 + S_3))$ increases with increasing x_{IL}. However, while Z_{slow} decreases with increasing x_{IL} for [bmim][BF_4] + water, for [hmim][BF_4] + water a linear increase up to $Z_{\mathrm{slow}} \approx 40$ is found for the highest aqueous solution of [hmim][BF_4]. This finding again suggests, that the presence of slow water molecules is not due to hydration of the ions but more likely due to formation of water clusters in these systems. Based on the restricted range of compositions for the aqueous solutions, the parameters suggest a slight increase in τ_3. Hence, also the bulk water dynamics might be slowed slightly.
Parameters for the highest frequency process scatter considerably, but the amplitude S_4 appears to increase slightly. Due to the proximity of this mode to the high frequency limit of this study, further analysis is not performed.

IL-rich solutions As noted above, the overall dynamics for pure [hmim][BF_4] are slower than for [bmim][BF_4] and [emim][BF_4]. Therefore contributions of the IL and of water could be resolved more reliably. This results in a different relaxation model for the IL-rich [hmim][BF_4] + H_2O mixtures, compared to the [bmim][BF_4] + water mixtures. Spectra of IL-rich mixtures were best described by a lower frequency Cole-Cole equation and two higher frequency Debye modes (fig. 4.22b). The parameters obtained using the CC+D+D model are summarized in table 4.8. However, for these mixtures the choice of the relaxation model is not unambiguous (i.e. a D+CC+D and a CC+CC+D model gave equally good fit qualities). Neither of these models could be quantitatively interpreted in a physically meaningful way, but gave qualitatively the same conclusions. These problems are probably a reflection of difficulties in separating other contributions from the broad IL relaxation (fig. 4.22). As can be seen in table 4.8, this results in a considerable scatter in the parameters for the IL-rich mixtures.
The relaxation times of the lower-frequency Cole-Cole mode (τ_1) and the higher frequency Debye mode (τ_4) are comparable to those observed in neat [hmim][BF_4] (table 4.8). Thus, they can be assigned to IL relaxation. However, especially the great scatter in the Cole-Cole broadness parameter, α, and in τ_1 reflects the problems in resolving this mode. Although the IL contribution and the water mode are well separated in time-scale ($\tau_1/\tau_2 \approx 10$), the broadness of this mode results in considerable contributions at higher frequencies, making it difficult to resolve the two modes, as can be seen from fig. 4.22b.
Nevertheless, despite the uncertainties in the choice of the relaxation model, it is obvious that a new process is emerging at $\sim 5\,\mathrm{GHz}$, when water is added to the IL. All of the different relaxation models, which gave similar fit qualities, yielded with a relaxation time of$\tau_2 \approx 30\,\mathrm{ps}$ for this process however, only a reliable determination of the amplitude

is not possible. Hence, it is unambiguous that this emerging relaxation mode is due to water. The relaxation time coincides with the slow water mode observed in the aqueous mixtures above. This supports the interpretation of this slow water mode being due to water clusters, suggesting that for the investigated [hmim][BF_4] + water mixtures, structural inhomogeneities are present. As noted above, the uncertainties in the amplitudes are very high so quantitative analysis of the amplitudes is not justified.

Concluding remarks

Aqueous mixtures of [Rmim][BF_4] were studied over the accessible composition range. Especially for the IL-rich mixtures, spectral overlap prevented a reliable resolution of the different bands. Nevertheless, the spectra reveal that the water process has a relaxation time of $\sim 30\,\mathrm{ps}$ in the IL-rich mixtures, which is about 4 times slower than in neat water. This is in agreement with a recent NMR study.[267] The data suggest that the IL modes are comparable to those observed in the neat IL.
For the diluted solutions the water relaxation splits into a slow water and a bulk-like component. In the literature different explanations for the slowing down of some water molecules have been given. On the one hand, it might be due to the formation of a more rigid water structure around the alkyl chains of the cation.[269,270] On the other hand, the presence of water clusters could lead to an increase in relaxation time.[278] Although the viscosity of the mixtures increase considerably with increasing x_{IL},[280] in IL-rich solutions the water mode is found at similar frequencies. This suggests the presence of water clusters with microscopic viscosities, differing from the bulk viscosity. Moreover, taking the ratio of water to IL molecules at high x_{IL} into account, it is unlikely alkyl chains of the cations are specifically hydrated.
All these findings reveal considerable structural changes at compositions where the upper critical solution temperature for [bmim][BF_4] is observed.[274,275] Such structural inhomogeneities in a system being in the vicinity of phase separation are also observed with scattering techniques[271] and might be reflected in the surface tension of the systems.[272] The present study suggests that these structural changes occur when no bulk water remains.

4.4 Binary mixtures RTIL + dimethylsulfoxide / propylene carbonate

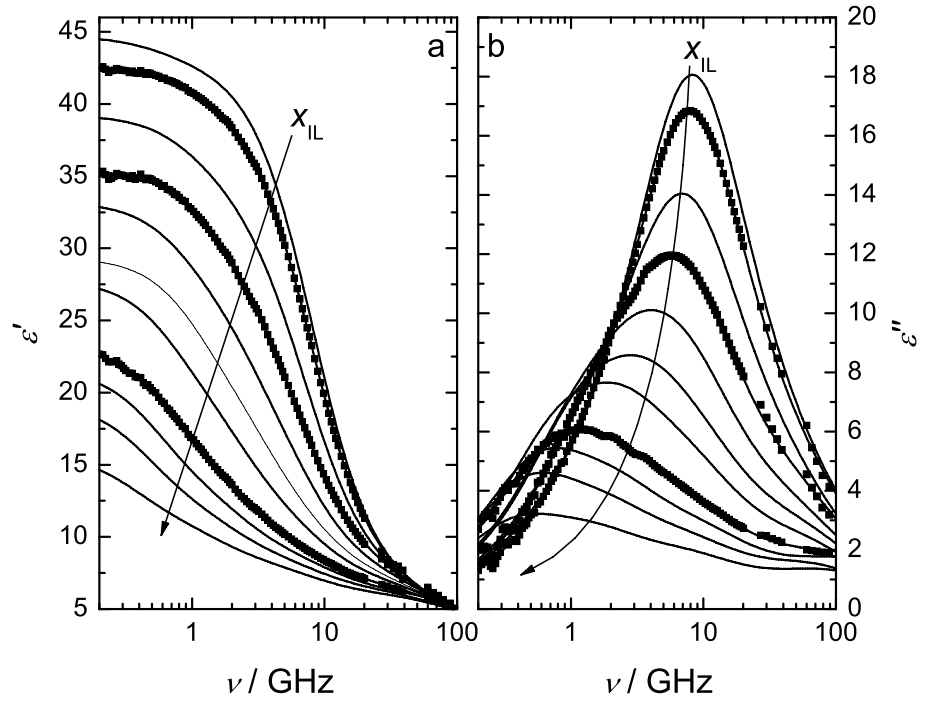

Figure 4.23: (**a**) Dielectric permittivity, ε', and (**b**) dielectric loss spectra, ε'' of [bmim][BF_4] + dimethylsulfoxide mixtures at 25 °C. Lines represent fits with a 4 Debye model, symbols represent experimental spectra (other omitted for visual clarity). Arrows indicate increasing IL concentration..

To study the effect of solvent polarity and ionizing properties, binary mixtures of [bmim][BF_4] with propylene carbonate and dimethylsulfoxide were studied. For all mixtures, $\hat{\varepsilon}(\nu)$ was determined in the frequency range $0.2 \lesssim \nu/\text{GHz} \leq 89$ (HP8720D VNA setup + A & E-band interferometers, section 2.3). Raw VNA data were obtained using air, mercury and the pure solvent (DMSO, PC) as primary calibration standards. Calibration errors were corrected with a Padé approximation using pure dimethylacetamide, benzonitrile, and 1-butanol as secondary standards (see section 2.3.3). All dielectric measurements were performed at (25.00 ± 0.05) °C. Typical experimental spectra for [bmim][BF_4] + DMSO mixtures are displayed in Figure 4.23. The corresponding densities and conductivities are summarized in table 4.9.

As for the data presented in the previous section, detailed analysis of the dielectric spectra for these mixtures was problematic due to spectral overlaps. Indeed, this situation was even worse for the mixtures of ILs with dimethylsulfoxide and propylene carbonate, since both have slower relaxation times than water[95,96] (fig. 4.24). Moreover, the two solvents exhibit an asymmetrically broadened main relaxation.[95,96]

The rather complicated dynamics of these solvents together with the slow relaxation times exacerbate the problems of reliable resolution of IL and solvent modes, as described in the previous section. The loss spectra of the present binary mixtures are very broad and rather featureless (fig. 4.23) and no physically meaningful description could be obtained for any of the investigated mixtures. Nevertheless, the spectra could be modelled with a superposition of four Debye equations. The parameters obtained are summarized in table 4.9. However, because no physically meaningful interpretation could be obtained, the spectra are just discussed qualitatively. It is emphasized that this model is just a mathematical description of $\hat{\varepsilon}(\nu)$ and the four modes cannot be assigned to specific chemical species.
As can be seen in fig. 4.23 the DMSO relaxation at $\sim 10\,\mathrm{GHz}$ decreases in amplitude as x_{IL} decreases. The spectra suggest that this mode is shifted to lower frequencies, with increasing IL content. This could be a reflection of the likely increase in viscosity, but might be as well as for the aqueous mixtures due to splitting into two contributions (see sections above). At high x_{IL} at least one lower-frequency relaxation is emerging, that can be assigned to IL-related modes. However, the spectra show no smooth variation with composition, and thus one can only speculate if this might be due to the presence of some ion-pair species at very low x_{IL}. Qualitatively, similar behavior is found for [bmim][BF_4] + propylene carbonate is found.

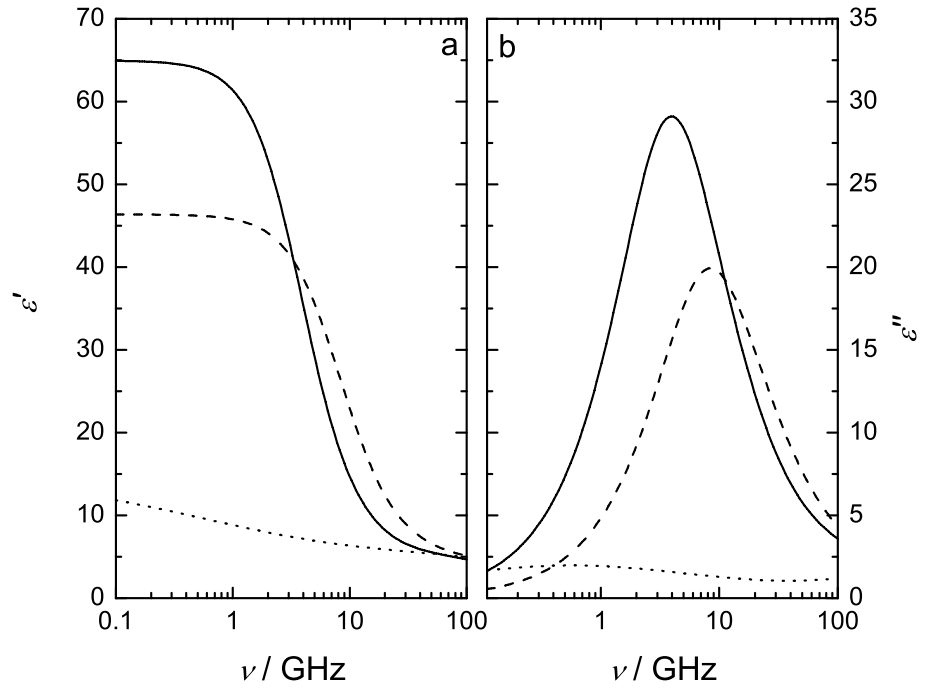

Figure 4.24: (**a**) Dielectric permittivity spectra, ε', and (**b**) dielectric loss spectra, ε'' of propylene carbonate[96] (solid line), dimethylsulfoxide[95] (dashed line) and [bmim][BF_4] (dotted line) at 25 °C.

Table 4.9: Mole fraction, x_{IL}, density, ρ, and electrical conductivity κ together with fit parameters of eq. 1.61 for the observed DR spectra of mixtures of [bmim][BF_4] with PC and DMSO at 25 °C assuming a 4 Debye model: static permittivities, ε; relaxation times, τ_j, S_j, of process j, and reduced error function of the overall fit, χ^2_{r}.[a]

x_{IL}	ρ	κ	ε	τ_1	S_1	τ_2	S_2	τ_3	S_3	τ_4	S_4	$\chi^2_{\mathrm{r}} \cdot 10^4$
[bmim][BF_4] + DMSO												
0.01925	1101.56	0.6869	44.70	252	2.01	40.0[b]	3.5	18.5	32.33	2.91	2.62	56
0.03427	1106.21	1.029	42.56	135	2.75	40.0[b]	2.7	19.1	29.94	2.78	3.00	69
0.07837	1117.80	1.558	39.21	151	4.52	40.0[b]	7.0	19.3	20.06	3.34	3.22	23
0.1247	1128.31	1.715	35.41	105	7.03	40.0[b]	4.9	21.0	15.66	2.81	3.68	124
0.1866	1139.50	1.672	33.19	172	6.32	52.8	9.5	20.1	9.67	2.90	3.31	24
0.2554	1150.71	1.502	29.34	139	9.16	41.9	8.6	16.0	4.32	2.57	3.03	68
0.3251	1159.40	1.310	27.78	211	8.22	62.4	8.0	17.6	4.52	2.41	2.73	24
0.4423	1171.71	1.015	23.18	233	8.02	69.0	5.3	17.2	3.28	1.96	2.63	42
0.5246	1178.20	0.8540	21.60	288	8.29	67.6	4.5	14.5	2.64	1.28	2.72	14
0.6132	1184.27	0.7110	19.29	343	7.23	78.5	3.5	17.9	2.28	2.11	2.22	10
0.7494	1192.13	0.5433	15.77	431	4.76	97.5	2.9	18.9	2.08	1.73	2.13	31
[bmim][BF_4] + PC												
0.02318	1201.32	0.5370	64.96	269	0	41.6	55.9	12.7	3.80	1.11	2.10	37
0.04836	1202.51	0.8728	60.58	180	2.10	44.9	45.8	21.4	6.64	1.99	2.43	27
0.1028	1204.30	1.230	57.04	156	4.57	45.7	42.4	16.1	4.10	2.06	2.14	27
0.1601	1205.43	1.346	51.05	158	8.54	51.2	32.2	17.1	3.96	2.43	2.41	79
0.2277	1206.17	1.332	46.14	169	11.36	57.7	24.5	17.9	3.77	2.13	2.96	18
0.3056	1206.51	1.229	41.34	196	13.72	63.2	17.9	15.8	3.30	2.17	2.52	25
0.4070	1206.44	1.055	36.66	240	14.35	71.7	12.7	16.8	3.14	2.32	2.41	23
0.5126	1206.03	0.8745	31.35	283	13.94	79.7	8.2	17.1	2.83	2.07	2.42	19
0.6192	1205.48	0.7150	26.57	313	12.77	77.0	5.3	16.2	2.31	1.89	2.37	12
0.7173	1204.39	0.5926	21.66	405	10.39	61.5	3.7	11.5	1.75	1.46	2.18	19
0.8497	1203.39	0.4627	18.66	478	7.86	76.9	3.1	15.0	1.70	1.59	2.23	18

[a] Units: ρ in $\mathrm{kg\,m^{-3}}$, κ in $\mathrm{S\,m^{-1}}$, τ_j in ps; [b] Parameter fixed during fitting procedure.

4.5 Conclusions

In this section dielectric relaxation studies of binary RTIL + polar solvent mixtures were presented. For the mixtures with dichloromethane detailed insight into the structures of the systems could be obtained. Especially the smooth transition from electrolyte-like to IL-like behavior as well as detailed information about correlations could be gained.

For aqueous mixtures resolution of different bands was challenging and, especially at intermediate compositions, no meaningful interpretation could be obtained. The mixtures appear at very high x_{IL} as well as at very low x_{IL} to be microscopically inhomogeneous. At intermediate compositions no physical interpretation of the observed relaxation behavior

could be given, which might be a reflection of the fact that some of the systems are in the vicinity of phase separation. However, for inhomogeneous systems additional dielectric modes due to effects like interfacial polarizations[90] can occur that might additionally complicate the spectra of these systems, and thus could contribute to the lower-frequency modes.
For solvents with even slower dynamics (propylene carbonate, dimethylsulfoxide) a meaningful separation of the observed spectra into single species contributions was not possible. Unambiguous resolution of the spectral contributions requires more accurate measurements. Improvement could be achieved with a better mathematical model for VNA probe heads and much higher quality "absolute" (non-VNA) dielectric data for the VNA calibration materials than are currently available. More important, for most of the systems, the lack of accurate data below 200 MHz inhibited a more reliable spectral resolution. Especially, for the IL mixtures this would be a prerequisite to accurately define the lower frequency modes, present in almost all systems investigated. Possibly, design of new cut-off type coaxial cells connected to the vector network analyzer might be able to yield sufficiently accurate low frequency data. Another possible improvement might be achieved with new developments in impedance analyzing equipment. However, this will still be experimentally challenging, because the unfavorable difference between η'' and ε'' at low frequencies will always be present for samples with high dc conductivity.
In addition, enhancement of measurements at high frequencies will better define the higher frequency modes. Thus, THz and far-infrared data would be desirable to more reliable separate the different contributions.

Summary and conclusion

This study reports a detailed investigation of the dynamics and dielectric properties of room temperature ionic liquids (RTILs). Various systems were studied, starting from neat imidazolium-based RTILs, to clarify their dynamics in their pure state. Furthermore, binary mixtures of RTILs with molecular solvents were investigated, which were chosen as model systems for ILs as reaction media and are particularly pertinent to potential technical applications.

Experimental techniques

To cover the broad frequency-range required for a detailed study of the dielectric properties of ILs several new experimental routes were developed. The vector network analyzer (VNA) was connected to the existing waveguide-transmission cells enhancing the sample throughput by a factor of five, compared to the previous interferometric measurements.[91] This setup is yielding accurate, absolute permittivity data at $8 \leq \nu/\mathrm{GHz} \leq 40$. Commercially available open-ended coaxial probes were evaluated over an enhanced frequency range ($0.2 \leq \nu/\mathrm{GHz} \leq 50$) and the calibration procedure was improved. This was achieved by current developments in coaxial techniques and commercial software.

Furthermore, the principle of operation of the VNA connected to cut-off type coaxial cell was proved, and highly accurate data for non-conducting samples could be obtained at frequencies above 50 MHz. This was only achieved by calibrating at the sample interface, while calibration procedures suggested in literature[82] were not successful. However, for electrolyte solutions there is still room for improvement, especially with respect to cell design.

It was shown for a dipolar solvent (dichloromethane), exhibiting rather simple dynamics that the spectra can be extended to THz and far-infrared frequencies without having experimental refractive indices above 2 THz but using Kramers-Kronig transformation. Further, the developed mathematical routines were successfully applied to RTILs.

Neat ionic liquids

The dielectric spectra at $0.2 \lesssim \nu/\mathrm{GHz} \leq 89\,\mathrm{GHz}$ and $5 \leq \theta/^{\circ}\mathrm{C} \leq 65$ revealed that the main mode in RTILs is mostly due to the dipolar cations. However, critical evaluation of the model used previously[30] to fit experimental spectra, produced an alternative, improved description.

Among the investigated samples, the salt 1-ethyl-3-methylimidazolium ethylsulfate was an exception, exhibiting a distinct anion mode in the dielectric spectra. While for all RTILs the study indicates strong correlations and to some extent cooperativity within the pure molten salts, these correlations are much more pronounced in 1-ethyl-3-methylimidazolium ethylsulfate. Despite some earlier expectations,[231,281] none of the studied compounds in neat form provided evidence for the existence of stable ion-pairs with a life-time longer than a few hundreds of picoseconds.

Studies over the limited frequency range previously available ($\nu \leq 89\,\mathrm{GHz}$) indicated that there are even higher-frequency modes present, that were not properly characterized. Hence, the frequency range was expanded to include terahertz and far-infrared frequencies ($\sim 10\,\mathrm{THz}$). This range was sufficient to fully characterize all relevant inter- and intramolecular modes. Although the spectra at these frequencies are rather flat and featureless, they indicate the presence of pronounced intermolecular vibrations and librations, characteristic of the intermolecular interactions occurring among the constituting ions.

Comparison of the broad-band spectra to results from molecular dynamics simulation[170] gave valuable insight into the molecular origin of the modes present in the spectra. On the other hand it was demonstrated, that these *in silico* experiments have their limitations and do not reliably reproduce the dynamics over the wide range of time-scales covered by dielectric spectroscopy.

Comparison of the present dielectric data with optical Kerr effect (OKE) spectroscopy, led to two surprising findings. First, the reorientation of the IL cations occurs via large angle jumps, as predicted by some simulations.[179] Even more surprising was that a huge low frequency mode was present in the OKE spectra, but almost absent in the dielectric spectra. It was attributed to the formation of mesoscopic aggregates, possibly due to pi-stacking within the imidazolium-based ILs. For future studies, the variation of this low frequency OKE mode with temperature might give further insights into the origin.

Binary mixtures RTIL + molecular solvent

Most detailed conclusions could be drawn from mixtures of RTILs with dichloromethane. Probably the most interesting feature of these model systems (for an IL as a reaction medium) was that the mixtures retain their character (insofar as these are reflected in their dynamics and dielectric properties) to surprisingly high levels of dilution ($x_{\mathrm{IL}} \approx 0.3$). Going through a smooth transition, at even higher dilutions the mixtures become rather electrolyte-like solutions, reflected in the formation of ion-pairs. The association constants at high dilutions are rather high and ion-pairs are the dominating species at $x_{\mathrm{IL}} \approx 0.05$. Despite some earlier expectations,[227] no stable solvent-separated ion-pairs, or higher aggregates are detected (life-time $\lesssim 200\,\mathrm{ps}$). The ion-pair contribution to the spectra can be interpreted assuming solely contact ion-pairs. The absence of stable higher aggregates is not surprising, since the charge of the constituting ions of a RTIL is rather delocalized thus being one out of a few prerequisites for a liquid salt at room temperature). Consequently, also the solvation of the ions is only weak.

Furthermore, the mixtures of 1-ethyl-3-methylimidazolium ethylsulfate with dichloromethane allowed the dipolar correlations among the ions to be disentangled, which would not have been possible on the basis of the pure component spectra.

The interpretation of IL + water mixture spectra turned out to be more complicated than anticipated due to strong spectral overlaps. Nevertheless, studies of 1-butyl-3-methyl -imi - dazolium chloride in water demonstrated that the degree of association of this IL in water is much less pronounced than the association of similar RTILs in dichloromethane.

The studies of aqueous mixtures indicated that water is present in two states: "bulk" water and an emerging "slow" water mode at low x_{IL}. Approaching the composition where the systems are in the vicinity of phase separation, the results suggest that almost no "bulk"-like water remains in the mixtures. The analysis of this "slow" water mode indicates clustering of water in the mixtures and heterogeneity can be inferred. At high x_{IL} the spectra suggest that water is solely present as "slow" water, but a reliable separation of the different contributions was not possible due to spectral overlaps. This situation could possibly improve with more accurate low frequency data that would be obtained by utilizing the ongoing developments in impedance analyzing techniques.

For mixtures of RTIL with propylene carbonate and dimethylsulfoxide, the spectral overlaps were even more pronounced and no physically meaningful separation of the spectral contributions could be achieved. Again, this issue could possibly be addressed by more precise low frequency data.

Appendix

A.1 Dielectric response of dichloromethane

For the accurate analysis of the binary mixtures RTIL + dichloromethane, detailed knowledge of the dielectric properties of the molecular solvent was necessary. Therefore dielectric spectra of DCM were determined in the framework of these studies at temperatures ranging from 5 °C to 35 °C, covering the frequency range of $8.5\,\mathrm{GHz} \leq \nu \leq 1\,\mathrm{THz}$. At 25 °C the spectrum was supplemented by THz-TDS transmission data and far-infrared spectra, taken from the literature.[282] Additionally, it is demonstrated that the spectra can be extended to far-infrared frequencies without having experimental refractive indices above 2 THz but using Kramers-Kronig transformation. The study resulted in the following publication:

Johannes Hunger, Alexander Stoppa, Andreas Thoman, Markus Walther, and Richard Buchner *"Broadband Dielectric Response of Dichloromethane" Chem. Phys. Lett.* **2009**, *471*, 85-91.

The following pages contain a reprint of this paper.

Chemical Physics Letters 471 (2009) 85–91

Contents lists available at ScienceDirect

Chemical Physics Letters

journal homepage: www.elsevier.com/locate/cplett

Broadband dielectric response of dichloromethane

Johannes Hunger [a], Alexander Stoppa [a], Andreas Thoman [b], Markus Walther [b], Richard Buchner [a,*]

[a] Institut für Physikalische und Theoretische Chemie, Universität Regensburg, D-93040 Regensburg, Germany
[b] Department of Molecular and Optical Physics, Albert-Ludwigs-Universität Freiburg, D-79104 Freiburg, Germany

ARTICLE INFO

Article history:
Received 17 December 2008
In final form 10 February 2009
Available online 13 February 2009

ABSTRACT

A systematic study of the dielectric response of dichloromethane over a broad frequency range ($8.5 \leqslant \nu/\mathrm{GHz} \leqslant 1000$; $\leqslant 4.3$ THz at 25 °C) at temperatures from 5 to 35 °C is reported. The spectra are best described by a superposition of three contributions. The dominating loss peak at ~70 GHz, fitted by a modified Debye equation accounting for inertial rise, represents the rotational diffusion of molecular dipoles. Additionally, two libration modes contribute, which are described by damped harmonic oscillators of resonance frequencies ~0.9 THz and ~2.1 THz. While the latter modes reflect the anisotropy of the dichloromethane molecule, the diffusive reorientation at long times appears to be rather isotropic.

1. Introduction

Due to its low boiling point (40 °C [1]), high density (1.3266 kg dm^{-3} [1]) and its immiscibility with hydrogen-bonding solvents like water, dichloromethane (DCM, CH_2Cl_2, Fig. 1) is widely used as a solvent in synthetic chemistry and technical applications, especially for separation processes [2]. Being a small molecule with the same C_{2v} symmetry and similar gas-phase dipole moment as water (DCM: $\mu = 1.61$ D [3]; H_2O: 1.85 D [1]) but without the ability to form H-bonds, the structure and dynamics of liquid DCM received considerable attention in the 1980s, when it was selected by the European Molecular Liquids Group as one of the target compounds for a collaborative project on the consistent evaluation of molecular dynamics in liquids [4].

At that time the far-infrared absorption spectrum of pure DCM [5,6] and its mixtures [3] were studied in some detail in the 30—200 cm^{-1} region, albeit with the limited accuracy then accessible. The aim was to gain information on intermolecular vibration and libration motions and to test interaction potentials for computer simulations [7]. However, only a small number of studies [8–10] explored the adjoining microwave to mm-wave frequencies because this region at ~70 GHz, where the main dielectric dispersion occurs [8], was and to some extent still remains difficult to access. To our knowledge the present investigation is the first study that addresses the temperature dependence of the dielectric spectrum of DCM in the GHz to THz region.

Due to its sensitivity to all kinds of dipole fluctuations dielectric spectroscopy (DS) is an efficient tool to study the dynamics and interaction in liquids [11,12]. Like conventional (far-)infrared spectroscopy DS probes the total polarization, $\vec{P}(t)$, of a sample in a time-dependent field, $\vec{E}(t)$, albeit at lower frequencies and thus longer timescales. In DS this response is conventionally expressed in terms of the complex permittivity spectrum, $\hat{\varepsilon}(\nu) = \varepsilon'(\nu) - \mathrm{i}\varepsilon''(\nu)$. The relative permittivity $\varepsilon'(\nu)$ shows a dispersion from the static permittivity, ε, to the high-frequency limit ε_∞. The dielectric loss, $\varepsilon''(\nu)$, expresses the energy dissipation which arises from the coupling of $\vec{E}(t)$ to dipole fluctuations.

In this Letter, we report the dielectric spectra of DCM in the temperature range of 5–35 °C, covering the frequency range of $8.5 \leqslant \nu/\mathrm{GHz} \leqslant 1000$ (0.28—33cm^{-1}). At 25 °C the spectrum was extended up to ~4.3 THz (144 cm^{-1}) by including literature data [5]. A thorough investigation of DCM dynamics appears to be timely because in contrast to previous assumptions [7] recent simulations and cluster calculations showed the importance of the quadrupole moment for the interactions in liquid DCM [13] and indicated a strong contribution of induced dipoles to the far-infrared spectrum [14]. Additionally, existing information on the dynamics of DCM obtained with dielectric/far-infrared [5,6], NMR [15], and Raman [16] spectroscopies is somewhat conflicting. As will be shown below the present data resolve most of these discrepancies and should thus help to improve the existing potential models. Last but not least the proper characterization of $\hat{\varepsilon}(\nu)$ for pure DCM is worthwhile because DCM solutions receive increasing attention in dielectric studies [17–20] and DCM appears to be a suitable standard for the calibration of certain dielectric spectrometers [21].

2. Experimental

Dichloromethane was obtained from Acros Organics, Belgium (analytical grade, >99.99%) and stored over freshly activated molecular sieve (3 Å). Coulometric Karl–Fischer titration yielded a water content of <5 ppm for the investigated sample. Although

* Corresponding author. Fax: +49 941 943 4532.
E-mail address: Richard.Buchner@chemie.uni-regensburg.de (R. Buchner).

0009-2614/$ - see front matter © 2009 Elsevier B.V. All rights reserved.
doi:10.1016/j.cplett.2009.02.024

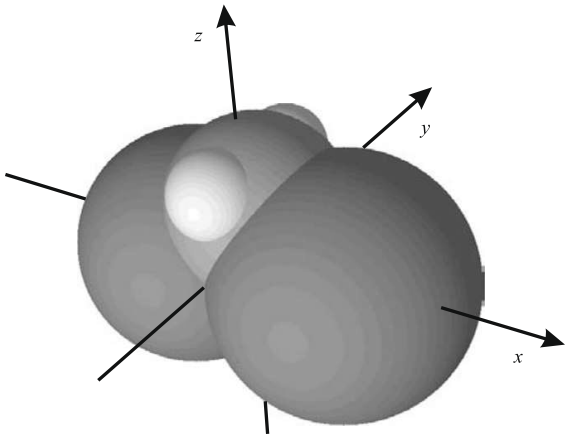

Fig. 1. Dichloromethane with its axes of inertia. Moments of inertia for rotation around x, y and z are $I_x = 2.62 \times 10^{-47}$ kg m^2, $I_y = 25.26 \times 10^{-47}$ kg m^2, and $I_z = 27.37 \times 10^{-47}$ kg m^2 [8]. The dipole moment of magnitude $\mu = 1.61$ D [3] is parallel to the z-axis.

the concentration of 1-pentene, added as a stabilizer to DCM by the manufacturer, was below the detection limit samples were kept at 35 °C for at least 3 h prior to measurements to avoid evaporation of the stabilizer during data collection.

Complex permittivity spectra, $\hat{\varepsilon}(\nu)$, were determined in the frequency range of $8.5 \leqslant \nu/\mathrm{GHz} \leqslant 1000$ by combining data obtained with four waveguide interferometers (IFM) [22] at $8.5 \leqslant \nu/\mathrm{GHz} \leqslant 89$ and a transmission THz-time-domain spectrometer (THz-TDS) [23] covering $0.117 \leqslant \nu/\mathrm{THz} \lesssim 1.0$. Except for the X-band IFM (8.5–12 GHz), operating only in the temperature range of $15 \leqslant \vartheta/^\circ\mathrm{C} \leqslant 35$, all instruments cover $5 \leqslant \vartheta/^\circ\mathrm{C} \leqslant 35$ with an accuracy of ±0.05 °C for the IFM and ±1 °C for the THz-TDS. None of these instruments requires calibration with a dielectric standard. As can be seen from Fig. 2 there is a seamless fit of the data points obtained with the various instruments, indicating the absence of systematic errors in $\hat{\varepsilon}(\nu)$.

At 25 °C the frequency range could be extended to 2 THz with a THz-TDS in reflection geometry [24]. Additionally, far-infrared absorption coefficients, α, covering 1.2–4.3 THz (40—144 cm^{-1}), were taken from Vij et al. [5] and converted to $\hat{\varepsilon}(\nu)$ with the help of the Kramers–Kronig (KK) relation [25]

$$n(\bar{\nu}_i) - n_\infty = \frac{1}{2\pi^2} \int_0^\infty \frac{\alpha(\bar{\nu})}{\bar{\nu}^2 - \bar{\nu}_i^2} \, \mathrm{d}\bar{\nu} \tag{1}$$

and the equations

$$\varepsilon' = n^2 - \left(\frac{\alpha}{4\pi\bar{\nu}}\right)^2 \tag{2}$$

$$\varepsilon'' = \frac{n\alpha}{2\pi\bar{\nu}} \tag{3}$$

relating the refractive index, $n(\bar{\nu})$, and the absorption coefficient, $\alpha(\bar{\nu})$, at wavenumber $\bar{\nu} = \nu/c_0$ to the corresponding permittivity, $\varepsilon'(\bar{\nu})$, and loss, $\varepsilon''(\bar{\nu})$; c_0 is the speed of light in vacuo [26].

For the KK transformation the data for $\varepsilon'(\bar{\nu})$ and $\varepsilon''(\bar{\nu})$ determined in our laboratory were first converted into $n(\bar{\nu})$ and $\alpha(\bar{\nu})$. The resulting absorption coefficients were combined with the $\alpha(\bar{\nu})$ values extracted from the digitized far-infrared spectrum of Ref. [5] at 298 K (their Fig. 1). To match both sets of data in the overlapping region of 1.2–2.3 THz (40—77 cm^{-1}) the $\alpha(\bar{\nu})$ values from the literature had to be multiplied by 1.1. This might be due to errors in the digitization of the graph, as well as due to inaccuracies of the far-infrared spectra themselves (no instrument details, like optical path length, were given). The refractive index was then calculated for the region $1.2 \leqslant \nu/\mathrm{THz} \leqslant 4.3$ (40—144 cm^{-1}) by numerical integration of Eq. (1) with the trapezoidal method. The anchor value for the refractive index, n_∞, was adjusted for best overlap of experimental and calculated $n(\bar{\nu})$ in 1.2–2.3 THz (40—77 cm^{-1}). The obtained $\hat{\varepsilon}(\nu)$ spectrum is displayed in Fig. 3; Fig. 4 shows the corresponding spectra of refractive index and absorption coefficient.

For the formal description of $\hat{\varepsilon}(\nu)$ various relaxation models based on sums of up to four individual contributions to the spectrum were tested with a non-linear least-squares routine which simultaneously fits $\varepsilon'(\nu)$ and $\varepsilon''(\nu)$ [27,28]. The quality of the fit was evaluated by the reduced error function χ^2_r

$$\chi^2_\mathrm{r} = \frac{1}{2N - m - 1} \left[\sum_{i=1}^{N} w_{\varepsilon'}(\nu_i) \delta\varepsilon'(\nu_i)^2 + \sum_{i=1}^{N} w_{\varepsilon''}(\nu_i) \delta\varepsilon''(\nu_i)^2 \right] \tag{4}$$

where $\delta\varepsilon'(\nu_i)$ and $\delta\varepsilon''(\nu_i)$ are the residuals, N is the number of data triples $(\nu_i, \varepsilon'(\nu_i), \varepsilon''(\nu_i))$, and m the number of the adjustable parameters. Experimental data were weighted statistically ($w_{\varepsilon''}(\nu_i) = |\varepsilon''(\nu_i)^{-1}|$ and $w_{\varepsilon'}(\nu_i) = |\varepsilon'(\nu_i)^{-1}|$) to give the values of ε' and ε'' equal importance in the simultaneous fit with Eqs. (5) and (6).

3. Results and discussion

3.1. Dichloromethane at 25 °C

In accordance with previous literature [8,9], at high frequencies, $\nu > 100$ GHz, the dielectric spectra of DCM (Figs. 2 and 3) deviate considerably from the shape expected for simple exponential relaxation, indicating the onset of molecular librations. Evaluation of the various fit models tested for the 25 °C spectra (Fig. 3) indeed revealed the presence of three modes: the main dispersion step centered at ~70 GHz and two high-frequency modes peaking at ~0.4 THz and ~1.8 THz in the $\hat{\varepsilon}(\nu)$ representation (corresponding to the shoulder at ~0.9 THz (~30 cm^{-1}) and the peak at ~2.3 THz (~77 cm^{-1}) in $\alpha(\nu)$, Fig. 4).

Two libration modes could be expected from the symmetry of CH_2Cl_2. Therefore, the high-frequency contributions were both modeled as damped harmonic oscillators (DHOs) with resonance frequencies, ν_i ($i = 2, 3$), and damping constants, γ_i. For the feature at ~70 GHz associated with DCM relaxation a symmetrically broadened Cole–Cole equation was suggested [8], albeit with a very small width parameter of $\alpha_\mathrm{CC} = 0.03$. For the present spectra a Debye equation (D, $\alpha_\mathrm{CC} \doteq 0$) is sufficient to model $\hat{\varepsilon}(\nu)$ at low frequencies. However, correction for the inertial rise of dipole reorientation is required to avoid unphysical far-infrared contributions of the Debye equation in the D + DHO + DHO description of the spectrum [29], see Fig. 4. We therefore use the modified Debye equation (D$^\mathrm{i}$) suggested by Turton and Wynne [30], which contains the inertial rise constant, γ_lib, in addition to the dielectric relaxation time, τ_1, yielding the D$^\mathrm{i}$ + DHO + DHO model

$$\hat{\varepsilon}(\nu) = \frac{\varepsilon - \varepsilon_2}{1 - (1 + \gamma_\mathrm{lib}\tau_1)^{-1}} \cdot \left(\frac{1}{1 + (\mathrm{i}2\pi\nu\tau_1)} - \frac{1}{1 + \mathrm{i}2\pi\nu\tau_1 + \gamma_\mathrm{lib}\tau_1} \right) + \frac{(\varepsilon_2 - \varepsilon_3)\nu_2^2}{\nu_2^2 - \nu^2 + \mathrm{i}\nu\gamma_2} + \frac{(\varepsilon_3 - \varepsilon_\infty)\nu_3^2}{\nu_3^2 - \nu^2 + \mathrm{i}\nu\gamma_3} + \varepsilon_\infty \tag{5}$$

In Eq. (5) the static relative permittivity ε, as well as ε_2, ε_3, and ε_∞ are the limits of the individual dispersion steps to $\varepsilon'(\nu)$ which define the amplitudes $S_1 = \varepsilon - \varepsilon_2$, $S_2 = \varepsilon_2 - \varepsilon_3$, and $S_3 = \varepsilon_3 - \varepsilon_\infty$ of the three modes. According to Turton and Wynne [30] the inertial rise constant, γ_lib, is in the order of the average librational frequency and thus associated with the resonance frequencies of the two DHO modes of Eq. (5). Trial fits, where γ_lib was varied in the range of 1.5–2.5 THz, revealed a small but not systematic effect on χ^2_r

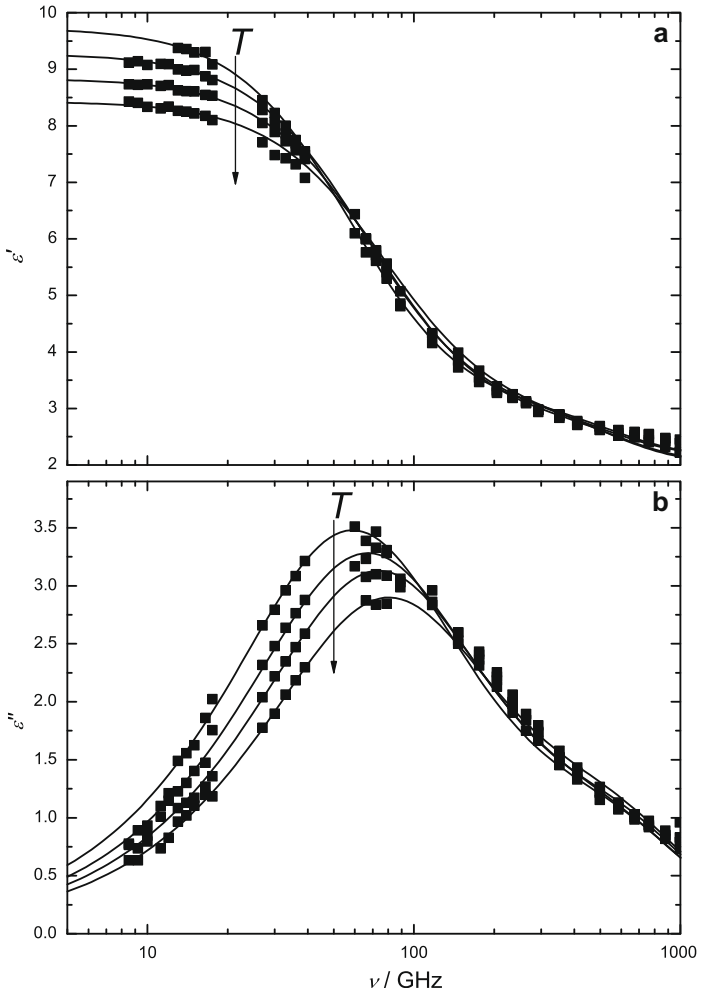

Fig. 2. (a) Dielectric permittivity, ε', and (b) dielectric loss, ε'', of dichloromethane at temperatures from 278.15 to 308.15 K. Symbols show experimental data, lines represent the D^i + DHO fit. Arrows indicate increasing temperature.

and negligible cross-correlations of this quantity with the remaining fit parameters. Thus, we fixed the inertial rise constant to $\gamma_{lib} = 2$ THz in the final fit presented in Table 1. As can be seen from Figs. 3 and 4 this D^i + DHO + DHO model provides a very good fit of the experimental spectrum at 25 °C, albeit with a small low-frequency shift for the calculated maximum ($\sim$71 cm^{-1}) of the absorption coefficient, α, relative to the experimental value ($\sim$77 cm^{-1}; Fig. 4).

As shown below, the relaxation centred $\sim$70 GHz, which dominates the dielectric spectrum, $\hat{\varepsilon}(\nu)$ (Fig. 3), can be unambiguously assigned to the rotational diffusion of CH_2Cl_2 dipoles. The two DHO modes resonating at $\sim$30 cm^{-1} (0.893 THz) and $\sim$71 cm^{-1} (2.13 THz) determine the shoulder and the peak observed for $\alpha(\nu)$ (Fig. 4). The ratio of the resonance frequencies, $\nu_3/\nu_2 \approx 2.4$, compares well with the ratio of libration frequencies expected from the moments of inertia perpendicular to the dipole vector, $\sqrt{I_y/I_x} \approx 3$ [8]. In accordance with the simulations of Isegawa and Kato [14] this suggests that the far-infrared spectrum of DCM is dominated by librations of the permanent dipoles. However, the simulations also reveal that further spectral contributions, arising from induced moments and especially cross-correlations, are far from negligible. Neglect of these broad bands in our fit model, Eq. (5), may explain the deviations between experimental and calculated spectrum around 70 cm^{-1} (Fig. 4). However, due to the limited accuracy of the digitized literature data [5] forming our experimental basis above 50 cm^{-1} implementation of a more elaborate fit model appeared not to be expedient.

3.2. Temperature dependence

Based on the above results, we now want to discuss the temperature dependence of DCM relaxation. Unfortunately, the spectral range of the THz-TDS in the transmission setup was limited to $\lesssim$ 1 THz due to the high absorption of DCM so that the low-frequency libration (ν_2 mode of Eq. (5)) is covered up to its resonance frequency ν_2, whereas only the onset of the ν_3 libration is in the experimental frequency window. Unfortunately, the latter contribution, which cannot be neglected at

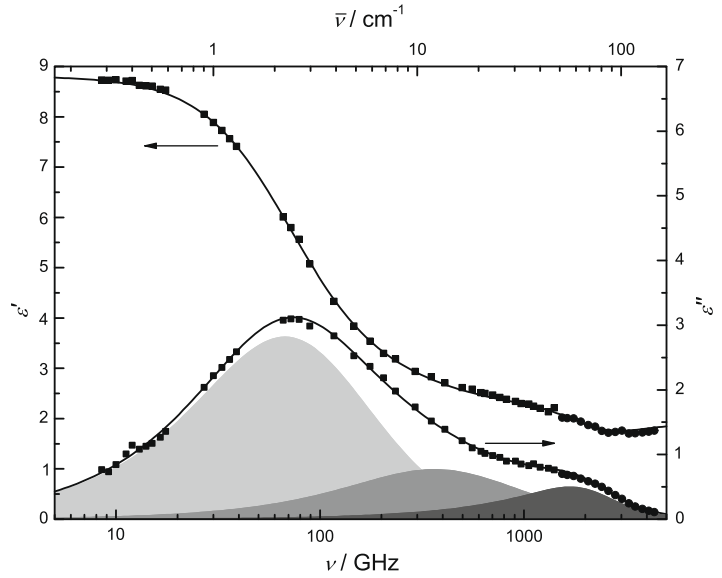

Fig. 3. Dielectric permittivity, ε', and loss, ε'', of dichloromethane at 25 °C: ■ experimental data of this work; ● values obtained by Kramers–Kronig transformation of literature data [5]. Lines represent fit with the $D^i + DHO + DHO$ model, shaded areas indicate the contributions of the modified Debye (D^i) and the two DHO modes.

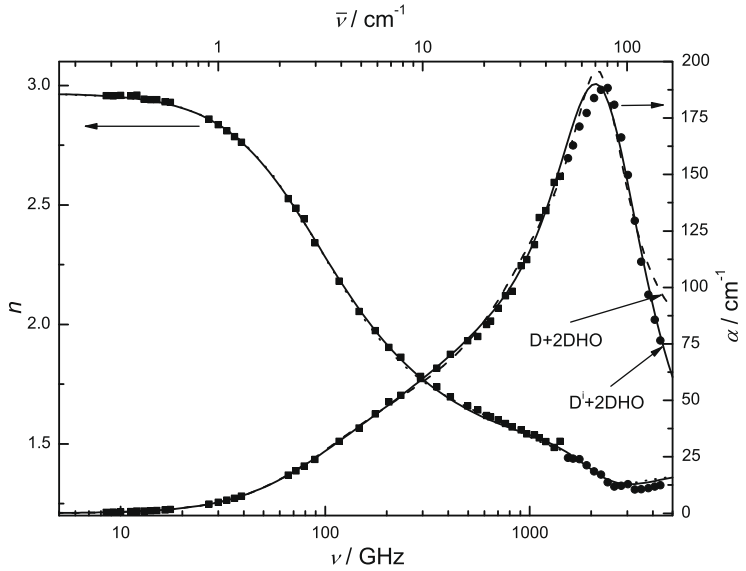

Fig. 4. Refractive index, n, and absorption coefficient, α, of dichloromethane at 25 °C: ■ experimental data of this work; ● values obtained by Kramers–Kronig transformation of literature data [5]. Solid lines represent fit with the modified $D^i + DHO + DHO$ model, dashed lines the fit with the classical D + DHO + DHO model.

Table 1
Parameters (limiting permittivities, ε_j, relaxation time, τ_1, inertial rise constant, γ_{lib}, damping constants, γ_j, resonance frequencies, ν_j, and reduced error function, χ_r^2) of the $D^i + DHO + DHO$ model, Eq. (5), fitting $\hat{\varepsilon}(\nu)$ of dichloromethane at 25 °C in the frequency range $8.5 \leqslant \nu/\text{GHz} \leqslant 4300$.

ε	τ_1 (ps)	γ_{lib} (THz)	ε_2	γ_2 (THz)	ν_2 (THz)	ε_3	γ_3 (THz)	ν_3 (THz)	ε_∞
8.81	2.23	2[a]	3.89	2.44	0.893	2.56	2.79	2.13	1.98

[a] Parameter fixed during fitting procedure. $\chi_r^2 = 96.4 \times 10^{-5}$.

~ 1 THz (see Fig. 3), is too far outside the spectral range covered in the experiment to be properly resolved in the fit. Consequently, its presence slightly biases the fits of the temperature-dependent spectra.

Table 2
Parameters (limiting permittivities, ε_i, relaxation time, τ_1, inertial rise constant, γ_{lib}, damping constant, γ_2, resonance frequency, ν_2, and reduced error function, χ_r^2) of the $D^i + DHO$ model at the investigated temperatures, T.

T (K)	ε	τ_1 (ps)	γ_{lib} (THz)	ε_2	γ_2 (THz)	ν_2 (THz)	ε_3	$\chi_r^2 \times 10^5$
278.15	9.73	2.74	2[a]	3.91	1.88	0.89[a]	2.44	228
288.15	9.27	2.41	2[a]	3.92	1.94	0.89[a]	2.43	242
298.15	8.83	2.17	2[a]	3.77	1.76	0.89[a]	2.36	188
308.15	8.43	2.03	2[a]	3.88	1.86	0.89[a]	2.34	369

[a] Parameter fixed during fit procedure.

Different models have been tested to describe the experimental data of Fig. 2. It was found that the best fit was achieved with the $D^i + DHO$ model

$$\hat{\varepsilon}(\nu) = \frac{\varepsilon - \varepsilon_2}{1 - (1 + \gamma_{lib}\tau_1)^{-1}} \cdot \left(\frac{1}{1 + (i2\pi\nu\tau_1)} - \frac{1}{1 + i2\pi\nu\tau_1 + \gamma_{lib}\tau_1} \right) + \frac{(\varepsilon_2 - \varepsilon_3)\nu_2^2}{\nu_2^2 - \nu^2 + i\nu\gamma_2} + \varepsilon_3 \quad (6)$$

where the resonance frequency of the DHO mode was fixed to the value obtained at 25 °C, $\nu_2 = 0.89$ THz. This procedure seems reasonable as in contrast to relaxation processes the location of libration modes depends only weakly on temperature [5].

The obtained parameters are listed in Table 2, Fig. 2 compares fits and experimental data. The small deviations at $\nu \gtrsim 100$ GHz can almost certainly be attributed to the small contribution of the neglected 2 THz resonance (Fig. 3). Nevertheless, comparison of the 298 K data from Table 2 with results of the full fit (Table 1) reveals that the dielectric parameters ε, ε_2, ε_3, and τ_1 obtained with the $D^i + DHO$ model are only weakly biased by the limitation of the spectral range to $\leqslant$1 THz (Fig. 5). At all temperatures the extrapolated static permittivities, ε, of this study are in excellent agreement with data obtained with conventional capacitor methods [1]. Additionally, the value of ε_∞ obtained with the $D^i + DHO + DHO$ model at 25 °C (Table 1 and Fig. 5) and the squared refractive index of Ref. [31] agree within our experimental uncertainty, suggesting that the full intermolecular dynamics of DCM is practically covered at 25 °C. On the other hand, the static permittivity and the relaxation time obtained by Vij et al. [8] from fitting a single Cole–Cole equation to their spectra deviate considerably from our results (Fig. 5). The same is true for the simulated ε and τ of Isegawa and Kato [14], probably reflecting the well-known difficulties encountered in the quantitative computer simulation of liquid-state dielectric properties [32].

Comparison of τ_1 with relaxation times from other experimental techniques allows to conclude on the mechanism behind the observed dielectric relaxation. For rotational diffusion of a molecule it is expected [11] that the molecular correlation times τ^L of rank L fulfill the relation

$$\tau^L = \frac{2\tau_{rot}}{L(L+1)} \quad (7)$$

where τ_{rot} ($= \tau^{L=1}$) is the rotational correlation time of a probed intramolecular vector. Correlation times accessible with NMR and Raman spectroscopy are single-particle relaxation times of rank $L = 2$. Dielectric spectroscopy probes $L = 1$ but the experimentally accessible relaxation time (τ_1 of Table 2) is a collective property [11] which has to be converted to the corresponding rotational correlation time with the Powles–Glarum equation [33,34]

$$\tau_{rot} = \frac{2\varepsilon + \varepsilon_\infty}{3\varepsilon}\tau_1 \quad (8)$$

The obtained values for τ_{rot} are displayed in Fig. 6.

For isotropic rotational diffusion τ_{rot} is independent of the chosen vector, whereas in the case of anisotropic reorientation CH_2Cl_2 rotation around the x-axis (Fig. 1) should be different from that around the y- and z-axes [15]. Thus τ_{rot} should depend on the orientation of the monitored vector relative to (x, y, z), with DS only monitoring rotations around x and y. If the moments of inertia, $I_x \ll I_y \approx I_z$, were determining DCM dynamics, then $\sqrt{10}\tau_x \approx \tau_y \approx \tau_z$ would be expected. The difference between reorientation around x and the other axes should be less pronounced (of the order of $1.5\tau_x \approx \tau_y \approx \tau_z$) if viscous friction combined with the asymmetry in the molecular shape predominates [15].

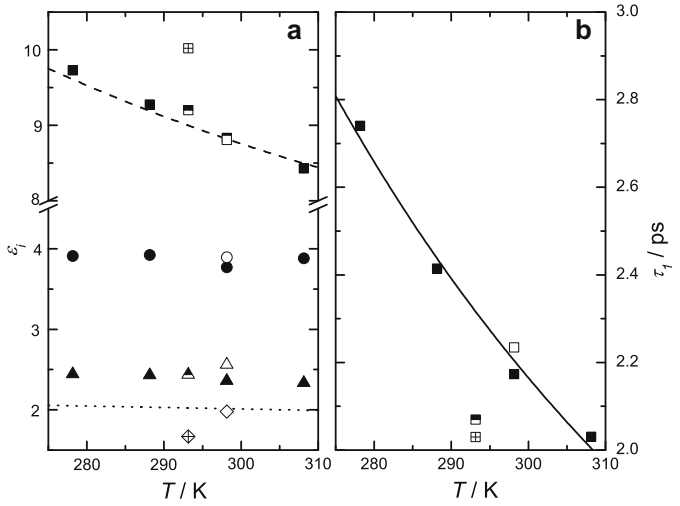

Fig. 5. (a) Limiting permittivities (ε: squares, ε_2: circles, ε_3: triangles, and ε_∞: diamonds) extracted from DCM spectra with Eqs. (5) and (6), together with the squared refractive index, $n^2_{633\,nm}$ ([31], dotted line) and the static permittivity, ε (dashed line), determined with low-frequency capacitance measurements [1]. (b) Relaxation time τ_1 (symbols) and fit with Eq. (10) (line). Open symbols represent parameters obtained at 25 °C with the $D^i + DHO + DHO$ model from the spectrum covering 8.5 GHz $\leqslant \nu \leqslant$ 4.3 THz; filled symbols show the results of the $D^i + DHO$ model applied to the restricted frequency range of 8.5 GHz $\leqslant \nu \lesssim$ 1 THz. Also included are literature data from Vij et al. [8] (half filled symbols) and from Isegawa and Kato [14] (open symbols with cross).

Intuitively, one would expect the latter situation for the diffusive reorientation of a molecule in a dense medium. However, based on the comparison of ^{13}C- and ^{35}Cl NMR data Rodriguez et al. [15] concluded that DCM reorientation is highly anisotropic and determined by inertial motion. This may be a reflection of different weights of both librational motions of DCM on the time-integrated relaxation times determined by ^{13}C- and ^{35}Cl NMR. On the other hand, it should be noted that the value of τ_{rot} from ^{35}Cl NMR is rather sensitive to the choice of the quadrupole coupling constant required for the analysis of the experimental relaxation rates. Hacura et al. [16] determined the rotational correlation times of the vectors associated with three Raman bands as a function of temperature and pressure. According to this study, and in contrast to the above NMR results, the observed correlation times for rotation around *x*, *y*, and *z* do not differ within experimental accuracy at those temperatures relevant to the present study, suggesting rather isotropic reorientation. The situation becomes even less clear when the widely scattering correlation times compiled in Ref. [7] are also considered.

Fig. 6 compares the τ_{rot} data determined in this investigation with rotational correlation times from ^{13}C NMR studies [15] and averaged τ_{rot} values calculated from the Raman data of Hacura et al. [16]. Clearly, the agreement between the different techniques is very good. Since none of the vectors probed by NMR and Raman coincides with the dipole vector it can be concluded that DCM reorientation is isotropic in the diffusive regime. This is in line with the observation that a Debye equation is sufficient to describe the low-frequency component of $\hat{\varepsilon}(\nu)$.

Analysis of the temperature dependence of τ_{rot} in terms of the extended Stokes–Einstein–Debye theory (SED) [35]

$$\tau_{rot} = \frac{3V_{eff}\eta}{k_B T} + \tau^0_{rot} \tag{9}$$

yields the effective volume of rotation, V_{eff}, required by a CH_2Cl_2 molecule. In Eq. (9) k_B is the Boltzmann constant and T the thermodynamic temperature. $V_{eff} = fCV_m$, is determined by the molecular volume, V_m, and the shape factor, f, of the particle [36]. Additionally, a hydrodynamic friction coefficient, C, appears which is generally treated as an empirical parameter but its limiting values for *stick* ($C_{stick} = 1$) and *slip* ($C_{slip} = 1 - f^{-2/3}$) boundary conditions are known. The empirical axis intercept, τ^0_{rot}, is occasionally interpreted as the correlation time of the freely rotating particle.

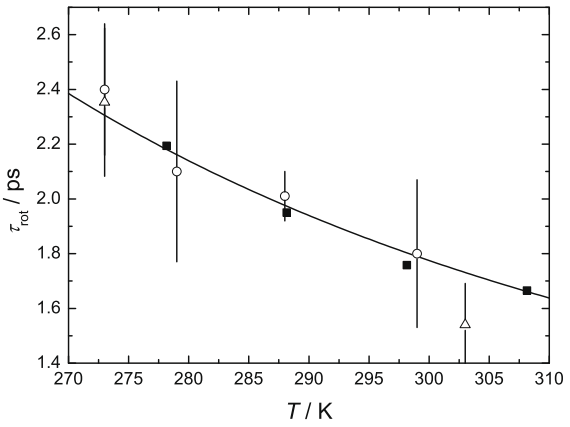

Fig. 6. Rotational correlation times, τ_{rot}, from dielectric spectroscopy (■, this study), ^{13}C NMR (○, Ref. [15]) and Raman spectroscopy (△, Ref. [16]). Line represents the fit of the DS data with Eq. (9).

The viscosities, η, required for the SED analysis of the rotational correlation times of this investigation were taken from the literature [1]. Assuming *slip* boundary conditions ($C_{slip} = 0.129$) a weighted fit of τ_{rot} *vs.* $1/T$ yields the molecular volume of $V_m = (25 \pm 1)$ Å^3 from the slope, whereas 59 Å^3 was estimated by approximating the DCM molecule as a prolate ellipsoid with principal axes of lengths $a = 6.52$ Å and $b = c = 4.16$ Å ($f = 1.230$; from van der Waals radii [37] of the atoms). This difference, yielding $C = 0.06$, may point at *sub-slip* friction for DCM reorientation. However, it should be kept in mind that a prolate ellipsoid is certainly only a rough approximation for CH_2Cl_2. Similar caution applies for the obtained axis intercept, $\tau^0_{rot} = (0.59 \pm 0.01)$ ps. Although comparable to the free-rotor correlation time [38] for rotation around the *y*-axis (0.3 ps) discussion of this quantity is not appropriate.

Further insight into the mechanism of DCM relaxation is provided by its Eyring [39] activation enthalpy, $\Delta H^{\neq}$, and entropy, $\Delta S^{\neq}$, which can be derived from the temperature dependence of τ_1

$$\ln(T\tau_1) = \left[\ln\left(\frac{h}{k_B}\right) - \frac{\Delta S^{\neq}}{R}\right] + \frac{\Delta H^{\neq}}{RT} \tag{10}$$

In Eq. (10) h and R are the Planck and the gas constant, respectively. From the τ_1 data of Table 2 the activation enthalpy of $\Delta H^{\neq} = (4.8 \pm 0.5)$ kJ mol^{-1} and the activation entropy of $\Delta S^{\neq} = (-5.8 \pm 1.8)$ J K^{-1} mol^{-1} were obtained (Fig. 5b). These values are comparable to the activation parameters of acetonitrile ($\Delta H^{\neq} = (4.6 \pm 0.2)$ kJ mol^{-1}; $\Delta S^{\neq} = (-9.8 \pm 0.6)$ J K^{-1} mol^{-1} [40]), which is also regarded as a simple dipolar liquid. The significantly smaller value of $|\Delta S^{\neq}|$ for DCM suggests that compared to acetonitrile smaller structural changes of the environment are required for the reorientation of a CH_2Cl_2 molecule, meaning that DCM dynamics are less cooperative.

Under the assumption that the fast dipole moment fluctuations associated with the librations do not correlate with the slower rotational diffusion, the effective dipole moment, μ_{eff}, of the DCM molecules in the liquid can be obtained from the relaxation amplitude, S_1, with the Cavell equation [41]

$$\frac{2\varepsilon + 1}{\varepsilon} \cdot S_1 = \frac{N_A c}{k_B T \varepsilon_0} \cdot \mu^2_{eff} \tag{11}$$

where N_A is the Avogadro constant, ε_0 the vacuum permittivity and c is the molar concentration of DCM, calculated from the density data of Ref. [1]. Averaging over all investigated temperatures the data of Table 2 yield the effective dipole moment of $\mu_{eff} = (1.93 \pm 0.04)$ D for CH_2Cl_2.

μ_{eff} relates to the dipole moment of the isolated molecule, μ, via

$$\mu_{eff} = \sqrt{g}\mu_{ap} = \frac{\sqrt{g}\mu}{1 - f_r\alpha} \tag{12}$$

where $\alpha = 6.82$ Å^3 [3] is the molecular polarizability and f_r the reaction field factor [42] of DCM. The Kirkwood factor $g = \mu^2_{eff}/\mu^2_{ap}$ is a measure for orientational correlations among the dipoles in the liquid [42].

Under the assumption of a spherical reaction field of radius $a/2 = 3.26$ Å for DCM insertion of $\mu = 1.61$ D [3] into Eq. (12) yields the value of $\mu_{ap} = 1.93$ D, thus $g = 1$. The virtual identity of the experimental μ_{eff} and the calculated μ_{ap} is certainly accidental.[1] Nevertheless, this finding indicates negligible orientational correlations among neighboring dipoles, a result which is in line with the inference from τ_1 that DCM relaxation can be viewed as essentially isotropic rotational diffusion of individual dipoles. This is also supported by a comparison of g with the Kirkwood correlation

[1] Insertion of $(\varepsilon - \varepsilon_\infty)$ instead of S_1, *i.e.* assumption that dipole fluctuations associated with librations and rotational diffusion are correlated, yields $g \approx 1.3$.

factors given by Richardi et al. [43]: $g_K = 1.07$ from experimental static permittivity data and $g_K = 1.15$ calculated with statistical mechanics (note the slightly different assumptions behind the Kirkwood–Fröhlich [42] and the Cavell [41] equations).

4. Conclusions

The dielectric properties of dichloromethane over a wide frequency range have been investigated. Data analysis reveals three contributions to $\hat{\varepsilon}(\nu)$, a relaxation at ~ 70 GHz modeled by a modified Debye equation accounting for inertial rise, and two fast modes at ~ 0.4 THz and ~ 1.8 THz described by damped harmonic oscillators with resonance frequencies of $\nu_2 = 0.89$ THz and $\nu_3 = 2.1$ THz. The relaxation at low frequencies can be assigned to rotational diffusion of the dipolar DCM molecules. The data suggest that the diffusive reorientation of the dipole vectors is isotropic. There are no indications for orientational correlations among the CH_2Cl_2 molecules. The two fast modes in the THz region are dominated by the libration of the permanent CH_2Cl_2 dipoles around the *x*- and *y*-axes of the molecule (Fig. 1), albeit some contributions from induced moments and dipole-induced dipole cross-correlations are likely.

Acknowledgements

The authors thank Prof. W. Kunz (Regensburg) and Prof. H. Helm (Freiburg) for the provision of laboratory facilities and Dr. D.A. Turton and Prof. K. Wynne for helpful discussion about fitting models.

References

[1] D.R. Lide (Ed.), CRC-Handbook of Chemistry and Physics, 85th edn., CRC-Press, Boca Raton, 2004.
[2] S.S. Chadwick, Ullmann's Encyclopedia of Industrial Chemistry, Wiley–VCH, Weinheim, 2006.
[3] M.W. Evans, G.J. Evans, W.T. Coffey, P. Grigolini, Molecular Dynamics, Wiley, New York, 1982.
[4] M.W. Evans, J. Yarwood, Adv. Mol. Relax. Interact. Process. 21 (1981) 1.
[5] J.K. Vij, C.J. Reid, G.J. Evans, M. Ferrario, M.W. Evans, Adv. Mol. Relax. Interact. Process. 22 (1982) 79.
[6] J.K. Vij, Y.P. Kalmykov, J. Chem. Phys. 99 (1993) 2506.
[7] M.W. Evans, M. Ferrario, Adv. Mol. Relax. Interact. Process. 23 (1982) 113.
[8] J.K. Vij, F. Hufnagel, T. Grochulski, J. Mol. Liq. 49 (1991) 1.
[9] Z. Kisiel, K. Leibler, A. Gerschel, J. Phys. E: Instrum. 17 (1984) 240.
[10] D. Bertolini, M. Cassettari, G. Salvetti, T.E.S. Veronesi, Rev. Sci. Instrum. 12 (1990) 61.
[11] C.F.J. Böttcher, P. Bordewijk, Theory of Electric Polarization, vol. 2, Elsevier, Amsterdam, 1978.
[12] F. Kremer, A. Schönhals (Eds.), Broadband Dielectric Spectroscopy, Springer, Berlin, 2003.
[13] H. Torii, J. Mol. Liq. 119 (2005) 31.
[14] M. Isegawa, S. Kato, J. Chem. Phys. 127 (2007) 244502.
[15] A.A. Rodriguez, S.J.H. Chen, M. Schwartz, J. Magn. Reson. 74 (1987) 114.
[16] A. Hacura, T.W. Zerda, M. Kaczmarski, J. Raman Spectrosc. 11 (1981) 427.
[17] B. Gestblom, I. Svorstøl, J. Songstad, J. Phys. Chem. 90 (1986) 4684.
[18] V.P. Pawar, S.C. Mehrotra, J. Mol. Liq. 108 (2003) 95.
[19] S. Schrödle, G. Annat, D.R. MacFarlane, M. Forsyth, R. Buchner, G. Hefter, Chem. Commun. (2006) 1748.
[20] J. Hunger, A. Stoppa, R. Buchner, G. Hefter, J. Phys. Chem. B 112 (2008) 12913.
[21] S. Schrödle, R. Buchner, W. Kunz, J. Phys. Chem. B 108 (2004) 6281.
[22] J. Barthel, K. Bachhuber, R. Buchner, H. Hetzenauer, M. Kleebauer, Ber. Bunsen-Ges. Phys. Chem. 95 (1991) 853.
[23] P. Uhd Jepsen, B.M. Fischer, A. Thoman, H. Helm, J.Y. Suh, R. Lopez, R.F. Haglund, Phys. Rev. B 74 (2006) 205103.
[24] B.M. Fischer, Ph.D. Dissertation, Freiburg, Germany, 2005.
[25] J.E. Bertie, S.L. Zhang, C.D. Keefe, Vib. Spectr. 8 (1995) 215.
[26] J.R. Birch, T.J. Parker, in: K.J. Button (Ed.), Infrared and Millimeter Waves, vol. 2, Academic Press, New York, 1979.
[27] R. Buchner, T. Chen, G. Hefter, J. Phys. Chem. B 108 (2004) 2365.
[28] A. Stoppa, J. Hunger, R. Buchner, G. Hefter, A. Thoman, H. Helm, J. Phys. Chem. B 112 (2008) 4854.
[29] S. Havriliak, S.J. Havriliak, Dielectric and Mechanical Relaxation in Materials, Hanser, New York, 1997.
[30] D.A. Turton, K. Wynne, J. Chem. Phys. 128 (2008) 154516.
[31] S. Valkai, J. Liszi, I. Szalai, J. Chem. Thermodynam. 30 (1998) 825.
[32] C. Schröder, J. Hunger, A. Stoppa, R. Buchner, O. Steinhauser, J. Chem. Phys. 129 (2008) 184501.
[33] J.G. Powles, J. Chem. Phys. 21 (1953) 633.
[34] S.H. Glarum, J. Chem. Phys. 33 (1960) 639.
[35] J.C. Dote, D. Kivelson, R.N. Schwartz, J. Chem. Phys. 85 (1981) 2169.
[36] J.C. Dote, D. Kivelson, J. Phys. Chem. 87 (1983) 3889.
[37] K. Tanabe, Spectrochim. Acta 32 (1976) 1129.
[38] F.J. Bartoli, T.A. Litovitz, J. Chem. Phys. 56 (1972) 413.
[39] S. Glasstone, K.J. Laidler, H. Eyring, The Theory of Rate Processes, McGraw-Hill, New York, 1941.
[40] A. Stoppa, S. Schrödle, G. Hefter, R. Buchner, unpublished results.
[41] E.A.S. Cavell, P.C. Knight, M.A. Sheikh, Trans. Faraday Soc. 67 (1971) 2225.
[42] C.F.J. Böttcher, Theory of Electric Polarization, vol. 1, Elsevier, Amsterdam, 1973.
[43] J. Richardi, P.H. Fries, H. Krienke, J. Phys. Chem. B 102 (1998) 5196.

A.2 Dielectric relaxation of water

Although water is probably the liquid most frequently investigated with spectroscopic techniques, the molecular mechanisms of its dynamic properties are far from being completely understood.[283] Dielectric spectroscopy (including THz and far-infrared spectroscopies) can contribute significantly to this understanding, since it yields information about the first rank orientational correlation time and experimental methods observing this quantity are scarce.

The main water relaxation (centred at $\sim 20\,\mathrm{GHz}$ at room temperature) occurs at microwave frequencies and is well characterized.[284] From measurements at high GHz and THz frequencies, there is mounting evidence for a fast relaxation mode at $\sim 300\,\mathrm{GHz}$.[86,87,181,285–290] A hydrogen-bond stretching vibration at $\sim 180\,\mathrm{cm}^{-1}$ ($\sim 5\,\mathrm{THz}$) and two librations[250,291] at $\sim 400\,\mathrm{cm}^{-1}$ ($\sim 12\,\mathrm{THz}$) and $\sim 690\,\mathrm{cm}^{-1}$ ($\sim 21\,\mathrm{THz}$) in the far-infrared range are also well established.

Another intermolecular mode, which is only observed occasionally in dielectric spectra[250,291] is the hydrogen-bond bending vibration at $\sim 50\,\mathrm{cm}^{-1}$ ($\sim 1.5\,\mathrm{THz}$). This mode is frequently not resolved because it is Raman active,[184,250,292,293] but only weakly IR active[250] thus has a very small amplitude in the DR experiment ($S \approx 0.2$).[250]

The fast water relaxation occurring between (0.1 and 1) ps (depending mainly on the investigated frequency range)[250] still attracts considerable attention and its molecular origin remains unclear. It was assigned to free or weakly hydrogen-bonded water molecules,[86,288] which is supported by the finding that this relaxation is found at about the same frequency in supercritical water.[294] This assignment also consistent with the observed activation energy and on its increasing (relative) amplitude with increasing temperature.[86,288] Other authors claim[287] that this process can be explained by the two state (low and high density) model of water inferred from MD simulations.[295] On the other hand, ultrafast spectroscopies seem to indicate that the dynamics of hydrogen-bond formation might be characteristic for this process,[296] which has considerable translational contributions.[184] Slow librations have also been claimed to provide the underlying mechanism.[297] However, the OKE and DR mode is not necessarily comparable, since there are indications that the underlying relaxation mechanism of dielectric and the mode present in four-wave mixing experiments have different origins.[288]

There are two optical Kerr effect studies[298,299] in the literature that describe, consistent with this work, a bi-exponential decay. However, the slow relaxation is difficult to detect, since the polarizability of water is almost isotropic.[299] Furthermore, these two studies come to totally different conclusions. While Winkler *et al.*[299] claim that the slow relaxation process is due to rotational diffusion of single molecules, Foggi *et al.*[298] interpret the OKE response as largely dominated by the hydrogen- bond network. Interestingly, the amplitude of the fast mode in OKE-spectra increases with increasing temperature.[298]

To contribute to the resolution of the underlying molecular mechanisms it is essential to know the relaxation parameters of the high frequency (dielectric) relaxation with sufficient accuracy. Several studies can be found in literature, dealing with this second (faster) relaxation process in water, but most of them are limited to restricted frequency or temperature ranges.[86,87,181,285–290] Up to now, no uniform picture was gained by these studies. For in-

stance, an increase[86,285] as well as a decrease[288,300] of the amplitude has been reported. Additionally, the observed activation energies of this process scatter considerably. These very different findings are probably related to the investigated frequency ranges, since this fast water process is overlapped with the main relaxation (at $\sim 20\,\mathrm{GHz}$) as well as with the slow $\sim 180\,\mathrm{cm}^{-1}$ (~ 5 THz) intermolecular vibration. Thus, it is essential to cover the entire relevant frequency range to obtain reliable relaxation parameters, which are a vital prerequisite for the interpretation of this mode.
Moreover, water is used for many non-absolute dielectric techniques for calibration purposes. Hence, it is crucial to know the relaxation parameters of neat water very accurately. Therefore, the dielectric spectra of H_2O were re-measured at $7 \leq \nu/\mathrm{GHz} \leq 40$ at temperatures ranging from 15 °C to 35 °C with the rectangular, variable-path-length waveguide transmission cells (see section 2.3.3). In the temperature range of 5 °C to 65 °C a frequency range of $12 \leq \nu/\mathrm{GHz} \leq 40$ was covered. At least two independent measurements (cells were re-filled) were performed with each cell at each temperature.
The obtained spectra were combined with selected literature data to cover the whole frequency range of interest, ranging from radio to far-infrared frequencies.

Literature spectra

Microwave measurements In addition to the present rectangular, variable-pathlength waveguide transmission measurements (section 2.3.3), carefully selected literature data were included in the spectra.
First high frequency measurements in Regensburg were performed by Stauber[290] with A- and E-band interferometers (section 2.3.2). To cover the high-frequency Debye process Stauber included the far-infrared data of Hasted.[301]
These spectra were supplemented by TDR and Ku-band data by Hölzl[86] and the temperature range was enlarged. Hölzl used interpolated THz data of Rønne[285] to cover the high frequency wing. Finally, Schrödle[87] interpolated data taken from a more detailed study by Rønne[286] to cover THz frequencies.
The results of this work are based on the spectra of Schrödle.[87] The previous interferometric measurements using X-, Ku-, and A- band were replaced by the present waveguide transmission measurements. The following temperature-dependent studies in the literature at microwave frequencies were considered: Barajas[302] at 9.355 GHz (5 °C to 65 °C), Richards[303] at 90 GHz (5 °C to 50 °C), Grant at 70 GHz (5 °C to 50 °C)[304], 34.88 GHz (5 °C to 65 °C)[305], 0.577 GHz and 1.744 GHz (5 °C to 65 °C)[306] were interpolated with appropriate polynomials, if necessary, and included. Data from Sheppard[307] at 1, 2, 3 and 4 GHz were rejected because deviations from other data were too high.
Several studies investigating the complex permittivity spectra of water at microwave frequencies at a certain or a limited number of temperatures (e.g. see Ref. 284 for an overview) can be found in the literature . However, to keep the data density similar at all temperatures, these spectra were not included, but some trial fits including the data of Pottel,[308] Kaatze,[309] Nightingale,[310] and Stuchly[311] had almost no influence on the obtained parameters (see table A.10).

Terahertz measurements A more critical issue is the inclusion of data at THz frequencies, since the number of studies is limited and the quality is generally worse than at microwave frequencies. Temperature dependent measurements at a reasonable number of temperatures were published by Hasted[301] and Zafar.[312] These spectra were interpolated to the temperatures of this work using appropriate polynomials. Moreover, Rønne published THz-TDS measurements.[285,286] These data, interpolated by Schrödle,[87] were also included. Unfortunately, the spectra of Yada *et al.*[288,289] are not tabulated and thus could not be included.
At 20 °C and 25 °C additional data were available.[313–315] Therefore, combined spectra at these temperatures were used to decide which data should be included or rejected. This comparison indicated that the data of Hasted[301] at $\nu > 280\,\mathrm{GHz}$ deviated considerably from the other spectra and were therefore excluded. The interpolated[87] data of Rønne[286] and Zafar,[312] were used over the entire frequency range.

Far-infrared measurements To cover the far-infrared range, the complex indices of refraction of Pinkley[316] (12 to 25 THz) and Zelsmann[291] (0.6 to 18 THz) were converted to $\hat{\varepsilon}(\nu)$ and inter- or extrapolated linearly to the temperatures of this study. Inter- or extrapolation of Ref. 291 was performed on basis of a restricted temperature range ($273.55 \leq T/\mathrm{K} \leq 330.35$).
Generally, agreement between the different spectral ranges was satisfactory, although at $T > 318\,\mathrm{K}$ the THz[87] and far-infrared data[291,316] start to deviate from each other, as noted by previous authors.[288] However, the far infrared data are essential for defining the resonant modes and since it was not possible to decide which data were more accurate, all were included.

Fitting procedure Because the accuracy of the permittivity data is generally an order of magnitude lower for frequency dependent measurements, than for traditional capacitance measurements,[22] the static permittivity was fixed to the value suggested by Ellison.[284]
For the description of pure water at microwave to far-infrared frequencies different fitting models have been suggested in the literature. Ellison[300] used a superposition of three Debye relaxations at microwave frequencies and two DHOs in the far-infrared range, although he refrained from a detailed interpretation of the different modes. Yada *et al.*[288,289] reported two Debye relaxation modes and two DHOs. The former represent the main and fast water process, while the first DHO accords to the intermolecular vibration and the second DHO subsumes the two librations. Rønne *et al.*[285–287] used only two Debye modes to model the spectra of water at THz frequencies. On the basis of a combined analysis of the dielectric and low-frequency Raman spectra, Fukasawa *et al.*[250] succeeded in resolving the two librations, the hydrogen-bond bending and stretching modes, and two Debye relaxations at 25 °C.
For this study, various models based on superpositions of up to 6 individual modes were tested. The fits indicated that at least four modes are required to model the experimental spectra. However, incorporation of a fifth mode improved the fit qualities. Thus, a superposition of two Debye equations and three DHOs yielded a consistent set of parameters and the lowest values for χ^2_r.

Results and discussion The parameters obtained with the D + D + DHO + DHO + DHO model are summarized in table A.10. As can be seen from table A.10, the extrapolated ε_∞ values agree almost perfectly with the squared refractive index, n_D^2, taken from literature,[114] with somewhat higher deviations at $T > 313.15\,\mathrm{K}$, but these deviations are much smaller than the accuracy of the extrapolated ε_∞ values. The spectrum of water at 40 °C with the contributions from the different modes is displayed in fig. A.25.

The main (low frequency) mode is assigned to the cooperative reorientational dynamics of the hydrogen-bonded water network[250] even though a recent OKE study[299] has suggested that it is a single molecule relaxation. However, that conclusion depends strongly on the literature data selected for comparison of the first and second rank reorientation times. A promising approach is the detailed analysis of MD trajectories, which suggests a five step reorientation mechanism.[317] Their mechanism does not require the breaking of an existing hydrogen bond prior to the water reorientation, but in the first step the environment has to rearrange to offer a hydrogen-bond acceptor. After this frame orientation, the water molecule performs a jump over an average angle of 68 °and a consecutive rearrangement of the frame takes place. Apparently, this mechanism is able to reproduce many observed correlation times[317,318] and it can explain the observed effects of the addition of ions,[319] or hydrophobic solutes[252] and activation energies.[317]

However, the present study will not focus on the main relaxation process because the temperature dependence of its dielectric relaxation parameters has already been discussed in detail elsewhere.[86]

The two higher-frequency DHO modes correspond to two librations[291] at $\sim 400\,\mathrm{cm}^{-1}$ ($\sim 12\,\mathrm{THz}$) and $\sim 690\,\mathrm{cm}^{-1}$ ($\sim 21\,\mathrm{THz}$). The resonance frequencies of this study are in excellent agreement with Ref. 291 and also the observation that the amplitudes, S_j, resonance frequencies, $\nu_{0,j}$ and damping constants, γ_j, are nearly independent of T is consistent with the assignment to librations.

The third, lowest-frequency DHO of this study at $\sim 5\,\mathrm{THz}$ coincides with the observed stretching vibration of a hydrogen-bond at $\sim 180\,\mathrm{cm}^{-1}$. The fit parameters (table A.10) suggest that its amplitude decreases with increasing temperature, which can be explained by the decreasing number of hydrogen-bonds, while the resonance frequency and shape of the mode is only weakly affected.

A hydrogen-bond bending vibration, which was observed previously[250,291] at $\sim 50\,\mathrm{cm}^{-1}$ ($\sim 1.5\,\mathrm{THz}$), is not observed in this study (i.e. fits incorporating a further DHO at $\sim 1.5\,\mathrm{THz}$ did not converge). Moreover, there are no systematic deviations of the fits from the experimental spectra at these frequencies that would indicate the necessity of an additional mode. However, as already mentioned above, this mode is mainly infrared active and, if resolved, has a very small amplitude (~ 0.2) in the dielectric spectrum.[250] Thus, it cannot be resolved, since the uncertainty of the spectra is about the same as the anticipated amplitude of this mode. Additionally, the systematic deviations of THz spectra from the far-infrared data, especially at $T \geq 318\,\mathrm{K}$, might complicate the resolution of this mode. Nevertheless, since the amplitude of the $1.5\,\mathrm{THz}$ mode is so small, its absence from the present fits is not expected to bias the remaining modes significantly.

The focus of this study is the second relaxation process. As already mentioned, literature relaxation parameters show not only considerably scatter, but also qualitatively by different

temperature dependences. The present study clearly yields a thermodynamically activated process. The Arrhenius and Eyring activation parameters (see section 1.5) can be obtained by linear regression of $\ln(\tau_2)$ or $\ln(\tau_2)+\ln T$ vs. $1/T$, respectively. Diagonal elements of the covariance matrix from the the non linear fitting procedure (see section 2.3.6) were used to weight the τ_2 values. These fits yielded an Arrhenius activation energy of $E_a(\tau_2) = (16.7 \pm 4.7)\,\mathrm{kJ\,mol^{-1}}$. Application of the Eyring theory yields $\Delta H^{\neq} = (14.2 \pm 4.7)\,\mathrm{kJ\,mol^{-1}}$ and $\Delta S^{\neq} = (39 \pm 16)\,\mathrm{J\,mol^{-1}\,K^{-1}}$. (cf. activation parameters for the main relaxation (τ_1): $\Delta H^{\neq}_{298} = (16.36 \pm 0.09)\,\mathrm{kJ\,mol^{-1}}$ & $\Delta S^{\neq}_{298} = (22.1 \pm 0.3)\,\mathrm{J\,mol^{-1}\,K^{-1}}$).[86]

The amplitude S_2 decreases quite drastically from ~ 2.5 at 5 °C to ~ 1.4 at 65 °C. This decrease cannot be due to the unresolved hydrogen-bond bending mode (at 1.5 THz), because its amplitude is much smaller.[250]

All these findings imply that the underlying relaxation mechanism of water in this frequency region must be more complicated than to be just due to free molecules and/or structural dynamics. Although recent MD simulations[317] give valuable insights into the mechanism of the main relaxation process in water, the fast water relaxation does not seem to be apparent in the simulations. Most likely, this is because the amplitude of the second mode is relatively small and therefore the underlying mechanism is not obvious from the analysis of the MD trajectories.

Before further discussion of mode 2 on the basis of the present data, one has to be aware that due to the deviations of the far-infrared and THz data at $T \geq 318\,\mathrm{K}$, as mentioned above, the parameters obtained at these temperatures are more uncertain and should be considered with caution.

On the basis of the recent data for mode 2, several explanations, given in the literature can be regraded. The assignment of free or weakly bound water molecules can be excluded. First, the amplitude S_2 as well as the relative relaxation amplitude $S_2/(S_2 + S_1)$ clearly decrease with increasing temperature. As the hydrogen bonding is weakened due to the increasing thermal energy an increase of the relative amplitude would be expected. Second, this mode is observed at about the same frequency in OKE spectroscopy.[298,299] If free or weakly bound water molecules caused mode 2, a relaxation time ratio close to 3 would be expected. In addition, the relaxation would not be expected to be Raman active due to the almost isotropic polarizabilty of the water molecule.[184]

Another explanation could be an alternative water relaxation mechanism (i.e. water can relax via two relaxation mechanisms). If this alternative mechanism was entropically unfavored, a decreasing amplitude with increasing temperature would be expected. Although the present Eyring activation parameters for mode 2 have large uncertainties, and strongly depend on the accuracy of the τ_2 values, this possibility can be ruled out. Irrespective of the inclusion or rejection of the τ_2 values at $T > 318\,\mathrm{K}$, the thermodynamic barrier for process 2 is always smaller than for process 1 (at least at temperatures where water exists als a liquid at atmospheric pressure).

Although, the observed dielectric parameters do not contradict the two state model of water[287] there is no obvious reason, why relaxation in the low density liquid should produce an OKE response, while the high density phase is almost Raman inactive.

On the other hand time-dependent anisotropy studies of excited molecules reported a fast decay[297] at $< 200\,\mathrm{fs}$. Including results from MD simulations,[320] it is suggested that this

initial decay is due to librations, involving a displacement of the O atom. Assuming this mode as the underlying mechanism of the second dielectric mode, the increasing number of available hydrogen-bond acceptors at higher temperatures might explain the decrease of S_2, as this mode can be understood as a "waiting vibration" of a water molecule, until a hydrogen-bond acceptor site becomes available. Since the geometry (i.e. the H-O-H angle) of the water molecule is not necessarily kept for this vibration, the OKE activity could be plausible. However, the observed activation energy of the present study contradicts this mechanism.

Another explanation is based on the observation that this relaxation must involve more than one water molecule, since it is Raman active.[184,250] The fast relaxation time might be an indication that the interpretation of an interaction-induced rotation,[210] which contains considerable translational components is the underlying mechanism. However, the observed decrease in S_2 might contradict this mechanism.

A more intuitive explanation, based on the above observations, might be a consecutive relaxation. After a successful relaxation via the mechanism of process 1, the surrounding environment is in a transition state, that can relax via process 2 to an energetically favored state. The consecutive step has a lower energetic barrier. Increased thermal motion and weakening of the hydrogen-bonded network would change the relative occupation of the two energetic levels, and thus the amplitude S_2 decreases quickly with increasing temperature. This interpretation is somewhat similar to the "exponential model" as described by other authors.[321]

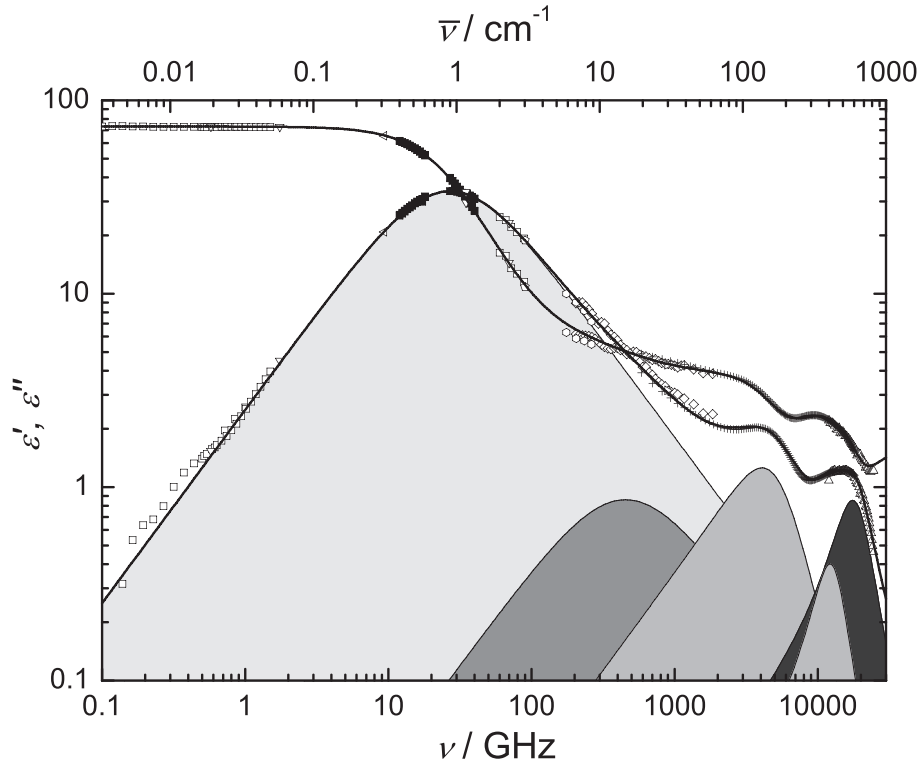

Figure A.25: Dielectric permittivity, $\varepsilon'(\nu)$, and dielectric loss, $\varepsilon''(\nu)$, spectra of water at 40 °C. Symbols represent experimental data, lines fit correspond to the D + D + DHO + DHO + DHO fit. Shaded areas indicate the contributions of the D and DHO modes to $\varepsilon''(\nu)$. (■: variable-pathlength waveguide transmission data of this work; □: Ref. 86; △: Ref. 316; ▽: Refs. 304–306; ◇: Ref.[286] interpolated by Schrödle;[87] ◁: Ref. 302; ▷: Ref. 312; +: Ref. 291; ⬠: Ref. 303; ⬡: Ref. 301)

Table A.10: Temperature dependence of the dielectric relaxation parameters of water: static permittivity, ε, relaxation times, τ_j, relaxation amplitudes S_j, resonance frequencies, $\nu_{0,j}$, damping constants, γ_j, infinite frequency permittivity, ε_∞, and variance of fit, χ^2_r, assuming a D+D+DHO+DHO model. n^2_D are squared refractive index values, interpolated from literature[114a]

T	ε^b	τ_1	S_1	τ_2	S_2	$\nu_{0,3}$	γ_3	S_3	$\nu_{0,4}$	γ_4	S_4	$\nu_{0,5}$	γ_5	S_5	ε_∞	n^2_D	$\chi^2_\mathrm{r} \cdot 10^4$
278.15	85.868	14.56	79.43	0.616	2.38	5.10	5.87	1.53	13.7	6.49	0.158	19.4	11.6	0.569	1.80	1.780	114
283.15	83.929	12.49	77.55	0.637	2.30	5.12	6.18	1.57	13.5	6.12	0.141	19.3	12.0	0.590	1.78	1.780	44
283.15[c]	83.929	12.51	77.51	0.664	2.32	5.13	6.27	1.59	13.5	6.31	0.152	19.3	11.8	0.576	1.78	1.780	51
288.15	82.033	10.69	75.76	0.515	2.25	5.09	5.91	1.49	13.3	6.73	0.171	19.1	11.9	0.568	1.79	1.779	55
288.15[c]	82.033	10.72	75.67	0.559	2.31	5.11	6.11	1.53	13.3	6.38	0.156	19.1	11.9	0.579	1.79	1.779	65
293.15	80.179	9.39	74.05	0.470	2.12	5.10	6.11	1.49	13.9	8.06	0.268	19.5	11.4	0.471	1.78	1.778	38
293.15[d]	80.179	9.42	74.02	0.489	2.13	5.11	6.22	1.51	13.1	6.49	0.163	19.0	12.1	0.579	1.77	1.778	41
298.15	78.368	8.25	72.27	0.495	2.02	5.14	6.63	1.57	13.1	6.52	0.171	18.9	12.0	0.568	1.77	1.776	33
298.15[e]	78.368	8.29	72.30	0.505	1.99	5.15	6.72	1.57	13.0	6.19	0.152	18.9	12.2	0.587	1.76	1.776	62
303.15	76.598	7.43	70.78	0.374	1.87	5.09	6.16	1.44	12.9	6.94	0.189	18.8	12.3	0.572	1.76	1.775	33
303.15[c]	76.598	7.41	70.71	0.401	1.89	5.10	6.35	1.48	12.9	6.87	0.189	18.8	12.2	0.566	1.76	1.775	47
308.15	75.168	6.70	68.96	0.591	1.99	5.30	8.09	1.74	12.9	5.97	0.153	18.6	12.1	0.568	1.76	1.773	35
313.15	73.176	5.92	67.50	0.351	1.72	5.08	6.43	1.43	12.7	7.35	0.227	18.6	12.2	0.547	1.75	1.772	37
318.15	71.523	5.28	66.10	0.287	1.56	5.09	6.50	1.36	12.6	7.27	0.223	18.4	12.4	0.554	1.72	1.769	56
323.15	69.907	4.72	64.90	0.151	1.62	4.93	4.84	0.89	12.9	9.43	0.366	18.5	11.6	0.433	1.69	1.767	92
328.15	68.328	4.31	63.30	0.147	1.64	4.89	4.90	0.88	13.0	9.91	0.409	18.3	11.4	0.401	1.70	1.765	100
333.15	66.784	3.92	61.94	0.110	1.69	4.82	4.40	0.68	13.3	10.64	0.487	18.4	10.2	0.301	1.68	1.762	66
338.15	65.276	3.65	60.13	0.196	1.32	4.93	6.58	1.28	12.6	8.94	0.410	18.0	10.9	0.405	1.73	1.760	71

[a] Units: T in K; τ_j in ps; $\nu_{0,j}$, γ_j in THz. [b] Parameter fixed to literature permittivity.[284] Parameters obtained including additionally data [c] from Ref. 309, [d] Refs. 310,311, [e] Ref. 308.

A.3 Relative permittivity of dimethylsulfoxide and *N*,*N*-dimethylformamide at temperatures from 278 K to 328 K and pressures from 0.1 MPa to 5 MPa

In the framework of this thesis, the static permittivities of N,N-dimethylformamide and dimethylsulfoxide were measured as function of temperature and pressure. The following pages contain the manuscript, in preparation for the Journal of Chemical and Engineering Data:

Johannes Hunger and Richard Buchner
Institut für Physikalische und Theoretische Chemie, Universität Regensburg, D-93040 Regensburg, Germany.

Mohamed E. Kandil, Eric May and Kenneth N. Marsh
Centre for Petroleum, Fuels and Energy, School of Mechanical Engineering, The University of Western Australia, Crawley WA 6009, Australia.

Glenn Hefter
Chemistry Department, Murdoch University, Murdoch, W.A. 6150, Australia.

Abstract Relative permittivities (ε_r) have been measured at two frequencies with a reentrant radio-frequency resonator in the pressure range (0.1 to 5) MPa at temperatures from (278 to 328) K for *N*,*N*-dimethylformamide (DMF) and (293 to 328) K for dimethylsulfoxide (DMSO). For DMF the present values lie within the rather large spread of literature values. For DMSO the present data are lower than the majority of literature data but agree with one other study. Possible sources of uncertainty are discussed. An empirical description of $\varepsilon_r(p,T)$ is given that can be used to calculate the temperature and pressure derivatives of ε_r. These derivatives are fundamental input parameters for modeling the effects of electric fields on these solvents, and for the theoretical description of the heat capacities, and enthalpic and volumetric properties of electrolyte solutions. Kirkwood *g* factors calculated using the present data show only minimal dipole-dipole correlations for both DMF and DMSO.

Introduction Accurate values of the pressure and temperature dependence of the relative permittivity (dielectric constant), ε_r, are of scientific and industrial interest, since they are required for the application of various theories and for reliable process simulation. For example, the pressure dependence of ε_r needs to be known to model the compression of a solvent by the electric field of an ion via the Drude-Nernst equation[322] or to apply the Debye-Hückel limiting law to the volumetric properties of electrolyte solutions.[323] Similar requirements exist for the first and second temperature derivatives of ε_r for modelling enthalpies and heat capacities.

However, reliable studies of $\varepsilon_r(p,T)$ of molecular solvents in the literature are scarce,[324] with most of the available experimental data, particularly for solvents suited to electrolyte studies, focused on $(\partial\varepsilon_r/\partial T)_p$ values, often obtained over very limited temperature ranges. In this work $\varepsilon_r(p,T)$ has been measured for N,N-dimethylformamide (DMF) and dimethylsulfoxide (DMSO), with a particular focus on $(\partial\varepsilon_r/\partial p)_T$. Both of these solvents are widely used in separation processes because they dissolve a very diverse range of organic and inorganic compounds: DMF is used on a large scale as a solvent for polymers and paints while DMSO has pharmaceutical applications.[325] Reliable data for $\varepsilon_r(p,T)$ of DMF and DMSO will improve the fundamental models used to describe them, which may in turn lead to better predictions of their thermophysical properties by the chemical engineering simulators used to design new industrial processes based on these solvents.

The experimental methods available to determine relative permittivity over a range of temperatures and pressures have been summarized recently.[22] One method well suited to $\varepsilon_r(p,T)$ measurements of fluids utilizes robust re-entrant cavity resonators. Measurements of $\varepsilon_r(p,T)$ with such instruments have been used to determine high-pressure phase boundaries and liquid volume fractions in binary[326–328] and multi-component hydrocarbon mixtures.[329,330] Re-entrant resonators have also been used for accurate measurements of molar polarizability and/or permittivity and dipole moments in non-polar fluids and mixtures[331,332] weakly polar pure fluids[333] and strongly polar water.[334–336] In the present study a three-lobed re-entrant radio-frequency resonator was used to determine the generalized complex permittivity, $\hat{\eta}(p,T)$, over the pressure range (0.1 to 5) MPa at temperatures from (278 to 328) K for DMF and (293 to 328) K for DMSO. The generalized complex permittivity, $\hat{\eta} = \varepsilon_r - \mathrm{i}\eta''$ where $\mathrm{i} = \sqrt{-1}$ and $\eta'' = \varepsilon'' + \kappa/(2\pi f \varepsilon_0)$; $\hat{\eta}$ comprises the relative permittivity, ε_r, the dielectric loss, ε'', and the Ohmic loss, which is determined by the electrical conductivity, κ, the frequency of the electromagnetic radiation, f, and the electric constant, $\varepsilon_0 = 8.854187817\ldots\cdot 10^{-12}\,\mathrm{F\,m^{-1}}$.[337] We are unaware of any similar data for these systems in the literature measured at pressures above ambient.

Apparatus and materials Analytical grade dimethylsulfoxide (mass fraction $w > 0.999$) and N,N-dimethylformamide ($w > 0.998$) were obtained from Ajax Finechem (Australia) and used without further purification. The water mass fraction, determined by coulometric Karl Fischer titration, was $4 \cdot 10^{-4}$ and $5.5 \cdot 10^{-4}$ for the DMSO and DMF, respectively. Conductivities of DMF and DMSO were determined with a four terminal conductivity probe to be $4 \cdot 10^{-4}\,\mathrm{S\,m^{-1}}$ and $1.3 \cdot 10^{-3}\,\mathrm{S\,m^{-1}}$ at 297 K, respectively.

A schematic of the re-entrant cavity resonator is shown in Figure A.26. This cavity had three "lobes" which resulted in three radio-frequency modes, with vacuum resonance frequencies of approximately 170 MHz, 675 MHz and 1.12 GHz. The relative deviations of these vacuum frequencies from those predicted with the nominal cavity dimensions using the extended waveguide model of Goodwin *et al.*[326] were −1.5 %, +1.0 % and +7.8 %, respectively. Such deviations are typical of those reported elsewhere.[328] While the vacuum resonance frequencies depended sensitively on the cavity dimensions, the measured values of $\hat{\eta}(p,T) \cong (f(p,T)/f(0,T))^2$ were insensitive to the cavity dimensions because they were derived from frequency ratios. The small effects of pressure and temperature on the

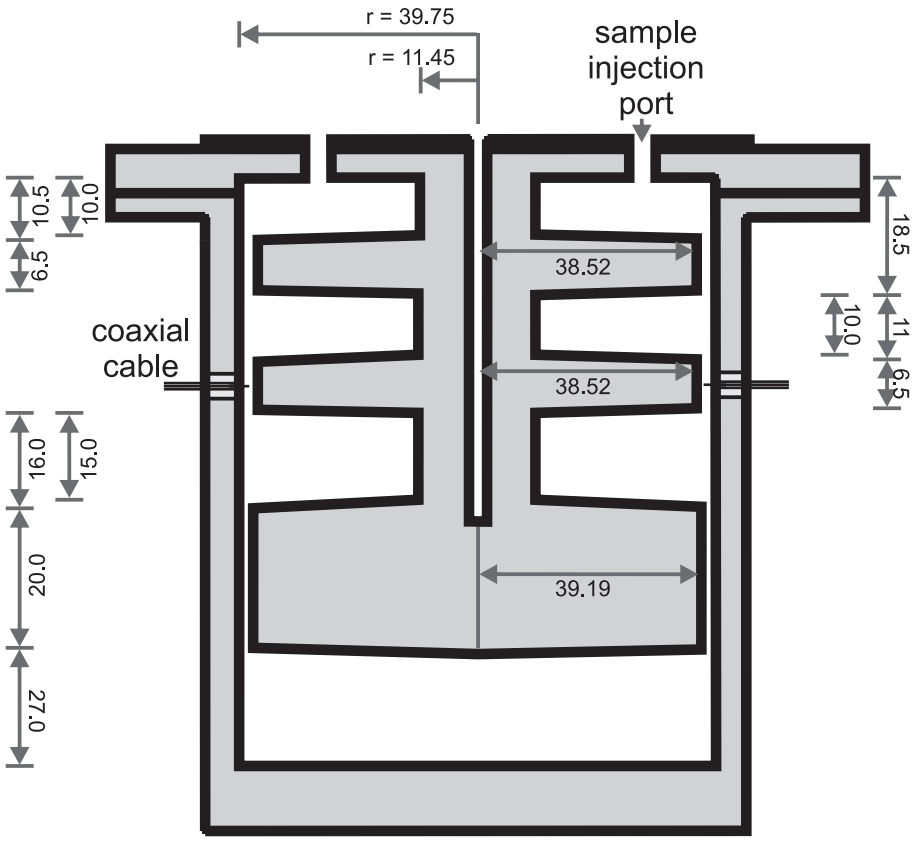

Figure A.26: Schematic representation of the three lobed cavity resonator.

vacuum resonance frequencies were accounted for by first calibrating the resonator with helium measurements as described in the next section.

The resonator was constructed from two type-316 stainless steel sections bolted together, with an indium O-ring providing a pressure seal and good electrical contact between the two sections. Unfortunately, the seal was not reliable at $p > 8\,\mathrm{MPa}$ or at temperatures above 328 K. The inner surfaces of the cavity that formed the boundaries for the RF resonances were plated with gold to a thickness of $30\,\mu\mathrm{m}$. This increased the quality factor of the resonances by decreasing the resistivity losses that occurred in the bounding conductor. High vacuum quality factors allow more reliable measurements of the imaginary part of $\hat{\eta}(p,T)$. Furthermore, the frequency dependence of the vacuum quality factor of the resonances is simpler to model if the boundary conductor is non-magnetic.[335]

A schematic of the experimental set-up used to make the measurements as a function of temperature and pressure is shown in Figure A.27. The cavity resonator was placed in a Julabo ME thermostat, filled with silicon oil M5 (Carl Roth, Germany), with a long term temperature stability of $\pm 0.02\,\mathrm{K}$. The temperatures of the bath and of the cavity were measured with two platinum resistance thermometers (PRT 100) connected to an Agilent 34970A Data Acquisition/switch Unit using a 4-wire configuration. The thermometer PRT1, used to measure the cavity temperature, was placed in the central well as shown in Figure A.27. The two PRTs were calibrated against a $25\,\Omega$ standard platinum resistance

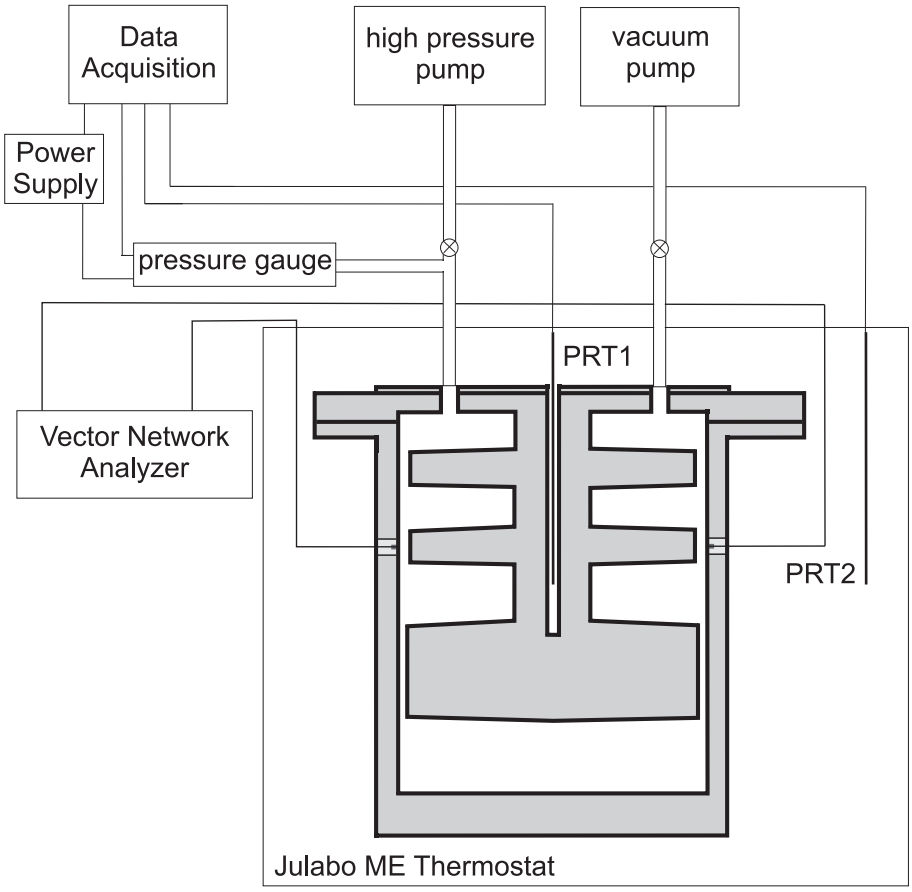

Figure A.27: Schematic of the experimental system used for the measurements.

thermometer (Hart Scientific Model 5681) with a standard uncertainty ±0.05 K. When the bath temperature was close to ambient, the agreement between the temperatures measured with the two PRTs was consistent with this uncertainty; however, at temperatures away from ambient, heat leaks into the resonator from elements located outside the bath resulted in differences of up to 0.2 K. The standard uncertainty in the temperature of the resonator was estimated at ±0.1 K.

Pressures within the cavity were monitored using a diaphragm strain-gauge type pressure transmitter (General Electric PTX 1400) with a full scale of 40 MPa. The transmitter was calibrated against a reference quartz crystal transducer (Paroscientific, Model 1000, 7 MPa full scale) located outside the bath, which was isolated from the resonator during the measurements of DMF and DMSO. The relative uncertainty of the pressure measurements made with the diaphragm strain-gauge transducer was ±0.25 % of reading while the repeatability of the transducer was better than ±1 kPa.

A computer controlled high pressure positive displacement pump (Quizix QX-6000, maximum pressure 40 MPa) was used to fill and then pressurize the solvent in the cavity. The filling process consisted of injecting about 240 cm^3 of liquid into the cavity, which had a total internal volume of 260 cm^3. A vacuum was then applied to the space above the liquid to degas the solvent. The remaining solvent volume was injected using the positive

displacement pump and, once full, the pump was used to check for trapped gas bubbles by measuring the effective compressibility of the liquid. In all the experiments reported, the effective compressibility of the liquids determined from the measured change in pressure corresponding to a known displaced volume agreed with the expected value[338–340] within the experimental uncertainty.
The electromagnetic resonances of the reentrant cavity were measured in transmission using a HP 8719ET vector network analyzer, with a frequency range of (0.05 to 13.5) GHz. The network analyzer recorded the complex scattering parameter $\hat{S}_{12}$ at 201 frequencies, spanning a range approximately ten times the resonance half-width, centered on the approximate resonance frequency. A typical sweep took about 50 s and about 10 sweeps were averaged when obtaining the $\hat{S}_{12}$ used to determine the resonance parameters.

Method Measurements of $\hat{\eta}(p, T)$ were made along isotherms. Following a change of bath temperature, approximately 3 h was required before the system was deemed to have achieved equilibrium, based on the rate of change of the measured pressure, temperature and resonance frequency. Following a change in pressure, approximately 0.8 h was required. Once the system had achieved equilibrium, the measured complex scattering parameters were fit to the theoretical resonance function:[326]

$$\hat{S}_{12}(f) = \frac{\hat{A}f}{f^2 + (f_j + \mathrm{i}g_j)^2} + \hat{B} \tag{A.6}$$

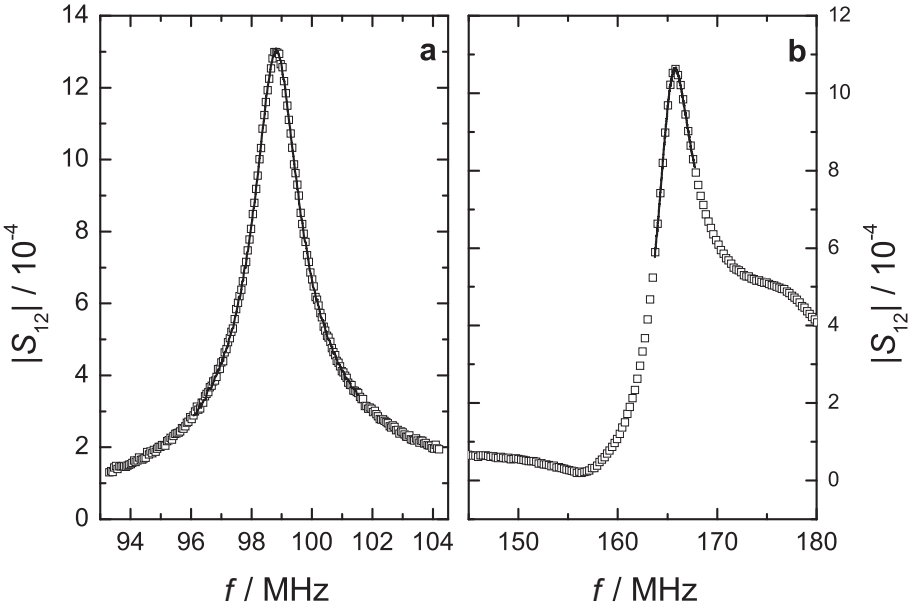

Figure A.28: Magnitude of the complex scattering parameter, $|\hat{S}_{12}|$, for: (**a**) Mode 2 and (**b**) Mode 3, for DMSO at $T \approx 293.15$ K and $p \approx 0.1$ MPa. Symbols represent measured values; line corresponds to fit with eq A.6.

Here f is the stimulus frequency, $\hat{A}$ and $\hat{B}$ are complex adjustable parameters and $(f_j + \mathrm{i}g_j)$ is the complex resonance frequency of mode j (= 1, 2 or 3). Non-linear least squares

regression of $\hat{S}_{12}$ to eq A.6 was used to determine the six parameters in the quantities $\hat{A}$, $\hat{B}$ and $(f_j + \mathrm{i}g_j)$. Figure A.28 shows values of $|\hat{S}_{12}|$ measured for the second and third modes with the cavity filled with DMSO at 293 K and 0.1 MPa. While Mode 1 was measurable when the cavity was evacuated or filled with helium, the high permittivity of the target solvents meant that Mode 1 was below the low-frequency limit of the network analyzer when the cavity was filled with either DMSO or DMF. When filled with these solvents, the Mode 2 resonance was located at approximately (95 to 120) MHz and, as can be seen in Figure A.28, was isolated from any other cavity resonances. In contrast Mode 3, which was located at approximately (165 to 200) MHz, was affected by interference from higher order modes. However, the interference did not seem to cause values of $\hat{\eta}(p,T)$ obtained from Mode 3 to differ significantly from those obtained from Mode 2, within the estimated experimental uncertainty. Accordingly, values of $\hat{\eta}(p,T)$ determined with both Modes 2 and 3 are reported in Tables A.14 and A.15.

The complex total permittivity of each fluid was determined from the measured resonance frequencies, half-widths and quality factors using the implicit model developed by Hamelin et al.[334] for the case of weak coupling to the measurement circuit.

$$\hat{\eta} = \left(\frac{f_{0j} + \mathrm{i}g_{0j}}{f_j + \mathrm{i}g_j}\right)^2 \frac{1 + (-1+\mathrm{i})(f_j/f_{0j})^{3/2}\hat{\eta}/Q^0_{\mathrm{s}j}}{1 + (-1+\mathrm{i})/Q^0_{\mathrm{s}j}} \tag{A.7}$$

In eq A.7 subscripts or superscripts '0' indicate properties of the vacuum resonance and $Q^0_{\mathrm{s}j} \equiv f_{0j}/2g_{0j}$ (≈ 2000) is the vacuum quality factor of mode j, determined by the effective resistivity of the bounding metal surface. The measured vacuum half-widths, g_{0j}, were about two to ten times larger than expected based on the literature electrical conductivity of gold;[341] this discrepancy can be attributed to the surface finish of the cavity's internal walls and is not critical to the measurements of $\hat{\eta}(p,T)$ because the values of $Q^0_{\mathrm{s}j}$ were stable. However, it was important to account for the changes in f_{0j} that occurred as the cavity temperature and fluid pressure were varied.

Helium calibration The relative permittivity of helium can be calculated as a function of temperature and pressure with an uncertainty smaller than corresponding measurements of $\varepsilon_{\mathrm{r}}(p,T)$.[342] Thus, resonance measurements when the cavity is filled with helium can be used to determine the effects of the cavity's thermal expansion and pressure dilation on the vacuum frequencies, thereby calibrating the resonator. For lossless fluids such as helium, with $\varepsilon_{\mathrm{r}} \approx 1$, eq A.7 simplifies to

$$\varepsilon_{\mathrm{r}}(p,T) = \left(\frac{f_{0j} + \mathrm{i}g_{0j}}{f_j + \mathrm{i}g_j}\right)^2 \left(\frac{1 + (-1+\mathrm{i})Q_j}{1 + (-1+\mathrm{i})/Q^0_{\mathrm{s}j}}\right) \tag{A.8}$$

where Q_j is the mode's measured quality factor at a given (p,T). The vacuum resonance half-width is essentially independent of pressure and temperature but the vacuum resonance frequency has the dependence

$$f_{0j} = f_{00j}(1 + \alpha_j(T - T_0) + \phi_j p) \tag{A.9}$$

Here f_{00j} is the resonance frequency of Mode j at $p = 0$ and an arbitrary reference temperature T_0, α_j is the effective temperature coefficient of the mode and ϕ_j is the effective pressure coefficient of the mode. Measurements of $(f_j + \mathrm{i}g_j)$ were made with the cavity filled with helium (mole fraction purity 0.999999) at pressures ranging from (0.1 to 3.9) MPa at $T_0 = 298.69\,\mathrm{K}$ and also at temperatures from (278 to 328) K at 0.1 MPa. At each condition, the value of $\varepsilon_\mathrm{r}(p, T)$ for helium was calculated using the equation of state of McCarty and Arp[343] and the polarizability correlation of Harvey and Lemmon[344] as implemented in the software REFPROP 8.0.[345] The calculated values of $\varepsilon_\mathrm{r}(p, T)$ for helium were used in eq A.8 to determine a value of f_{0j} corresponding to each pressure and temperature. The results of the pressure and temperature calibrations are shown in Figure A.29. Linear least squares regression of the data shown in Figure A.29 was used to derive the parameters f_{00j}, α_j and ϕ_j for each mode. The results for Modes 2 and 3 are summarized in Table A.11 and are comparable to those measured by other workers[328,331] with similar reentrant cavities. The effective temperature coefficients of both modes are also in reasonable agreement with the coefficient of thermal expansion for stainless steel ($\alpha = 1.59 \cdot 10^{-5}\,\mathrm{K}^{-1}$).[346] Also shown in Table A.11 are the measured vacuum resonance half-widths, used in eqs A.7 and A.8 for the analysis of all the data obtained for helium, DMF and DMSO.

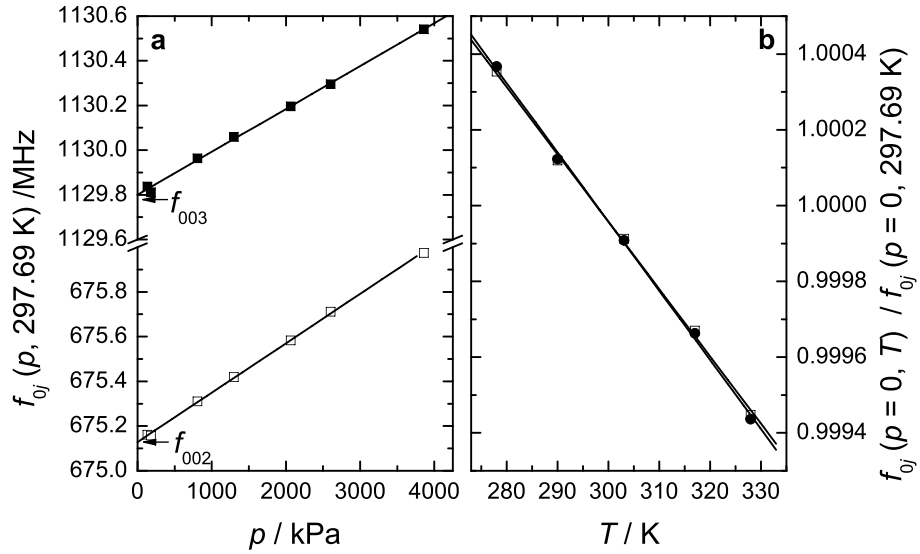

Figure A.29: Pressure calibration at $T = 298.69\,\mathrm{K}$ (**a**) and temperature calibration (**b**) of Mode 2 (open symbols) and Mode 3 (closed symbols) of the three-lobed reentrant cavity resonator. Lines represent the linear regression. f_{0j} are the resonance frequencies corrected for the relative permittivity of He.

Results and discussion Temperatures, pressures, frequencies and $\hat{\eta}$ values obtained from the analysis with eq A.7 are presented in Table A.14 for DMF and Table A.15 for DMSO, with pressures listed in temporal order. From an analysis of the effects of uncertainties in temperature and pressure and the repeatability of the resonance frequency, an uncertainty of 0.1 in ε_r was estimated.

Table A.11: Vacuum resonance frequencies f_{00j} at $T_0 = 298.69\,\mathrm{K}$, measured vacuum half-widths g_{0j}, pressure coefficients, ϕ_j, and temperature coefficients, α_j, for Modes 2 and 3.

j	f_{00j}/MHz	g_{0j}/MHz	$10^7\ \phi_j$/kPa^{-1}	$10^5\ \alpha_j$/K^{-1}
2	675.128 ± 0.004	0.2063 ± 0.004	3.29 ± 0.03	-1.77 ± 0.04
3	1129.803 ± 0.008	0.2567 ± 0.008	1.68 ± 0.03	-1.83 ± 0.04

Modeling A least squares regression of $\varepsilon_\mathrm{r}(p,T)$ via the empirical eq A.10 was used to determine the adjustable parameters A_1, A_2, B_1, B_2 and C_1.

$$\varepsilon_\mathrm{r}(p,T) = A_1 + A_2 p + (B_1 + B_2 p)T + C_1 T^2 \tag{A.10}$$

The parameters B_2 and C_1 were not statistically significant and thus were set equal to zero for DMF and DMSO, respectively. The other parameters, together with fit qualities, are summarized in Table A.12. The derivatives $(\partial\varepsilon_\mathrm{r}/\partial T)_p$ and $(\partial\varepsilon_\mathrm{r}/\partial p)_T$ are much smaller for DMSO than for DMF, which is a reflection of the much higher melting temperature of DMSO ($T_\mathrm{m} = 291.04\,\mathrm{K}$) cf. DMF ($T_\mathrm{m} = 212.7\,\mathrm{K}$),[114] because both solvents have similar molecular weights, dipole moments and densities (see below), but the isothermal compressibility of DMF[338,339] is higher than for DMSO.[340] The low values of the derivatives and the rather small temperature range of this study inevitably result in higher uncertainties in the parameters of eq A.10 for DMSO cf. DMF (Table A.12). The pressure and temperature derivatives for both solvents are significantly lower than for water.[347]

Table A.12: Regression parameters for three dimensional fit of $\varepsilon_\mathrm{r}(p,T)$ using eq A.10 for mode 2 for DMF and DMSO. The standard error of the regression, σ, is also shown.

	A_1	$A_2 \cdot 10^6\,\mathrm{kPa}$	$B_1 \cdot \mathrm{K}$	$B_2 \cdot 10^7\,\mathrm{kPa\,K}$	$C_1 \cdot 10^4\,\mathrm{K}^2$	σ
DMF	141.31 ± 0.66	28.6 ± 1.0	-0.520 ± 0.004	-	5.75 ± 0.07	0.018
DMSO	85.13 ± 0.06	-43.8 ± 2.4	-0.1312 ± 0.0002	1.8 ± 0.8	-	0.014

Literature comparison The existing relative permeability data for both DMF and DMSO have been compiled recently by Wohlfarth.[348,349] However, many of the values listed by Wohlfarth are replicates, in that they are pure component data in papers from the same laboratory reporting results for mixtures. Some of the pure component values reported in these papers, mostly without comment, differ by as much as 2, suggesting that they are of low accuracy. Unfortunately, the equations recommended by Wohlfarth[114] appear to have been fit to all the data without weighting for uncertainty.

The available literature results for DMF are summarized in Table A.16 and graphed in Figure A.32. At $T = 298.15\,\mathrm{K}$ and $p = 0.1\,\mathrm{MPa}$ the reported values vary from 36.7 to 40.21 with values grouped around 39.4 ± 0.4 and 37.3 ± 0.6, in the latter being in agreement with the present value of 37.26 ± 0.02. Perhaps fortuitously, the present $\varepsilon_\mathrm{r}(T)$ values agree well with the equation given by Wohlfarth.[114] For DMF $(\partial\varepsilon_\mathrm{r}/\partial p)_T = (28.6 \pm 1.0)\,\mathrm{TPa}^{-1}$ is virtually constant at temperatures of this study and also the temperature derivatives $(\partial\varepsilon_\mathrm{r}/\partial T)_p = (-0.1771 \pm 0.0058)\,\mathrm{K}^{-1}$ (at $T = 298.15\,\mathrm{K}$) and $(\partial^2\varepsilon_\mathrm{r}/\partial T^2)_p = (11.5 \pm 0.1) \cdot 10^{-4}\,\mathrm{K}^{-2}$ did not show a significant variation with pressure.
Literature values for DMSO[349] are presented in Table A.17 and Figure A.33. There is considerable scatter in these data but most are higher than the present results, although it may be noted that the greatest differences occur for the ε_r values determined by time domain spectroscopy, which have a high uncertainty. The differences between the present and literature values at $p = 0.1\,\mathrm{MPa}$ are too large to be due to water contamination even though the water content of the literature samples is often not stated and that of the present sample is very low ($< 0.2\,\mathrm{mol}\ \%\ \mathrm{H_2O}$). Further discussion of possible sources of this puzzling discrepancy is given in the following section. Values of $(\partial\varepsilon_\mathrm{r}/\partial p)_T$ for DMSO + water mixtures has been studied at 298.15 K by Uosaki et al.[350] at pressures up to 50 MPa. Graphical extrapolation of these data gave a value of $(12.3 \pm 0.3)\,\mathrm{TPa}^{-1}$ for pure DMSO. This value agrees, within the our experimental uncertainty, with the present value of $(10 \pm 20)\,\mathrm{TPa}^{-1}$, bearing in mind the limited pressure range of the present study. The value for $(\partial\varepsilon_\mathrm{r}/\partial T)_{101.3\,\mathrm{kPa}} = (-0.1312 \pm 0.002)\,\mathrm{K}^{-1}$ obtained is considerably smaller than for DMF decreases by 0.7 % at 5 MPa.

Sources of uncertainty The presence of air in the cavity would produce low permittivities, but the pressure test agreed well with the calculated compressibilities of the solvents and in addition hysteresis would be expected within a pressure cycle. Since almost no hysteresis was observed, it is unlikely that the cavity was not filled completely. Uncertainties in the temperature of $\pm 0.1\,\mathrm{K}$ result in an uncertainty in ε_r of ca. ± 0.03.
The data analysis model makes a small contribution to the overall uncertainty.[329] Eq A.8 is only valid for weak coupling to the external circuit; however on resonance, $|\hat{S}_{12}|$ was about 0.001, far from the critical value of 1, and thus coupling effects were negligible. The model is also only accurate to first order in $1/Q$; for DMF and DMSO, terms of order $(1/Q)^2$ would amount to an uncertainty in ε_r of about 0.02. However, traditional methods like capacitor techniques also have to assume equivalent circuits, and the results so obtained may be biased by parasitic capacitances in the experimental setup especially if the solvent conductivity is high.
Another source of uncertainty is the possible dispersion of the permittivity at the relatively high measurement frequencies (ca. 100 to 110 MHz for Mode 2 and 170 to 185 MHz for Mode 3). However, dielectric relaxation (DR) data[94] suggest that frequency dispersion should only produce differences from the static permittivity ranging from 0.001 to 0.004 at ambient pressure. Dispersion can however explain the difference between the values obtained from Mode 2, $\varepsilon_{\mathrm{r},2}$, and Mode 3, $\varepsilon_{\mathrm{r},3}$. Values of $\varepsilon_{\mathrm{r},2} - \varepsilon_{\mathrm{r},3}$ varying from 0.007 to 0.011 were observed, which are broadly consistent, given the uncertainties in both techniques, with the DR spectroscopic values of 0.0015 to 0.007 at temperatures from 278 K to 328 K.

Sample impurities, primarily water, can be a source of uncertainty. For DMSO and to a lesser extent DMF the addition of water leads to a higher permittivity. There are several studies in the literature on the relative permittivity of binary DMSO + water[350–353] as well as of DMF + water[354] show that increases with increase in water content. In summary the estimated standard uncertainty in ε_r is 0.1.

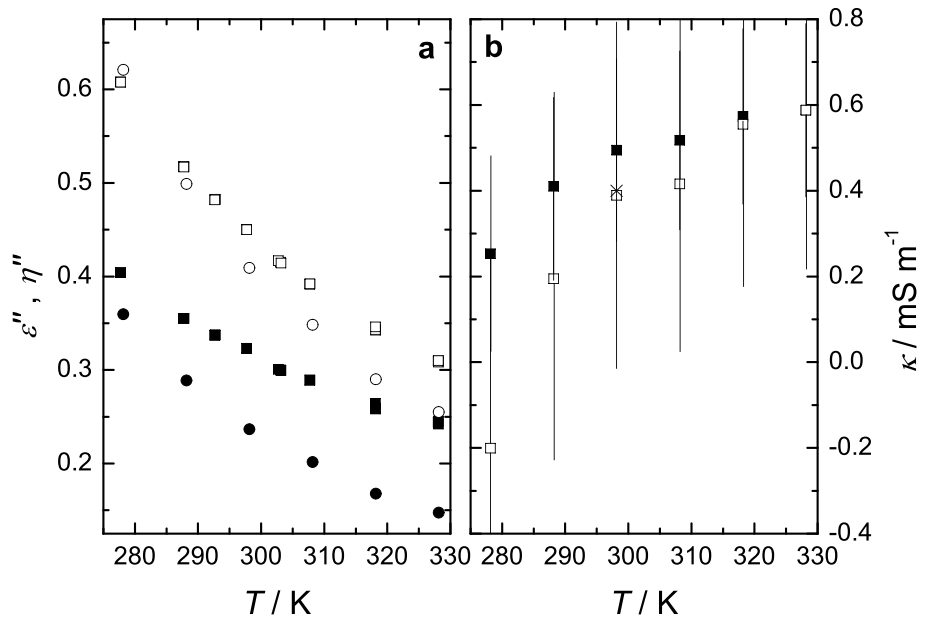

Figure A.30: (**a**) Total loss, η'' for DMF at $\approx 110\,\mathrm{MHz}$ (■) and $\approx 185\,\mathrm{MHz}$ (□) of this work and dielectric loss, ε'', taken from ref. 94 at $\approx 110\,\mathrm{MHz}$ (●) and $\approx 185\,\mathrm{MHz}$ (○). (**b**) Conductivity, κ, calculated from the difference $\eta'' - \varepsilon''$ ($= \kappa/(2\pi f \varepsilon_0)$) $\approx 110\,\mathrm{MHz}$ (■) and $\approx 185\,\mathrm{MHz}$ (□). × represents the measured value.

The conductivity, κ, of the target solvents can be estimated at these frequencies by combining the measured η'' with DR estimates of the dielectric loss, ε''. Figure A.30a shows that the difference $\eta'' - \varepsilon''$ is smaller for the Mode 3 than for the Mode 2. This is because the ohmic loss (conductivity) contribution scales with $1/f$. The uncertainty in η'' measured with the resonator is approximately 0.03 (equal to that of ε_r) whereas the uncertainty of the DR values is $\sim 2\,\%$. The conductivity calculated from the difference $\eta'' - \varepsilon''$ is shown in Figure A.30b, and has an uncertainty of $\pm 0.2\,\mathrm{mS\,m^{-1}}$ and $\pm 0.4\,\mathrm{mS\,m^{-1}}$ for Mode 2 and Mode 2, respectively . Thus, the deviation in the two conductivities determined using the two modes and the DR data is within the uncertainty of the determination. Nevertheless, the κ values derived are of the right order of magnitude for the DMF sample used. The deviation increases at lower temperatures but this may be because κ is smaller at lower temperatures causing the relative uncertainty to increase. For DMSO the DR spectrum is only available at $25\,^\circ\mathrm{C}$[95] but the slower dynamics of DMSO can explain the larger discrepancy between $\varepsilon_{r,2}$ and $\varepsilon_{r,3}$, which ranges from 0.04 to 0.05, and also the higher absolute values of ε'' compared with DMF. The conductivity values obtained from Mode 2 and Mode 3, respectively: $(2.2 \pm 1.1) \cdot 10^{-4}\,\mathrm{S\,m^{-1}}$ and $(0.5 \pm 1.3) \cdot 10^{-4}\,\mathrm{S\,m^{-1}}$, are somewhat lower than the values measured at room temperature with a conductivity probe (see above).

Kirkwood correlation factors The Kirkwood-Fröhlich theory,[54,55] derived from statistical mechanics, can be used to gain insight into the molecular interactions in a single component dipolar liquid through the Kirkwood g factor obtained from:

$$g\mu^2 = \frac{9\varepsilon_0 k_\mathrm{B} T M}{\rho N_\mathrm{A}} \frac{(\varepsilon_\mathrm{r} - \varepsilon_{\mathrm{r}\infty})(2\varepsilon_\mathrm{r} + \varepsilon_{\mathrm{r}\infty})}{\varepsilon_\mathrm{r}(\varepsilon_{\mathrm{r}\infty} + 2)^2} \tag{A.11}$$

where k_B and N_A are the Boltzmann and Avogadro constants, respectively, M is the molar mass, ρ the molar density, $\varepsilon_{\mathrm{r}\infty}$ the infinite frequency permittivity of the liquid, and μ is the dipole moment of the isolated molecule. For a random alignment of the molecular-level dipoles in a liquid $g = 1$, whereas values of $g < 1$ or $g > 1$ respectively indicate antiparallel and parallel statistical alignments. Kirkwood g factors thus yield indirect information on the structure of a liquid. For the calculation of g as a function of temperature and pressure, density data $\rho(p, T)$ as well as $\varepsilon_{\mathrm{r}\infty}$ values are required. Various available $\rho(p, T)$ data sets available for DMF[338,339] at $288.15 \leq T/\mathrm{K} \leq 313.15$ were combined and used to interpolate or extrapolate $\rho(p, T)$ to give the densities in Table A.13. For DMSO $\rho(p, T)$ was taken from ref. 340. For both DMF and DMSO, $\varepsilon_{\mathrm{r}\infty}$ was approximated as $1.1n^2$, where n is the refractive index of the liquid at the sodium D line.[355] Values of $n(p, T)$ were calculated from the Lorentz-Lorenz[34] equation:

Table A.13: Interpolated static permittivity, εr, obtained from Mode 2, densities, ρ, interpolated from literature,[338,340,356] and Kirkwood correlations factors, g, calculated according to eq A.11 for DMF and DMSO.

	ε_r		$\rho/\mathrm{kg\,dm^{-1}}$		g	
T/K	$p = 0.1\,\mathrm{MPa}$	$p = 5\,\mathrm{MPa}$	$p = 0.1\,\mathrm{MPa}$	$p = 5\,\mathrm{MPa}$	$p = 0.1\,\mathrm{MPa}$	$p = 5\,\mathrm{MPa}$
			DMF			
278.15	41.04	41.18	0.9628	0.9655	1.03	1.03
288.15	39.09	39.23	0.9535	0.9564	1.04	1.04
298.15	37.26	37.40	0.9441	0.9471	1.04	1.04
308.15	35.54	35.68	0.9346	0.9378	1.04	1.04
318.15	33.94	34.08	0.9250	0.9284	1.04	1.04
328.15	32.45	32.59	0.9153	0.9189	1.05	1.04
			DMSO			
293.15	46.68	46.72	1.0997	1.1023	1.02	1.01
298.15	46.02	46.07	1.0954	1.0980	1.03	1.02
308.15	44.71	44.77	1.0866	1.0893	1.05	1.04
318.15	43.40	43.46	1.0779	1.0807	1.06	1.06
328.15	42.09	42.16	1.0691	1.0720	1.08	1.07

$$[R] = \frac{n^2 - 1}{n^2 + 2} \cdot \frac{M}{\rho N_\mathrm{A}} \tag{A.12}$$

assuming a constant molar refraction, $[R]$ of 19.97 $cm^3\,mol^{-1}$ for DMF and 20.23 $cm^3\,mol^{-1}$ for DMSO.[357] The dipole moments of DMF and DMSO were taken from as $\mu = 3.82$ D and $\mu = 3.96$ D respectively.[114] The calculated correlation factors are summarized in Table A.13. The present correlation factors agree well with the values obtained with other experimental techniques[94,358–360] and molecular dynamic simulations.[361] At all temperatures and pressures g values are higher than unity, suggesting a marginal preference for parallel alignment of the molecular dipoles in both solvents. The effects of temperature (at $p = 0.1$ MPa) and pressure (at $T = 298.15$ K) on the correlation factor are plotted in Figure A.31. The present data indicate that g increases with increasing temperature and decreasing pressure, which yields a small negative activation energy for the dipole-dipole interaction. However, the variation of g with T and p is very small (Table A.13) so these trends may well be just a reflection of the uncertainties in $\varepsilon_{r\infty}$ and ρ. In particular, $\varepsilon_{r\infty}$ could be greater than $1.1n^2$ due to atomic polarization and the neglect of effects due to inter- and intramolecular vibrations (it is known that DMF exhibits a high frequency mode at ≈ 160 GHz[94]).

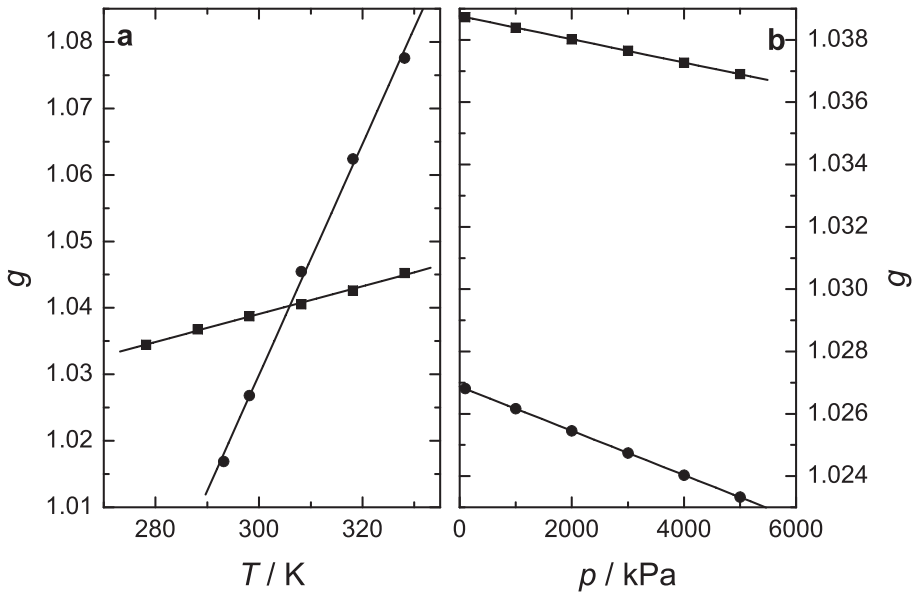

Figure A.31: Kirkwood correlation factors calculated from eq A.11 at (**a**) $p = 0.1$ MPa; (**b**) $T = 298.15$ K for DMF (■) and DMSO (●). Lines are for visual aid.

Concluding remarks Relative permittivities (ε_r) have been measured at two frequencies with a re-entrant radio-frequency resonator in the pressure range (0.1 to 5) MPa at temperatures of (278 to 328) K for DMF and (293 to 328) K for DMSO. For DMF the present values lie within the rather large spread of literature values. For DMSO the present data are lower than the majority of literature data but agree with one other study. Possible sources of uncertainty are discussed. An empirical description of $\varepsilon_r(p, T)$ is given that can be used to calculate the temperature and pressure derivatives of. These derivatives are fundamental input parameters for modeling the effects of electric fields on the solvents,

and for the theoretical description of the enthalpies, heat capacities and volumetric properties of electrolyte solutions. Kirkwood g factors calculated using the present data show only minimal dipole-dipole correlations for both DMF and DMSO.
Radio-frequency and microwave resonant cavities are probably the most precise technique currently available for measuring $\varepsilon_{\mathrm{r}}(p,T)$ of fluids of conductance $\lesssim 1 \cdot 10^{-2}\,\mathrm{S\,m^{-1}}$. The present cavity is limited in both its temperature and pressure range. Ideally for measurements of $\varepsilon_{\mathrm{r}}(p,T)$ a cavity should be usable at pressures up to at least 100 MPa and be capable of operating over a 200 K temperature range. It should have at least two modes with vacuum frequencies sufficiently high so that the instrumentation can cope with the addition of a high permittivity fluid. However, the need to keep the volume of high purity sample used to a minimum should also be kept in mind.

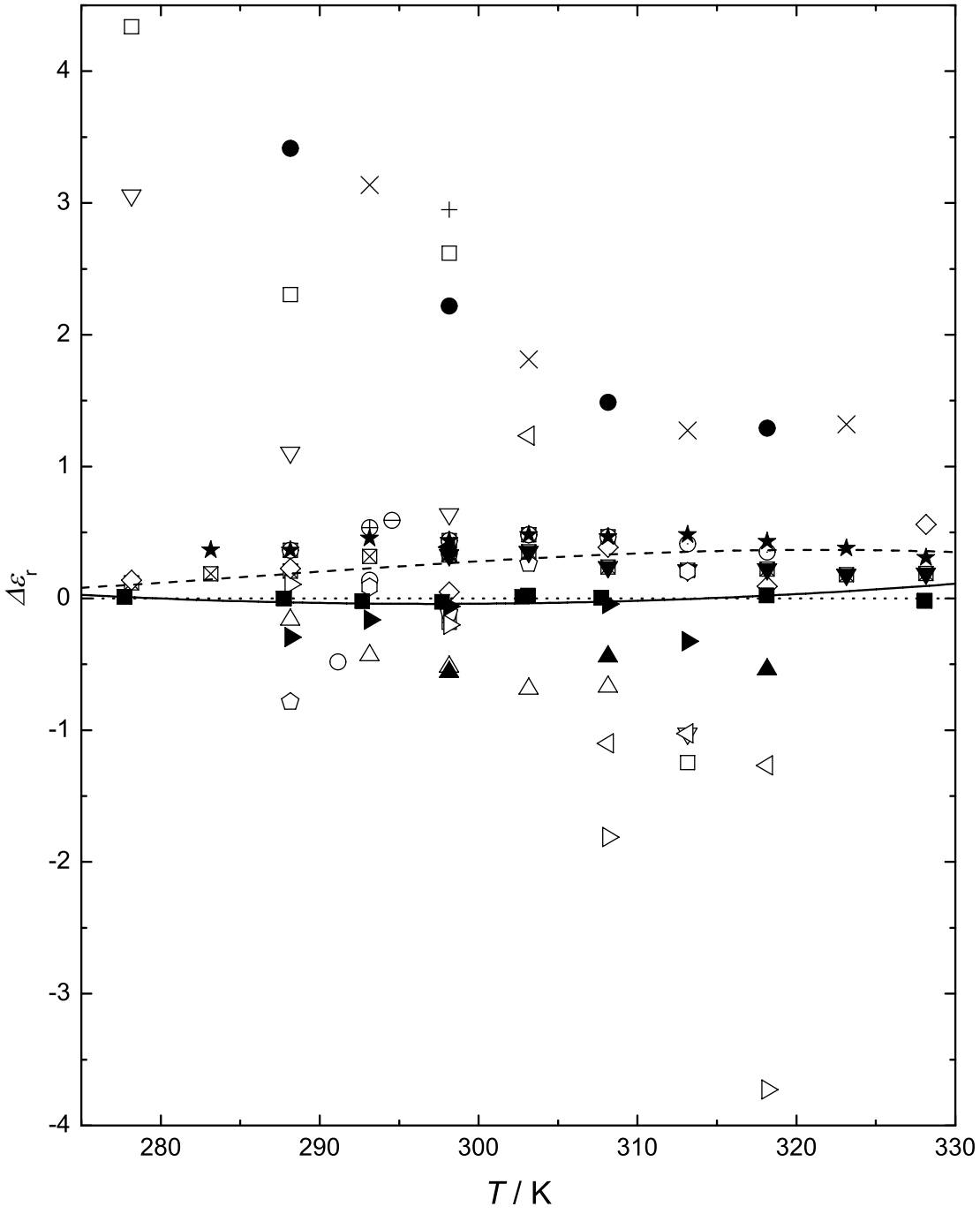

Figure A.32: Absolute deviations, $\triangle\varepsilon_\mathrm{r} = \varepsilon_\mathrm{r,lit} - \varepsilon_\mathrm{r}$, of literature data for DMF at $p = 101.3\,\mathrm{kPa}$ from permittivities, ε_r, calculated from eq A.10 of this work obtained from Mode 2: ■: measured values of this work, ⊠: Ref. 374, □: Ref. 379, ⊞: Ref. 382, ⬠: Ref. 362, ⊟: Ref. 365, ○: Ref. 368, ⊙: Ref. 370, ⊖: Ref. 373, ⊕: Ref. 372, ⊗: Ref. 376, △: Ref. 359, ▽: Ref. 378, ×: Ref. 381, +: Ref. 363, ◁: Ref. 364, ▷: Ref. 366, ◊: Ref. 94, ●: Ref. 369, ▲: Ref. 375, ▼: Ref. 377, ◀: Ref. 380, ▶: Ref. 358, ★: Ref. 367, ⬡: Ref. 371. Solid line represents $\varepsilon_\mathrm{r}(T)$ recommended in Ref. 114, dashed line recommended in Ref. 383, dotted line equals zero.

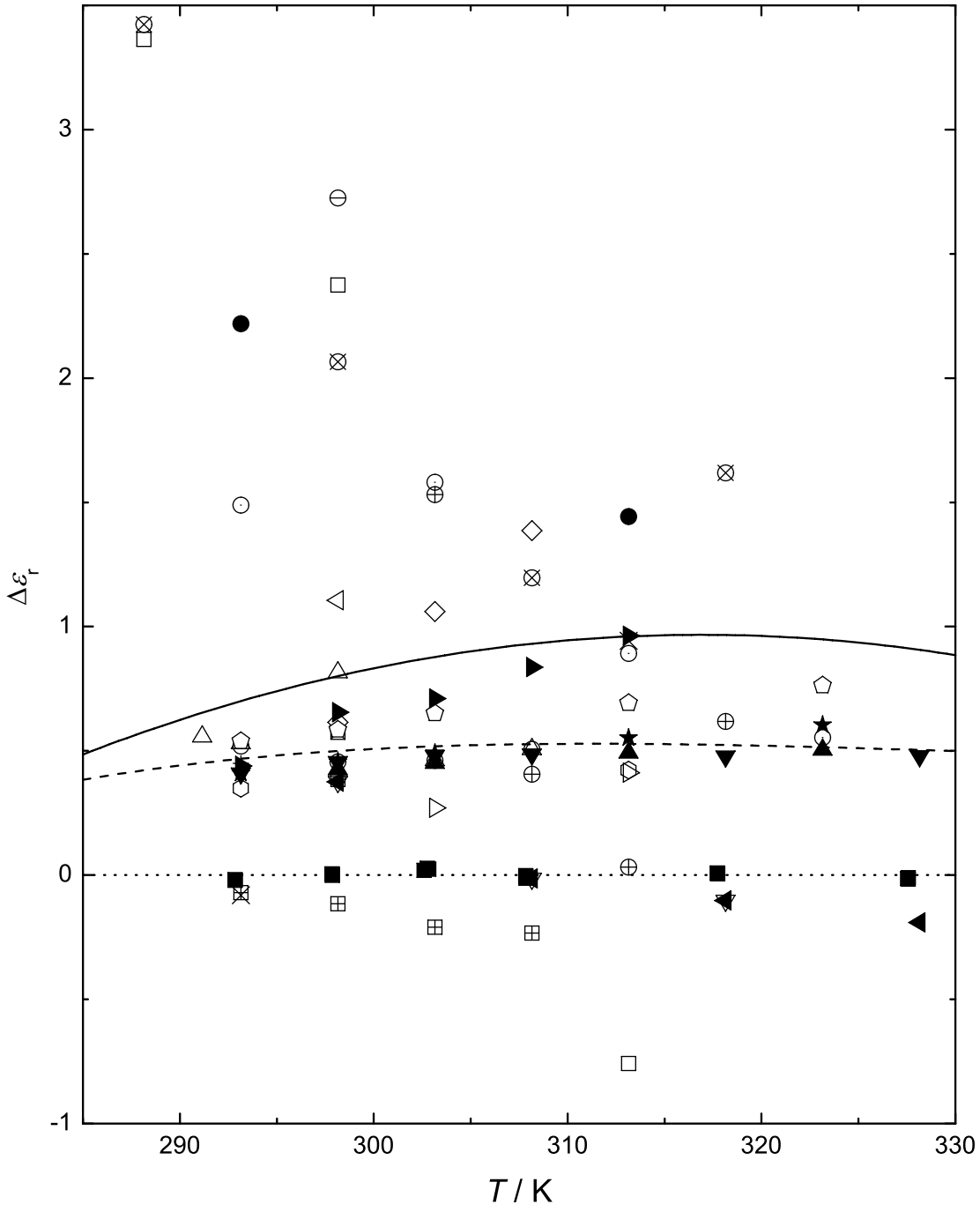

Figure A.33: Absolute deviations, $\triangle\varepsilon_r = \varepsilon_{r,lit} - \varepsilon_r$, of literature data for DMSO at $p = 101.3\,kPa$ from permittivities, ε_r, calculated from eq A.10 of this work obtained from Mode 2: ■: measured values of this work, □: Ref. 352, ⊞: Ref. 393, ⊠: Ref. 396, ⊟: Ref. 350, ○: Ref. 359, ⊙: Ref. 385, ⊖: Ref. 363, ⊕: Ref. 364, ⊗: Ref. 375, △: Ref. 391, ▽: Ref. 394, ×: Ref. 356, +: Ref. 398, ◁: Ref. 380, ▷: Ref. 386, ◊: Ref. 388, ⬠: Ref. 392, ●: Ref. 384, ▲: Ref. 397, ▼: Ref. 389, ◀: Ref. 395, ▶: Ref. 387, ★: Ref. 390, ⬡: Ref. 371. Solid line represents $\varepsilon_r(T)$ recommended in Ref. 114, dashed line recommended in Ref. 399, dotted line equals zero.

Table A.14: Temperature, T, pressure, p, and resonance frequencies, f_j, of modes $j = 2$ and $j = 3$ for N,N-dimethylformamide. $\varepsilon_{\mathrm{r},j}$ and η''_j are the real and imaginary parts of the generalized complex permittivity obtained with eq A.7.

T/K	p/kPa	f_2/MHz	$\varepsilon_{\mathrm{r},2}$	η''_2	f_3/MHz	$\varepsilon_{\mathrm{r},3}$	η''_3
277.74	110	105.248	41.138	0.404	176.165	41.128	0.608
277.74	5088	105.241	41.279	0.410	176.013	41.267	0.620
277.73	2589	105.240	41.211	0.407	176.083	41.200	0.614
277.72	111	105.246	41.140	0.404	176.161	41.130	0.608
277.72	290	105.244	41.146	0.404	176.153	41.136	0.608
277.73	589	105.245	41.153	0.405	176.147	41.143	0.609
277.73	1088	105.244	41.168	0.405	176.131	41.157	0.610
277.73	2087	105.240	41.198	0.407	176.096	41.187	0.613
277.73	3086	105.238	41.227	0.408	176.064	41.216	0.615
277.73	4086	105.236	41.256	0.409	176.032	41.245	0.618
277.73	5086	105.240	41.279	0.410	176.012	41.268	0.620
277.73	2587	105.241	41.211	0.407	176.083	41.200	0.614
277.72	106	105.246	41.140	0.404	176.162	41.129	0.608
287.71	104	107.833	39.177	0.355	180.488	39.169	0.518
287.71	5081	107.815	39.318	0.360	180.317	39.309	0.528
287.74	2581	107.828	39.244	0.357	180.410	39.235	0.522
287.77	102	107.846	39.167	0.355	180.512	39.158	0.517
287.75	281	107.842	39.175	0.355	180.500	39.166	0.518
287.74	581	107.838	39.186	0.356	180.483	39.177	0.519
287.74	1080	107.834	39.201	0.356	180.463	39.192	0.520
287.74	2079	107.828	39.231	0.357	180.423	39.223	0.522
287.75	3081	107.826	39.259	0.358	180.389	39.251	0.524
287.75	4083	107.822	39.287	0.359	180.356	39.278	0.526
287.76	5087	107.827	39.309	0.360	180.336	39.300	0.527
287.75	2587	107.830	39.243	0.357	180.413	39.234	0.522
287.75	110	107.841	39.171	0.355	180.503	39.162	0.517
292.67	109	109.153	38.229	0.337	182.698	38.220	0.482
292.68	5084	109.126	38.373	0.341	182.511	38.363	0.491
292.68	2583	109.140	38.300	0.339	182.607	38.291	0.486
292.68	105	109.155	38.228	0.337	182.702	38.219	0.482
292.68	284	109.152	38.234	0.337	182.693	38.225	0.483
292.68	583	109.150	38.243	0.338	182.680	38.234	0.483

Table A.14 continued.

T/K	p/kPa	f_2/MHz	$\varepsilon_{r,2}$	η''_2	f_3/MHz	$\varepsilon_{r,3}$	η''_3
292.68	1083	109.146	38.258	0.338	182.660	38.249	0.484
292.68	2082	109.139	38.288	0.339	182.619	38.279	0.486
292.68	3081	109.135	38.317	0.340	182.582	38.307	0.488
292.68	4080	109.129	38.346	0.340	182.543	38.337	0.489
292.68	5080	109.125	38.373	0.341	182.510	38.363	0.491
292.68	2582	109.137	38.302	0.339	182.601	38.293	0.487
292.68	103	109.153	38.229	0.338	182.700	38.220	0.482
292.68	5081	109.126	38.373	0.341	182.511	38.363	0.492
292.68	2586	109.138	38.301	0.339	182.604	38.292	0.487
292.68	108	109.154	38.228	0.338	182.701	38.219	0.483
297.68	109	110.472	37.315	0.323	184.906	37.307	0.450
297.69	288	110.471	37.320	0.323	184.898	37.312	0.450
297.69	588	110.467	37.330	0.323	184.882	37.322	0.451
297.68	1088	110.459	37.348	0.324	184.855	37.340	0.452
297.69	2089	110.454	37.376	0.324	184.816	37.368	0.453
297.71	3089	110.453	37.401	0.325	184.785	37.393	0.454
297.72	4089	110.447	37.430	0.325	184.744	37.422	0.456
297.72	5090	110.442	37.458	0.326	184.707	37.450	0.457
297.72	3090	110.455	37.400	0.325	184.788	37.392	0.454
297.71	1091	110.470	37.341	0.324	184.872	37.333	0.451
297.71	112	110.475	37.313	0.323	184.909	37.306	0.450
302.73	101	111.734	36.471	0.301	187.016	36.464	0.417
302.73	5078	111.707	36.608	0.304	186.820	36.601	0.424
302.73	2579	111.711	36.545	0.302	186.905	36.537	0.420
303.11	101	111.818	36.415	0.300	187.158	36.408	0.415
303.11	281	111.816	36.421	0.300	187.148	36.414	0.415
303.12	581	111.818	36.427	0.300	187.142	36.420	0.416
303.11	1082	111.810	36.444	0.300	187.113	36.437	0.416
303.12	2085	111.805	36.472	0.301	187.075	36.465	0.418
303.13	3088	111.797	36.501	0.301	187.031	36.494	0.419
303.13	4088	111.790	36.529	0.302	186.990	36.522	0.420
303.13	5088	111.797	36.549	0.302	186.969	36.543	0.422
303.12	2589	111.800	36.487	0.301	187.052	36.480	0.418
303.12	112	111.821	36.414	0.300	187.162	36.406	0.414

Table A.14 continued.

T/K	p/kPa	f_2/MHz	$\varepsilon_{r,2}$	η''_2	f_3/MHz	$\varepsilon_{r,3}$	η''_3
307.72	111	113.056	35.617	0.290	189.229	35.610	0.392
307.71	5089	113.016	35.759	0.292	189.011	35.752	0.399
307.71	2589	113.028	35.693	0.291	189.109	35.685	0.396
307.72	111	113.055	35.618	0.289	189.230	35.610	0.392
307.73	290	113.055	35.622	0.289	189.224	35.614	0.392
307.73	588	113.050	35.632	0.290	189.206	35.624	0.393
307.74	1088	113.048	35.645	0.290	189.187	35.637	0.393
307.76	2086	113.040	35.673	0.290	189.144	35.666	0.395
307.76	3085	113.031	35.702	0.290	189.098	35.695	0.396
307.74	4085	113.016	35.736	0.291	189.042	35.728	0.397
307.75	5084	113.024	35.754	0.291	189.023	35.747	0.399
307.72	2583	113.028	35.693	0.290	189.110	35.685	0.395
307.72	104	113.053	35.619	0.289	189.226	35.611	0.392
318.12	101	115.754	33.964	0.258	193.747	33.956	0.343
318.15	5079	115.723	34.094	0.261	193.531	34.089	0.348
318.14	2586	115.724	34.037	0.260	193.620	34.029	0.346
318.13	109	115.756	33.964	0.259	193.751	33.955	0.343
318.13	288	115.752	33.969	0.259	193.740	33.961	0.343
318.13	588	115.747	33.979	0.259	193.722	33.971	0.344
318.13	1088	115.740	33.995	0.260	193.694	33.986	0.344
318.12	2088	115.725	34.026	0.260	193.637	34.018	0.345
318.12	3088	115.711	34.056	0.261	193.582	34.048	0.346
318.12	4088	115.710	34.079	0.261	193.547	34.072	0.347
318.12	5088	115.714	34.099	0.265	193.517	34.094	0.350
318.12	2591	115.716	34.042	0.264	193.607	34.034	0.348
318.12	113	115.749	33.968	0.264	193.740	33.959	0.346
328.09	111	118.427	32.438	0.245	198.222	32.429	0.310
328.07	5087	118.362	32.580	0.246	197.947	32.574	0.314
328.07	2587	118.376	32.519	0.245	198.058	32.510	0.312
328.02	109	118.406	32.449	0.244	198.189	32.440	0.310
328.04	287	118.405	32.453	0.244	198.181	32.445	0.310
328.03	584	118.397	32.464	0.244	198.157	32.456	0.310
328.04	1084	118.389	32.479	0.244	198.127	32.471	0.310
328.05	2082	118.374	32.509	0.244	198.070	32.501	0.311
328.05	3081	118.355	32.541	0.244	198.004	32.533	0.312
328.04	4080	118.346	32.567	0.244	197.956	32.560	0.313
328.04	5079	118.349	32.587	0.244	197.923	32.582	0.313
328.05	2580	118.362	32.526	0.243	198.034	32.518	0.311
328.07	101	118.411	32.447	0.242	198.195	32.438	0.309

Table A.15: Temperature, T, pressure, p, and resonance frequencies, f_j, of modes $j = 2$ and $j = 3$ for dimethylsulfoxide. $\varepsilon_{r,j}$ and η''_j are the real and imaginary parts of the generalized complex permittivity obtained with eq A.7.

T/K	p/kPa	f_2/MHz	$\varepsilon_{r,2}$	η''_2	f_3/MHz	$\varepsilon_{r,3}$	η''_3
292.85	110	98.751	46.701	0.564	165.344	46.655	0.895
292.85	5090	98.871	46.740	0.572	165.415	46.692	0.909
292.84	2591	98.810	46.721	0.568	165.378	46.674	0.902
292.85	113	98.752	46.700	0.565	165.344	46.654	0.895
292.84	293	98.755	46.702	0.565	165.345	46.657	0.895
292.85	592	98.762	46.705	0.565	165.348	46.660	0.896
292.84	1092	98.773	46.710	0.566	165.353	46.665	0.898
292.83	2091	98.795	46.720	0.568	165.364	46.674	0.901
292.84	3091	98.820	46.727	0.569	165.379	46.682	0.904
292.84	4091	98.844	46.735	0.571	165.394	46.689	0.907
292.84	5091	98.870	46.741	0.573	165.411	46.695	0.910
292.84	2591	98.810	46.721	0.568	165.374	46.676	0.902
292.84	112	98.751	46.701	0.565	165.341	46.656	0.895
297.86	111	99.426	46.062	0.523	166.462	46.024	0.816
297.86	5090	99.537	46.109	0.529	166.516	46.070	0.829
297.86	2590	99.479	46.087	0.526	166.484	46.050	0.823
297.85	111	99.422	46.065	0.523	166.453	46.028	0.816
297.86	291	99.425	46.068	0.523	166.453	46.031	0.817
297.86	591	99.431	46.071	0.523	166.455	46.035	0.818
297.86	1089	99.441	46.077	0.524	166.458	46.041	0.819
297.86	2089	99.464	46.086	0.525	166.469	46.050	0.821
297.86	3089	99.486	46.095	0.526	166.480	46.059	0.824
297.86	4089	99.509	46.104	0.528	166.492	46.068	0.826
297.86	5091	99.533	46.113	0.529	166.507	46.075	0.829
297.85	2591	99.475	46.091	0.526	166.474	46.055	0.823
297.86	114	99.419	46.068	0.523	166.446	46.032	0.816
302.77	112	100.089	45.446	0.489	167.566	45.412	0.750
302.78	5089	100.208	45.487	0.494	167.632	45.452	0.761
302.82	2589	100.154	45.461	0.491	167.607	45.428	0.755
302.84	111	100.103	45.433	0.489	167.587	45.401	0.749
302.84	291	100.107	45.435	0.489	167.588	45.403	0.750
302.85	591	100.114	45.438	0.489	167.592	45.406	0.750
302.84	1091	100.123	45.444	0.490	167.594	45.412	0.751
302.83	2090	100.143	45.456	0.491	167.600	45.424	0.754
302.63	3090	100.141	45.488	0.493	167.569	45.456	0.758
302.62	4091	100.163	45.498	0.495	167.580	45.466	0.760
302.62	5091	100.191	45.503	0.496	167.599	45.471	0.762
302.61	2591	100.129	45.484	0.493	167.561	45.453	0.757
302.6	101	100.072	45.461	0.489	167.532	45.431	0.751

Table A.15 continued.

T/K	p/kPa	f_2/MHz	$\varepsilon_{r,2}$	η''_2	f_3/MHz	$\varepsilon_{r,3}$	η''_3
307.85	111	100.868	44.739	0.457	168.902	44.690	0.690
307.85	5087	100.964	44.801	0.461	168.927	44.752	0.700
307.84	2587	100.911	44.774	0.459	168.905	44.726	0.694
307.84	109	100.859	44.747	0.457	168.884	44.700	0.690
307.85	288	100.862	44.750	0.457	168.883	44.703	0.690
307.85	587	100.866	44.755	0.457	168.882	44.708	0.691
307.85	1086	100.874	44.763	0.458	168.882	44.715	0.692
307.85	2086	100.894	44.775	0.459	168.888	44.727	0.693
307.84	3086	100.913	44.787	0.459	168.893	44.740	0.695
307.84	4086	100.934	44.797	0.460	168.902	44.750	0.696
307.85	5085	100.956	44.807	0.461	168.912	44.759	0.699
307.85	2584	100.906	44.778	0.459	168.894	44.731	0.694
307.84	107	100.854	44.751	0.457	168.873	44.705	0.689
317.75	116	102.326	43.459	0.411	171.296	43.436	0.599
317.75	5093	102.415	43.526	0.414	171.315	43.499	0.606
317.74	2595	102.366	43.496	0.413	171.299	43.470	0.602
317.73	117	102.320	43.464	0.411	171.289	43.439	0.599
317.74	296	102.325	43.466	0.411	171.292	43.440	0.599
317.77	595	102.332	43.468	0.411	171.298	43.442	0.600
317.75	1094	102.338	43.477	0.412	171.295	43.451	0.600
317.76	2093	102.357	43.490	0.412	171.299	43.463	0.602
317.78	3092	102.379	43.499	0.413	171.309	43.473	0.603
317.78	4092	102.396	43.513	0.414	171.312	43.486	0.605
317.78	5092	102.420	43.522	0.414	171.326	43.493	0.606
317.75	2592	102.367	43.495	0.413	171.304	43.468	0.603
317.73	113	102.318	43.466	0.412	171.289	43.439	0.599
327.57	99	103.885	42.150	0.376	173.884	42.138	0.528
327.57	5073	103.972	42.218	0.379	173.895	42.204	0.534
327.54	2573	103.918	42.193	0.378	173.874	42.179	0.532
327.54	95	103.877	42.157	0.377	173.874	42.143	0.529
327.55	274	103.881	42.159	0.378	173.876	42.145	0.529
327.56	572	103.885	42.164	0.378	173.875	42.150	0.530
327.57	1071	103.893	42.171	0.378	173.875	42.157	0.530
327.56	2070	103.907	42.187	0.378	173.873	42.172	0.531
327.56	3069	103.924	42.201	0.379	173.873	42.186	0.533
327.56	4068	103.940	42.216	0.380	173.874	42.200	0.534
327.57	5067	103.968	42.221	0.380	173.894	42.204	0.535
327.57	2569	103.916	42.194	0.379	173.876	42.177	0.532
327.57	91	103.877	42.157	0.379	173.878	42.141	0.529

Table A.16: Temperature, T, literature permittivity value, $\varepsilon_{r,lit}$ and absolute deviations, $\triangle\varepsilon_r = \varepsilon_{r,lit} - \varepsilon_r$, for DMF at $p = 101.3\,kPa$ from permittivities, ε_r calculated from eq A.10 of this work obtained from Mode 2.

T / K	$\varepsilon_{r,lit}$	$\Delta\varepsilon_r$
Bass *et al.*[358]		
273.15	42.0	-0.1
288.15	38.8	-0.3
293.15	38.0	-0.2
298.15	37.2	-0.1
303.15	35.5	0.0
313.15	34.4	-0.3
333.15	31.4	-0.3
Winkelmann *et al.*[367]		
283.15	40.42	0.37
288.15	39.46	0.37
293.15	38.62	0.46
298.15	37.70	0.44
303.15	36.87	0.48
308.15	36.01	0.47
313.15	35.21	0.48
318.15	34.37	0.43
323.15	33.56	0.38
328.15	32.76	0.31
Galiyarova *et al.*[371]		
273.15	42.05	-0.01
293.15	38.25	0.09
313.15	34.93	0.20
333.15	32.00	0.25
Marchetti *et al.*[374]		
278.15	41.16	0.12
283.15	40.24	0.19
288.15	39.30	0.21
293.15	38.48	0.32
298.15	37.59	0.33
303.15	36.74	0.35
308.15	35.78	0.24
313.15	34.94	0.21
318.15	34.16	0.22
323.15	33.36	0.18
328.15	32.64	0.19
333.15	31.94	0.19
Kumbharkhane *et al.*[379]		
278.15	45.38	4.34
288.15	41.40	2.31
298.15	39.88	2.62
313.15	33.48	1.25
D'Aprano *et al.*[382]		
298.15	37.08	-0.18
Kinart[362]		
288.15	38.31	-0.78
298.15	37.15	-0.11
303.15	36.65	0.26
Kinart[365]		
288.15	39.46	0.37
298.15	37.70	0.44
303.15	36.87	0.48
308.15	36.01	0.47
Kinart *et al.*[368]		
288.15	39.46	0.37
291.15	38.05	-0.48
298.15	37.70	0.44
303.15	36.87	0.48
Kinart *et al.*[370]		
293.15	38.30	0.14
298.15	37.70	0.44
303.15	36.87	0.48
308.15	36.01	0.47
313.15	35.14	0.41
318.15	34.29	0.35
Usacheva *et al.*[372]		
293.15	38.7	0.5
Lou *et al.*[373]		
294.55	38.5	0.6
Bakshi *et al.*[376]		
298.15	37.6	0.3
Kinart *et al.*[359]		
288.15	38.93	-0.16
293.15	37.73	-0.43
298.15	36.74	-0.52
303.15	35.70	-0.69
308.15	34.87	-0.67
Ashire *et al.*[378]		
278.15	44.1	3.1
288.15	40.2	1.1
298.15	37.9	0.6
313.15	33.7	-1.0
Khirade *et al.*[381]		
293.15	41.3	3.1
303.15	38.2	1.8
313.15	36.0	1.3
323.15	34.5	1.3
Chaudhari *et al.*[363]		
298.15	40.21	2.95
Chaudhari *et al.*[364]		
303.15	37.62	1.23
308.15	34.44	-1.10
313.15	33.70	-1.03
318.15	32.67	-1.27
Pawar *et al.*[366]		
288.15	39.20	0.11
298.15	37.06	-0.20
308.15	33.73	-1.81
318.15	30.21	-3.73
Chaudhari *et al.*[369]		
288.15	42.51	3.42
298.15	39.48	2.22
308.15	37.03	1.49
318.15	35.23	1.29
Barthel *et al.*[94]		
278.15	41.18	0.14
288.15	39.32	0.23
298.15	37.31	0.05
308.15	35.93	0.39
318.15	34.03	0.09
328.15	33.01	0.56
Chaudhari *et al.*[375]		
298.15	36.7	-0.6
308.15	35.1	-0.4
318.15	33.4	-0.5
Cocchi *et al.*[377]		
298.15	37.59	0.33
303.15	36.74	0.35
308.15	35.78	0.24
313.15	34.94	0.21
318.15	34.16	0.22
323.15	33.36	0.18
328.15	32.64	0.19
333.15	31.94	0.19
Sengwa *et al.*[380]		
298.15	37.65	0.39

Table A.17: Temperature, T, literature permittivity value, $\varepsilon_{r,lit}$ and absolute deviations, $\triangle\varepsilon_r = \varepsilon_{r,lit} - \varepsilon_r$, for DMSO at $p = 101.3\,kPa$ from permittivities, ε_r, calculated from eq A.10 of this work obtained from Mode 2.

T / K	$\varepsilon_{r,lit}$	$\Delta\varepsilon_r$
Schläfer *et al.*[384]		
293.15	47.22	0.54
298.15	46.61	0.59
303.15	46.02	0.65
313.15	44.75	0.69
323.15	43.51	0.76
Garnsey *et al.*[387]		
293.15	47.12	0.44
298.15	46.68	0.66
303.15	46.08	0.71
308.15	45.55	0.84
313.15	45.02	0.96
Tommila *et al.*[390]		
293.15	47.09	0.41
298.15	46.48	0.46
303.15	45.86	0.49
313.15	44.61	0.55
323.15	43.35	0.60
333.15	42.07	0.64
Tommila *et al.*[392]		
293.15	47.22	0.54
298.15	46.61	0.59
303.15	46.02	0.65
313.15	44.75	0.69
323.15	43.51	0.76
Yao *et al.*[395]		
298.15	46.4	0.4
308.15	44.7	0.0
318.15	43.3	-0.1
328.15	41.9	-0.2
Casteel *et al.*[397]		
298.15	46.45	0.43
303.15	45.82	0.45
313.15	44.55	0.49
323.15	43.25	0.50
Galiyarova *et al.*[371]		
293.15	47.03	0.35
313.15	44.48	0.42
Jannelli *et al.*[386]		
303.15	45.64	0.27
313.15	44.47	0.41
Ritzoulis[388]		
298.15	46.64	0.62
303.15	46.43	1.06
308.15	46.10	1.39
Roch[389]		
293.15	47.09	0.41
298.15	46.48	0.46
303.15	45.85	0.48
308.15	45.2	0.49
318.15	43.88	0.48
328.15	42.57	0.48
Puranik *et al.*[352]		
288.15	50.7	3.4
298.15	48.4	2.4
313.15	43.3	-0.8
Romanowski *et al.*[393]		
293.15	46.61	-0.07
298.15	45.91	-0.11
303.15	45.16	-0.21
308.15	44.48	-0.23
Bakshi *et al.*[396]		
298.15	46.6	0.6
Uosaki *et al.*[350]		
298.15	46.41	0.39
Kinart *et al.*[359]		
293.15	47.20	0.52
298.15	46.48	0.46
303.15	45.83	0.46
308.15	45.22	0.51
Khirade *et al.*[385]		
293.15	48.17	1.49
303.15	46.95	1.58
313.15	44.95	0.89
323.15	43.30	0.55
Chaudhari *et al.*[363]		
298.15	48.75	2.23
Chaudhari *et al.*[364]		
303.15	46.90	1.53
308.15	45.12	0.41
313.15	44.09	0.03
318.15	44.02	0.62
Kinart *et al.*[391]		
291.15	47.50	0.56
293.15	47.21	0.53
298.15	46.84	0.82
303.15	45.83	0.46
308.15	45.22	0.51
Chaudhari *et al.*[375]		
288.15	50.76	3.42
298.15	48.09	2.07
308.15	45.91	1.20
318.15	45.02	1.62
Chauhan *et al.*[394]		
298.15	46.4	0.4
308.15	44.7	0.0
318.15	43.3	-0.1
Gabrielian *et al.*[356]		
293.15	46.6	0.1
313.15	45.0	0.9
333.15	43.0	1.6
Gregory *et al.*[398]		
293.15	47.13	0.45
298.15	46.49	0.47
303.15	45.86	0.49
Sengwa *et al.*[380]		
298.15	47.13	1.11

A.4 Dielectric spectroscopy of aqueous solutions of guanidinium chloride and carbonate

In the framework of this thesis, aqueous solutions of guandinium chloride and guanidinium carbonate were investigated. The following pages contain the manuscript, in preparation for the Journal of Physical Chemistry B:

Johannes Hunger, Stefan Niedermayer and Richard Buchner
Institut für Physikalische und Theoretische Chemie, Universität Regensburg, D-93040 Regensburg, Germany.

Glenn Hefter
Chemistry Department, Murdoch University, Murdoch, W.A. 6150, Australia.

Introduction

Guanidinium salts (Gdm^+, $C(NH_2)_3^+$) are widely used for biochemical and biophysical applications to destabilize or completely denature proteins in solution.[400] Despite many studies about the interaction of this cation with water and proteins, the mechanism by which proteins are destabilized is still unclear.[401,402] It is thought that the main reason is the direct interaction of the cation with the protein.[403] There are additionally indications that these salts alter the water structure, that might influence proteins.[404] Moreover, a recent combined neutron diffraction and molecular dynamics study[405] observes strong aggregation to nanometer scale aggregates of Gdm_2CO_3 in water. Interestingly, in GdmCl solutions these aggreagtes appear to be absent.[405]
To monitor aggregation, dielectric relaxation spectroscopy is a powerful tool.[23,24] In this section dielectric spectra of aqueous Gdm_2CO_3 and GdmCl solutions over a broad range of frequencies ($0.2 \leq \nu/\mathrm{GHz} \leq 89$) are reported.

Experimental section

Guanidinium carbonate (Gdm_2CO_3) was obtained from Merck, Germany (>99 %), while guanidinium chloride (GdmCl) was synthesized by adding a slight molar excess ($\sim 20\,\%$) of concentrated HCl (analytical grade, 36 %, Fisher Scientific, UK) to an aqueous solution of Gdm_2CO_3. The raw product was dried and recrystallized thrice from ethanol (analytical grade, >99.9 %, J. T. Baker, Holland). Both salts were dried under vacuum ($p < 10^{-8}$ bar) at ∼80 °C for 3 days. Aqueous solutions were prepared with degassed Millipore (Milli-Q) water several days before use.
For all solutions, $\hat{\varepsilon}(\nu)$ was determined in the frequency range $0.2 \lesssim \nu/\mathrm{GHz} \leq 89$ (HP8720D VNA setup + A & E-band interferometer, section 2.3). Raw VNA data were obtained using air, mercury and water as primary calibration standards. Calibration errors were corrected with a Padé approximation using pure dimethylacetamide and propylene carbonate as secondary standards (see section 2.3.3). All dielectric measurements were performed at $(25.00 \pm 0.05)\,^\circ\mathrm{C}$. Typical experimental spectra for aqueous solutions of GdmCl and Gdm_2CO_3 are displayed in Figures A.34 and A.35.

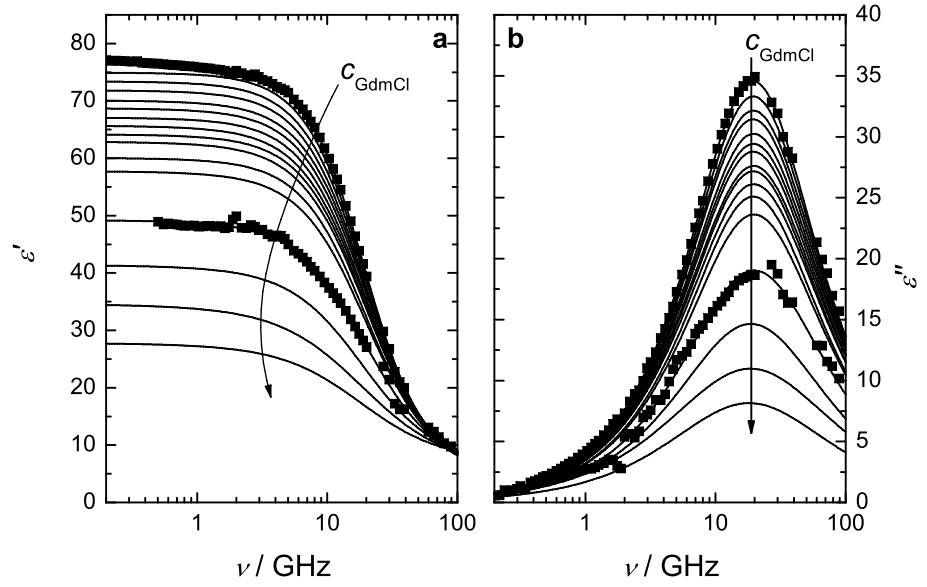

Figure A.34: (**a**) Relative permittivity, $\varepsilon'(\nu)$, and (**b**) dielectric loss, $\varepsilon''(\nu)$, spectra of aqueous solutions of GdmCl at 25 °C. Symbols show typical experimental data (others are omitted for visual clarity); lines represent the CC fit; arrows indicate increasing c_{GdmCl}.

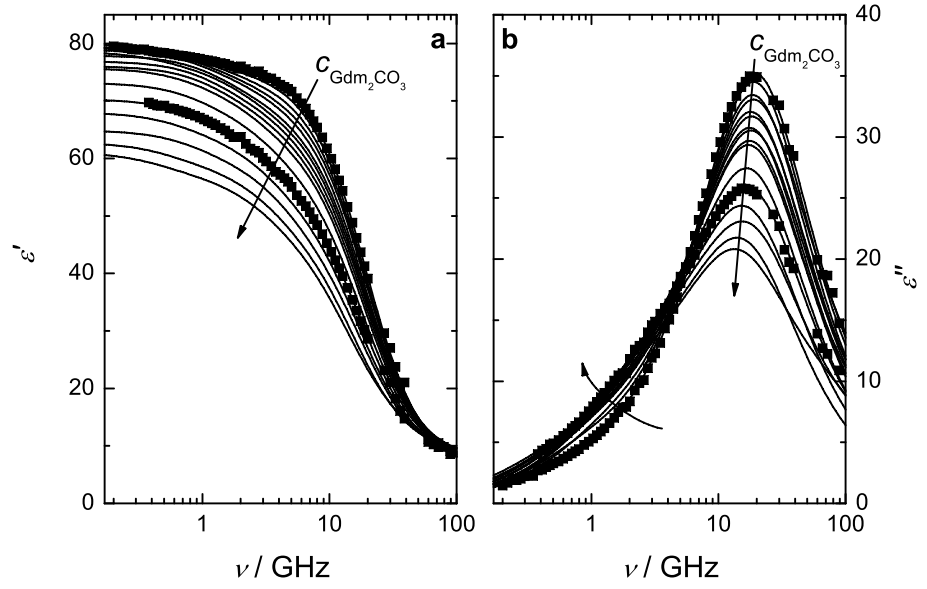

Figure A.35: (**a**) Relative permittivity, $\varepsilon'(\nu)$, and (**b**) dielectric loss, $\varepsilon''(\nu)$, spectra of aqueous solutions of Gdm_2CO_3 at 25 °C. Symbols show typical experimental data (others are omitted for visual clarity); lines represent the DDDD or DDD fit for spectra with $\nu_{\max} = 89\,\mathrm{GHz}$ or 20 GHz, respectively; arrows indicate increasing $c_{\mathrm{Gdm_2CO_3}}$.

Solution densities, ρ, and electrical conductivities of the solutions, κ, are collected in Table A.18. For the calculation of the polarizability of the Gdm^+ ion, the refractive indicies at 25 °C, n_{D}^{25}, of some aqueous GdmCl solutions were measured with an Abbé type

refractometer (Carl Zeiss Jena, Germany) using the sodium D line with an accuracy of ±0.05 %.

Table A.18: Weight fractions, w_j, molar concentrations of Gdm^+, c_{Gdm^+}, and of water, c_{H_2O} in aqueous solutions of GdmCl and Gdm_2CO_3 and the measured densities, ρ, and electrical conductivities, κ, of those solutions at 25 °C.[a]

w_{GdmCl}	ρ	c_{Gdm^+}	c_{H_2O}	κ	$w_{Gdm_2CO_3}$	ρ	c_{Gdm^+}	c_{H_2O}	κ
GdmCl					Gdm_2CO_3				
0.01483	1001.42	0.1555	54.748	1.599	0.01480	1003.87	0.1650	54.884	1.187
0.02879	1005.34[b]	0.3030	54.184	2.983[c]	0.02763	1009.45	0.3096	54.471	1.916
0.04316	1009.31[b]	0.4560	53.593	4.259[c]	0.04009	1014.83	0.4516	54.059	2.530
0.05733	1013.41	0.6082	53.014	5.409	0.05176	1019.94	0.5860	53.671	3.040
0.07240	1017.41[b]	0.7711	52.372	6.690[c]	0.06644	1026.03	0.7568	53.155	3.628
0.08538	1021.01[b]	0.9125	51.823	7.716[c]	0.08072	1032.05	0.9247	52.650	4.144
0.1004	1025.46	1.078	51.191	8.815	0.09154	1036.61	1.053	52.259	4.509
0.1150	1029.27[b]	1.239	50.549	9.959[c]	0.1036	1041.75	1.198	51.823	4.854
0.1286	1033.26	1.390	49.968	10.86	0.1179	1047.61	1.371	51.282	5.308
0.1428	1037.04[b]	1.550	49.333	11.95[c]	0.1314	1053.26	1.536	50.771	5.679
0.1663	1043.81	1.817	48.291	13.48	0.1665	1068.53[b]	1.975	49.424	6.519[c]
0.1913	1050.68[b]	2.104	47.153	15.17[c]	0.2007	1082.18	2.411	48.004	7.182
0.2855	1077.09	3.219	42.708	20.39	0.2304	1096.37[b]	2.804	46.825	7.637[c]
0.3800	1104.58[b]	4.394	38.004	24.43[c]	0.2590	1110.11	3.192	45.646	7.983
0.4789	1133.10	5.680	32.767	26.59	0.2884	1122.04[b]	3.592	44.310	8.224[c]
0.5713	1160.85	6.943	27.614	26.40	0.3089	1130.93	3.879	43.370	8.335

[a] Units: ρ in $kg\,m^{-3}$; c_{Gdm^+}, c_{H_2O} in $mol\,L^{-1}$; κ in $S\,m^{-1}$; [b] interpolated with a quadratic equation; [c] interpolated with the Casteel-Amis equation.[406]

Results and discussion

Guanidinium chloride The experimental spectra for aqueous solutions of GdmCl were best described by a single Cole-Cole equation as observed previously for aqueous NaCl and $MgCl_2$ solutions.[99,184] For spectra without IFM data (ν_{max} = 20 GHz) the spectra cover only the low-frequency part of the main absorption and the main dispersion is not completely characterized. Therefore the infinite frequency permittivity was fixed to the value obtained by linear interpolation of ε_∞ where ν_{max} = 89 GHz to avoid systematic deviations of the obtained parameters due to imperfections of the VNA data at the high frequency limit of the instrument. The parameters so obtained are summarized in Table A.19. For the 5 most dilute solutions the fit quality was improved by adding an additional Debye equation at low frequencies, with for ion pairs quite slow relaxation times (∼ 350 ps), but the amplitude was too low to reliably separate this process. This process might also be due to imperfections in the short-circuit calibration of the VNA, since such effects are

observed for samples with high dc conductivity, which is the case for aqueous GdmCl solutions.

Table A.19: Fit parameters for the observed DR spectra of aqueous solutions of GdmCl at 25 °C, assuming a CC model: static permittivities, ε, infinite frequency permittivities, ε_∞; relaxation time, τ_1, CC broadness parameter, α_1, and reduced error function of the overall fit, χ^2_r.[a]

c_{Gdm^+}	ε	τ_1	α_1	ε_∞	$\chi^2_r/10^{-4}$
0.1555	76.44	8.19	0.0213	4.98	115
0.3030	74.96	8.15	0.0324	4.86[b]	124
0.4560	73.43	8.15	0.0405	4.9[b]	138
0.6082	71.87	8.20	0.0415	4.76	258
0.7711	70.10	8.13	0.0467	4.99[b]	64
0.9125	68.75	8.13	0.0506	5.03[b]	60
1.078	67.11	8.16	0.0494	4.91	130
1.239	65.71	8.11	0.0588	5.13[b]	69
1.390	64.19	8.16	0.0529	5.14	218
1.550	62.90	8.07	0.0631	5.22[b]	90
1.817	60.08	8.15	0.0528	5.56	195
2.104	57.77	8.06	0.0653	5.41[b]	147
3.219	49.25	8.02	0.0874	5.57	383
4.394	41.39	8.51	0.112	6.41[b]	476
5.680	34.61	8.57	0.172	5.74	581
6.943	27.81	8.78	0.157	6.90	965

[a] Units: τ_j in ps; [b] $\nu_{max} = 20$ GHz, parameter fixed during fitting procedure. Fixed at the value interpolated linearly from spectra with $\nu_{max} = 89$ GHz.

The observation of a single, symmetrically broadened relaxation process for GdmCl(aq) is in accordance with the DRS results obtained for aqueous solutions of NaCl[99] and $MgCl_2$.[184] The observed process can be assigned to the cooperative reorientation of the three dimensional hydrogen bond network of water.[250] A fast water mode observed in other electrolyte solutions[250,407] could not be resolved but was subsumed with the symmetrically broadened CC mode. The relaxation time τ_1 increases with increasing salt concentration after an initial decrease. This might be interpreted as a weakening of the hydrogen bonded structure of water by GdmCl and is common for electrolytes.[184]

For the analysis of the solvent relaxation eq. 1.69 can be used to calculate the apparent (i.e., the DRS-detected) concentration of H_2O, $c^{app}_{H_2O}$, by assuming that μ_{eff,H_2O} is the same as in neat water (and thus can be calculated from the appropriate relaxation parameters of neat water, see appendix A.2) and a spherical reaction field ($A = 1/3$). Note that for

the calculation of S_1 a constant value of $\varepsilon_\infty = 4.08$ which is based on extensive high-frequency measurements of pure water (see appendix A.2) was used rather than the fit values shown in Table A.19.[408] Since water has a high relaxation amplitude and only a moderately-fast relaxation time, kinetic polarization effects[99,253,254] cannot be neglected in aqueous electrolyte solutions. These were accounted for by assuming slip boundary conditions for the correction of the amplitudes S_1.[99] From the difference between the observed apparent concentration and the analytical concentration, c_{H_2O}, effective solvation numbers, Z_{ib}, corresponding to the number of water molecules "irrotationally bound (ib)" on the DRS timescale per unit of concentration, can be obtained (eq. 4.5).

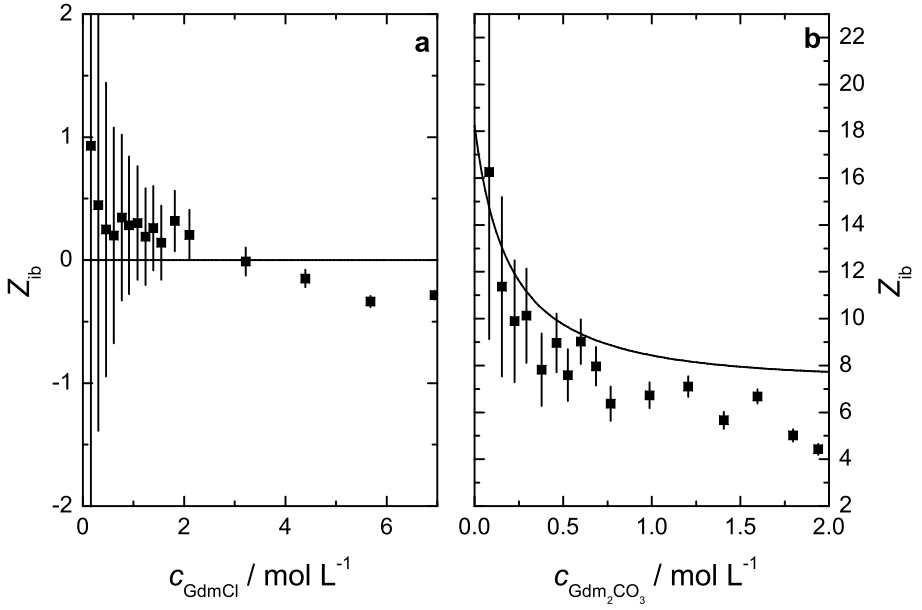

Figure A.36: Solvation numbers, Z_{ib} of aqueous solutions of (**a**) GdmCl and (**b**) Gdm_2CO_3 at 25 °C; error bars were estimated assuming $\Delta S_1 = 0.01\varepsilon$. Lines represent (**a**) $Z_{ib} = 0$ and (**b**) $Z_{ib}(CO_3^{2-})$.

Evaluation of the Z_{ib} values obtained for the aqueous GdmCl solutions (Figure A.36a) yields within the likely experimental error, effective solvation numbers ≈ 0 over the whole composition range investigated. This means that water molecules are too weakly bound to both Gdm^+ and Cl^- to disappear from the DR spectrum. The absence of a hydration shell for Cl^- at 25 °C has been observed previously.[99,251] The finding that the relaxation amplitude reproduces almost perfectly the analytical water concentration, suggests again that the above mentioned additional Debye process for dilute solutions is rather due to experimental inaccuracies than due to a real relaxation process (e.g. ion pair process).

Guanidinium carbonate In contrast to the chloride salt the Gdm_2CO_3 solutions require four relaxation processes to model the experimental spectra. The lowest χ_r^2 values were obtained with a superposition of four Debye equations (DDDD model). For spectra where only VNA data were available the highest frequency process is outside the spectral range and three Debye modes were sufficient to model the spectra (DDD model). The

parameters obtained are summarized in Table A.20. A representative spectrum with the individual contributions of the four processes is displayed in Figure A.37.

Table A.20: Fit parameters for the observed DR spectra of aqueous solutions of Gd_2CO_3 at 25 °C assuming a DDDD or DDD model for spectra with $\nu_{max} = 89$ GHz or 20 GHz, respectively: static permittivities, ε; relaxation times, τ_j, and limiting permittivities, ε_j, and ε_{j+1} of process j ($\varepsilon_1 = \varepsilon$, $\varepsilon_5 = \varepsilon_\infty$) and reduced error function of the overall fit, χ^2_r.[a]

c_{Gdm^+}	ε	τ_1	ε_2	τ_2	ε_2	τ_3	ε_4	τ_4	ε_∞	$\chi^2_r/10^{-4}$
0.1650	79.39	219	76.45	40.0[b]	75.27	8.23	5.76	0.5[b]	3.86	88
0.3096	79.91	176	75.15	40.0[b]	73.73	8.33	5.87	0.5[b]	4.62	113
0.4516[c]	79.19	129	73.81	40.0[b]	72.18	8.19	6.68	-	-	21
0.5860	79.49	156	74.29	49.7	70.38	8.34	7.10	0.80	1.78	71
0.7568[c]	78.92	143	73.72	51.0	69.35	8.58	7.32	-	-	38
0.9247	77.91	107	70.72	35.6	66.77	8.38	6.58	1.1	5.55	115
1.053[c]	78.25	191	73.99	55.8	66.23	8.60	7.43	-	-	44
1.198	76.91	116	69.95	35.6	63.52	8.34	6.82	0.59	3.87	74
1.371[c]	76.05	116	69.36	38.2	62.46	8.49	7.13	-	-	40
1.536	75.71	180	71.66	55.3	62.32	8.81	7.58	0.84	4.52	130
1.975[c]	73.16	155	67.82	43.3	57.65	8.75	7.53	-	-	26
2.411	70.29	155	64.63	37.2	52.77	8.56	7.21	0.5[b]	5.85	75
2.804[c]	68.01	209	63.42	44.8	51.74	9.28	8.32	-	-	25
3.192	64.89	167	59.46	46.3	46.29	8.79	8.06	0.5[b]	2.94	55
3.592[c]	62.78	258	58.28	44.3	46.57	9.87	8.72	-	-	27
3.879	61.05	309	56.57	48.1	45.80	11.1	11.80	1.9	4.23	45

[a] Units: τ_j in ps; [b] Parameter fixed during fitting procedure; [c] $\nu_{max} = 20$ GHz.

Solvent relaxation The two higher frequency modes (processes 3 and 4) are water relaxations: the dominant cooperative relaxation of the H-bonded water network centred at ~ 18 GHz and the much smaller-amplitude fast water process centred at ~ 300 GHz.[250] The latter is almost outside the range of the present measurements and is detectable only in the spectra recorded up to 89 GHz.

For Gdm_2CO_3(aq) solutions, the main relaxation time τ_3 increases monotonically with increasing electrolyte concentration. According to the previous section, the effective solvation numbers, Z_{ib} for Gdm_2CO_3(aq) can be obtained from the total water amplitude using eqs. (1.69) and (4.5). Note that $\varepsilon_\infty = 4.08$ was assumed throughout.[408] Com-

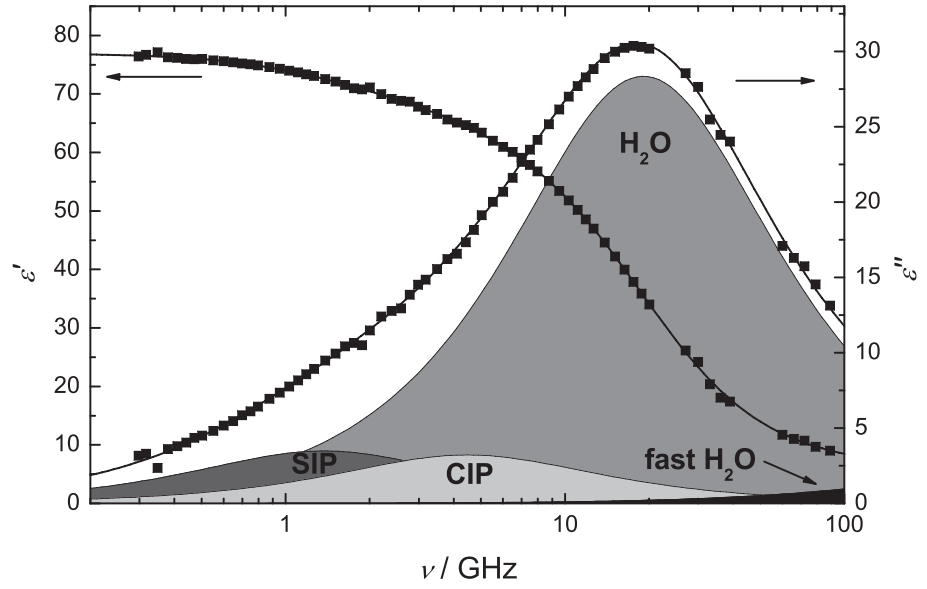

Figure A.37: Relative permittivity, $\varepsilon'(\nu)$, and loss, $\varepsilon''(\nu)$, spectrum of a representative aqueous solution of Gdm_2CO_3 at 25 °C ($c_{Gdm^+} = 1.198\ \mathrm{mol\,L^{-1}}$). Symbols represent experimental data, lines show the DDDD fit, shaded areas indicate the contributions of the solvent separated ion pair (SIP), the contact ion pair (CIP), the cooperative relaxation of water H-bond network "H_2O" and the fast water relaxation "fast H_2O".

parison with of the present solvation numbers with the hydratation number for CO_3^{2-}† in Na_2CO_3(aq)[407] reveals (Figure A.36b) that present Z_{ib} values are even lower than the $Z_{ib}(CO_3^{2-})$ in Na_2CO_3(aq), suggesting again that Gdm^+ has no stable solvation shell by means of DRS and that carbonate hydration is less than in aqueous solutions of the sodium salt.

This could hint to nanometer scale aggregates as predicted by MD simulations and found by neutron diffraction experiments,[405] but the formation of such nanometer scale aggregates would imply that the difference between the carbonate solvation in Na_2CO_3 and in Gdm_2CO_3 would increase with increasing electrolyte concentration. But since the carbonate solvation in both systems appears to be rather shifted by a constant value (Figure A.36b), nanometer scale aggregates are not the likely reason for the difference. A more straightforward explanation is the difference in the present ion-pair species: In Na_2CO_3(aq) SIPs/SSIPs are present[407] whereas in Gdm_2CO_3 the combination CIPs/SIPs is detected (see below). Therefore this difference appears to be the likely reason for the different solvation numbers, since it is expected that the formation of a CIP/SIP releases more water molecules from the hydration shell than the formation of a SIP/SSIP.

† The DR data of Ref. 407 and Ref. 99 were reanalyzed, assuming eq. (1.69) and $\varepsilon_\infty = 4.08$ throughout yielding the solvation numbers for aqueous solutions of NaCl, $Z_{ib}(NaCl, c)$, and for Na_2CO_3, $Z_{ib}(Na_2CO_3, c)$ at 25 °C. Since $Z_{ib}(Cl^-) = 0$[99,251] ($Z_{ib}(NaCl) = Z_{ib}(Na^+)$), the solvation numbers for the carbonate anion was obtained assuming the total ion density as the main criterion for the concentration dependence: $Z_{ib}(CO_3^{2-}, c) = Z_{ib}(Na_2CO_3, c) - 2Z_{ib}(NaCl, c = 3/2c_{Na_2CO_3})$

The absence of irrotationally-bound water molecules around the Gdm^+ ion is consistent with the delocalisation of the cationic charge over the whole ion, which results in a very low effective charge density. It may be further noted that the present measurements yield no evidence for "slow" water in solutions containing the guanidinium ion, which suggests that Gdm^+ ions fit into the 3-D water structure without disrupting it significantly.

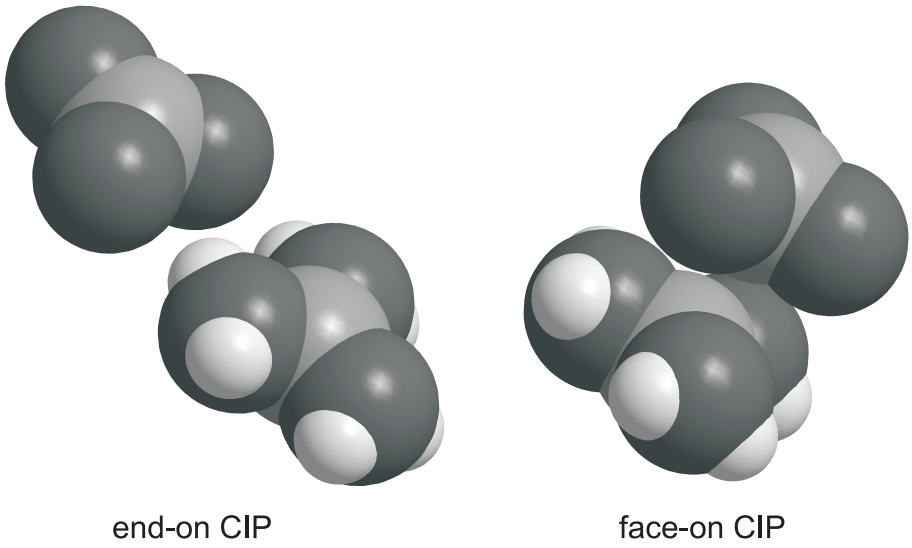

Figure A.38: Geometries of the "face-on" and the "end-on" coordination for CIPs of Gdm_2CO_3.

Solute relaxations The two lower frequency modes in Gdm_2CO_3(aq), processes 1 and 2, can be assigned to two different ion-pair species, analogous to those observed for Na_2CO_3(aq).[407] However, the possible structures of ion pairs involving Gdm^+ are more complex than those containing the monatomic closed-shell Na^+. Thus, in addition to the usual double-solvent-separated (2SIP), solvent-shared (SIP) and contact (CIP) ion-pair types, the trigonal planar, unsaturated Gdm^+ ion can coordinate to the similarly shaped and delocalized CO_3^{2-} ion either "face-on" or "end-on" (Figure A.38). The possibility of triple ions (TIs) or the larger aggregates reported by Mason *et al.*[405,409] must also be considered. None of these species can be excluded *a priori* but, since Gdm^+ is only weakly hydrated, 2SIP species are probably unlikely to form. To relate the observed relaxation times, τ_j, which are collective properties of the sample, to specific molecular properties they must be converted to microscopic relaxation times τ_j'. This can be done using the Powles-Glarum equation (eq 1.82).
The τ_j' values for different ion pairs species can be predicted from their geometry via the Stokes-Einstein-Debye (SED) theory from the effective volume of rotation of the species, $V_{\mathrm{eff},j}$ (eq. 1.78).
Comparison of the observed and calculated values of τ_j' provides a means of identifying the nature of the relaxing species. To this end the geometry of Gdm^+ was estimated using crystallographic data[410] and the van der Waals radii of Bondi[120] yielding $a = b = 311\,\mathrm{pm}$

and $c = 170\,\mathrm{pm}$ for the major and minor radii of the oblate ellipsoid, respectively. For convenience, and following previous practice,[407] both carbonate and water were assumed to be spherical,[‡] with $r_{CO_3^{2-}} = 178\,\mathrm{pm}$[411] and $r_{H_2O} = 142.5\,\mathrm{pm}$.[412] The experimentally determined mean microscopic relaxation times for the more dilute solutions $\tau_1' = (104 \pm 26)\,\mathrm{ps}$ and $\tau_2' = (30 \pm 5)\,\mathrm{ps}$ agree very well with the relaxation times of the "end-on" coordinated SIP and CIP species respectively, assuming slip boundary conditions. TIs can be ruled out, since their even larger molecular volume results in much longer relaxation times. The relaxation times predicted for the "face-on" SIP/2SIP ion pairs are significantly lower than the observed values (Table A.21) and on addition can be excluded on the basis of the weak hydration shell of Gdm^+ and also the recent molecular dynamics simulations by Mason *et al.*[405] that found there was a preference for "end-on" coordination.

Table A.21: Microscopic relaxation times, τ' of different ion pair species estimated via eq. 1.78 assuming stick and slip boundary conditions and prolate ellipsoidal geometry with major axis, r_1 and minor axis r_2.[a]

IP species	r_1	r_2	τ'_{stick}	τ'_{slip}
face-on coordination				
CIP	348	311	94	1.9
SIP	490.5	311	160	21
2SIP	633	311	250	63
end-on coordination				
CIP	489	178	89	35
SIP	631.5	178	160	80
2SIP	774	178	250	150

[a] Units: r_j in pm; τ_j' in ps.

To analyse the two ion pair processes quantitatively, the effective dipole moments of the ion pairs have to be obtained for the application of eq. 1.69. The calculation of the ion pair dipole moments yields $\mu_{CIP} = 37.1\,\mathrm{D}$ and $\mu_{SIP} = 58.8\,\mathrm{D}$ assuming spherical ions ($r_{Gdm^+} = 311\,\mathrm{pm}$[120,410], $r_{CO_3^{2-}} = 178\,\mathrm{pm}$[411], $r_{H_2O} = 142.5\,\mathrm{pm}$[412]) and the center of hydrodynamic stress as the pivot.[412] Using a different pivot (e.g. the geometric center) of the ion pairs biases the results by about 5 %, which is less than the scatter of the data. Polarizabilities of the anion and water were taken from literature ($\alpha_{H_2O} = 1.44\,\mathrm{Å}^3$, $\alpha_{CO_3^{2-}} = 4.56\,\mathrm{Å}^3$).[411,412] The polarizability of Gdm^+ was obtained from refractive index measurements of GdmCl(aq) as a function of concentration (Table A.22). Linear regression of the molar refractivity against the mole fraction of GdmCl yielded the polarizability of the salt, α_{GdmCl}. Subtraction of α_{Cl^-}[411] then gave $\alpha_{Gdm^+} = 5.97\,\mathrm{Å}^3$. Calculation of the ion pair properties is described in detail elsewhere.[412]

Insertion of the ion pair parameters into eq. 1.69 yields the ion-pair concentrations c_{CIP} and c_{SIP} (Figure A.39a). Although the data scatter considerably a coherent picture, found for

[‡]Calculations using a more realistic oblate ellipsoid for CO_3^{2-} had only a small effect on the τ' values.

Table A.22: Weight fraction, w_{GdmCl}, mole fraction of GdmCl, x_{GdmCl}, density, ρ, and refractive index, n_{D}^{25}, of aqueous solutions of GdmCl at 25 °C.[a]

w_{GdmCl}	x_{GdmCl} / 10^{-4}	ρ	n_{D}^{25}
0.004956	9.386	998.56	1.33336
0.009565	18.18	999.93	1.33419
0.01384	26.40	1001.20	1.33494
0.01937	37.12	1002.79	1.33609

[a] Units: ρ in $\mathrm{kg\,m^{-3}}$.

many associating electrolytes in solution and consistent with the well-established Eigen-Tamm mechanism is obtained. That is, at low salt concentrations the associated species are mostly SIPs, which are progressively displaced by CIPs as the salt concentration increases. From the ion-pair concentrations obtained via eq. (1.69), the concentration-dependent overall association constant $K_{\mathrm{A}} = c_{\mathrm{IP}}/(c_{\mathrm{Gdm^+}} c_{\mathrm{CO_3^-}})$ can be calculated, where $c_{\mathrm{IP}} = c_{\mathrm{CIP}} + c_{\mathrm{SIP}}$. To obtain the standard association constant at infinite dilution, K_{A}^0, the K_{A} values were fitted for convenience to a semiempirical Guggenheim-type equation (eq. 4.1)

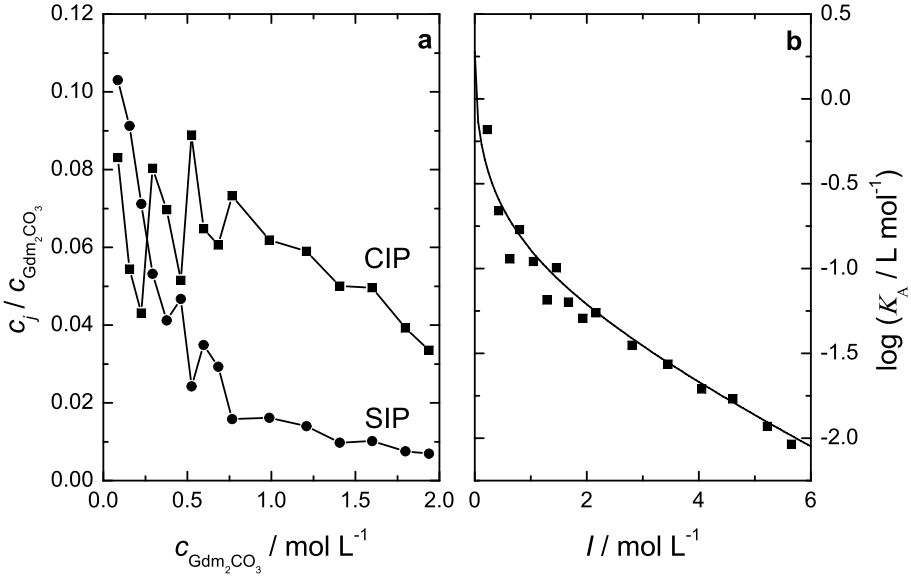

Figure A.39: (**a**) Relative concentrations of CIPs, and SIPs in aqueous solutions of Gdm_2CO_3 at 25 °C. Note that $(c_j/c_{\mathrm{Gdm_2CO_3}}) \to 0$ as $c_{\mathrm{Gdm_2CO_3}} \to 0$ (**b**) Extrapolation of the overall association constant, K_{A}, vs. ionic strength, I, according to eq. 4.1.

The extrapolation of K_{A} via eq. (4.1) (Figure A.39b) yields the rather small standard association constant of $\log(K_{\mathrm{A}}^0/\mathrm{L\,mol^{-1}}) = 0.28 \pm 0.05$. The weak association is of course

the reason for the considerable scattering of the data because the ion pair amplitudes are consequently small.

Speciation of aqueous solutions of guanidinium salts The present DRS investigation of the aqueous solutions of GdmCl and Gdm_2CO_3 indicates that their behaviour is broadly similar to the corresponding sodium salts.[99,407] For example, as for NaCl(aq),[99] no ion pairing could be detected for GdmCl(aq); on the other hand, Gdm^+ is more weakly hydrated than Na^+ since no irrotational bonding could be detected ($Z_{ib}(Gdm^+) \approx 0$, cf. $Z_{ib}(Na^+) \approx 4.5$). As for Na_2CO_3(aq),[407] two ion pair processes were detected for Gdm_2CO_3(aq) but, consistent with the weaker hydration of Gdm^+ cf. Na^+, they were attributed to SIPs and CIPs rather than the 2SIPs and SIPs observed for Na_2CO_3(aq).[407] In the same vein, the overall standard association constant $K^0_A(GdmCO_3^-(aq))$ is significantly smaller than that reported for $NaCO_3^-$(aq), which is probably just a reflection of the much lower charge density of Gdm^+.

However, the present data for GdmCl(aq) provide neither evidence for the presence of hetero ion pairs (CIPs/SIPs) nor for Gdm^+-Gdm^+ ion pairing as reported by Mason *et al.*[409] from neutron diffraction (ND) experiments and molecular dynamics (MD) simulations. On the one hand latter aggregates are not expected to appear in the DR spectra because the average lifetime of such stacked Gdm^+ pairs (29 ps[409]) is much shorter than the typical relaxation time of such aggregates and they are likely to have a very low dipole moment. On the other hand the more pronounced hetero ion-pairing (CIPs/SIPs), as found in the simulations,[409] should appear as separate modes, since such species have a large dipole moment. While the present data yield zero hydration numbers for GdmCl(aq), the MD simulation predicts in average 9.9 water molecules bound to Gdm^+. The absence of ion-pairs as well as of a stable hydration shell by means of DRS in contrast to the findings by Mason *et al.*[409] can be explained by too weak interaction of Gdm^+ with Cl^- as well as with H_2O.

The present data for Gdm_2CO_3(aq) are in accordance with the findings of Mason *et al.*[405] concerning the hetero ion-pairing (CIPs/SIPs) and the "end-on" coordination of the ion-pair species. As an additional feature of Gdm_2CO_3(aq) (in contrast to GdCl(aq)) nanometer-scale ion-aggregates are observed by neutron diffraction experiments. While it is unlikely that such aggregates are stable enough to appear as separate mode in the DR spectra due to rotation of the aggregate such nanoscale-aggragates can lead to DR process due to interfacial effects at the "phase-boundaries" of the "particle" in the solution.[34] Although such effects are not observed in the present study, such aggregates cannot be excluded on this basis, because it is necessary that either counter-ions are condensed on the surface or the static permittivity of the particle and of the surrounding medium differ considerably.

However, the observation of comparable concentration dependence of $Z_{ib}(CO_3^{2-})$ in aqueous Gdm_2CO_3 solutions and Na_2CO_3(aq) somehow contradict the presence of nanoscale aggregates, since they appear to have very few water molecules incorporated. If the aggregates are present in Gdm_2CO_3(aq) a much steeper decrease of $Z_{ib}(CO_3^{2-})$(c) would be expected. Additionally it might be argued that the persistence of discrete ion pairs in Gdm_2CO_3(aq) up to high salt concentrations makes the presence of larger aggregates unlikely.

In this context, optical Kerr-effect (OKE) spectroscopy of the present solutions would be of interest because it has recently been shown[180] that aggregates, similar to those proposed by Mason *et al.*, with low dipole moments were readily detected by OKE spectroscopy, which responds to polarizability. Due to its weak sensitivity to translational modes, in addition to the sensitivity to rotational modes, comparison with DRS could yield information on heterogeneity in electrolyte solutions.[184]

Bibliography

[1] Walden, P. *Bull. Acad. Impér. Sci. St. Pétersbourg* **1914**, *8*, 405.

[2] Wilkes, J. S.; Zaworotko, M. J. *J. Chem. Soc., Chem. Commun.* **1992**, 965.

[3] Freemantle, M. *Chem. Eng. News* **1998**, *76*, 32.

[4] MacFarlane, D. R.; Seddon, K. R. *Aust. J. Chem.* **2007**, *60*, 3.

[5] Brennecke, J. F.; Maginn, E. J. *AIChE J.* **2001**, *47*, 2384.

[6] Earle, M. J.; Esperanca, J. M. S. S.; Gilea, M. A.; Lopes, J. N. C.; Rebelo, L. P. N.; Magee, J. W.; Seddon, K. R.; Widegren, J. A. *Nature* **2006**, *439*, 831.

[7] Poole, C. F. *J. Chromatogr. A* **2004**, *1037*, 49.

[8] Yang, J. Z.; Wang, B.; Zhang, Q. G.; Tong, J. *Fluid Phase Equilib.* **2007**, *251*, 68.

[9] Wooster, T. J.; Johanson, K. M.; Fraser, K. J.; MacFarlane, D. R.; Scott, J. L. *Green. Chem.* **2006**, *8*, 691.

[10] Scammells, P. J.; Scott, J. L.; Singer, R. D. *Aust. J. Chem.* **2005**, *58*, 155.

[11] Hunger, J.; Stoppa, A.; Schrödle, S.; Hefter, G.; Buchner, R. *ChemPhysChem* **2009**, *10*, 723.

[12] Plechkova, N. V.; Seddon, K. R. *Chem. Soc. Rev.* **2008**, *37*, 123.

[13] Pârvulescu, V. I.; Hardacre, C. *Chem. Rev.* **2007**, *107*, 2615.

[14] van Rantwiijk, F.; Sheldon, R. A. *Chem. Rev.* **2007**, *107*, 2757.

[15] Haumann, M.; Riisager, A. *Chem. Rev.* **2007**, *107*, 2615.

[16] Martins, M. A. P.; Frizzo, C. P.; Moreira, D. N.; Zanatta, N.; Bonacorso, H. G. *Chem. Rev.* **2008**, *108*, 2015.

[17] Blanchard, L. A.; Hancu, D.; Beckman, E. J.; Brenecke, J. F. *Nature* **1999**, *399*, 28.

[18] El Abedin, S. Z.; Endres, F. *Acc. Chem. Res.* **2007**, *40*, 1106.

[19] Armand, M.; Enders, F.; MacFarlane, D. R.; Ohno, H.; Scrosati, B. *Nature Mater.* **2009**, *8*, 621.

[20] MacFarlane, D. R.; Forsyth, M.; Howlett, P. C.; Pringle, J. M.; Sun, J.; Annat, G.; Neil, W.; Izgorodina, E. I. *Acc. Chem. Res.* **2007**, *40*, 1165.

[21] Reichardt, C. *Green. Chem.* **2005**, *7*, 339.

[22] Moldover, M. R.; Marsh, K. N.; Barthel, J.; Buchner, R. In *Relative permittivity and refractive index*; Goodwin, A. R. H., Marsh, K. N., Wakeham, W. A., Eds.; Elsevier: Amsterdam, 2003; Vol. VI.

[23] Buchner, R.; Hefter, G. *Phys. Chem. Chem. Phys.* **2009**, *11*, 8954.

[24] Buchner, R. *Pure Appl. Chem.* **2008**, *80*, 1239.

[25] Weingärtner, H.; Knocks, A.; Schrader, E.; Kaatze, U. *J. Phys. Chem. A* **2001**, *105*, 8646.

[26] Asaki, M. L. T.; Redondo, A.; Zawodzinski, T. A.; Taylor, A. J. *J. Chem. Phys.* **2002**, *116*, 10377.

[27] Wakai, C.; Oleinikova, A.; Ott, M.; Weingärtner, H. *J. Phys. Chem. B* **2005**, *109*, 17028.

[28] Weingärtner, H. *Z. Phys. Chem.* **2006**, *220*, 1395.

[29] Schrödle, S.; Annat, G.; MacFarlane, D. R.; Forsyth, M.; Buchner, R.; Hefter, G. *Chem. Commun.* **2006**, 1748.

[30] Daguenet, C.; Dyson, P. J.; Krossing, I.; Olleinikova, A.; Slattery, J.; Wakai, C.; Weingärtner, H. *J. Phys. Chem. B* **2006**, *110*, 12682.

[31] Weingärtner, H. *Angew. Chem. Int. Ed.* **2008**, *47*, 654.

[32] Maxwell, J. C. *Treatise in Electricity and Magnetism*; Claredon Press: Oxford, 1881.

[33] Greschner, G. S. *Maxwellgleichungen*; Hüthig: Basel, 1981.

[34] Böttcher, C. F. J. *Theory of Electric Polarization*; Elsevier: Amsterdam, 1978; Vol. 1 and 2.

[35] Falkenhagen, H. *Theorie der Elektrolyte*; Hirzel: Leipzig, 1971.

[36] Ghowsi, K.; Gale, R. J. *J. Electrochem. Soc.* **1989**, *136*, 2806.

[37] Barthel, J.; Buchner, R. *Chem. Soc. Rev.* **1992**, *21*, 263.

[38] Barthel, J.; Buchner, R.; Steger, H. *Wiss. Zeitschr. THLM* **1989**, *31*, 409.

[39] Chalmers, J. M.; Griffiths, P. R. *Handbook of Vibrational Spectroscopy*; Wiley–VCH: Weinheim, 2001.

[40] Wagner, K. W. *Arch. Electrotechn.* **1914**, *2*, 371.

[41] Barthel, J.; Buchner, R.; Eberspächer, P.-N.; Münsterer, M.; Stauber, J.; Wurm, B. *J. Mol. Liq.* **1998**, *78*, 83.

[42] Debye, P. *Polar Molecules*; Dover: New York, 1930.

[43] Pellat, H. *Ann. Chim. Phys.* **1899**, *18*, 150.

[44] Cole, K. S.; Cole, R. H. *J. Chem. Phys.* **1941**, *9*, 341.

[45] Cole, K. S.; Cole, R. H. *J. Chem. Phys.* **1942**, *9*, 98.

[46] Davidson, D. W.; Cole, R. H. *J. Chem. Phys.* **1950**, *18*, 1417.

[47] Davidson, D. W.; Cole, R. H. *J. Chem. Phys.* **1951**, *19*, 1484.

[48] Havriliak, S.; Negami, S. *J. Polym. Sci., Part C* **1966**, *14*, 99.

[49] Williams, G.; Watts, D. C. *Trans. Faraday Soc.* **1970**, *66*, 80.

[50] Alvarez, F.; Alegría, A.; Colmenero, J. *Phys. Rev. B* **1993**, *47*, 125.

[51] Havriliak, S.; Havriliak, S. J. *Dielectric and Mechanical Relaxation in Materials*; Hanser: New York, 1997.

[52] Turton, D. A.; Wynne, K. *J. Chem. Phys.* **2008**, *128*, 154516.

[53] Onsager, L. *J. Am. Chem. Soc.* **1936**, *58*, 1486.

[54] Kirkwood, J. G. *J. Chem. Phys.* **1939**, *7*, 911–919.

[55] Fröhlich, H. *Theory of Dielectrics*, 2nd ed.; Oxford University Press: Oxford, 1965.

[56] Cavell, E. A. S.; Knight, P. C.; Sheikh, M. A. *Trans. Faraday Soc.* **1971**, *67*, 2225.

[57] Dote, J. L.; Kivelson, D.; Schwartz, R. N. *J. Phys. Chem.* **1981**, *85*, 2169.

[58] Dote, J. C.; Kivelson, D. *J. Phys. Chem.* **1983**, *87*, 3889.

[59] Powles, J. G. *J. Chem. Phys.* **1953**, *21*, 633.

[60] Glarum, S. H. *J. Chem. Phys.* **1960**, *33*, 639.

[61] Madden, P.; Kivelson, D. *Adv. Chem. Phys.* **1984**, *56*, 467.

[62] Moore, W. J.; Hummel, D. O. *Physikalische Chemie*; de Gruyter: Berlin, 1986.

[63] Glasstone, S.; Laidler, K. J.; Eyring, H. *The Theory of Rate Processes*; McGraw Hill: New York, 1977.

[64] Tammann, G.; Hesse, G. *Z. Anorg. Allg. Chem.* **1926**, *156*, 245.

[65] Fulcher, G. S. *J. Am. Chem. Soc.* **1925**, *8*, 339.

[66] Vogel, H. *Phys. Z.* **1921**, *22*, 645.

[67] Doolittle, A. K. *J. Appl. Phys.* **1951**, *87*, 1471.

[68] William, M. L.; Landel, R. F.; Ferry, J. D. *J. Am. Chem. Soc.* **1955**, *77*, 3701.

[69] Angell, C. A.; Smith, D. L. *J. Phys. Chem.* **1982**, *86*, 3845.

[70] Angell, C. A. *J. Non–Cryst. Solids* **1991**, *131-133*, 13.

[71] Angell, C. A. *J. Chem. Educ.* **1970**, *47*, 583.

[72] Ediger, M. D.; Angell, C. A.; Nagel, S. R. *J. Phys. Chem.* **1996**, *100*, 13200.

[73] Kauzmann, W. *Chem. Rev.* **1948**, *43*, 219.

[74] Seddon, K. R.; Stark, A.; Torres, M.-J. *Pure Appl. Chem.* **2000**, *72*, 2275.

[75] Wasserscheid, P. *Chem. Unserer Zeit* **2003**, *37*, 52.

[76] Stoppa, A.; Hunger, J.; Buchner, R. *J. Chem. Eng. Data* **2009**, *54*, 472.

[77] Cammarata, L.; Kazarian, S. G.; Slater, P. A.; Welton, T. *Phys. Chem. Chem. Phys.* **2001**, *3*, 5192.

[78] Fredlake, C. P.; Crosthwaite, J. M.; Hert, D. G.; Aki, S. N.; Brennecke, J. F. *J. Chem. Eng. Data* **2004**, *49*, 954.

[79] Holbrey, J. D.; Seddon, K. R. *J. Chem. Soc. Dalton Trans.* **1999**, *13*, 2133.

[80] Marsh, K. N.; Brennecke, J. F.; Chirico, R. D.; Frenkel, M.; Heintz, A.; Magee, J. W.; Peters, C. J.; Rebelo, L. P. N.; Seddon, K. R. *Pure Appl Chem.* **2009**, *81*, 781.

[81] MacFarlane, D. R.; Forsyth, S. A.; Golding, J.; Deacon, G. B. *Green Chemistry* **2002**, *4*, 444.

[82] Göttmann, O.; Kaatze, U.; Petong, P. *Meas. Sci. Technol.* **1996**, *7*, 525.

[83] Buchner, R.; Barthel, J. *Ber. Bunsenges. Phys. Chem.* **1997**, *101*, 1509.

[84] Cole, R. H. *J. Phys. Chem.* **1975**, *79*, 1469.

[85] Cole, R. H.; Mashimo, S.; Winsor, P. *J. Phys. Chem.* **1980**, *84*, 786.

[86] Hölzl, C. Ph.D. thesis, Regensburg, 1998.

[87] Schrödle, S. Ph.D. thesis, Regensburg, 2005.

[88] Barthel, J.; Buchner, R.; Eberspächer, P. N.; M"unsterer, M.; Stauber, J.; Wurm, B. *J. Mol. Liq.* **1998**, *78*, 83.

[89] Bertolini, D.; Cassettari, M.; Salvetti, G.; E., T.; Veronesi, S. *Rev. Sci. Instrum.* **1990**, *12*, 61.

[90] Hunger, J. Diploma Thesis, Regensburg, 2006.

[91] Barthel, J.; Bachhuber, K.; Buchner, R.; Hetzenauer, H.; Kleebauer, M. *Ber. Bunsen–Ges. Phys. Chem.* **1991**, *95*, 853.

[92] Levine, H.; Papas, C. H. *J. Appl. Phys.* **1951**, *22*, 29.

[93] Blackham, D. V. *IEEE Trans. Instr. Meas.* **1997**, *46*, 1093.

[94] Barthel, J.; Buchner, R.; Wurm, B. *J. Mol. Liq.* **2002**, *98-99*, 51–69.

[95] Barthel, J.; Bachhuber, K.; Buchner, R.; Gill, J. B.; Kleebauer, M. *Chem. Phys. Lett.* **1990**, *167*, 62.

[96] Barthel, J.; Buchner, R.; Hölzl, C.; Münsterer, M. *Z. Phys. Chem.* **2000**, *214*, 1213.

[97] Schrödle, S.; Hefter, G.; Kunz, W.; Buchner, R. *Langmuir* **2006**, *22*, 924.

[98] Pickl, H. Ph.D. thesis, Regensburg, 1998.

[99] Buchner, R.; Hefter, G.; May, P. M. *J. Phys. Chem. A* **1999**, *103*, 1.

[100] Schrödle, S. Diploma Thesis, Regensburg, 2002.

[101] Hunger, J.; Stoppa, A.; Thoman, A.; Walther, R., M.and Buchner *Chem. Phys. Lett.* **2009**, *471*, 85.

[102] Razaz, M.; Davies, J. B. *IEEE Trans. Microwave Theory Tech.* **1979**, *27*, 564.

[103] Jepsen, M. U.; Fischer, B. M.; Thoman, A.; Helm, H.; Suh, J. Y.; Lopez, R.; Haglund, R. F. *Phys. Rev. B* **2006**, *74*, 205103.

[104] Birch, J. R.; Dromey, J. D.; Lesurf, J. *NPL Report DES 69*; NPL: Teddington, UK, 1981.

[105] Fischer, B. M. Ph.D. thesis, Freiburg, 2005.

[106] Schrader, B. *Infrared and Raman Spectroscopy. Methods and Applications*; VCH: Weinheim, 1995.

[107] Birch, J. R.; Parker, T. J. In *Infrared and Millimeter Waves*; Button, K. J., Ed.; Academic Press: New York, 1979; Vol. 2.

[108] Bertie, J. E.; Zhang, S. L.; Keefe, C. D. *Vib. Spectr.* **1995**, *8*, 215.

[109] Kanwal, R. P. *Linear Integral Equations: theory and technique*; Birkhäuser: Boston, 1996.

[110] Gregory, A. P.; Clarke, R. N. *Meas. Sci. Technol.* **2007**, *18*, 1372.

[111] Hunger, J.; Stoppa, A.; Hefter, G.; Buchner, R. *J. Phys. Chem. B* **2008**, *112*, 12913.

[112] Bevington, P. R. *Data Reduction and Error Analysis for the Physical Sciencies*; McGraw–Hill: New York, 1969.

[113] Steger, H. Ph.D. thesis, Regensburg, 1988.

[114] *CRC–Handbook of Chemistry and Physics*, 85th ed.; Lide, D. R., Ed.; CRC–Press: Boca Raton, USA, 2004.

[115] Wachter, R.; Barthel, J. *Ber. Bunsenges. Phys. Chem.* **1979**, *83*, 634.

[116] Wachter, R.; Barthel, J. *Electrochim. Acta* **1971**, *16*, 713.

[117] Barthel, J.; Wachter, R.; Gores, H. J. In *Modern Aspects of Electrochemistry*; Conway, B. E., Bockris, J. O., Eds.; Plenum: New York, 1979; Vol. 13.

[118] Stewart, J. J. P. MOPAC2009, Stewart Computational.

[119] Ahlrichs, R.; Bär, M.; Häser, M.; Horn, H.; Kömel, C. *Chem. Phys. Lett.* **1989**, *162*, 165.

[120] Bondi, A. *J. Phys. Chem.* **1964**, *68*, 441.

[121] Klamt, A.; Schüürmann, G. *J. Chem. Soc. Perkin Trans.* **1993**, *2*, 799.

[122] Senda, N. Winmostar, version 3.78f (URL: http://winmostar.com/).

[123] Chang, H.; Li, J.; Fayer, M. D. *J. Chem. Phys.* **2003**, *119*, 13017.

[124] Giraud, G.; Gordon, C. M.; Dunkin, I. A.; Wynne, K. *J. Chem. Phys.* **2003**, *119*, 464.

[125] Shirota, H.; Funston, A. M.; Wishart, J. F.; Castner, E. W. *J. Chem. Phys.* **2005**, *122*, 184512.

[126] Xiao, D.; Rajian, J. R.; Li, S.; Bartsch, R. A.; Quitevis, E. L. *J. Phys. Chem. B* **2006**, *110*, 16174.

[127] Xiao, D.; Rajian, J. R.; Cady, A.; Li, S.; Bartsch, R. A.; Quitevis, E. L. *J. Phys. Chem. B* **2007**, *111*, 4669.

[128] Antony, J. H.; Dölle, A.; Mertens, D.; Wasserscheid, P.; Carper, W. R.; Wahlbeck, P. G. *J. Phys. Chem. A* **2005**, *109*, 6676.

[129] Wulf, A.; Ludwig, R.; Sasisanker, P.; Weingärtner, H. *Chem. Phys. Lett.* **2007**, *439*, 323.

[130] Antony, J. H.; Mertens, D.; Dölle, A.; Wasserscheid, P.; Carpenter, W. R. *ChemPhysChem* **2003**, *4*, 588.

[131] Huang, J. F.; Chen, P. Y.; Sun, I. W.; Wang, S. P. *Inorg. Chim. Acta* **2001**, *320*, 7.

[132] Heimer, N. E.; Wilkes, J. S.; Wahlbeck, P. G.; Carper, W. R. *J. Phys. Chem. A* **2006**, *110*, 868.

[133] Hyun, B. R.; Dzyuba, S. V.; Bartsch, R. A.; Quitevis, E. L. *J. Phys. Chem. B* **2002**, *106*, 7579.

[134] Dahl, K.; Sando, G. M.; Fox, D. M.; Sutto, T. E.; Owrutsky, J. C. *J. Chem. Phys.* **2005**, *123*, 084504.

[135] Halder, M.; Sanders Headley, L.; Mukherjee, P.; Song, X.; Petrich, J. W. *J. Phys. Chem. A* **2006**, *110*, 8623.

[136] Jin, H.; Baker, G. A.; Arzhantsev, S.; Dong, J.; Maroncelli, M. *J. Phys. Chem. B* **2007**, *111*, 7291.

[137] Arzhantsev, S.; Jin, H.; Baker, G. A.; Maroncelli, M. *J. Phys. Chem. B* **2007**, *111*, 4978.

[138] Hui, J.; Xiang, L.; Maroncelli, M. *J. Phys. Chem. B* **2007**, *111*, 13473.

[139] Kashyap, H. K.; Biswas, R. *J. Phys. Chem. B* **2008**, *112*, 12431.

[140] Triolo, A.; Russina, O.; Hardacre, C.; Nieuwenhuyzen, M.; Gonzalez, M. A.; Grimm, H. *J. Phys. Chem. B* **2005**, *109*, 22061.

[141] Inamura, Y.; Yamamuro, O.; Hayashi, S.; Hamaguchi, H. *Physica B* **2006**, *385*, 732.

[142] Triolo, A.; Mandanici, A.; Russina, O.; Rodriguez-Mora, V.; Cutroni, M.; Hardacre, C.; Nieuwenhuyzen, M.; Bleif, H. J.; Keller, L.; Ramos, M. A. *J. Phys. Chem. B* **2006**, *110*, 21357.

[143] Koeberg, M.; Wu, C.-C.; Kim, D.; Bonn, M. *Chem. Phys. Lett.* **2007**, *439*, 60.

[144] Yamamoto, K.; Tani, M.; Hangyo, M. *J. Phys. Chem. B* **2007**, *111*, 4854.

[145] Schrödle, S.; Annat, G.; MacFarlane, D. R.; Forsyth, M.; Buchner, R.; Hefter, G. *Aust. J. Chem.* **2007**, *60*, 6.

[146] Stoppa, A.; Hunger, J.; Thoman, A.; Helm, H.; Hefter, G.; Buchner, R. *J. Phys. Chem. B* **2008**, *112*, 4854.

[147] Weingärtner, H.; Sasisanker, P.; Daguenet, C.; Dyson, P. J.; Krossing, I.; Olleinikova, A.; Slattery, J.; Schubert, T. *J. Phys. Chem. B* **2007**, *111*, 4775.

[148] Schröder, C.; Wakai, C.; Weingärtner, H.; Steinhauser, O. *J. Chem. Phys.* **2007**, *126*, 084511.

[149] Rivera, A.; Rössler, E. A. *Phys. Rev. B* **2006**, *73*, 212201.

[150] Rivera, A.; Brodin, A.; Pugachev, A.; Rössler, E. A. *J. Chem. Phys.* **2007**, *126*, 114503.

[151] Sangoro, J.; Iacob, C.; Serghei, A.; Naumov, S.; Galvosas, P.; Kärger, J.; Wespe, C.; Bordusa, F.; Stoppa, A.; Hunger, J.; Buchner, R.; Kremer, F. *J. Chem. Phys.* **2008**, *128*, 214509.

[152] Horng, M. L.; Gardecki, J. A.; Papazyan, A.; Maroncelli, M. *J. Chem. Phys.* **1995**, *99*, 17311.

[153] Jin, H.; O'Hare, B.; Dong, J.; Arzhantsev, S.; Baker, G. A.; Wishart, J. F.; Benesi, A. J.; Maroncelli, M. *J. Phys. Chem. B* **2008**, *112*, 81.

[154] Widegren, J. A.; Saurer, E. M.; Marsh, K. N.; Magee, J. W. *J. Chem. Thermodyn.* **2005**, *37*, 569.

[155] Tokuda, H.; Tsuzuki, S.; Susan, M. A. B. H.; Hayamizu, K.; Watanabe, M. *J. Phys. Chem. B* **2006**, *110*, 19593.

[156] Vila, J.; Gines, P.; Pico, J. M.; Franjo, C.; Jimenez, E.; Varela, L. M.; Cabeza, O. *Fluid Phase Equilib.* **2006**, *242*, 141.

[157] Yoshida, Y.; Baba, O.; Saito, G. *J. Phys. Chem. B* **2007**, *111*, 4742.

[158] Zhou, Q.; Wang, L.-S.; Chen, H.-P. *J. Chem. Eng. Data* **2006**, *51*, 905.

[159] Troncoso, J.; Cerdeiriña, C. A.; Sanmamed, Y. A.; Romaní, L.; Rebelo, L. P. N. *J. Chem. Eng. Data* **2006**, *51*, 1856.

[160] Kumelan, J.; Pérez-Salado Kamps, S.; Tuma, D.; Maurer, G. *J. Chem. Thermodyn.* **2006**, *38*, 1396.

[161] Sanmamed, Y. A.; González-Salgado, D.; Troncoso, J.; Cerdeiriña, C. A.; Romaní, L. *Fluid Phase Equilib.* **2007**, *252*, 96.

[162] Navia, P.; Troncoso, J.; Romani, L. *J. Chem. Eng. Data* **2007**, *52*, 1369.

[163] Shiflett, M. B.; Yokozeki, A. *J. Chem. Eng. Data* **2007**, *52*, 1302.

[164] Leong, T. I.; Sun, I. W.; Deng, M. J.; Wu, C. M.; Chen, P. Y. *J. Electrochem. Soc* **2008**, *155*, F55.

[165] Kato, R.; Gmehling, J. *J. Chem. Thermodyn.* **2005**, *37*, 603.

[166] Lunkenheimer, P.; Schneider, U.; Brand, R.; Loidl, A. *Contemp. Phys.* **2000**, *41*, 15.

[167] Zhu, J.; Chen, J.; Li, C.; Fei, W. *J. Chem. Eng. Data* **2007**, *52*, 812.

[168] Marcus, Y. *The Properties of Solvents*; Wiley: Chichester, 1999.

[169] Zhang, S.; Li, X.; Chen, H.; Wang, J.; Zhang, J.; Zhang, M. *J. Chem. Eng. Data* **2004**, *49*, 760.

[170] Schröder, C.; Haberler, M.; Steinhauser, O. *J. Chem. Phys.* **2008**, *128*, 134501.

[171] Hunger, J.; Stoppa, A.; Buchner, R.; Hefter, G. *J. Phys. Chem. B* **2009**, *113*, 9527.

[172] Wu, J.; Stark, J. P. W. *Meas. Sci. Technol.* **2006**, *17*, 781.

[173] Crowhurst, L.; Mawdsley, P. R.; Perez-Arlandis, J. M.; Salter, P. A.; Welton, T. *Phys. Chem. Chem. Phys.* **2003**, *5*, 2790.

[174] Huang, M. M.; Weingärtner, H. *ChemPhysChem* **2008**, *9*, 2172.

[175] Kosmulski, M.; Marczewska-Boczkowska, K.; Żukowski, P.; Subocz, J.; Saneluta, C. *Croat. Chem. Acta* **2007**, *80*, 461.

[176] Schröder, C.; Rudas, T.; Steinhauser, O. *J. Chem. Phys.* **2006**, *125*, 244506.

[177] Qiao, B.; Krekeler, C.; Berger, R.; Delle Site, L.; Holm, C. *J. Phys. Chem. B* **2008**, *112*, 1743.

[178] Schröder, C.; Rudas, T.; Neumayer, G.; Gansterer, W.; Steinhauser, O. *J. Chem. Phys.* **2007**, *127*, 044505.

[179] Shim, Y.; Kim, J. K. *J. Phys. Chem. B* **2008**, *112*, 11028.

[180] Turton, D. A.; Hunger, J.; Stoppa, A.; Hefter, G.; Thoman, A.; Walther, M.; Buchner, R.; Wynne, K. *J. Am. Chem. Soc.* **2009**, *131*, 11140.

[181] Buchner, R.; Barthel, J.; Stauber, J. *Chem. Phys. Lett.* **1999**, *306*, 57.

[182] McDonagh, P. M.; Reardon, J. F. *J. Solution Chem.* **1996**, *25*, 607.

[183] Köddermann, T.; Ludwig, R.; Paschek, D. *ChemPhysChem* **2008**, *9*, 1851.

[184] Turton, D. A.; Hunger, J.; Hefter, G.; Buchner, R.; Wynne, K. *J. Chem. Phys.* **2008**, *128*, 161102.

[185] Shim, Y.; Kim, H. J. *J. Phys. Chem. B* **2008**, *112*, 11028.

[186] Böwing, A. G.; Jess, A. *Chem. Eng. Sci.* **2007**, *62*, 1760.

[187] Mečiarová, M.; Cigáň, M.; Toma, S.; Gáplovský, A. *Eur. J. Org. Chem.* **2008**, 4408.

[188] Hut'ka, M.; Toma, S. *Monatsh. Chemie* **2007**, *138*, 1175.

[189] Marszałł, M. P.; Bączek, T.; Kaliszan, R. *J. Sep. Sci.* **2006**, *29*, 1138.

[190] Alonso, L.; Arce, A.; Francisco, M.; Soto, A. *Fluid Phase Equilib.* **2008**, *270*, 97.

[191] Arce, A.; Rodriguez, H.; Soto, A. *Green Chem.* **2007**, *9*, 247.

[192] Fröba, A. P.; Kremer, H.; Leipertz, A. *J. Phys. Chem. B* **2008**, *112*, 12410.

[193] Fernández, A.; Torrecila, J. S.; García, J.; Rodríguez, F. *J. Chem. Eng. Data* **2007**, *52*, 1979.

[194] Fernández, A.; García, J.; Torrecila, J. S.; Oliet, M.; Rodríguez, F. *J. Chem. Eng. Data* **2008**, *53*, 1518.

[195] Gomez, E.; Gonzalez, B.; Calvar, N.; Tojo, E.; Dominguez, A. *J. Chem. Eng. Data* **2006**, *51*, 2096.

[196] Singh, T.; Kumar, A. *J. Phys. Chem. B* **2008**, *112*, 12968.

[197] Shirota, H.; Castner, E. W. *J. Phys. Chem. B* **2005**, *109*, 21576.

[198] de Andrade, J.; Böes, E. S.; Stassen, H. *J. Phys. Chem. B* **2008**, *112*, 8966.

[199] Kelkar, M. S.; Shi, W.; Maginn, E. J. *Ind. Eng. Chem. Res.* **2008**, *47*, 9115.

[200] Fumino, K.; Wulf, A.; Ludwig, R. *Angew. Chem. Int. Ed.* **2008**, *47*, 8731.

[201] Fumino, K.; Wulf, A.; Ludwig, R. *Angew. Chem. Int. Ed.* **2008**, *47*, 3830.

[202] Schröder, C.; Hunger, J.; Stoppa, A.; Buchner, R.; Steinhauser, O. *J. Chem. Phys.* **2008**, *129*, 184501.

[203] Schröder, C.; Steinhauser, O. *J. Chem. Phys.* **2008**, *128*, 224503.

[204] Lamoureux, G.; Harder, E.; Vorobyov, I. V.; Roux, B.; MacKerell, A. D. *Chem. Phys. Lett.* **2006**, *418*, 245.

[205] Buchner, R.; Chen, T.; Hefter, G. *J. Phys. Chem. B* **2004**, *108*, 2365.

[206] Stoppa, A.; Asenbaum, A.; Buchner, R. unpublished results.

[207] Kumar, A. *J. Solution Chem.* **2008**, *37*, 203.

[208] Wagner, M.; Stanga, O.; Schrör, W. *Phys. Chem. Chem. Phys.* **2004**, *6*, 4421.

[209] Lohse, P. W.; Bürsing, R.; Lenzer, T.; Oum, K. *J. Phys. Chem. B* **2008**, *112*, 3048.

[210] Turton, D. A.; Wynne, K. *Phys. Chem. Chem. Phys.* **2009**, *submitted*, .

[211] Talaty, E. R.; Raja, S.; Storhaug, V. J.; Dölle, A.; Carper, W. R. *J. Phys. Chem. B* **2004**, *108*, 13177.

[212] Blochowicz, T.; Tschirwitz, C.; Benkhof, S.; Rössler, E. A. *J. Chem. Phys.* **2003**, *118*, 7544.

[213] Lunkenheimer, P.; Loidl, A. *Chem. Phys.* **2002**, *284*, 205.

[214] Stoppa, A.; Buchner, R.; Hefter, G. *J. Mol. Liq.*, in press (doi: 10.1016/j.molliq.2009.05.001).

[215] Avent, A. G.; Chaloner, P. A.; Day, M. P.; Seddon, K. R.; Welton, T. *J. Chem. Soc. Dalton Trans.* **1994**, *23*, 3405.

[216] Canongia Lopes, J. N. A.; Pádua, A. A. H. *J. Phys. Chem. B* **2006**, *110*, 3330.

[217] Triolo, A.; Russina, O.; Bleif, H. J.; Di Cola, E. *J. Phys. Chem. B* **2007**, *111*, 4641.

[218] Kuang, Q. L.; Zhang, J.; Wang, Z. G. *J. Phys. Chem. B* **2007**, *111*, 9858.

[219] Wasserscheid, P.; Welton, T. *Ionic Liquids in Synthesis*; Wiley–VCH: Weinheim, 2003.

[220] Welton, T. *Chem. Rev.* **1999**, *99*, 2071.

[221] Endres, F.; El Abedin, S. Z. *Phys. Chem. Chem. Phys.* **2006**, *8*, 2101.

[222] Leys, J.; Wübbenhorst, M.; Menon, C. P.; Rajesh, R.; Thoen, J.; Nockermann, P.; Thijs, B.; Binnemans, K.; Longuemart, S. *J. Chem. Phys.* **2008**, *128*, 064509.

[223] Zhao, Y.; Gao, S.; Wang, J.; Tang, J. *J. Phys. Chem. B* **2008**, *112*, 2031.

[224] Greaves, T.; Weerawardena, A.; Krodkiewska, I.; Drummond, C. *J. Phys. Chem. B* **2008**, *112*, 896.

[225] Fujii, K.; Soejima, Y.; Kyoshoin, Y.; Fukuda, S.; Kanzaki, R.; Umebayashi, Y.; Yamaguchi, T.; Ishiguro, S.; Takamuku, T. *J. Phys. Chem. B* **2008**, *112*, 4329.

[226] Rivera-Calzada, A.; Kaminski, K.; Leon, C.; Paluch, M. *J. Phys. Chem. B* **2008**, *112*, 3110.

[227] Dupont, J. *J. Braz. Chem. Soc.* **2004**, *15*, 341.

[228] Hardacre, C.; Holbrey, J. D.; McMath, S. E. J.; Bowron, D. T.; Soper, A. K. *J. Chem. Phys.* **2003**, *118*, 273.

[229] Akilan, C.; Rohman, N.; Hefter, G.; Buchner, R. *ChemPhysChem* **2006**, *7*, 2319.

[230] Marcus, Y.; Hefter, G. *Chem. Rev.* **2006**, *106*, 4585.

[231] Köddermann, T.; Wertz, C.; Heintz, A.; Ludwig, R. *ChemPhysChem* **2006**, *7*, 1944.

[232] Wu, X.; Liu, Z.; Huang, S.; Wang, W. *Phys. Chem. Chem. Phys.* **2004**, *7*, 2771.

[233] Hefter, G. *Pure Appl. Chem* **2006**, *78*, 1571.

[234] Buchner, R. Dielectric Spectroscopy of Solutions. In *Novel Approaches to the Structure and Dynamics of Liquids: Experiments, Theories and Simulations*; Samios, J., Durov, V. A., Eds.; Kluwer: Dordrecht, 2004; Vol. 133, p 265.

[235] Wang, J.; Tian, Y.; Zhao, Y.; Zhuo, K. *Green Chem.* **2003**, *5*, 618.

[236] Zahn, S.; Uhlig, F.; Thar, J.; Spickermann, C.; Kirchner, B. *Angew. Chem. Int. Ed.* **2008**, *47*, 3639.

[237] Katsuta, S.; Imai, K.; Kudo, Y.; Takeda, Y.; Seki, H.; Nakakoshi, M. *J. Chem. Eng. Data* **2008**, *53*, 1528.

[238] Buchner, R. *J. Mol. Liq.* **1995**, *63*, 55.

[239] Gutman, V. *The Donor–Acceptor Approach to Molecular Interactions*; Plenum: New York, 1978.

[240] Krummen, M.; Wasserscheid, P.; Gmehling, P. *J. Chem. Eng. Data* **2002**, *47*, 1411.

[241] Vij, J. K.; Hufnagel, F.; Grochulski, T. *J. Mol. Liq.* **1991**, *49*, 1.

[242] Buchner, R.; Chen, T.; Hefter, G. *J. Phys. Chem. B* **2004**, *108*, 2365.

[243] Dorbritz, S.; Ruth, W.; Kragel, U. *Adv. Synth. Catal.* **2005**, *347*, 1273.

[244] Susan, M. A. B. H.; Noda, A.; Mitsushima, S.; Watanabe, M. *Chem. Commun.* **2003**, 938.

[245] Kordesch, K.; Simader, G. *Fuel Cells and Their Applications*; VCH: Weinheim, 1996.

[246] Rosamilia, A. E.; Strauss, C. R.; Scott, J. L. *Pure Appl. Chem.* **2007**, *79*, 1869.

[247] MacFarlane, D. R.; Pringle, J. M.; Johansson, K. M.; Forsyth, S. A.; Forsyth, M. *Chem. Commun.* **2006**, 1905.

[248] de Souza, R. F.; Padilha, J. C.; Gonçalves, R. S.; Dupont, J. *Electrochem. Commun.* **2003**, *5*, 728.

[249] Guan, W.; Yang, J. Z.; Li, L.; Wang, H.; Zhang, Q. G. *Fluid Phase Equilib.* **2006**, *239*, 161.

[250] Fukasawa, T.; Sato, T.; Watanabe, J.; Hama, Y.; Kunz, W.; Buchner, R. *Phys. Rev. Lett.* **2005**, *95*, 197802.

[251] Buchner, R.; Hölzl, C.; Stauber, J.; Barthel, J. *Phys. Chem. Chem. Phys.* **2002**, *4*, 2169.

[252] Laage, D.; Stirnemann, G.; Hynes, J. T. *J. Phys. Chem. B* **2009**, *113*, 2428.

[253] Hubbard, J. B.; Onsager, L. *J. Chem. Phys.* **1977**, *67*, 4850.

[254] Hubbard, J. B. *J. Chem. Phys.* **1978**, *68*, 1649.

[255] Spickermann, C.; Thar, J.; Lehmann, S. B. C.; Zahn, S.; Hunger, J.; Buchner, R.; Hunt, P. A.; Welton, T.; Kirchner, B. *J. Chem. Phys.* **2008**, *129*, 104505.

[256] Jeon, Y.; Sung, J.; Kim, D.; Seo, C.; Cheong, H.; Ouchi, Y.; Ozawa, R.; Hamaguchi, H. *J. Phys. Chem. B* **2008**, *112*, 923.

[257] Raju, S. G.; Balasubramanian, S. *J. Phys. Chem. B* **2009**, *113*, 4799.

[258] Bešter-Rogač, M.; Hunger, J.; Stoppa, A.; Buchner, R. unpublished results.

[259] Barthel, J. M. G.; Krienke, H.; Kunz, W. *Physical Chemistry of Electrolyte Solutions – Modern Aspects*; Springer: New York, 1998.

[260] Bešter-Rogač, M.; Neueder, R.; Barthel, J. *J. Solution Chem.* **1999**, *28*, 1071.

[261] Wang, H.; Wang, J.; Zhang, S.; Pei, Y.; Zhuo, K. *ChemPhysChem* **2009**, *10*, 2516.

[262] Katayanagi, H.; Nishikawa, K.; Shimozaki, H.; Miki, K.; Westh, P.; Koga, Y. *J. Phys. Chem. B* **2004**, *108*, 19451.

[263] Miki, K.; Westh, P.; Nishikawa, K.; Koga, Y. *J. Phys. Chem. B* **2005**, *109*, 9014.

[264] Nakakoshi, M.; Ishihara, S.; Utsumi, H.; Seki, H.; Koga, Y.; Nishikawa, K. *Chem. Phys. Lett.* **2006**, *427*, 87.

[265] Neumayer, G.; Schröder, C.; Steinhauser, O. *J. Chem. Phys.* **2009**, *131*, 174509.

[266] Dominguez-Vidal, A.; Kaun, N.; Ayora-Caãnada, M. J.; Lendl, B. *J. Phys. Chem. B* **2007**, *111*, 4446.

[267] Takamuku, T.; Kyoshoin, Y.; Shimomura, T.; Kittaka, S.; Yamaguchi, T. *J. Phys. Chem. B* **2009**, *113*, 10817.

[268] Zhang, L.; Xu, Z.; Wang, Y.; Li, H. *J. Phys. Chem. B* **2008**, *112*, 6411.

[269] Umebayashi, Y.; Jiang, J.-C.; Shan, Y.-L.; Lin, K.-H.; Fujii, K.; Seki, S.; Ishiguro, S.-I.; Lin, S. H.; Chang, H.-C. *J. Chem. Phys.* **2009**, *130*, 124503.

[270] Chang, C.-H.; Jiang, Y.-C.; Liou, Y.-C.; Hung, C.-H.; Lai, T.-Y.; Lin, S. H. *J. Chem. Phys.* **2008**, *129*, 044506.

[271] Almásy, L.; Turmine, M.; Perera, A. *J. Phys. Chem. B* **2008**, *112*, 2382.

[272] Malham, I. B.; Letellier, P.; Turmine, M. *J. Phys. Chem. B* **2006**, *110*, 14212.

[273] Villagrán, C.; Deetlefs, M.; Pitner, W. R.; Hardacre, C. *Anal. Chem.* **2004**, *76*, 2118.

[274] Wagner, M.; Stanga, O.; Schrör, W. *Phys. Chem. Chem. Phys.* **2003**, *5*, 3943.

[275] Lin, H. M.; Tien, H.-Y.; Hone, Y.-T.; Lee, M. J. *Fluid Phase Equilib.* **2007**, *253*, 130.

[276] Fernandez, P.; Schrödle, S.; Buchner, R.; Kunz, W. *ChemPhysChem* **2003**, *4*, 1065.

[277] Petersen, C.; Tielrooij, K. J.; Bakker, H. J. *J. Chem. Phys.* **2009**, *130*, 214511.

[278] Moreno, M.; Castiglione, F.; Mele, A.; Pasqui, C.; Raos, G. *J. Phys. Chem. B* **2008**, *112*, 7826.

[279] Buchner, R.; Barthel, J. *J. Mol. Liq.* **1995**, *63*, 55.

[280] Liu, W.; Cheng, L.; Zhang, A.; Wang, H.; Yu, M. *J. Mol. Liq.* **2008**, *140*, 68.

[281] Tsuzuki, S.; Tokuda, H.; Hayamizu, K.; Watanabe, M. *J. Phys. Chem. B* **2005**, *109*, 16474.

[282] Vij, J. K.; Reid, C. J.; Evans, G. J.; Ferrario, M.; Evans, M. W. *Adv. Mol. Relax. Interact. Process.* **1982**, *22*, 79.

[283] Teixeira, J.; Bellissent-Funel, M. C.; Chen, S. H. *J. Mol. Liq.* **1991**, *48*, 123.

[284] Ellison, W. J.; Lamkaouchi, K.; Moreau, J. M. *J. Mol. Liq.* **1986**, *68*, 171.

[285] Rønne, C.; Thrane, L.; Åstrand, P. O.; Wallqvist, A.; Mikkelsen, K. V.; Keiding, S. R. *J. Chem. Phys.* **1997**, *107*, 5319.

[286] Rønne, C.; Keiding, S. R. *J. Mol. Liq.* **2002**, *101*, 199.

[287] Rønne, C.; Åstrand, P. O.; Keiding, R. *Phys. Rev. Lett.* **1999**, *82*, 2888.

[288] Yada, H.; Nagai, M.; Tanaka, K. *Chem. Phys. Lett.* **2008**, *464*, 166.

[289] Yada, H.; Nagai, M.; Tanaka, K. *Chem. Phys. Lett.* **2009**, *473*, 279.

[290] Stauber, J. Ph.D. thesis, Regensburg, 1996.

[291] Zelsmann, H. R. *J. Mol. Struct.* **1995**, *350*, 94.

[292] Fecko, C. J.; Eaves, J. D.; Tokmakoff, A. *J. Chem. Phys.* **2002**, *117*, 1139.

[293] Ratajska-Gadomska, B.; Białkowski, B.; Gadomski, W.; Radzewicz, C. *Chem. Phys. Lett.* **2006**, *429*, 575.

[294] Okada, K.; Yao, M.; Hiejima, Y.; Kohno, H.; Kajihara, Y. *J. Chem. Phys.* **1999**, *110*, 3029.

[295] Yeh, Y.; Mou, C. Y. *J. Phys. Chem. B* **1999**, *103*, 3699.

[296] Rezus, Y. L.; Bakker, H. J. *J. Chem. Phys.* **2005**, *123*, 114502.

[297] Bakker, H. J.; Rezus, Y. L. A.; Timmer, R. L. A. *J. Phys. Chem. A* **2008**, *112*, 112.

[298] Foggi, P.; Bellini, M.; Kien, D. P.; Vercuque, I.; Righini, R. *J. Phys. Chem. A* **1997**, *101*, 7029.

[299] Winkler, K.; Lindner, J.; Bürsing, H.; Vöhringer, P. *J. Chem. Phys.* **2000**, *113*, 4674.

[300] Ellison, W. J. *J. Phys. Chem. Ref. Data* **2007**, *36*, 1.

[301] Hasted, J. B.; Husain, S. K.; Frescura, F. A. M.; Birch, J. R. *Infrared Phys.* **1987**, *27*, 11.

[302] Barajas, O.; Buckmaster, H. A. *J. Phys. Condens. Matter* **1992**, *4*, 8671.

[303] Richards, M. G. M.; Sheppard, R. J. *Meas. Sci. Tech.* **1991**, *2*, 663.

[304] Grant, E. H.; Szwarnowski, S.; Sheppard, R. J. *J. Am. Chem. Soc.* **1981**, 47.

[305] Grant, E. H.; Shack, R. *Brit. J. Appl. Phys.* **1967**, *18*, 1807.

[306] Grant, E. H. *J. Chem. Phys.* **1957**, *6*, 1575.

[307] Sheppard, R. J. Ph.D. thesis, London, 1971.

[308] Pottel, R.; Kaatze, U.; Uhlendorf, V. Brussels, 1980, Final report to the B.C.R. project 148.

[309] Kaatze, U. *J. Chem. Eng. Data* **1989**, *34*, 371.

[310] Nightingale, N. R. V.; Teixeira, J.; Geiger, A.; Blumberg, R. L. *Physica* **1981**, *106A*, 260.

[311] Stuchly, M. A.; Stuchly, S. S. *IEEE Trans. Instrum. Meas.* **1980**, *29*, 176.

[312] Zafar, M. S.; Hasted, J. B.; Chamberlain, J. *Nature Phys. Sci.* **1973**, *243*, 106.

[313] Simpson, O.; Bean, B. L.; Perkowitz, S. *J. Opt. Soc. Am.* **1979**, *69*, 1723.

[314] Blue, M. D. *J. Geophys. Res.* **1980**, *85*, 1101.

[315] Czumaj, Z. *Mol. Phys.* **1990**, *69*, 787.

[316] Pinkley, L. W.; Sethna, P. P.; Williams, D. *J. Opt. Soc. Am.* **1977**, *67*, 494.

[317] Laage, D.; Hynes, T. *J. Phys. Chem. B* **2008**, *112*, 14230.

[318] Laage, D. *J. Phys. Chem. B* **2009**, *113*, 2684.

[319] Laage, D.; Hynes, J. T. *Proc. Natl. Acad. Sci. U.S.A.* **2007**, *104*, 11167.

[320] Laage, D.; Hynes, J. T. *Chem. Phys. Lett.* **2006**, *433*, 80.

[321] Yamaguchi, T.; Chong, S.-H.; Hirata, F. *J. Chem. Phys.* **2002**, *116*, 2502.

[322] Drude, P.; Nernst, W. *Z. Phys. Chem* **1894**, *15*, 79–85.

[323] Brouillette, D.; Perron, G.; Desnoyers, J. E. *J. Solution Chem.* **1998**, *27*, 151–182.

[324] Marcus, Y.; Hefter, G. *J. Solution Chem.* **1999**, *28*, 575–592.

[325] Chadwick, S. S. *Ulmann's Encyclopedia of Industrial Chemistry*; Wiley–VCH: Weinheim, 2006.

[326] Goodwin, A. R. H.; Mehl, J. B.; Moldover, M. R. *Rev. Sci. Instrum.* **1996**, *67*, 4294–4303.

[327] Kandil, M. E.; Marsh, K. N.; Goodwin, A. R. H. *J. Chem. Eng. Data* **2007**, *52*, 1660–1671.

[328] May, E. F.; Edwards, T. J.; Mann, T. J.; Edwards, C. *Int. J. Thermophys.* **2003**, *24*, 1509–1525.

[329] May, E. F.; Edwards, T. J.; Mann, T. J.; Edwards, C.; Miller, R. C. *Fluid Phase Equilib.* **2001**, *185*, 339–347.

[330] May, E. F.; Edwards, T. J.; Mann, T. J.; Edwards, C. *Fluid Phase Equilib.* **2004**, *215*, 245–252.

[331] May, E. F.; Miller, R. C.; Goodwin, A. R. H. *J. Chem. Eng. Data* **2002**, *47*, 102–105.

[332] Kandil, M. E.; Marsh, K. N.; Goodwin, A. R. H. *J. Chem. Eng. Data* **2008**, *53*, 1056–1065.

[333] Goodwin, A. R. H.; Mehl, J. B. *Int. J. Thermophys.* **1997**, *18*, 795–806.

[334] Hamelin, J.; Mehl, J. B.; Moldover, M. R. *Int. J. Thermophys.* **1998**, *19*, 1359–1380.

[335] Hamelin, J.; Mehl, J. B.; Moldover, M. R. *Rev. Sci. Instrum.* **1998**, *69*, 255–260.

[336] Anderson, G. S.; Miller, R. C.; Goodwin, A. R. H. *J. Chem. Eng. Data* **2000**, *45*, 549–554.

[337] http://physics.nist.gov/cuu/Constants/index.html.

[338] Zúñiga Moreno, A.; Galicia-Luna, L. A. *J. Chem. Eng. Data* **2005**, *50*, 1224–1233.

[339] García-Giménez, P.; Martínez-López, J. F.; Blanco, S. T.; Velasco, I.; Otín, S. *J. Chem. Eng. Data* **2007**, *52*, 2368–2374.

[340] Petitet, J. P.; Bezot, P.; Hesse-Bezot, C. *Physica B* **1988**, *153*, 181–190.

[341] http://www.kayelaby.npl.co.uk/general_physics/2_6/2_6_1.htm.

[342] Schmidt, J. W.; Gavioso, R. M.; May, E. F.; Moldover, M. R. *Phys. Rev. Lett.* **2007**, *98*, 254504.

[343] McCarty, R. D.; Arp, V. D. *Adv. Cryo. Eng.* **1990**, *35*, 1465–1475.

[344] Harvey, A. H.; Lemmon, E. W. *Int. J. Thermophys.* **2005**, *26*, 31.

[345] Lemmon, E. W.; McLinden, M. O.; Huber, M. L. *Reference Fluid Thermodynamic and Transport Properties*, NIST Standard Reference Database 23, Version 8.0 (Nat. Inst. Stands. Technol., Gaithersburg, Maryland, 2007).

[346] Bauccio, M. *ASM Metals Reference Book*; ASM International: Ohio, 1993.

[347] Fernández, D. P.; Goodwin, A. R. H.; Lemmon, E. W.; Levelt Sengers, J. M. H.; Williams, R. C. *J. Phys. Chem. Ref. Data* **1997**, *26*, 1125–1166.

[348] Wohlfarth, C. Dielectric Constant of *N*,*N*–dimethylformamide. In *Static Dielectric Constants of Pure Liquids and Binary Liquid Mixtures*; Madelung, O., Ed.; Springer: Berlin, 2008; Vol. 17, pp 175–182.

[349] Wohlfarth, C. Dielectric Constant of Dimethylsulfoxide. In *Static Dielectric Constants of Pure Liquids and Binary Liquid Mixtures*; Madelung, O., Ed.; Springer: Berlin, 2008; Vol. 17, pp 140–143.

[350] Uosaki, Y.; Kitaura, S.; Moriyoshi, T. *J. Chem. Eng. Data* **1997**, *42*, 580–584.

[351] Kaatze, U.; Pottel, R.; Schäfer, M. *J. Phys. Chem.* **1989**, *93*, 5623–5627.

[352] Puranik, S. M.; Kumbharkhane, A. C.; Mehrotra, S. C. *J. Chem. Soc. Faraday Trans.* **1992**, *88*, 433–435.

[353] Cooke, C.; McCallum, C.; Pethybridge, A. D.; Prue, J. E. *Electrochim. Acta* **1975**, *20*, 591–598.

[354] Kim, J. I.; Cecal, A.; Born, H. J.; Gomaa, E. A. *Z. Phys. Chem. N.F.* **1978**, *110*, 209–227.

[355] Stokes, R. H.; Marsh, K. N. *J. Chem. Thermodyn.* **1976**, *8*, 709–723.

[356] Gabrielian, L. S.; Markarian, S. A. *J. Mol. Liq.* **2004**, *112*, 137–140.

[357] Pacak, P. *J. Solution Chem.* **1987**, *16*, 71–77.

[358] Bass, S. J.; Nathan, W. I.; Meighan, R. M.; Cole, R. H. *J. Phys. Chem.* **1964**, *68*, 509–515.

[359] Kinart, C. M.; Bald, A.; Kinart, W. J.; Kolasinski, A. *Phys. Chem. Liq.* **1998**, *36*, 245–256.

[360] Prestbbo, E. W.; McHale, J. L. *J. Chem. Eng. Data* **1984**, *29*, 387–389.

[361] Richardi, J.; Krienke, H.; Fries, P. H. *Chem. Phys. Lett.* **1997**, *273*, 115–121.

[362] Kinart, C. M. *Phys. Chem. Liq* **1994**, *27*, 25–32.

[363] Chaudhari, A.; More, N. M.; Mehrotra, S. C. *Bull. Korean Chem. Soc.* **2001**, *22*, 257–361.

[364] Chaudhari, A.; Patil, C. S.; Shankarwar, A. G.; Arbad, B. R.; Mehrotra, S. C. *J. Korean Chem. Soc.* **2001**, *45*, 201–206.

[365] Kinart, C. M. *Phys. Chem. Liq* **1994**, *27*, 115–121.

[366] Pawar, V. P.; Mehrotra, S. C. *J. Solution Chem.* **2002**, *31*, 577–588.

[367] Winkelmann, J.; Quitzsch, K. *Z. Phys. Chem.* **1972**, *250*, 355–366.

[368] Kinart, C. M.; Kinart, W. J. *Pol. J. Chem.* **1994**, *68*, 349–357.

[369] Chaudhari, A.; Chauhari, H.; Mehrotra, S. *J. Chin. Chem. Soc* **2002**, *49*, 489–494.

[370] Kinart, C. M.; Kinart, W. J. *Phys. Chem. Liq.* **1996**, *31*, 1–8.

[371] Galiyarova, N. M.; Shakhparonov, M. I. *Fiz. Fiz. Khim. Zhidk.* **1980**, *4*, 57–74.

[372] Usacheva, T. M.; Lifanova, N. V.; Zhuravlev, V. I.; Shakhparonov, M. I. *Colloid J.* **1996**, *58*, 91–95.

[373] Lou, J.; Hatton, T. A.; Laibinis, P. E. *J. Phys. Chem. A* **1997**, *101*, 5262–5268.

[374] Marchetti, A.; Preti, C.; Tagliazucchi, M.; Tassi, L.; Tosi, G. *J. Chem. Eng. Data* **1991**, *36*, 365–368.

[375] Chaudhari, A.; Chaudhari, H. C.; Mehrotra, S. C. *Bull. Korean Chem. Soc.* **2004**, *25*, 1403–1407.

[376] Bakshi, M. S.; Kaur, G. *J. Chem. Eng. Data* **1997**, *42*, 298–300.

[377] Cocchi, M.; Franchini, G.; Marchetti, A.; Pigani, L.; Seeber, R.; Tassi, L.; Ulrici, A.; Zanardi, C.; Zanni, P. *Ann. Chim.* **2004**, *94*, 165–176.

[378] Ahire, S.; Chaudhari, A.; Lokhande, M.; Mehrotra, S. C. *J. Chem. Eng. Data* **1998**, *27*, 993–1008.

[379] Kumbharkhane, A. C.; Puranik, S. M.; Mehrota, S. C. *J. Solution Chem.* **1993**, *22*, 219–229.

[380] Sengwa, R. J.; Madhvi,; Sankhla, S. S. *Phys. Chem. Liq.* **2006**, *44*, 637–653.

[381] Khirade, P. W.; Chaudhari, A.; Shinde, J. B.; Helambe, S. N.; Mehrotra, S. C. *J. Solution Chem.* **1999**, *28*, 1031–1043.

[382] D'Aprano, A.; Sesta, B.; Princi, A.; Filipi, C.; Iammarino, M. *J. Electroanal. Chem.* **1994**, *365*, 119–124.

[383] Barthel, J.; Neueder, R. Conductivities, transference numbers, and limiting ionic conductivities of protophilic H-bond donor and aprotic solvents. I: Amides. In *Electrolyte Data Collection (Part 1g)*; Kreysa, G., Ed.; DECHEMA: Frankfurt, 2001; Vol. XII, p 131.

[384] Schläfer, H. L.; Schaffernicht, W. *Angew. Chem.* **1960**, *72*, 618–626.

[385] Khirade, P. W.; Chaudhari, A.; Shinde, J. B.; Helambe, S. N.; Mehrotra, S. C. *J. Chem. Eng. Data* **1999**, *44*, 879–881.

[386] Jannelli, L.; Pansini, M. *J. Chem. Eng. Data* **1985**, *30*, 428–431.

[387] Garnsey, R.; Prue, J. E. *Trans. Faraday Soc.* **1968**, *64*, 1206–1218.

[388] Ritzoulis, G. *Can. J. Chem.* **1989**, *67*, 1105–1108.

[389] Roch, H. Ph.D. thesis, Regensburg, 1991.

[390] Tommila, E.; Autio, T. *Suom. Kemistil. B* **1969**, *42*, 107–110.

[391] Kinart, C. M.; Kinart, W. J.; Cwiklinska, A.; Checinska, D. *J. Mol. Liq.* **2002**, *100*, 65–80.

[392] Tommila, E.; Yrjoevuori, R. *Suom. Kemistil. B* **1969**, *42*, 90–93.

[393] Romanowski, S. J.; Kinart, C. M.; Kinart, W. J. *J. Chem. Soc. Faraday Trans.* **1995**, *91*, 65–70.

[394] Chauhan, M. S.; Kumar, G.; Chauhan, S.; Gupta, S. *Indian J. Chem. A* **2004**, *43*, 734–738.

[395] Yao, N. P.; Bennion, D. N. *J. Electrochem. Soc.* **1971**, *118*, 1097–1106.

[396] Bakshi, M. S.; Singh, J.; Kaur, H.; Ahmad, S. T.; Kaur, G. *J. Chem. Eng. Data* **1996**, *41*, 1459–1461.

[397] Casteel, J. F.; Sears, P. G. *J. Chem. Eng. Data* **1974**, *19*, 196–200.

[398] Gregory, A. P.; Clarke, R. N. *Meas. Sci. Technol.* **2005**, *16*, 1506–1516.

[399] Barthel, J.; Neueder, R. Conductivities, transference numbers, and limiting ionic conductivities of protophilic H-bond donor and aprotic solvents. II: Aprotic solvents, except amides. In *Electrolyte Data Collection (Part 1h)*; Kreysa, G., Ed.; DECHEMA: Frankfurt, 2003; Vol. XII, p 9.

[400] Svedberg, T. *Nature (London, U. K.)* **1937**, *139*, 1051.

[401] Tanford, C. *Adv. Protein Chem.* **1970**, *24*, 1.

[402] Schellman, J. A. *Biophys. Chem.* **2002**, *96*, 91.

[403] Mason, P. E.; Neilson, G. W.; Dempsey, C. E.; Barnes, A. C.; Cruickshank, J. M. *Proc. Natl. Acad. Sci. U.S.A.* **2003**, *100*, 4557.

[404] Scott, J. N.; Nucci, N. V.; Vanderkooi, J. M. *J. Phys. Chem. A* **2008**, *112*, 10939.

[405] Mason, P. E.; Neilson, G. W.; Kline, S. R.; Dempsey, C. E.; Brady, J. W. *J. Phys. Chem. B* **2006**, *110*, 13477.

[406] Casteel, J. F.; Amis, E. S. *J. Chem. Eng. Data* **1972**, *17*, 55.

[407] Capewell, S. G.; Buchner, R.; Hefter, G.; May, P. M. *Phys. Chem. Chem. Phys.* **1999**, *1*, 1933.

[408] Schrödle, S.; Wachter, W.; Buchner, R.; Hefter, G. *Inorg. Chem.* **2008**, *47*, 8619.

[409] Mason, P. E.; Neilson, G. W.; Enderby, J. E.; Saboungi, M.-L.; Dempsey, C. E.; MacKerell, A. D.; Brady, J. W. *J. Am. Chem. Soc.* **2004**, *126*, 11462.

[410] Runde, W.; Neu, M. P.; Van Pelt, C.; Scott, B. L. *Inorg. Chem.* **2000**, *39*, 1050.

[411] Marcus, Y. *Ion Properties*; Marcel Dekker: New York, 1997.

[412] Barthel, J.; Hetzenauer, H.; Buchner, R. *Ber. Bunsenges. Phys. Chem.* **1992**, *96*, 1424.

Regensburg, den 21. Dezember 2009

Johannes Hunger